CHARACTERISTICS OF HYPERSONIC WING-ELEVON-COVE FLOWS

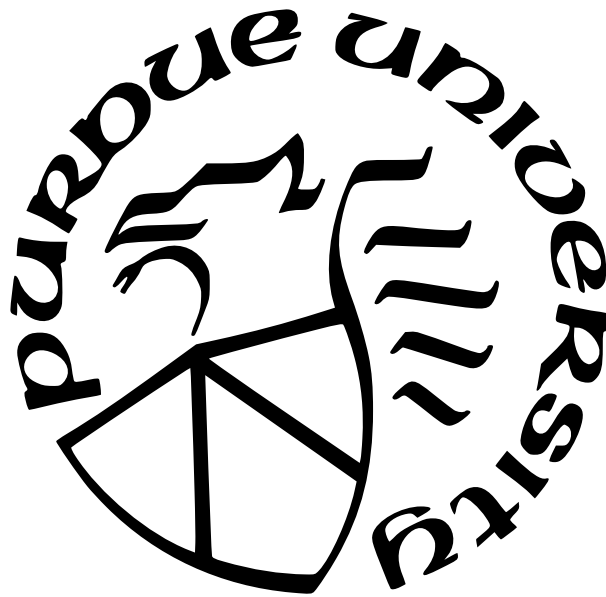by

Robert Anthony Alviani

A Dissertation

Submitted to the Faculty of Purdue University

In Partial Fulfillment of the Requirements for the degree of

Doctor of Philosophy

School of Aeronautics and Astronautics

West Lafayette, Indiana

December 2022

THE PURDUE UNIVERSITY GRADUATE SCHOOL
STATEMENT OF COMMITTEE APPROVAL

Dr. Jonathan Poggie, Co-Chair

School of Aeronautics and Astronautics

Dr. Gregory Blaisdell, Co-Chair

School of Aeronautics and Astronautics

Dr. Joseph Jewell

School of Aeronautics and Astronautics

Dr. Sally Bane

School of Aeronautics and Astronautics

Approved by:

Dr. Gregory Blaisdell

To Myles, Rob, and Dan

ACKNOWLEDGMENTS

I will first acknowledge and thank Dr. Jonathan Poggie and Dr. Gregory Blaisdell for advising me through my PhD at Purdue University. With their guidance, I have been able to flourish as a researcher and an engineer. This is especially commendable when done during the COVID-19 pandemic. I would also like to thank my advisors for bringing me onto the team and providing funding for my research, tuition, and travel while at Purdue (see below). This acknowledgement extends to Purdue University for supplementing this funding, for one year, by awarding me the Ross Fellowship. I appreciate the other members of my PhD committee, Dr. Joseph Jewell and Dr. Sally Bane, who helped facilitate this work. Lastly, I will acknowledge Dr. William Crossley and the Purdue School of Aeronautics and Astronautics facility for providing a fulfilling educational curriculum.

Thank you to my mother, Francesca, my father, Michael, my brothers, Chris and Nick, and thank you Jimmy, Kathy, and my godmother, Anne Marie Petrock, for all inspiring me throughout my entire life. Thank you to my friends and colleagues at Purdue, Akshay Deshpande, Jonathan Gaskins, Andrew Shuck, Devon Fano, Ian Hall, Laura Holifield, and many others. Thank you to old friends who kept in touch, Laith Abwini, Jess Obrien, Allie and Andrew Wilford, Kevin Subramanian, and Christopher Sholy, and thank you to the rest of my friends and family, as well as those we lost along the way. Last, but not least, thank you Millie the dog for providing unconditional love and support at any time of the day.

TABLE OF CONTENTS

LIST OF TABLES

LIST OF FIGURES

11

ABBREVIATIONS

AFOSR	Air Force Office of Scientific Research
AFRL	Air Force Research Laboratory
ARL	Army Research Laboratory
ASL	Purdue Aerospace Sciences Lab
BAM6QT	Boeing/AFOSR Mach-6 Quiet Tunnel
DoD	Department of Defense
DSRC	DoD Supercomputing Resource Center
ERDC	Army Engineer Research and Development Center
HPCMP	High Performance Computing Modernization Program
NASA	The National Aeronautics and Space Administration
TALon	Tennessee Aerothermodynamics Laboratory
TSP	Temperature Sensitive Paint
UTSI	The University of Tennessee Space Institute

ABSTRACT

Hypersonic flight vehicle development heavily relies on continued research focused on hypersonic flows. The prediction of aerothermodynamic loading, i.e., surface pressure and heat transfer, under flight conditions is a fundamental design requirement. However, hypersonic flight involves severe flowfield environments and complex flow phenomena which require specific experimental considerations or the use of computational fluid dynamics to accurately characterize. The Reynolds numbers and Mach numbers in hypersonic flight are high, and the hypersonic regime is generally associated with large levels of aerothermodynamic loading. Shock-wave/boundary-layer interactions also occur near flight vehicle surfaces, such as leading-edges and control surfaces. These interactions have a significant influence on vehicle performance and introduce large-scale flow separation, unsteadiness, and increased aerothermodynamic loading. The low-frequency behavior of the unsteady shock-motion is a concern for hypersonic flight vehicles because the oscillations produce prolonged fluctuations of intense aerothermodynamic loadings and can lead to structure failure. Therefore, research on shock-wave/boundary-layer interactions has clear practical applications in the development of hypersonic flight vehicles, and by studying their characteristics, a better understanding of fundamental design requirements can be obtained.

These interactions are strongly determined by the local geometry of the flight vehicle. Small physical deviations from smooth aerodynamic surfaces can significantly affect the flowfield and resultant aerothermodynamic loading. Most studies focused on hypersonic flows, however, employ simplified surface geometries as a necessary requirement to facilitate the experiment. This routine idealization leads to overlooking geometric imperfections and ignoring their effects on the local flowfield, which introduces discrepancies between experimental and flight parameters. Relevant geometric imperfections encompass any deviations from a smooth aerodynamic surface, such as roughness, steps, gaps, and cavities. Hypersonic gaps have limited available research and are prevalent on flight vehicles. Gaps found near control surfaces are large enough to significantly alter the flow structure, shock-wave/boundary-layer interaction, and aerothermodynamic loading. A need therefore exists for investigation of geometric imperfections in hypersonic flight, specifically for gaps and cavities.

16

This dissertation covers a computational investigation into hypersonic flight vehicle geometric imperfections, with a focus on wing-elevon-cove configurations. The primary region of focus for the overall research was the cove region at the juncture of the main wing element and the elevon. This region is associated with the shock-wave/boundary-layer interaction produced by the control surface deflection. There also exists a centrifugal instability at the cove, due to streamline curvature, which is associated with the production of Görtler vortices. The content includes three projects revolving around hypersonic wing-elevon-cove flows. These flows were computed with improved delayed detached-eddy simulation.

The first project was a computational investigation simulating the NASA experimental study done by W.D. Deveikis and W. Bartlett in 1978. This experiment consisted of hypersonic high Reynolds number wind tunnel tests for a shuttle-type reentry vehicle. The computational aerothermodynamic surface loadings for this project were compared to the experimental published data. Grounded with the agreement with mean surface data, this project expanded on the topics explored in the experimental study to include topics such as flow visualization and statistical analysis. The second and third project are extensions of this work and were done in collaboration with Purdue University and the University of Tennessee Space Institute (UTSI). A swept wing-elevon-cove model was designed by Carson Lay, of Purdue University, and is currently being employed in ongoing experiments in the Purdue Boeing/AFOSR Mach 6 Quiet Tunnel (BAM6QT) and at the Tennessee Aerothermodynamics Laboratory (TALon). A computational investigation on hypersonic high Reynolds number wing-elevon-cove flows was conducted with this model, where both corresponding experimental facility conditions were employed. At this time, the experimental data are limited; however, future experimental and computational collaboration is expected.

The motivation behind this research was to expand the knowledge on hypersonic wing-elevon-cove flows, gap heating, and the low-frequency unsteadiness in shock-wave/boundary-layer interactions. Therefore, the intended goal of this work was to provide an accurate characterization of the three hypersonic wing-elevon-cove flows. This was accomplished by using computational data to produce flowfield visualizations, analyze aerothermodynamic loadings, and conduct statistical flow analyses. The results on the three hypersonic wing-elevon-cove computations are presented, analyzed, and discussed throughout this dissertation.

1. INTRODUCTION

With the current enthusiasm to develop hypersonic flight vehicles, such as NASA's X-43A concept vehicle shown in Figure 1.1, there is an emerging need for increased research efforts focused on hypersonic flows. Accurate characterization of hypersonic flow provides reliable prediction of the resultant aerothermodynamic loading, i.e., surface pressure and heat transfer, which is a fundamental requirement for flight vehicle design [1]–[3]. Both experimental and computational techniques for simulating aerothermodynamic loads in flight have been developed and improved simultaneously over the last century [4]–[6]. However, the hypersonic regime introduces severe environments and complex flow phenomena, which require specific experimental considerations or the use of high fidelity computational fluid dynamics to accurately characterize. Shock-wave/boundary-layer interactions, for example, have significant influence on vehicle performance by introducing large-scale flow separation, unsteadiness, and increased aerothermodynamic loading [7], [8]. Wind tunnel experiments can capture these interactions but are costly. Measurements of important quantities, such as turbulent statistics, e.g., $\overline{u_i' u_i'}$, can also be challenging to obtain, especially near surfaces. Complications that also affect experimental studies include wind tunnel surface boundary-layer interference, freestream turbulence levels, and other physical limitations [9]–[13].

Research on hypersonic flows has heavily relied on computational fluid dynamics, due to these experimental complications. Computational fluid dynamics facilitates targeted measurement and flexibility, provides full flowfield data collection, and produces results in shorter timeframes compared to wind tunnel experiments. However, in order to obtain statistically significant results in a hypersonic simulation, large computational resources are required. This is a consequence of the scaling with Reynolds number for high fidelity simulations. The computational cost of direct numerical simulation scales proportionally with Re^3, and wall-resolved large-eddy simulation scales proportionally with $Re^{2.4}$ [14]–[17]. Computations also have varying degree of accuracy and uncertainty, depending on the computational model and mesh resolution. Therefore, the collaboration between experimental and computational studies can be useful, as the advantages of both can be utilized in order to provide the full characterization of hypersonic flows.

Figure 1.1. Concept image of the NASA X-43A hypersonic vehicle [18].

The hypersonic flow regime is generally associated with large Reynolds numbers, high Mach numbers, and intense aerothermodynamic loading. In addition, shock-wave/boundary-layer interactions occur at various flight vehicle surfaces, such as leading-edges and control surfaces, and produce regions of surface loading maxima. These interactions are strongly determined by the geometry of the flight vehicle. Local physical discrepancies between flight vehicle geometry and the experimental model can lead to inaccurate simulation of the flow characteristics. However, the routine idealization of surface models is done as a necessary requirement to facilitate experimental and computational research. Consequently, this idealization may overlook geometric imperfections and ignore their effects on the local shock-wave/boundary-layer interaction and the overall flowfield.

Relevant geometric imperfections encompass any deviations from a smooth aerodynamic surface, such as roughness, steps, gaps, and cavities. These "imperfections" are generally thermo-structural design features and not necessarily accidents of manufacturing. For instance, gaps in panels allow for thermal expansion to avoid buckling. Research on roughness has strongly focused on its effect on boundary-layers and transition [19]–[25]. Gaps and cavities have comparatively limited research, are prevalent on flight vehicles, and are large enough to significantly alter the flow structure, shock-wave/boundary-layer interaction, and

resultant aerothermodynamic loading. Therefore, a need exists for further investigation of geometric imperfections in hypersonic flight, specifically for gaps and cavities, in order to better understand their resultant effects on the flowfield.

One example of the importance of research on geometric imperfections can be found with hypersonic gap heating. It is required to have reliable prediction of local aerothermodynamic loading in hypersonic flows in order to define thermal protection systems [26]–[29]. Research on hypersonic gaps have universally shown localized regions of high aerothermal heating inside of gap environments [30]–[34]. This aerothermal heating depicts positive correlation with increasing gap size, angle of attack, and Reynolds number [30], [35], [36]. Factors that also significantly affect the gap aerothermal heating include the boundary-layer state, local surface geometry, and the presence of separation or shock-waves [37]–[39]. Without the accurate representative of hypersonic flight vehicle geometry, these local regions of aerothermal gap heating would go unprotected and could lead to structural failure.

Hypersonic gap-induced surface heating research can be traced back to the space exploration orbiter missions. As space travel requires hypersonic reentry, regions of maximum aerothermal heating pose significant flight risks. This research led to the strategic placement of thermal protection tiles [2], [40], [41]. During this time, a large focus of gap heating research was conducted on the "cove" region on the shuttle. The cove region is the gap between the wing and elevon, which is required for smooth control surface movement, and exists for any flight vehicle with control surfaces. This research corresponded to shuttle-type vehicles, such as the United States Endeavour, provided in a photograph in Figure 1.2. The cove environment for this spacecraft, located at the juncture of the main wing element and the elevon, is also provided with two photographs in Figure 1.3. This figure displays a close-up view of the trailing-edge of the wing-elevon-cove for the Endeavour.

In the NASA hypersonic wing-elevon-cove studies, the regions inside and around the cove were shown to experience locally high aerothermal heating [42]–[45]. In order to reduce this heating, novel cove sealing technologies were designed and implemented. A schematic of the special type of cove sealing technologies, which were developed to reduce this aerothermodynamic loading in the cove environment, is provided in Figure 1.4. This type of innovation depicts the practicality of research on hypersonic geometric imperfections.

Figure 1.2. The United States Space Shuttle Endeavour. Photograph taken by Robert Alviani, California Science Center, Jan. 8th, 2022.
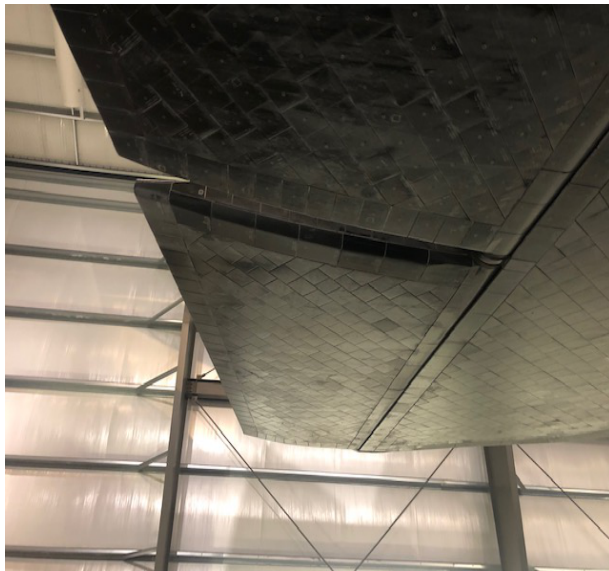
(a) Trailing-edge wing and elevon.

(b) Wing-elevon-cove juncture.

Figure 1.3. Close-up views of the Endeavour wing-elevon-cove region. Photographs taken by Robert Alviani, California Science Center, Jan. 8th, 2022.
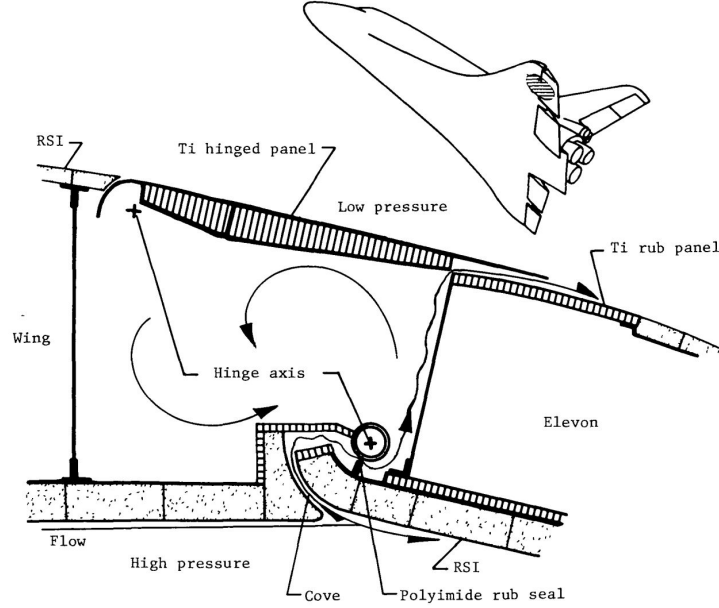
Figure 1.4. Schematic of the NASA shuttle-type wing-elevon-cove sealing technology developed to reduce aerothermal heating loads [42].

1.1 Shock-Wave/Boundary-Layer Interaction

Shock-wave/boundary-layer interactions are often characterized as unsteady and highly three-dimensional. These interactions introduce low-frequency flowfield oscillations, large-scale flow separation, and exceedingly high aerothermodynamic loading [8], [46], [47]. Shock-wave/boundary-layer interactions are determined by the local surface geometry, flowfield properties, and the upstream boundary-layer state. For example, the important parameters associated with compression ramp shock-wave/boundary-layer interactions, e.g., separation vortex size, shock angle, and reattachment position, are determined by the ramp deflection and the local boundary-layer properties [48]–[51]. The characteristics of a backwards-facing step, or reattaching shear-layer, shock-wave/boundary-layer interaction is similarly determined by the size of the step and the upstream boundary-layer state [52]–[57]. Local geometric changes will alter the flow behavior, characteristics, and structure of these interactions. The introduction of increased geometric complexity will also strongly affect these

interactions. For instance, the inclusion of sidewalls or a deflected downstream surface will produce vastly different shock-wave/boundary-layer interaction characteristics [50], [54].

Unsteadiness plays a critical role in shock-wave/boundary-layer interaction. This unsteadiness significantly affects the instantaneous flowfield characteristics and the resultant surface loading. The unsteady oscillations of the shock-wave induce prolonged fluctuations of locally high aerothermodynamic loading, which can lead to structural failure. In addition, large-scale turbulent structures, such as Görtler vortices, are produced in regions of shock-wave/boundary-layer interaction. The unsteadiness of these interactions are often characterized by their spectral content. Spectral analyses of shock-wave/boundary-layer interactions have universally depicted their low-frequency behavior [46], [47], [52], [58]–[60]. For further context, the surface pressure spectra in regions of shock-wave/boundary-layer interaction display frequency content orders of magnitude lower than the frequency content of the incoming turbulent boundary-layer. The temporal scale of the low-frequency motion is $\mathcal{O}(10 - 100\delta/U_\infty)$, compared to the characteristic temporal scale of $\mathcal{O}(\delta/U_\infty)$ for the upstream turbulent boundary-layer [61].

Analyses of time-resolved flows have depicted the coherent correlated movement of the low-frequency shock system [46], [47], [52], [62]–[71]. For instance, the unsteady shock-motion of a compressible reattaching shear-layer is driven by vortex shedding of the compressible shear-layer [52], [65]–[67], the large-scale expansion and contraction of the separation region [47], [68]–[70], and the turbulence of the upstream boundary-layer [62], [63], [71]. The influence of these components on the shock system is contested and strongly depends on the interaction. Research indicates that this unsteadiness may be, in part, driven by the unsteadiness of the upstream turbulent boundary-layer [46], [63], [72]. This research provides evidence of high correlation between the upstream unsteadiness and the separation shock unsteadiness. This dependence has shown proportionality to the strength of the shock-wave/boundary-layer interaction, i.e., weaker interactions are more strongly affected by the upstream boundary-layer. There are other experiments, however, which argue that the shock-motion is driven by the instability of the separation vortex [64], [69]. Overall, the characteristic nature and the underlying mechanisms associated with shock-wave/boundary-layer interaction unsteadiness are still largely unknown.

1.1.1 Compression Ramp

Control surface deflection on a hypersonic flight vehicle produces a shock-wave/boundary-layer interaction which is similar to a compression ramp. A schematic of a generic compression ramp shock-wave/boundary-layer interaction is provided in Figure 1.5. This compression ramp interaction covers the basic components of a shock-wave/boundary-layer interaction. These components consist of an upstream boundary-layer, a large-scale separation region, shock-waves, and a separated shear-layer [48], [49]. In this type of interaction, the upstream boundary-layer separates ahead of the downstream deflected ramp. When the boundary-layer separates, a region of recirculation is created beneath the shear-layer. Due to the boundary-layer deflection, compression waves form in the boundary-layer, which coalesce downstream into the separation shock. At reattachment, compression waves are formed again as the boundary-layer is redirected to align with the deflected ramp angle. These waves coalesce and form the reattachment shock. The regions of separation produce large aerothermodynamic loading. Through the interaction on the flat surface, there is a characteristic increase of surface pressure, followed by a surface pressure plateau. On the deflected surface, there is a large increase of pressure, and heat transfer, produced as the boundary-layer reattaches and redevelops along the downstream surface. The low-frequency unsteadiness in compression ramp shock-wave/boundary-layer interaction is associated with the oscillations of the separation and reattachment shock-waves, as well as the large-scale expansion and contraction of the separation vortex [50], [73], [74].
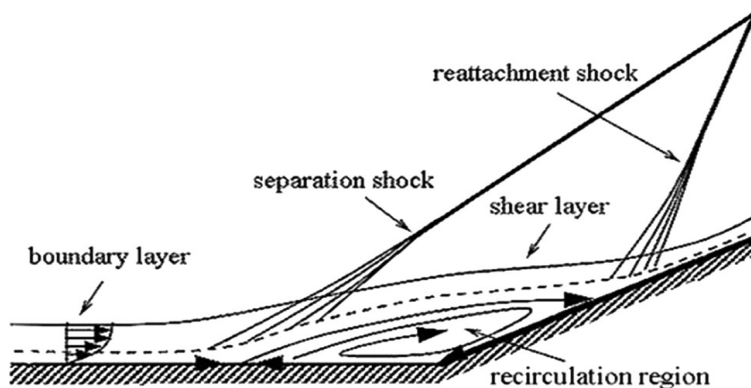
Figure 1.5. Schematic of a compression ramp shock-wave/boundary-layer interaction [51]. Included with permission from the author.

1.1.2 Backwards-Facing Step

A backwards-facing step, or a reattaching compressible shear-layer, shock-wave/boundary-layer interaction can be found in gap regions of hypersonic flight vehicles. A schematic of the general components of a backwards-facing step shock-wave/boundary-layer interaction is provided in Figure 1.6. These components include the upstream boundary-layer, a separated shear-layer, an expansion-fan region, a recirculation region, and a reattachment shock. The upstream boundary-layer separates at the immediate face of the step. There is an expansion-fan created as the boundary-layer deflects downward. A large-scale recirculation region is produced, which is separated from the boundary-layer by the shear-layer. As the separated boundary-layer reattaches downstream, multiple compression waves form and then coalesce to create the reattachment shock. For this interaction, large aerothermodynamic surface loading is found at reattachment, similarly to the compression ramp [55]. Large-scale coherent structures are produced by the Kelvin-Helmholtz instability of the separated shear-layer, which propagate downstream in the redeveloping boundary-layer [75]–[77]. In general, the shock-wave/boundary-layer interaction is unsteady and produces low-frequency dominated spectra in the shock system [52], [53], [56]. The shock-motion for this interaction is driven as the shear-layer oscillates vertically, in a flapping motion, and as the separation region expands and contracts [50], [54].
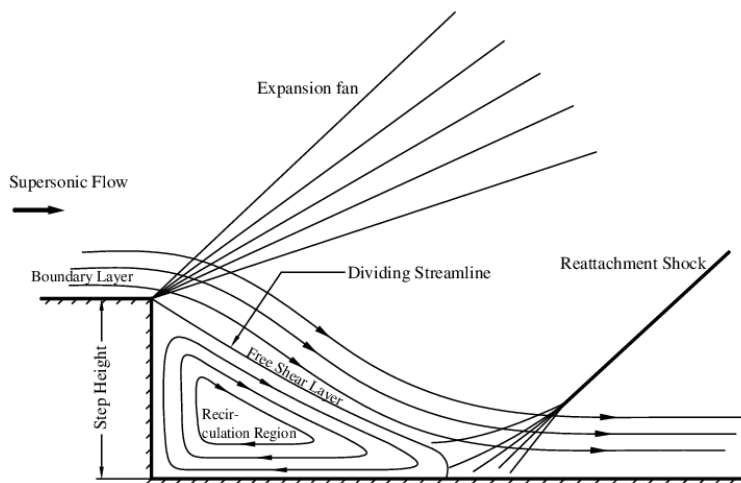
Figure 1.6. Schematic of a backwards-facing step shock-wave/boundary-layer interaction [57]. Included with permission from the author.

1.1.3 Wing-Elevon-Cove

This dissertation covers hypersonic wing-elevon-cove shock-wave/boundary-layer inter-actions. These interactions comprise a combination of a backwards-facing step and a com-pression ramp shock-wave/boundary-layer interaction, similar to a flame holder [47], [53], [54], [65] or a backwards-facing step-ramp [78]. In addition, the internal cavity, or cove, allows for flow to exit the separation vortex, which further complicates the flow structure. Schematics of two wing-elevon-cove shock-wave/boundary-layer interactions are provided in Figure 1.7. This figure depicts two different flow situations, one where there is no cove leak-age (left), i.e., flow is not allowed to exit through the cove, and one with full cove leakage (right), i.e., flow is allowed to exit through the cove region. The general structure of the shock-wave/boundary-layer interaction contains the same components previously discussed, which include a separated shear-layer, a separation vortex, shock-waves, and boundary-layer separation/reattachment. With cove sealing, the flowfield resembles the backwards-facing step-ramp configuration. This is seen in the left figure, where the boundary-layer separates and reattaches, creating a reattachment shock-wave. There is no flow through the cove here. Without the cove sealing, seen in the right figure, the flow is allowed to enter the cavity and produces divergent streamlines at reattachment. The qualitative changes in flow structure are seen between these figures, where cove sealing affects the shock-angle, the shape and size of the separation vortex, and the reattachment location.
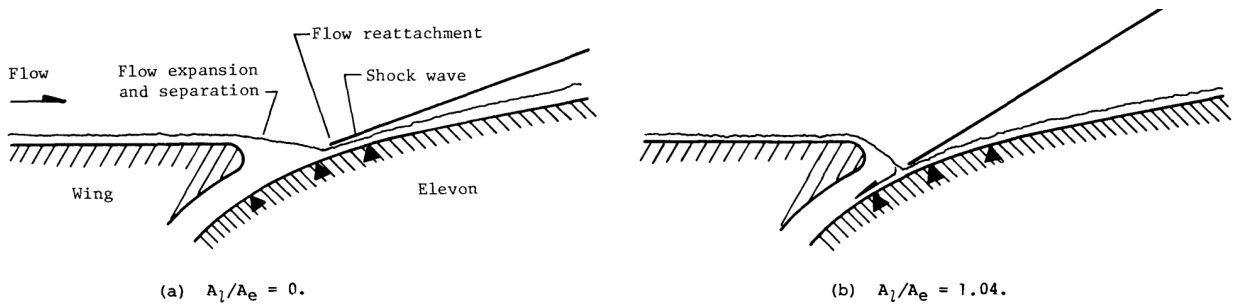
Figure 1.7. Schematic of a wing-elevon-cove shock-wave/boundary-layer in-teraction for a sealed (left) and non-sealed (right) cove [42].

1.2 Flow Instabilities

Natural flow instabilities are associated with the generation of turbulence and turbulent structures [79]. These flow instabilities exist in separated shear-layers and at flow separation and reattachment. The fixed Kelvin-Helmholtz flow instability in backwards-facing step flows, for example, produces vortices in the separated shear-layer. Non-fixed instabilities exist at boundary-layer separation and reattachment in compression ramps, which are associated with the Kelvin-Helmholtz instability, in the separated shear-layer, and a centrifugal instability, due to streamline curvature. These instabilities lead to the generation, propagation, and growth of turbulent structures in the redeveloping boundary-layer, such as Görtler vortices. These structures significantly affect the resultant flowfield and flow characteristics. In addition, improved delayed detached-eddy simulation does not resolve turbulence in the upstream boundary-layer, and as a result, the onset of unsteadiness in computations is reliant on these flow instabilities.

1.2.1 Kelvin-Helmholtz Instability

The Kelvin-Helmholtz instability exists in a shear flow, where two regions of different flow conditions interact [79]. The mechanism of unsteady vortex generation is depicted in Figure 1.8. In this figure, two regions of flow with differing velocities mix and produce vortices through linear and non-linear growth regions. This instability is also relevant for supersonic flows. For instance, the separated shear-layer in a compression ramp shock-wave/boundary-layer interaction produces downstream vortices as a result of the Kelvin-Helmholtz instability [75], [76], [80]. This instability also exists at the trailing-edge of a wing or control surface, as the boundary-layer sheds from the structure. The growth of the shear-layer is strongly dependent on the local flowfield and the nature of the shock-wave/boundary-layer interaction [52], [65]–[67]. For wing-elevon-cove shock-wave/boundary-layer interactions, the Kelvin-Helmholtz instability is partially responsible for the onset of unsteadiness in the cove region, like compression ramps; however, centrifugal instabilities are known to have a larger effect [81]–[85].
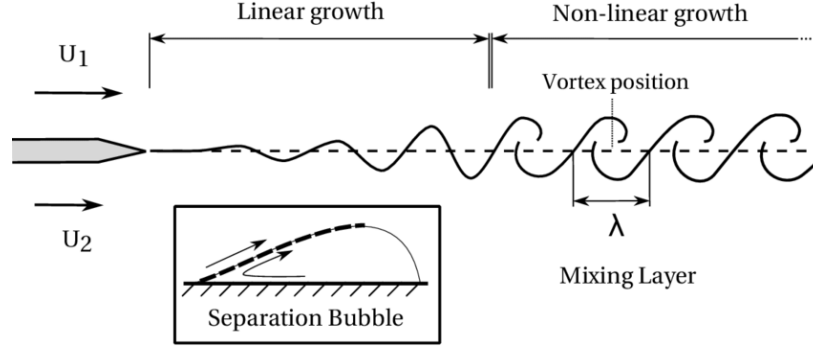
Figure 1.8. Schematic of the Kelvin-Helmholtz instability mechanism in a shear-layer flow [86]. Included with permission from the author.

1.2.2 Görtler Centrifugal Instability

Wall-bounded boundary-layers developing on surfaces with concave curvature are influenced by a natural centrifugal instability mechanism [81]–[85]. This type of flow can be found on many aerodynamic surfaces, e.g., airfoils and fuselages. This instability produces counter-rotating vortices, known as Görtler vortices, that are orientated in the streamwise direction. These vortices are three-dimensional and produce spanwise variation in the boundary-layer. Research on this instability in low-speed flow was first done by Görtler, where the linear evolution of Görtler vortices was investigated [87]. This research was expanded on by employing normal mode analysis [88], [89], resulting in a real eigenvalue problem, with three parameters,

$$F(\mathcal{G}, \beta, \sigma) = 0. \tag{1.1}$$

The three characteristic parameters associated with the instability mechanism are the Görtler number, $\mathcal{G}$, the wave number β, and the growth rate σ. The Görtler number, $\mathcal{G}$, is inversely proportional to the radius of curvature, $\mathcal{R}$, and represents a measure of the influence of centrifugal effects. The spacing between the adjacent vortices, λ, is inversely related to the wave number, and the growth rate is related to flow stability. The Görtler number, based on boundary-layer thickness, δ, is defined as

$$\mathcal{G} = Re_\delta \left(\frac{\delta}{\mathcal{R}} \right)^{1/2}. \qquad (1.2)$$

Higher Görtler numbers are associated with the onset of this centrifugal instability, whereas lower values suggest stable flows [90], [91]. However, as the normal mode analysis was applied to laminar boundary-layers, rather than general flows, and there are no thresholds available for the present application, these parameters are generally used as initial guidelines for investigation.

Görtler vortices in a boundary-layer developing on a concave surface are depicted in Figure 1.9. The boundary-layer height is δ, the vortices are separated by the distance λ, and the surface curvature has a radius of curvature $\mathcal{R}$. The Görtler vortices are contained within the boundary-layer height and develop near the surface. The streamlines on the vortices depict the counter-rotation of adjacent vortices. In hypersonic flows, the locations between these adjacent vortices experience near-stagnation flow, where exceedingly large aerothermal heating occurs [73], [74], [90], [91]. These stagnation locations also leave characteristic heat flux streaks on surfaces, which have been ubiquitously observed in hypersonic flows where these vortices are present.

Concave surface curvature is not required for Görtler vortex development. Streamline curvature can produce the same centrifugal instability that results in the production of Görtler vortices [73], [74], [90], [91]. There is large streamline curvature associated with compression ramp, backwards-facing step, and wing-elevon-cove shock-wave/boundary-layer interactions. The streamline curvature is produced at reattachment for these interactions. The production of streamline curvature for a compression ramp is displayed in the schematic provided in Figure 1.10. In this figure, the streamline curvature created as the boundary-layer separates and consequently reattaches downstream is depicted. There are three separate contested definitions of the relevant radius of streamline curvature shown here. In general, however, the primary streamline curvature is associated with the shear-layer turning as it reattaches, seen in the left diagram. Therefore, reattachment is associated with the production of Görtler vortices in many hypersonic compression ramp interactions [90], [92]–[94].
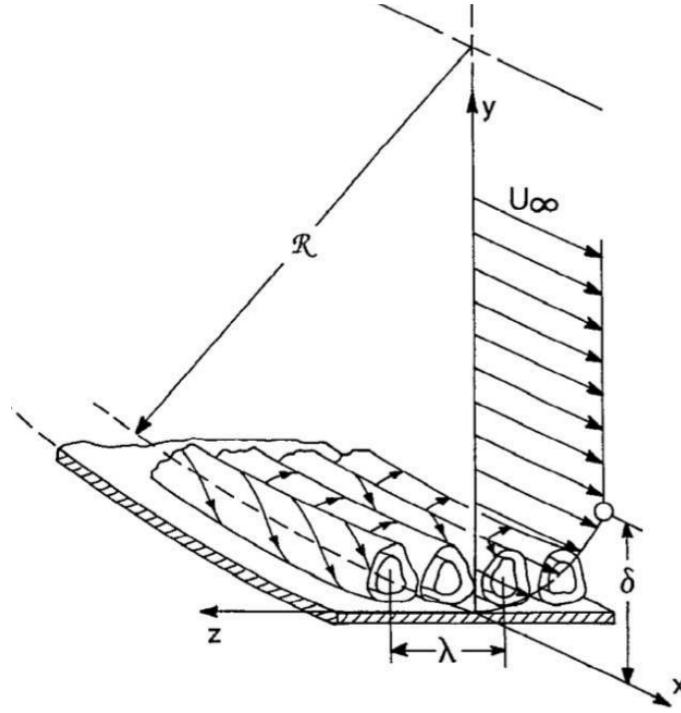
Figure 1.9. Schematic of Görtler vortices in a boundary-layer on a concave wall [88]. Included with permission from the author.
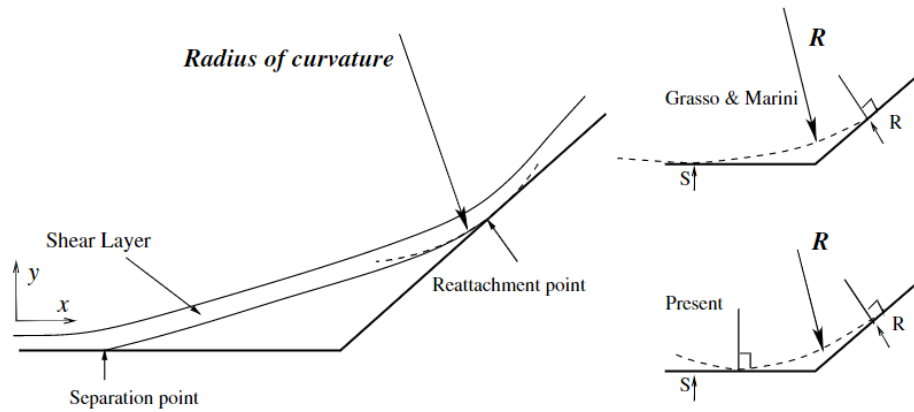
Figure 1.10. Schematic of the concave streamline curvature at boundary-layer reattachment [90]. Included with permission from the author.

Görtler vortices in hypersonic flows are associated with locally high regions of aerothermal heating and characteristic streak formations [90], [92]–[94]. These hypersonic streak formations are prevalent downstream of shock-wave/boundary-layer interactions with positive streamline curvature, such as compression ramps, backwards-facing steps, and wing-elevon-coves. As the boundary-layer reattaches and develops downstream of the compression ramp separation, characteristic streaks are often observed as a result of Görtler vortices. These streaks are produced by the nodal locations between adjacent vortices, which act similarly to a stagnation flow region on the surface and produce exceedingly high levels of aerothermodynamic loading [90]. An experimental example of these streak formations is provided in Figure 1.11. This figure displays an oil-flow visualization of the surface loading for a Mach 7.5 compression ramp [91]. The coherent boundary-layer reattachment line, the shock-impingement line, and the characteristic streak formations are all depicted here. These streaks are highlighted in this figure due to their effect on the local aerothermodynamic loading, which is a major concern for hypersonic flight vehicles.
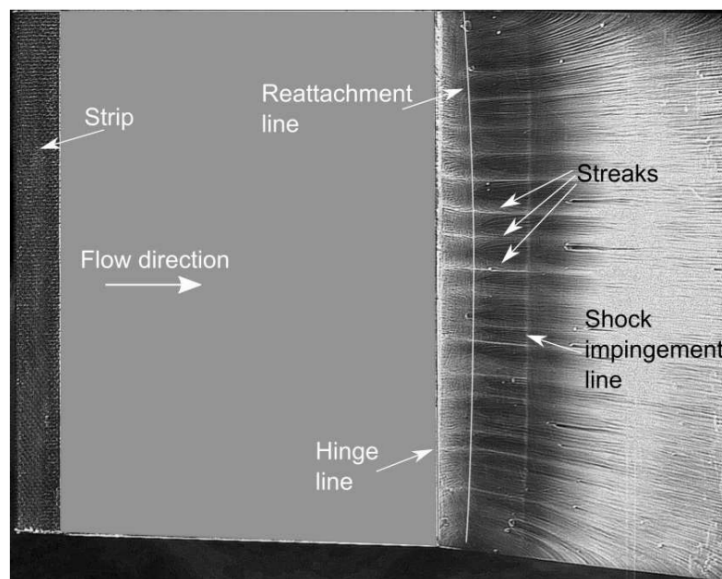
Figure 1.11. Oil-flow visualization of the surface loading for a Mach 7.5 compression ramp [91]. Included with permission from the author.

1.3 Dissertation Overview

This dissertation comprises three related projects on hypersonic wing-elevon-cove flows. The primary region of focus for the overall research was the cove at the juncture of the main wing element and the elevon. The motivation was to expand the knowledge on hypersonic wing-elevon-cove flows, gap heating, and the low-frequency unsteadiness in shock-wave/boundary-layer interactions. The overall goal was to do this by providing an accurate characterization of hypersonic wing-elevon-cove flows. This was accomplished by employing computational data to produce flowfield visualizations, analyze aerothermodynamic loadings, and conduct statistical flow analyses. These results are discussed throughout this dissertation and correspond to the three wing-elevon-cove projects.

The three wing-elevon-cove projects were computationally simulated with improved delayed detached-eddy simulation. The first project was a computational investigation of the wing-elevon-cove juncture of a generic space shuttle structure, based on an experimental study done by W. D. Deveikis and W. Bartlett in 1978 [42]. This project compares computational results to the experimental published data and expands on the original experimental study in several meaningful ways, e.g., flow visualization and statistical analysis. The second and third project are an extension of this work and were done in collaboration with Purdue University and the University of Tennessee Space Institute (UTSI). A wing-elevon-cove model was developed by Carson Lay, of Purdue University. The model is currently being employed in ongoing experiments in the Purdue Boeing/AFOSR Mach 6 Quiet Tunnel (BAM6QT) and at the Tennessee Aerothermodynamics Laboratory (TALon). A computational investigation was done for each of these wind tunnels, and for clarity, these studies are separated into two projects.

The general overview of this dissertation is as follows. Chapter 1 provided the introduction to the problem of geometric imperfections in hypersonic flows and the need to expand research in the area. Chapter 2 outlines the three major projects that are involved in this research. First, overviews of the governing fluid dynamics equations and the data analysis techniques are provided. The experimental facilities associated with the projects are then discussed, with a brief description of each facility's respective capabilities. Next, the

computational methodologies of the research for this dissertation are provided in detail, which include information on the employed flow conditions and computational meshes. The next three chapters contain the results and discussions of each of the three wing-elevon-cove projects, in comprehensive detail. Chapter 3 provides the research and data analyses associated with the first project. Chapter 4 provides the computational results of the Purdue swept wing-elevon-cove model in the Purdue BAM6QT flow conditions. Chapter 5 provides a similar computational investigation, employing the center portion of the Purdue wing-elevon-cove model in the UTSI TALon flow conditions. The last chapter, Chapter 6, contains the overview, discussion, and concluding remarks on this research.

2. METHODOLOGY

The research contained in this dissertation comprise an overall computational investigation on the characteristics of three hypersonic wing-elevon-cove flows. This chapter provides an overview of the research methodologies associated with these three projects, such as the computational and experimental configurations. First, the numerical formulations for the computations and the statistical data analysis techniques are outlined. This includes the governing equations of the computational fluid dynamics models, such as the Navier-Stokes equations, as well as the statistical tools employed, such as power spectral density and coherence. The research methodologies for the three hypersonic wing-elevon-cove projects are then discussed. An overview of the associated experimental studies and facilities is provided, and then the methodologies associated with the computational studies, including computational meshes and freestream flow conditions, are outlined.

2.1 Governing Equations and Data Analysis

The governing equations employed for these computations are the compressible Navier-Stokes equations. Derived from the conservation of mass, momentum, and energy, the Navier-Stokes equations dictate the nature of fluid dynamics [95]. The three-dimensional compressible Navier-Stokes equations, in differential form, are

$$\frac{\partial \rho}{\partial t} + \frac{\partial(\rho u_{\mathrm{j}})}{\partial x_{\mathrm{j}}} = 0, \tag{2.1}$$

$$\frac{\partial(\rho u_{\mathrm{i}})}{\partial t} + \frac{\partial(\rho u_{\mathrm{i}} u_{\mathrm{j}} + p\delta_{\mathrm{ij}})}{\partial x_{\mathrm{j}}} = \frac{\partial \tau_{\mathrm{ij}}}{\partial x_{\mathrm{j}}}, \tag{2.2}$$

and

$$\frac{\partial(\rho \mathrm{e})}{\partial t} + \frac{\partial(\rho \mathrm{e} u_{\mathrm{j}} + p u_{\mathrm{j}})}{\partial x_{\mathrm{j}}} = \frac{\partial(\tau_{\mathrm{ji}} u_{\mathrm{i}} - q_{\mathrm{j}})}{\partial x_{\mathrm{j}}}. \tag{2.3}$$

These equations are the conservation equations. Equation (2.1) is the conservation of mass, (2.2) is the conservation of momentum, and (2.3) is the conservation of energy. The

variables, in order of appearance, are density, ρ, velocity, u_j, viscous stress, τ_{ij}, pressure, p, energy plus kinetic energy (per unit mass), e, and heat flux, q_j.

By applying Fourier's law [96], heat flux can be represented as the conduction of energy due to temperature gradients. Similarly, Newton's constitutive law [95] provides proportionality of the viscous stress tensor to flow velocity gradients; if the flow is incompressible, then the viscous stress is directly proportional to the flow strain rate, S_{ij}. The Fourier's law and Newton's constitutive law are

$$q_j = -k \frac{\partial T}{\partial x_j} \tag{2.4}$$

and

$$\tau_{ij} = \mu \left(\frac{\partial u_i}{\partial x_j} + \frac{\partial u_j}{\partial x_i} - \frac{2}{3} \frac{\partial u_k}{\partial x_k} \delta_{ij} \right). \tag{2.5}$$

In (2.4)-(2.5), T is temperature, k is thermal conductivity, and μ is dynamic viscosity. Dynamic viscosity and thermal conductivity must also be modeled. Sutherland's model first assumes that viscosity and thermal conductivity are a function of temperature. By introducing various gas-dependent constants, μ_0, T_0, k_0, and S, viscosity and thermal conductivity are then modeled as

$$\mu = \mu_0 \left(\frac{T}{T_0} \right)^{\frac{3}{2}} \frac{T_0 + S}{T + S} \tag{2.6}$$

and

$$k = k_0 \left(\frac{T}{T_0} \right)^{\frac{3}{2}} \frac{T_0 + S}{T + S}. \tag{2.7}$$

In turbulent flow, the time-dependent variables in (2.1)-(2.3) can be split into mean and fluctuating portions, which is known as Reynolds decomposition. This is done to obtain the Reynolds-averaged Navier-Stokes equations. The time-averaged mean value of an arbitrary variable, ϕ, is $\overline{\phi}$, and the fluctuating unsteady portion is ϕ'. Reynolds-averaging integrates

ϕ over a time-span, Δt, which is assumed to be a statistically significant amount of time. The definition of this averaging, considering the limit as $\Delta t \to \infty$, is

$$\bar{\phi} = \lim_{\Delta t \to \infty} \frac{1}{\Delta t} \int_{\Delta t} \phi(t) \ dt. \tag{2.8}$$

Reynolds-averaging can be used to produce the Reynolds-averaged Navier-Stokes equations. Favre-averaging allows for this procedure to be done in a relatively simple way with the compressible Navier-Stokes equations, by applying mass-averaging to ϕ. A Favre-averaged variable is denoted by a tilde, such as $\tilde{\phi}$, to distinguish from time-averaged variables. The Favre-averaging of a variable ϕ, with consideration of compressibility, is

$$\tilde{\phi} = \frac{1}{\bar{\rho}} \lim_{\Delta t \to \infty} \frac{1}{\Delta t} \int_{\Delta t} \rho(t)\phi(t) \ dt. \tag{2.9}$$

The application of time-averaging and mass-averaging, in (2.8)-(2.9), to the compressible Navier-Stokes equations, in (2.1)-(2.3), produces the three-dimensional compressible Reynolds-averaged Navier-Stokes equations,

$$\frac{\partial \bar{\rho}}{\partial t} + \frac{\partial (\bar{\rho}\tilde{u}_j)}{\partial x_j} = 0, \tag{2.10}$$

$$\frac{\partial (\bar{\rho}\tilde{u}_i)}{\partial t} + \frac{\partial}{\partial x_j}(\bar{\rho}\tilde{u}_i\tilde{u}_j + \bar{\rho}\widetilde{u_i'u_j'} + \bar{p}\delta_{ij}) = \frac{\partial \bar{\tau}_{ij}}{\partial x_j}, \tag{2.11}$$

and

$$\frac{\partial (\bar{\rho}\tilde{e})}{\partial t} + \frac{\partial}{\partial x_j}(\bar{\rho}\tilde{e}\tilde{u}_j + \bar{\rho}\widetilde{e'u_j'} + \overline{pu_j}) = \frac{\partial}{\partial x_j}(\overline{\tau_{ji}u_i} - \bar{q}_j). \tag{2.12}$$

In (2.10)-(2.12), $\tilde{u}_i$ and $\tilde{e}$ are Favre-averaged primitive variables, and $\bar{\rho}$ and $\bar{p}$ are time-averaged variables. The time-averaged viscous stress tensor is $\bar{\tau}_{ij}$, and the time-averaged heat flux is $\bar{q}_j$. Several additional terms that arise in Favre-averaging have the following definitions. In the momentum equation, $\bar{\rho}\widetilde{u_i'u_j'}$ is referred to as the Reynolds Stress tensor,

36

and $\overline{pu_j}$ is the time-averaged pressure-velocity moment. In the energy equation, $\bar{\rho}\widetilde{e'u_j'}$ is the turbulent transfer of heat, and $\overline{\tau_{ji}u_i}$ is the time-averaged viscous shear-velocity moment. The modified mass-averaged total energy (per unit mass) is

$$\tilde{e} = c_v\tilde{T} + \frac{1}{2}\tilde{u}_j\tilde{u}_j + \frac{1}{2}\widetilde{u_j'u_j'}, \tag{2.13}$$

and the modified constitutive ideal gas relationship is

$$\bar{p} = \bar{\rho}R\tilde{T}. \tag{2.14}$$

At this point, (2.10)-(2.12) are not complete, as several terms need to be modeled, referred to as the turbulence closure problem [5], [95], [97]–[99]. This procedure is the basis of computational fluid dynamics in the Reynolds-averaged Navier-Stokes formulation. Specifically, the Reynolds stress tensor, $\bar{\rho}\widetilde{u_i'u_j'}$, needs to be obtained with a turbulence model. Turbulence models employ algebraic equations, or differential transport models, to close the Reynolds-averaged Navier-Stokes equations. The turbulence model employed in this dissertation is the one-equation Spalart-Allmaras turbulence model.

2.1.1 Spalart-Allmaras Turbulence Model

To simplify the notation in this section, mass-averaging tildes and time-averaged bars are not included. The Spalart-Allmaras turbulence model is well used because it is robust and provides acceptable results for a variety of flows [97], [100]–[102]. The model was specifically designed for external aerodynamics, i.e., wall-bounded flows. The Spalart-Allmaras turbulence model, solving for the SA variable, $\tilde{\nu}$, employs the one-equation transport equation,

$$\frac{\partial \tilde{\nu}}{\partial t} + \frac{\partial(\tilde{\nu}u_j)}{\partial x_j} = C_{b1}(1 - f_{t2})\tilde{S}\tilde{\nu} + \frac{1}{\sigma}\left(\frac{\partial}{\partial x_j}\left[(\nu + \tilde{\nu})\frac{\partial \tilde{\nu}}{\partial x_j}\right] + C_{b2}\left|\frac{\partial \tilde{\nu}}{\partial x_j}\right|^2\right) \tag{2.15}$$
$$- \left[C_{w1}f_w - \left(\frac{C_{b1}}{\kappa^2}\right)f_{t2}\right]\left(\frac{\tilde{\nu}}{d}\right)^2 + f_{t1}\Delta U^2.$$

In (2.15), the closest distance to the surface is d. This length-scale is important in the formulation of detached-eddy simulation, which is discussed in the following section. By solving (2.15) for the SA variable, $\tilde{\nu}$, the turbulent kinematic eddy viscosity,

$$\nu_t = \rho\tilde{\nu}f_{v1},\tag{2.16}$$

can be calculated, which is then used to obtain the turbulent dynamic eddy viscosity,

$$\mu_t = \rho\nu_t.\tag{2.17}$$

The remainder of the nomenclature in (2.15), excluding the values and definitions associated with numerical constants, are defined as follows:

$$
\begin{gathered}
\chi = \frac{\tilde{\nu}}{\nu}, \qquad f_{v1} = \frac{\chi^3}{\chi^3 + C_{v1}^3}, \qquad f_{v2} = 1 - \frac{\chi}{1 + \chi f_{v1}}, \\
\tilde{S} = S + \frac{\tilde{\nu}}{\kappa^2 d^2}f_{v2}, \qquad S = \sqrt{2\Omega_{ij}\Omega_{ij}}, \qquad \Omega_{ij} = \frac{1}{2}\left(\frac{\partial u_i}{\partial x_j} - \frac{\partial u_j}{\partial x_i}\right), \\
f_{t1} = C_{t1}g_t\mathrm{e}^{-C_{t2}\frac{\omega_t^2}{\Delta U^2}(d^2 + g_t^2 d_t^2)}, \qquad f_{t2} = C_{t3}\mathrm{e}^{-C_{t4}\chi^2}, \\
f_w = g\left(\frac{1 + C_{w3}^6}{g^6 + C_{w3}^6}\right)^{\frac{1}{6}}, \qquad g = r + C_{w2}(r^6 - r), \qquad \text{and} \qquad r = \frac{\tilde{\nu}}{\tilde{S}\kappa^2 d^2}.
\end{gathered}
\tag{2.18}
$$

Boundary conditions for the model allow for an input of turbulence intensity to determine $\tilde{\nu}$ in the freestream, and is often set to be proportional to ν_∞. At the wall, $\tilde{\nu}$ is set to 0. The Spalart-Allmaras turbulence model utilizes (2.15)-(2.17) to obtain the turbulent eddy viscosity, μ_t. The eddy viscosity is then applied to the Boussinesq approximation,

$$-\bar{\rho}\widetilde{u_i'u_j'} = \mu_t\left(\frac{\partial\tilde{u}_i}{\partial x_j} + \frac{\partial\tilde{u}_j}{\partial x_i} - \frac{2}{3}\frac{\partial\tilde{u}_k}{\partial x_k}\delta_{ij}\right) - \frac{2}{3}\bar{\rho}\widetilde{u_k'u_k'}\delta_{ij},\tag{2.19}$$

to obtain the Reynolds stress tensor.

2.1.2 Detached-Eddy Simulation

While the Reynolds-average Navier-Stokes equations can be versatile, they often have limitations in their capability to accurately capture the relevant flow physics, especially for separated and unsteady flows [103]–[105]. These limitations lead to non-physical results and poor predictions of important design parameters, such as the aerothermodynamic loading in shock-wave/boundary-layer interactions [106]–[110]. Computationally expensive, higher fidelity models, such as large-eddy simulation, provide more reliable computational predictions. The computational cost of wall-resolved large-eddy simulation for higher Reynolds number flows is often too great, but can be reduced without much loss of fidelity, by applying wall-modeling [111] or implicit methods [112].

Further reduction of computational cost while using large-eddy simulation can be obtained with hybrid methods, such as detached-eddy simulation. Hybrid methods employ the Reynolds-average Navier-Stokes equations in near-surface attached boundary-layers and in the freestream and large-eddy simulation in highly resolved focus regions. As a result, hybrid methods greatly reduce unnecessary cost, while maintaining a high level of fidelity, making these methods favorable for large-scale computations [113]–[117]. In regions where the Reynolds-average Navier-Stokes equations are employed, e.g., low-resolution regions, near surfaces, in attached boundary-layers, or in the freestream, the eddy viscosity, μ_t, is determined from a transport equation, such as the Spalart-Allmaras model in (2.15). In regions where large-eddy simulation is employed, e.g., large-scale separation, downstream of a natural instability, or in areas of highly refined grid spacing, a sub-grid scale model is employed.

Sub-grid scale models decompose instantaneous variables into filtered and sub-filtered variables, similar to Reynolds decomposition [118]. The filtered, or spatial-averaged, variable field is obtained from low-pass filtering. The sub-grid stress tensor also needs to be closed, similarly to the Reynolds-average Navier-Stokes equations, and must be computed with a sub-grid model. For example, consider the Smagorinsky-Lilly model [119]. This model assumes that energy is transferred from large to small scales, through the energy cascade, and that the inertial subrange is associated with the resolved scales of the computational

grid. This model, however, has known issues, such as being too dissipative for transition studies and producing incorrect near-wall behavior. The Smagorinsky-Lilly model computes the sub-grid stress tensor as

$$\tau_{\text{ij,sgs}} = \tau_{\text{ij}} - \frac{1}{3}\tau_{kk}\delta_{\text{ij}} = -2(C_s\Delta)^2|S|S_{\text{ij}}, \tag{2.20}$$

where C_s is a constant and S_{ij} is the filtered strain rate tensor. Furthermore, the turbulent eddy viscosity is modeled as

$$\mu_{t,\text{sgs}} = \rho(C_s\Delta)^2|S|, \tag{2.21}$$

where Δ is the filter width and $|S|$ is proportional to the filtered strain rate tensor.

First formulations of detached-eddy simulation switched between the Reynolds-average Navier-Stokes equations and large-eddy simulation with a distance function [114], defined as

$$\tilde{d} = \min(d, C_{\text{DES}}\Delta), \tag{2.22}$$

where d is the distance from the surface and $\Delta = \max(\Delta x, \Delta y, \Delta z)$. The Reynolds-average Navier-Stokes equations are applied when the length-scale $\tilde{d} \ll \Delta$, and large-eddy simulation sub-grid scale modeling is applied when $\tilde{d} \gg \Delta$. The drawback to this formation is that areas between regions which employ the Reynolds-averaged Navier-Stokes equations and regions which employ large-eddy simulation produce numerical issues and grid-density dependence [115]. One reason for this is that the turbulent eddy viscosities obtained with the Reynolds-averaged Navier-Stokes equations and with large-eddy simulation scale differently [114]. Another is that in attached boundary-layers, as grid spacing is reduced to activate large-eddy simulation, the resolution is not yet sufficient to resolve internal velocity fluctuations, which is referred to as modeled-stress depletion [120]. This issue is corrected in the delayed detached-eddy simulation formation, which uses a function, f_d, to detect attached boundary-layers, and an altered length-scale,

$$\tilde{d} = d - f_d \text{max}(0, d - C_{\text{DES}}\Delta). \tag{2.23}$$

Further issues were found in the delayed detached-eddy simulation formation by Travin et al. [116], where non-physical reductions in skin friction were observed in delayed detached-eddy simulations of channel flow with highly resolved grids. To solve this, improved delayed detached-eddy simulation was developed as a combination of delayed detached-eddy simulation and wall-modeled large-eddy simulation [117]. This formation changes the evaluation of the grid-filter, Δ, as well as the blending of the gray areas. The new grid-filter,

$$\Delta_{\text{filter}} = \text{min}(\text{max}(C_w d_w, C_w h_{\text{max}}, h_w), \Delta), \tag{2.24}$$

is a modified function of the largest directional cell-size. This function incorporates the wall-normal distance, d_w, and height of the cell in wall normal-direction, h_w. Furthermore, the improved delayed detached-eddy simulation length-scale is defined as

$$\tilde{d} = f_{\text{hyb}}(1 + f_{\text{restore}})d + (1 - f_{\text{hyb}})d_{\text{LES}}. \tag{2.25}$$

The function f_{hyb} acts in a similar manner to the delayed detached-eddy simulation function, f_d. The additional large-eddy simulation length-scale in (2.25) is defined as

$$d_{\text{LES}} = C_{\text{DES}}\Psi\Delta_{\text{filter}}, \tag{2.26}$$

where the functions Ψ and f_{restore} are defined by local boundary-layer flow parameters.

2.1.3 Discrete Statistical Analysis

An investigation of the unsteady flow statistics was conducted for each of the computational investigations. Digital signal processing, which was employed to analyze the unsteady flow data, applies statistical methods to time-dependent signals. In discrete statistical analy-

sis, signals need to contain weakly-stationary, zero-mean, and random time-series data [121]–[123]. These signals were collected from the flowfield, such as velocity fluctuations, and on surfaces, such as time-dependent wall pressure.

The majority of these analyses are done in the frequency domain by employing Fourier transforms. In order to facilitate comparison to data with other researchers, such as with the experimental teams or with relevant literature, all spectra presented in this dissertation are non-dimensionalized as the Strouhal number,

$$S_t = \frac{f\overline{L_r}}{u_\infty}, \tag{2.27}$$

where $\overline{L_r}$ is the time-averaged reattachment length. The specific length-scale and velocity used in (2.27) are flow dependent and thus a choice exists in determining the appropriate parameters. This non-dimensionalization normalizes the frequency by a characteristic frequency, f_c, which is associated with the unit Strouhal number, $S_t = 1$. This characteristic frequency, as defined above, is $f_c = u_\infty/\overline{L_r}$. It is also common to use the boundary-layer height, δ, as a length-scale, or the edge-velocity, u_e, as the velocity.

In discrete statistical signal analysis, expected values are often used to determine statistical properties between two signals. In unsteady turbulent flows, signals are obtained through fluctuating variables, such as pressure, density, velocity, and heat flux. The first expected value, which is equal to the time-averaged value of any variable, $\phi(t)$, where $t = n\Delta t$, is

$$\overline{\phi} = \frac{1}{N}\sum_{n=0}^{N-1}\phi(n\Delta t). \tag{2.28}$$

In line with the time-averaged mean, the variance, σ^2, is the second expected value, or second moment, of random variables. The standard deviation of data, σ, is equal to the root of the variance. For discrete data, the variance is calculated as

$$\sigma^2 = \frac{1}{N}\sum_{n=0}^{n=N-1}|\phi(n\Delta t) - \overline{\phi}|^2. \tag{2.29}$$

The statistical data analysis techniques, which are useful for analyzing unsteady flow statistics, include cross-covariance and autocovariance (correlation), power spectral density, and coherence. Correlations, both in space and time, are used to determine various spatial and temporal relationships in the flow. These correlations can also determine temporal relationships within an individual signal. The cross-covariance function for two zero-mean, weakly-stationary signals, $\alpha(t)$ and $\beta(t)$, is discretely estimated as

$$R_{\alpha\beta}(m\Delta t) = \begin{cases} \sum_{n=0}^{N-m-1} \alpha_{n+m}\beta_n^* & m \geq 0 \\ R_{\beta\alpha}^*(-m\Delta t) & m < 0 \end{cases}, \tag{2.30}$$

where m represents an index lag and the time-delay is $\tau = m\Delta t$. The correlation coefficient is equal to the cross-covariance normalized by both of the signals' standard deviations, $\sigma_\alpha\sigma_\beta$. The autocovariance of a signal is given by (2.30) if the signals are the same, i.e., $\alpha(t) = \beta(t)$.

Power spectral densities are useful to determine the energy content and the frequency dominance of signals in the flow. The energy content of the signal $\alpha(t)$, in the frequency domain, is computed with the discrete Fourier transform of the autocovariance function,

$$G(f) = \sum_{n=0}^{N-1} R_{\alpha\alpha}(n\Delta t)e^{-i2\pi fn\Delta t}. \tag{2.31}$$

Power spectral densities are often presented as premultiplied power spectral densities, defined as $fG(f)/\sigma^2$. The cross-power spectral density can also be calculated for two signals, by utilizing the Fourier transform of the cross-covariance function, $R_{\alpha\beta}$. Cross-power spectral densities can be employed in calculations of signal coherence.

The coherence, γ, of two zero-mean, weakly-stationary signals, $\alpha(t)$ and $\beta(t)$, is used to determine the correlation between the signals' spectra, in the frequency domain. Coherence employs the power spectral density of the cross-correlation between the two signals, which is normalized by the power spectral densities of each signal's autocovariance function, $G(f)$. The coherence of two signals is calculated as

$$\gamma = \frac{|G(f)_{\alpha\beta}|^2}{G(f)_{\alpha\alpha}G(f)_{\beta\beta}}. \tag{2.32}$$

2.2 Experimental and Computational Methodologies

The Department of Defense (DoD) software package, CREATE-AV Kestrel, was utilized to carry out all computations. Kestrel is a package of computational fluid dynamics solvers and tools that includes capabilities for prescribed body motion, propulsion, and multi-physics modeling [124]. The specific tool used for this work, KCFD, is a finite-volume, unstructured, and cell-centered solver. Computational resources were provided by DoD high-performance computing (HPC) facilities, including the U.S. Army Research Laboratory (ARL) cluster Excalibur (decommissioned), the U.S. Air Force Research Laboratory (AFRL) cluster Warhawk, and the U.S. Navy cluster Narwhal. Meshes were produced with the grid creation software Pointwise, and post-processing of data was done using the software Tecplot and MATLAB.

All projects used similar computational configurations, with slight differences in boundary-conditions and data collection procedures. These computations employed improved delayed detached-eddy simulation in order to capture the unsteady flow characteristics. The inviscid flux scheme for the computations was HLLE++ [125], and the viscous flux scheme was LDD+. A sub-iterative point-implicit temporal scheme [126] was utilized. Spatial and temporal accuracy for these computations were second-order. Reactive gas effects are not considered for these analyses. The working gas considered was air and assumed to be thermally, $p = \rho R T$, and calorically, $e = C_v T$, perfect.

2.2.1 NASA Experiment and Computation

The first of the three projects revolved around a NASA experiment conducted by Deveikis and Bartlett in 1978 [42]. In this study, hypersonic flow over a wing-elevon-cove configuration was simulated, which represented the windward surface of a shuttle-type reentry vehicle. The cove is the area between the main wing element and the elevon, which is required to allow for elevon deflection. Mach 6.9 flow was achieved with NASA Langley's 8-foot high-temperature structures tunnel [127]. The facility holds a hypersonic blowdown wind tunnel, and a schematic is provided in Figure 2.1. The tunnel operates at a nominal Mach number of 7. Total pressures range from 4 to 24 MPa, total temperatures range from 1390 K to 2000 K, and freestream unit Reynolds number range from 10^6 to 10^7 m^{-1}. The tunnel equivalent

altitude range is between 25 km and 40 km [127]. The gas-medium used in the tunnel is a combination of the combustion products of methane gas and air, produced in the high-pressure combustion chamber. The specific heat ratio of the air/methane gas is 1.38, close to natural air at 1.4. Deveikis reports that the aerodynamic pressure and heating coefficients obtained in this test medium are comparable to those obtained in facilities utilizing only air [42], [127]. This gas is allowed to expand through a 2.4 m diameter nozzle and is then diffused and pumped through the test section to atmosphere conditions using a single-stage ejector. Inside the test section, the stream consists of 4.3 m free jet and a usable testing section with a diameter of 1.2 m. In order to protect the model during startup, the tunnel allows for the model to be stored and then inserted into the test section using a hydraulically actuated elevator [127].
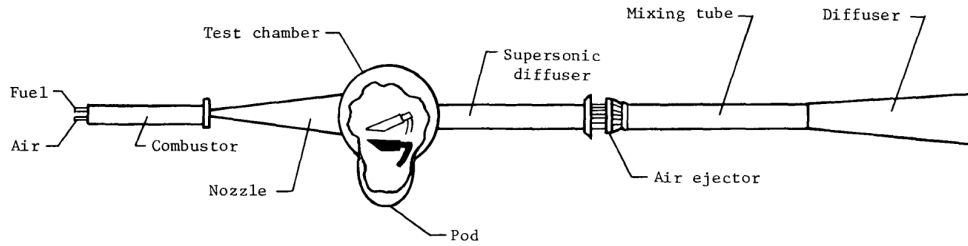
Figure 2.1. NASA Langley 8-foot high temperature structures tunnel [127].

The purpose of these experiments was to conduct research on hypersonic gap heating for a shuttle-type wing-elevon-cove configuration. The experimental setup is provided in Figure 2.2. These tests focused on the effects of hot turbulent boundary-layer ingestion for various cove exit-to-inlet area ratios. A total of 41 tests were done, varying the exit-to-inlet ratio from 0 (sealed) to 1 (full leakage). Pressure and heat flux data were obtained on the wing, elevon, and interior cove surfaces using pressure orifices and thermocouples. For the majority of tests, the model was set to an angle of attack of -12 deg, with an elevon deflection of 15 deg. The freestream Mach number for all tests was approximately 6.9. High Reynolds number tests, with an average value of $Re = 4.4 \times 10^6$ m^{-1}, and low Reynolds number tests, with an average value of $Re = 1.31 \times 10^6$ m^{-1}, were done. This project simulate done of these tests, with the unit Reynolds number $Re = 4.29 \times 10^6$ m^{-1}.
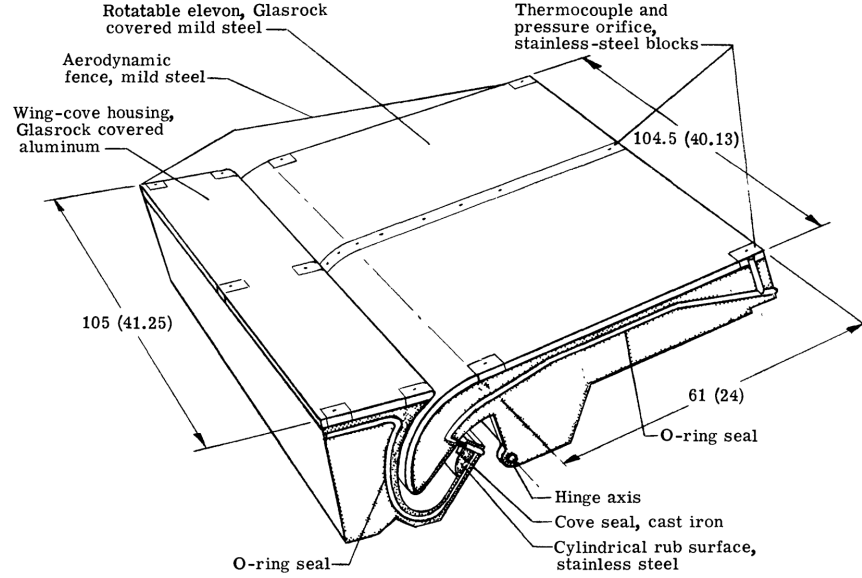
Figure 2.2. Experimental apparatus for the 1978 NASA wing-elevon-cove experimental study [42].

The chord lengths of the wing and elevon were 1.24 m and 0.69 m, respectively, with a total span length of 1.05 m. Aerodynamic fences on the sidewalls of the model were used to channel upstream surface flow across the cove entrance. The wing and elevon surfaces were covered with 12.7 mm thick Glasrock tiles for thermal protection, and data acquisition devices for surface pressure and heat flux were embedded in the Glasrock surfaces. To create fully turbulent flow at the cove entrance, the boundary-layer was tripped near the leading-edge with 2.4 mm diameter spheres. The average boundary-layer thickness at the reference location for high Reynolds number tests, located 25.4 mm upstream of the wing-elevon juncture, was $\delta_{\text{cove}} = 21.6$ mm. A local two-dimensional schematic of the wing-elevon juncture and cove region is provided in Figure 2.3. The length of the cove, i.e., the distance between the interior wing and elevon surfaces, was 12.7 mm. The end of the cove was either sealed, partially sealed, or fully open to regulate flow exiting the cove to an outside cavity, near freestream pressure; this method was based on an early shuttle orbiter design for cove sealing. The geometry of the cove region is created about an axis of rotation, providing smooth control surface movement into and out of the cove. A more detailed diagram of the cove geometry can be found in the published experimental study [42].

46
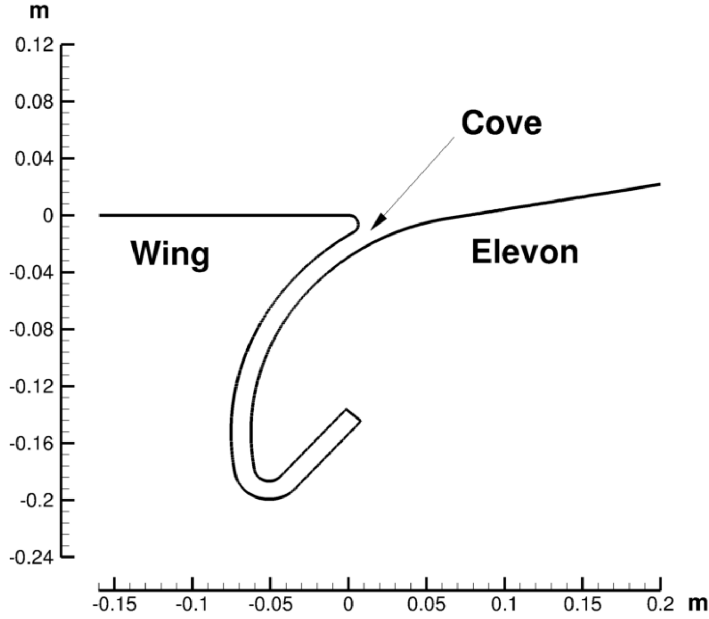
Figure 2.3. Two-dimensional schematic of the local wing-elevon juncture and cove region, to scale with the experimental study and computations.

One particular test was simulated out of the 41 experiments provided by the NASA experimental study. This test employed fully turbulent, Mach 6.9, high Reynolds number flow, at an angle of attack of -12 deg and an elevon deflection of 15 deg. The freestream, boundary-layer, and selected configurational properties for this test are provided in Table 2.1. This computation utilized periodic boundary conditions and focused primarily on the centerline flow. The outlet cove boundary condition was a subsonic pressure outlet set to near freestream pressure, $P_e = 1900$ Pa. Surface boundary conditions were no-slip isothermal surfaces, set to $T_w = 293.15$ K. The time-step was $\Delta t = 1 \times 10^{-7}$ s. The total number of iterations was 150,000, with 3 subiterations, corresponding to 15 ms of physical time. Unsteady data collection included the complete flowfield and unsteady planar extraction, as well as surface loading and other flowfield time-series data output. The entire flowfield dataset was sampled at a frequency of $f_s = 500$ Hz. Unsteady two-dimensional planes were taken more frequently at a sampling frequency of $f_s = 10$ kHz. All other data, such as surface aerothermodynamic loading and fluctuations at specified flowfield locations, were taken at every time step, or at a sampling frequency of $f_s = 10$ MHz. Computational resources were

provided by the U.S. ARL HPC cluster Excalibur (decommissioned). Excalibur used Intel Haswell E5-2698 64-bit processors, which were clocked at 2.3 GHz and had 16 cores per CPU, with 2 CPUs per node. This computation used 200 nodes, with 16 ranks and 2 threads per node, for a total of 3400 cores, taking roughly 400 hours to obtain statistical significance.

Table 2.1. Freestream, boundary-layer, and selected properties for the NASA wing-elevon-cove experiment and computation.

Parameter	Value
M_∞	6.86
$T_{o,\infty}$ (K)	2300
$P_{o,\infty}$ (kPa)	7030
u_∞ (m/s)	2040
Re_∞ (m^{-1})	4.29×10^6
$Re_{x,\text{cove}}$	6.15×10^6
δ_{cove} (mm)	21.6
α (deg)	-12
δ_f (deg)	15

The mesh is constructed by a combination of several structured block-domains, shown in Figure 2.4. The surface domain is numerically sharp at the leading-edge. Mesh development incorporated multiple progressions of the grid in order to determine optimal resolution and grid independence. The blocks were created so that they were consistent with Spalart's recommendations for detached-eddy simulation [128]. Three distinct regions are outlined by Spalart for detached-eddy simulation: the Euler region, the viscous region, and the focus region. Reynolds-averaged Navier-Stokes equations are employed in the Euler region and viscous region blocks, whereas large-eddy simulation is employed in the focus region blocks. Therefore, each block is created with careful consideration of the flow in that region.

The Euler region block is far from the surface and is the least resolved. The height of this block is set to fully capture the leading-edge oblique shock-wave. The viscous regions near the surface are well resolved, with $\Delta y_w^+ \leq 1$. The exterior and interior (cove) focus region blocks are highly resolved for large-eddy simulation [118], [129], with a constant grid-filter of $\Delta = 0.5$ mm, set by the spanwise grid spacing. In these blocks, the grid spacings, in inner coordinates, are $\Delta x^+ \approx 70$, $\Delta y^+ \approx 60$, and $\Delta z^+ \approx 80$. These spacings are held

nearly constant in the zoomed-in portion of the mesh shown in Figure 2.4 but are stretched downstream of reattachment with a ratio of 1.2. At the edge of the boundary-layer, the scaled coordinate spacings are $\Delta x/\delta_{\mathrm{cove}} \approx 0.05$, $\Delta y/\delta_{\mathrm{cove}} \approx 0.04$, and $\Delta z/\delta_{\mathrm{cove}} \approx 0.05$. The exterior focus region block is sized in order to expand and fully capture the downstream reattachment shock-wave. The Euler region block consists of 51x1001x201 points, the incoming flat-plate viscous region block consists of 401x201x201 points, the exterior focus region block consists of 801x801x201 points, and the interior focus region block consists of 401x901x201 points. The complete mesh comprised 230 million cell-volumes.
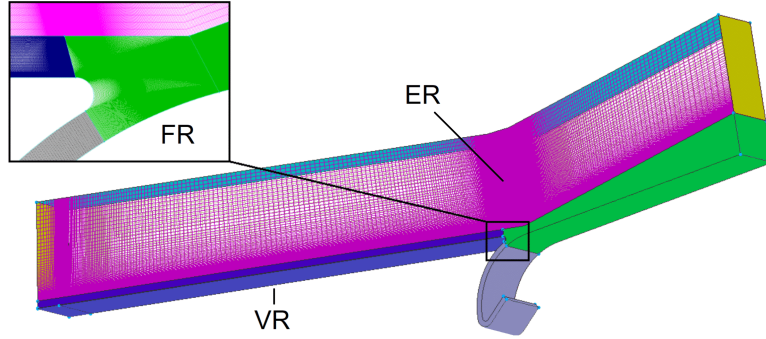
Figure 2.4. Multi-block structured three-dimensional computational mesh used in the NASA wing-elevon-cove computation.

2.2.2 Purdue BAM6QT Experiment and Computation

The Purdue BAM6QT wind tunnel is a high Reynolds number, hypersonic, quiet wind tunnel located in the Purdue Aerospace Sciences Laboratory (ASL). The BAM6QT wind tunnel is able to remain quiet at a unit Reynolds number of over 10^7 per meter and is primarily focused on facilitating transition research [130], [131]. The BAM6QT is a Ludwieg tube with a long driver tube connected to a converging-diverging nozzle. Run times average approximately 5 seconds for quiet Mach 6 flow. The nozzle was designed to minimize centrifugal instabilities and is polished to a mirror finish to reduce roughness effects [130]. The BAM6QT wind tunnel can operate at higher stagnation pressures with the bleed-slot bypass section closed, which allows for versatility of experiments. The range for stagnation

pressures for the wind tunnel is 150-250 psi, providing unit Reynolds numbers of 10^7 to 10^8 m^{-1}. A schematic of the Purdue BAM6QT wind tunnel is provided in Figure 2.5.
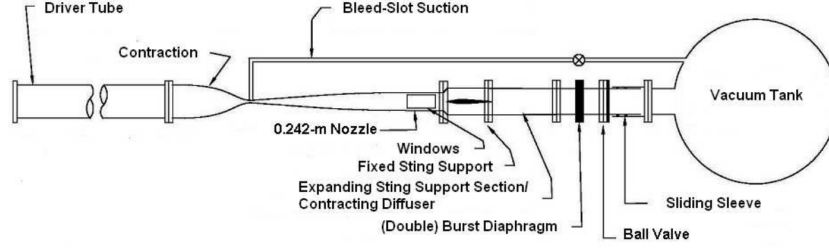
Figure 2.5. Schematic of Purdue Boeing/AFOSR Mach 6 Quiet Wind Tunnel (BAM6QT) [131]. Included with permission from the author.

The swept wing-elevon model analyzed for this project was designed by Carson Lay, of Purdue University. Ongoing experiments for this swept wing-elevon model are being conducted in the Purdue BAM6QT wind tunnel. Complementary UTSI experiments are also currently ongoing in the TALon Mach 4 Ludwieg tube. However, experimental data are limited at this time. A three-dimensional perspective of the model is provided in Figure 2.6. The model is identical for both wind tunnel experiments, however the UTSI model is twice the size of the Purdue model. Dimensions listed hereafter refer to the Purdue model. The model consists of a three-dimensional swept-wing, with an elevon attached to the trailing-edge. The elevon is deflected 12 deg. Between the wing and elevon are three gap regions, which include the primary cove region and two additional side gaps. In experiments, the swept wing-elevon model was placed on the ceiling of the Purdue BAM6QT wind tunnel, which acts as a representative fuselage. This surrounding surface is included in the computation.

The ceiling of the wind tunnel is represented by a 0.66 m flat plate so that the boundary-layer can grow to match the corresponding wind tunnel displacement thickness, $\delta^* = 5.8$ mm, at the beginning of the model. The wing has a constant sweep of 25 deg from the z-axis. The airfoil cross-section of the wing consists of two straight ramped sections connected by a flat section. The airfoil is symmetric about its chord line. Due to the swept leading-edge, the chord lengths of the airfoil cross-sections decrease from the root to the tip. The root cord length of the swept wing-elevon model is 0.423 m, the centerline chord length is 0.379 m,

and the tip chord length is 0.334 m. The chord length of the elevon alone is 0.1 m and is constant. The elevon is also symmetric about its chord line. The span of the wing is 0.19 m and the span of the elevon is 0.135 m. The cove region and the side gaps consist of constant-length regions between the wing and elevon of 2.52 mm. The cove region is created by two concentric circles about a center of rotation, located in the cylindrical elevon's leading-edge $(x, y) = (0.3275, 0)$ m. The radius of curvature of the concave wing-cove surface is 8.15 mm. The radius of curvature of the convex elevon-cove surface is 5.63 mm. The radii of the blunt leading-edge of the wing and the trailing-edges of the wing and elevon are $D = 425$ μm.
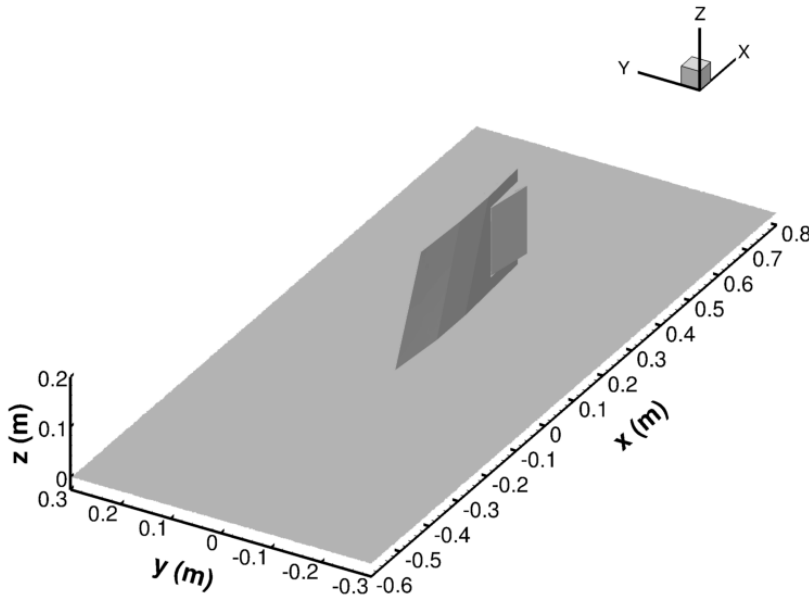
Figure 2.6. Three-dimensional perspective of the Purdue swept wing-elevon-cove surface model and the surrounding wind tunnel surface.

For the Purdue BAM6QT wind tunnel, the flow conditions correspond to fully turbulent, hypersonic, high Reynolds number flow, at zero angle of attack. Freestream conditions, and selected properties, are provided in Table 2.2. The total number of iterations was 200,000, at a time-step of $\Delta t = 1 \times 10^{-7}$ s, resulting in a simulated time of 20 ms. All data were averaged over the computational time. No periodic boundary conditions were used, and all freestream boundaries used modified Riemann invariant conditions. Surfaces used isothermal wall boundary conditions, set to $T_w = 293.15$ K. This wall temperature

matches the approximate experimental value for non-sequential runs. Computational data were collected for the entire flowfield and for all surfaces. The computational resources were provided by the U.S. Navy HPC cluster Narwhal. Narwhal uses 2.6-GHz AMD Epyc 7H12 processors, which have 64 cores per CPU, with 2 CPUs per node. The computation employed 50 nodes, for a total of 6400 cores, taking roughly 150 hours to run to completion.

Table 2.2. Freestream, boundary-layer, and selected properties for the Purdue BAM6QT wing-elevon-cove experiment and computation.

Parameter	Value
M_∞	6
$T_{o,\infty}$ (K)	433
$P_{o,\infty}$ (kPa)	1034
u_∞ (m/s)	874
Re_∞ (m^{-1})	1.1×10^7
$Re_{x,\text{cove}}$	3.5×10^6
δ_{cove} (mm)	15.6
α (deg)	0
δ_f (deg)	12

The primary mesh for this project is provided in Figure 2.7. The surface model was made to exactly represent the physical model used in experiments, unlike the spanwise idealization employed in the UTSI TALon computation. This configuration is complex and hard to mesh with completely structured blocks. Thus, the mesh was created with the use of T-Rex hybrid unstructured meshing, allowing for high levels of resolution where needed. T-Rex hybrid unstructured meshing incorporates structured meshing near surfaces and allows for higher fidelity results for wall-bounded flows compared to pure unstructured meshing [132]–[134]. The unstructured solving algorithm used was voxel, which attempts to produce isotropic cube cells in the freestream to improve the computational fidelity [135], [136]. On all surfaces, the near-wall grid is highly resolved, with $\Delta y_w^+ \leq 1$. However, due to the complicated structure of this model near the deflected elevon, grid spacing is not held constant, which may have affected the improved detached-eddy simulation numerical fidelity. Unfortunately, due to mesh size limitations in KCFD, further refinement was not possible. Grid spacings,

in inner coordinates, for the focus regions ranged $\Delta x^+ \approx 50 - 200$, $\Delta y^+ \approx 80 - 160$, and $\Delta z^+ \approx 70 - 300$. The unstructured computational mesh comprised 250 million cell-volumes.

The improved delayed detached-eddy simulation was unable to resolve significant unsteadiness in the shock-wave/boundary-layer interaction at the cove juncture. To facilitate an unsteady computation, a parametric sweep was done by modifying various geometric parameters. The results of this parametric sweep predicted a Reynolds number dependence for the onset of unsteadiness in the cove region. Improved delayed detached-eddy simulation generally requires flow instabilities to produce unsteadiness in the computation due to the lack of resolved turbulence in the upstream boundary-layer [113]–[117]. Modified computations with stronger shock-wave/boundary-layer interactions, or significantly higher cove Reynolds numbers, Re_{cove}, successfully produced unsteady shock-wave/boundary-layer interactions. Despite having a large freestream Reynolds number of $Re = 1.1 \times 10^7$ m^{-1}, this wing-elevon-cove configuration has the lowest Görtler number, $\mathcal{G} = 1.5$, and cove Reynolds number, $Re_{\text{cove}} = 6 \times 10^6$, of all three computations. Therefore, the onset of the unsteadiness in this computation may be linked to the Görtler number and the centrifugal instability. While several of these computational modifications produced significant flow unsteadiness, the required configurations were unobtainable in the Purdue BAM6QT wind tunnel. The goal of this research involved collaborative efforts with the Purdue ASL experimental team, and for this reason, the experimental conditions and model were used in the computation.

2.2.3   UTSI TALon Experiment and Computation

The UTSI TALon Mach 4 Ludwieg tube flow conditions were used for the final project of the three. The UTSI experiments, however, are currently still in progress and there are no corresponding experimental data included in this dissertation. The tunnel has a two-dimensional planar nozzle with a relatively large test section, sized 24 in by 24 in by 72 in. The UTSI TALon facility was built with the intention to bridge the gap between foundational research facilities and large-scale facilities. This relatively new facility was designed to include a plethora of optical diagnostic techniques, including schlieren imaging, pressure sensitive paint, laser differential interferometry, and particle image velocimetry [137]. The Mach 4
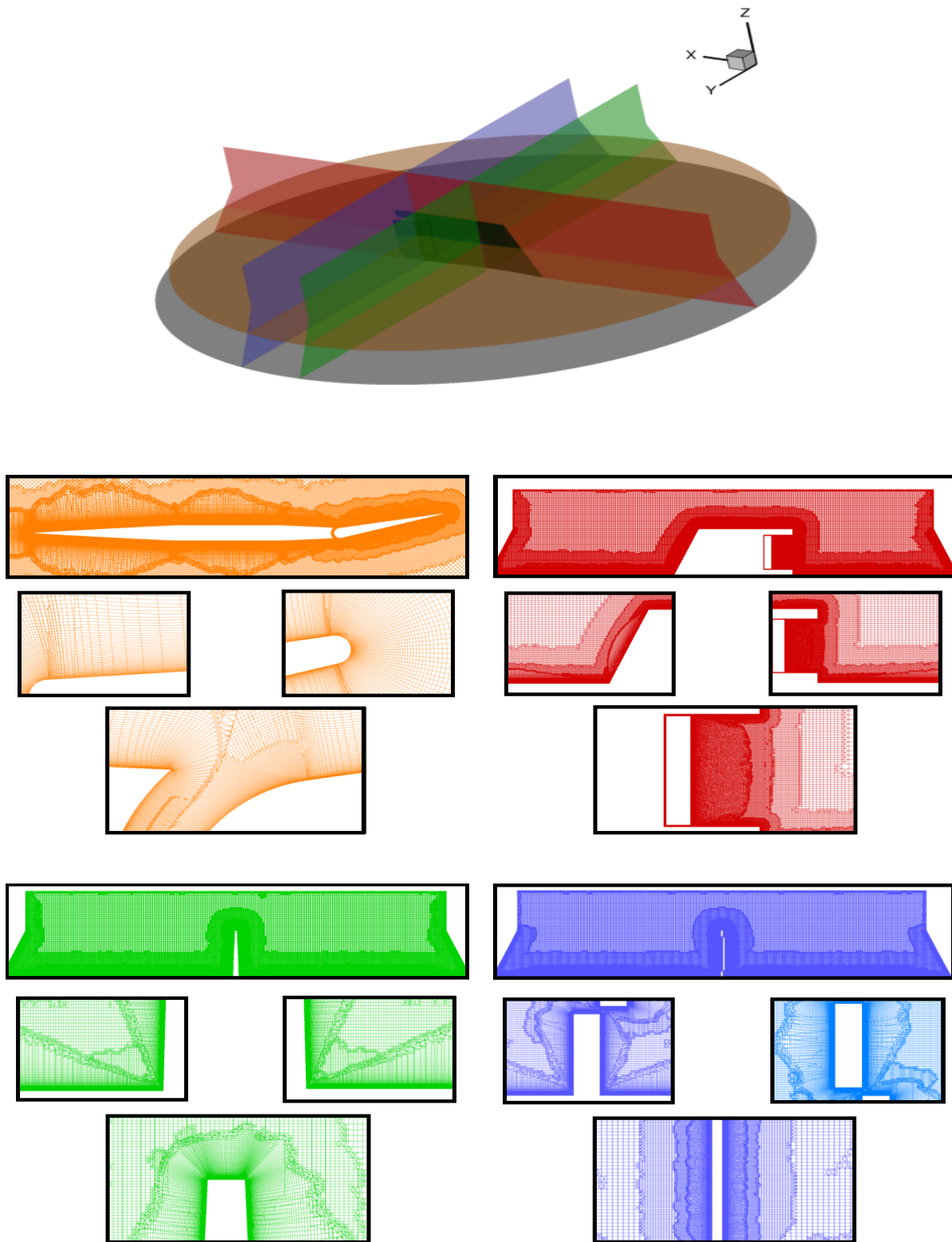
Figure 2.7. Color-coded perspectives of the three-dimensional unstructured mesh used in the Purdue BAM6QT wing-elevon-cove computation.

Ludwieg tube can run for approximately 100 ms. The flow is driven by a 150 psi driver tube, and the unit Reynolds number range is $\text{Re} = 10^6$ to 10^7 m^{-1}. The overall layout of the UTSI TALon Mach 4 Ludwieg tube, with included components, is provided in Figure 2.8.
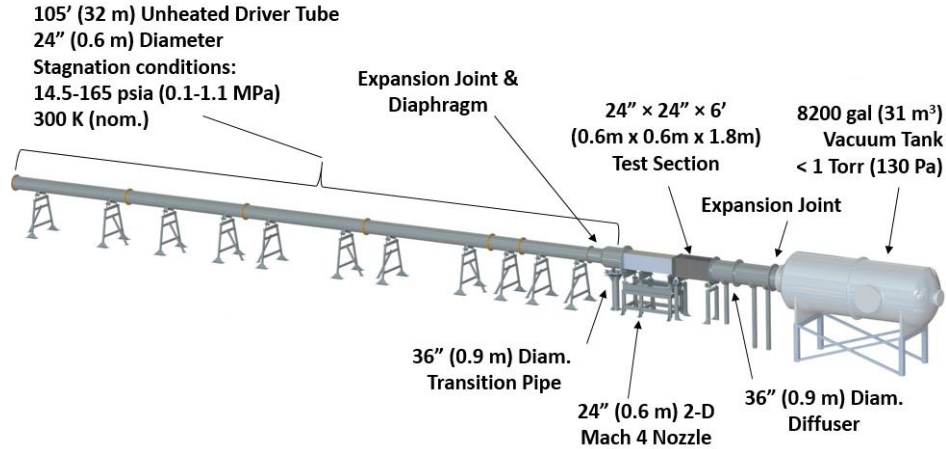
Figure 2.8. The Tennessee Aerothermodynamics Laboratory (TALon) Mach 4 Ludwieg tube [137]. Included with permission from the author.

To moderate the computational cost of the simulation, the Purdue swept wing-elevon-cove model was idealized in the span, omitting the side gap regions and the surrounding wind tunnel surface. The centerline cross-section of the scaled model was symmetrically extruded in the span to allow for flow three-dimensionality; however, the leading-edge sweep of the model was not included. This reduction of the computational domain allows for more precise meshing and data collection compared to the unstructured T-Rex hybrid meshing used for the Purdue BAM6QT computation. The scaled wing-elevon-cove model is provided in Figure 2.9, with the dimensions of the model included. This model consists of the centerline portion of the full model displayed in Figure 2.6. The wing is 0.658 m long, the cove is 6 mm in length, the elevon is 0.188 m long, the airfoil thickness is 0.04 m, and the span of the domain is 0.05 m. For reference, the span of the full scaled model elevon is 0.27 m, and the computation modeled roughly 20% of this span.

For the TALon wind tunnel experiment and computation, the flow conditions correspond to fully turbulent, Mach 4, high Reynolds number flow, at zero angle of attack. The elevon deflection for this configuration is also 12 deg. The UTSI TALon wind tunnel produces
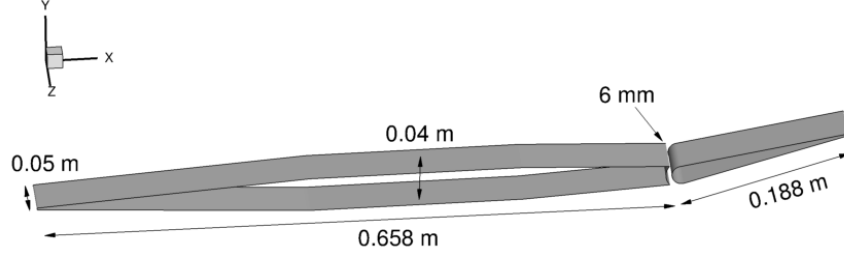
Figure 2.9. Three-dimensional perspective of the scaled wing-elevon-cove model, with included dimensions, used in the UTSI TALon computation.

higher freestream, and cove, Reynolds numbers compared to the Purdue BAM6QT wind tunnel. This facilitated the onset of unsteadiness in the shock-wave/boundary-layer interaction, which allowed for the characterization of the unsteady flowfield. The freestream conditions, and selected properties, are provided in Table 2.3. This computation utilized periodic boundary conditions and primarily focused on the centerline flow. Surface boundary conditions were no-slip isothermal surfaces, set to $T_w = 293.15$ K. The time-step was $\Delta t = 1 \times 10^{-7}$ s. The total number of iterations was 200,000, with 3 subiterations, corresponding to 20 ms of physical time. Unsteady data were collected for the complete flowfield, in two-dimensional planes, for all surfaces, and in various individual locations in the domain. The entire flowfield was sampled at a frequency of $f_s = 500$ Hz. Unsteady two-dimensional planes were taken more frequently, at a sampling frequency of $f_s = 10$ kHz. All other data, such as surface aerothermodynamic loading and fluctuations at specified flowfield locations, were taken at every time step, or at a sampling frequency of $f_s = 10$ MHz. The computational resources were provided by the U.S. AFRL HPC cluster Warhawk. Warhawk uses AMD EPYC 7H12 processors clocked at 2.3 GHz, which have 64 cores per CPU, with 2 CPUs per node. The computation employed 75 nodes, for a total of 9600 cores, taking roughly 300 hours to obtain statistical significance.

Selected views of the computational mesh are provided in Figure 2.10. This figure depicts the wing-elevon-cove centerline mesh, as well as the homogeneous spanwise grid spacing. This mesh was constructed in a fully structured manner, which facilitated precise meshing and data collection. As with the other two computations, the near-wall resolutions are high, with $\Delta y_w^+ \leq 1$. The exterior and interior (cove) focus regions are sufficiently resolved for large-

Table 2.3. Freestream, boundary-layer, and selected properties for the UTSI TALon wing-elevon-cove experiment and computation.

Parameter	Value
M_∞	4
$T_{o,\infty}$ (K)	295
$P_{o,\infty}$ (kPa)	483
u_∞ (m/s)	672
Re_∞ (m^{-1})	1.9×10^7
$Re_{x,\text{cove}}$	1.14×10^7
δ_{cove} (mm)	30
α (deg)	0
δ_f (deg)	12

eddy simulation. In these regions, the grid spacings, in inner coordinates, are $\Delta x^+ \approx 50$ and $\Delta y^+ \approx 50$. The spanwise mesh is homogenous and contains a constant grid spacing, in inner coordinates, of $\Delta z^+ \approx 60$. These spacings are held constant along the model length, allowing for the sustainment of turbulence. The complete mesh comprised 250 million cells.
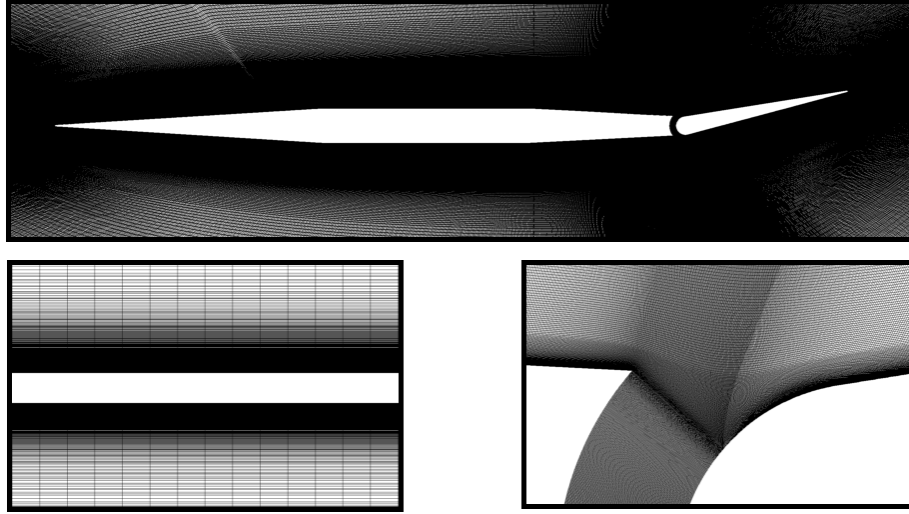
Figure 2.10. Planar perspectives of the computational mesh used in the UTSI TALon computation, including the span (left) and the local cove (right).

3. NASA WING-ELEVON-COVE

This chapter provides the computational results for the first wing-elevon-cove project. This study used a model and freestream flow conditions corresponding to the NASA experiments performed by Devekis and Bartlett [42]. The initial research goal was to assess the fidelity of our computational tools by simulating the hypersonic wing-elevon-cove flows studied in these experiments. After acceptable agreement to the experimental results was obtained, the next research goal was to expand on the published work. The NASA experiments focused on time-averaged aerothermodynamic surface loading and did not publish flowfield visualizations or conduct statistical analysis. Consequently, this project aimed to expand on these two areas.

One set of the NASA experimental test configurations was used for the computation. The freestream conditions for this test correspond to fully turbulent hypersonic flow, at a high unit Reynolds number of $Re = 4.29 \times 10^6$ m^{-1}. The angle of attack for this test was -12 deg and the elevon deflection was 15 deg. Relevant parameters can be found in Table 2.1. The computational model used was improved delayed detached-eddy simulation, which provides high fidelity results in focus regions and allows for accurate characterization of the unsteady flowfield. To facilitate comparison with the experiment, the cross-sectional geometry was identical to the NASA experimental wing-elevon-cove model. The computational domain, however, only included a portion of the full experimental span. The total span length for the experimental model and the computational domain were 1.05 m and 0.1512 m, respectively. A diagram of the three-dimensional wing-elevon-cove configuration is provided in Figure 3.1. In this figure, the computational domain is highlighted and the dimensions for the wing-elevon-cove model are included. The chord lengths of the wing and elevon were 1.24 m and 0.69 m, respectively. The length of the cove, i.e., the distance between the interior wing and elevon surfaces, was 12.7 mm. A two-dimensional schematic of the local cove region was previously provided in Figure 2.3.

This computation utilized periodic boundary conditions on each side of the domain. In Figure 3.1, the flow enters the domain on the left and exits the domain on the right through modified Riemann invariant boundary conditions. The leading-edge of the wing is numerically sharp. The outlet cove boundary condition was a subsonic pressure outlet set
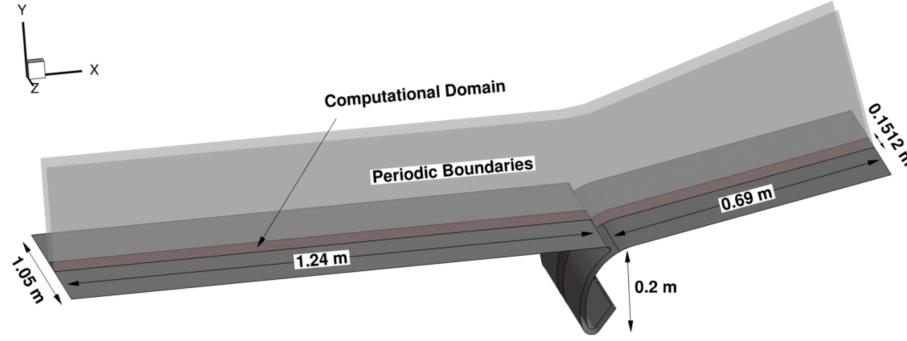
Figure 3.1. Schematic of the three-dimensional wing-elevon-cove model. The computational domain is highlighted as a portion of the experimental domain.

to P_e = 1900 Pa. The wall boundary conditions were no-slip isothermal surfaces, set to T_w = 293.15 K. The mesh used in the computation was constructed by a combination of several structured block-domains. The total mesh cell-volume count was 230 million. All surface boundaries have $\Delta y_w^+ \leq 1$. The inner coordinate grid spacings in the focus region are $\Delta x^+ \approx 70$, $\Delta y^+ \approx 60$, and $\Delta z^+ \approx 80$. A diagram of the computational mesh can be found in Figure 2.4. The total time simulated was 15 ms, and the time-step was $\Delta t = 1 \times 10^{-7}$ s. Unsteady data collection included the complete flowfield and unsteady planar extraction, as well as surface loading and other flowfield time-series data output. The entire flowfield dataset was sampled at a frequency of f_s = 500 Hz. Unsteady two-dimensional planes were taken more frequently at a sampling frequency of f_s = 10 kHz. All other data, such as surface loading and fluctuations at specified flowfield locations, were taken at every time step, or at a sampling frequency of f_s = 10 MHz.

A large part of the data analysis focused on the unsteady fluctuations in the flow. The low-frequency behavior of the shock-wave/boundary-layer interaction was primarily investigated. Flowfield visualization and resultant aerothermodynamic loading are also provided for further context. Collectively, the research presented here attempts to provide an accurate characterization of the hypersonic flowfield. The order of the data presentation for this project follows flow visualization, aerothermodynamic loading, and statistical analysis. The

final section is a discussion of the work presented in this chapter. These results have been previously published and the full papers can be found in the references [138]–[140].

3.1 Flow Visualization

Flow visualizations of the time-averaged and unsteady fluctuating flowfields are provided and discussed in this section. The streamwise mean flow structure at the cove juncture is displayed with temperature, velocity, and density gradient magnitude contours. These figures provide the general mean flow characteristics. The unsteady shock-wave/boundary-layer interaction at the cove juncture is depicted with instantaneous density gradient magnitude contours at various computational times. The three-dimensional unsteady turbulent flowfield is visualized through constant Q-Criterion iso-surfaces and a spanwise vorticity magnitude contour. These visualizations provide further context to the resultant aerothermodynamic loading and the unsteady flow statistics.

The freestream inflow is at a -12 deg angle of attack relative to the wing-elevon-cove model. At the numerically sharp leading-edge of the wing surface, an oblique shock-wave forms due to the difference in flow angle. The boundary-layer develops along the wing surface and separates at the wing's trailing-edge. There is a shock-wave/boundary-layer interaction in this region caused by the boundary-layer separation and downstream 15 deg elevon deflection. A time-averaged contour at the cove of non-dimensional temperature, $\overline{T}/T_{o,\infty}$, is provided in Figure 3.2. The contour is a two-dimensional planar extract taken at the centerline, $z = 0$ m. This figure depicts several characteristic mean flow phenomena in this region. There is an expansion-fan, a reattachment shock, and a redeveloping boundary-layer on the elevon surface. The boundary-layer ingestion into the cove and the region of high temperature at the shock-front are depicted here. The reattachment shock creates an exceedingly high temperature of 1400 K, which is equal to $0.60T_{o,\infty}$. Reported experimental cove temperatures reached $0.5T_{o,\infty}$ near the cove entrance. There is a localized low temperature region inside of the cove attributed to a small secondary separation vortex. Temperatures inside of the cove reach a near-constant equilibrium value of 900 K, or $0.39T_{o,\infty}$. The experimental values were similar in magnitude, equal to $0.37T_{o,\infty}$.
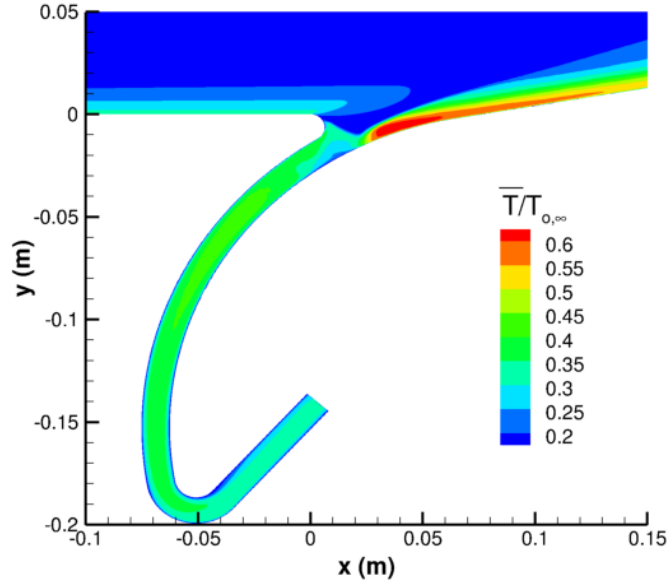
Figure 3.2. Contour of time-averaged non-dimensional temperature, $\overline{T}/T_{o,\infty}$, at the cove. Centerline, $z = 0$ m, planar extract.

The centerline, $z = 0$ m, flow structure at the local cove juncture is displayed in Figure 3.3. This figure is a contour of time-averaged non-dimensional velocity, $\overline{u}/u_{\infty}$. The sectional streamlines provide added visualization of the mean flowfield in this region. Some of the flow phenomena depicted in this figure include boundary-layer separation and reattachment, a separated shear-layer, flow recirculation, and cove flow entrainment. The upstream boundary-layer immediately separates at the edge of the wing main element and creates a shear-layer that expands and reattaches downstream. Flow is entrained between the separation vortex and the elevon surface. The external boundary-layer is forced to turn, first expanding, and then compressing, creating a region of shock-wave/boundary-layer interaction. At reattachment, the external boundary-layer redevelops along the elevon surface and exits through the outflow boundary. Flow beneath the external boundary-layer is entrained into the separation vortex or into the cove. The region of divergent streamlines near the elevon surface, separating the entrained cove flow and the external boundary-layer, corre-

sponds to the mean boundary-layer reattachment position. Flow through the cove is mostly subsonic and exits out of the pressure boundary at freestream pressure.
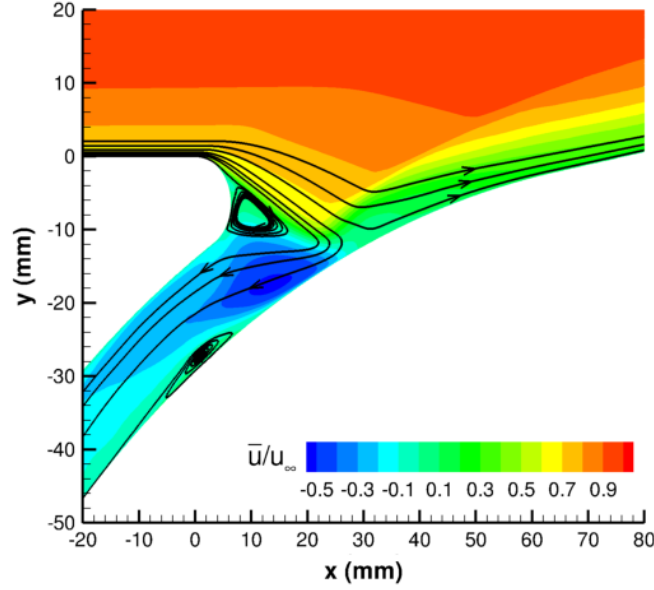
Figure 3.3. Contour of time-averaged non-dimensional velocity, $\overline{u}/u_\infty$, at the local cove juncture. Centerline, $z = 0$ m, planar extract. Sectional streamlines are included to depict flow structure.

Time-averaged density gradients can be used to depict the mean structure of the shock-wave/boundary-layer interaction. For instance, at the cove juncture, there are several regions of high density gradients, such as the shock-wave and the expansion-fan. A contour of time-averaged density gradient magnitude, $|\overline{\nabla \rho}|$, is provided in Figure 3.4, for the local cove juncture. The contour is a two-dimensional planar extract taken at the centerline, $z = 0$ m. The banded contour-color scaling is exponential to provide the full range of density gradients present. This figure depicts the mean expansion-fan region at the edge of the main wing element, the mean reattachment shock-wave, the mean shear-layer, and the mean shear-layer/shock-wave impingement location. Due to the time-averaging in this figure, which averages out the unsteady fluctuations, the characteristic unsteady behavior of the flow in this region is not depicted. However, this figure provides a useful reference for the mean flow structure of the shock-wave/boundary-layer interaction.
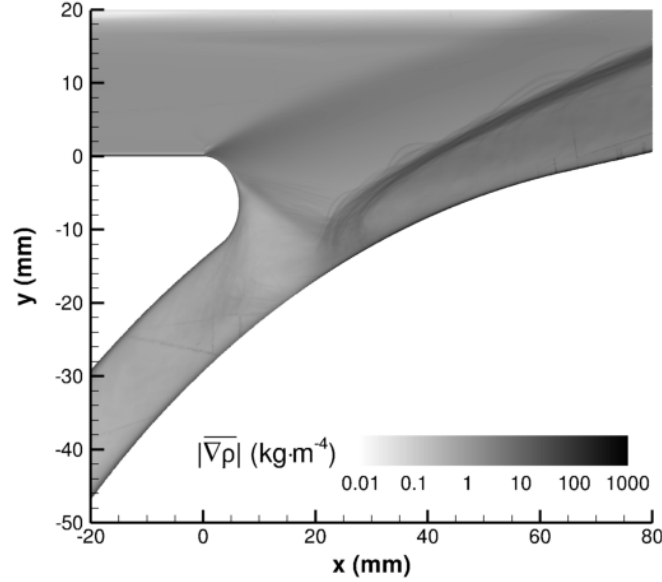
Figure 3.4. Contour of time-averaged density gradient magnitude, $|\overline{\nabla\rho}|$, at the local cove juncture. Centerline, $z = 0$ m, planar extract.

3.1.1 Instantaneous Flow

To visualize the chaotic unsteady flow at the cove juncture, density gradient magnitude contours are employed again in Figure 3.5. This figure provides four instantaneous planar extracts taken at the centerline, $z = 0$ m. The time difference between each frame is $\Delta t = 0.05$ ms, and the first frame starts at a computational time of $t = 6.5$ ms. The red marker, i′, corresponds to the shear-layer/shock-wave impingement location. The blue and yellows markers, i″ and i‴, correspond to distortions in the shock-wave.

In the first frame, Figure 3.5a, important flow phenomena such as the shear-layer, the shock-wave, and the shear-layer/shock-wave impingement are visible. The structure of the shock-wave/boundary-layer interaction here is similar to the mean structure shown in Figure 3.4. The marker i′ provides the location of the shear-layer/shock-wave impingement location. There are no major distortions present in the shear-layer or the shock-wave. However, the chaotic entrained flow inside of the cove is depicted through the turbulent mixing

of eddies. After $\Delta t = 0.05$ ms, in Figure 3.5b, a distortion in the shock-wave is shown in the region between i′ and i″. The shear-layer/shock-wave impingement location and the shock-front have shifted slightly upstream. Flow entrainment into the separation vortex and the cove is visible in this frame. The propagation of large coherent turbulent structures can be seen in the redeveloping boundary-layer. The next instantaneous frame, Figure 3.5c, depicts the shear-layer flapping motion as the shear-layer is forced downward to the elevon surface. The shear-layer/shock-wave impingement follows this movement. This motion displaces the shock-front downward, producing a large distortion in the shock-wave. The creation of co-herent turbulent structures is seen in this region, which propagate downstream in the next frame. The shock-wave distortion also propagates downstream, as seen in Figure 3.5d. The portion of the shock-wave which is distorted now ranges between i″ and i‴, spanning over 40 mm. The shear-layer/shock-wave impingement and the shock-front remain close to the elevon surface and near the mean reattachment location.

Collectively, the unsteady behavior displayed in Figure 3.5 highlights the chaotic turbulent nature of the flow in this region. The shock-wave/boundary-layer interaction system produces high levels of unsteadiness and will be shown, in the next section, to exhibit low-frequency coherent movement. This behavior is the primary interest for this research, as outlined in the introduction, due its importance for hypersonic flight vehicle design.

Visualization of the three-dimensional instantaneous flowfield can provide further context to this unsteadiness. Specifically, Q-Criterion iso-surfaces facilitate the detection and visualization of vortex structures [141]. Therefore, Q-Criterion iso-surfaces are employed in Figure 3.6 to visualize the three-dimensional turbulence. In this figure, iso-surfaces are contour-colored by velocity magnitude, $|V|$. The chaotic turbulent environment is depicted here, where the shock-wave/boundary-layer interaction region is highlighted and enlarged. Turbulent eddies inside of the cove dissipate through the cove and exit out of the pressure outlet. The turbulent structures of the separated shear-layer, redeveloping boundary-layer, and cove flow entrainment region are all visible in the enlarged frame. These turbulent structures originate in this region, due the natural centrifugal instability, and propagate downstream. There is an elongation of the structures that is seen, which is exacerbated by the grid stretching downstream of the shock-wave/boundary-layer interaction.
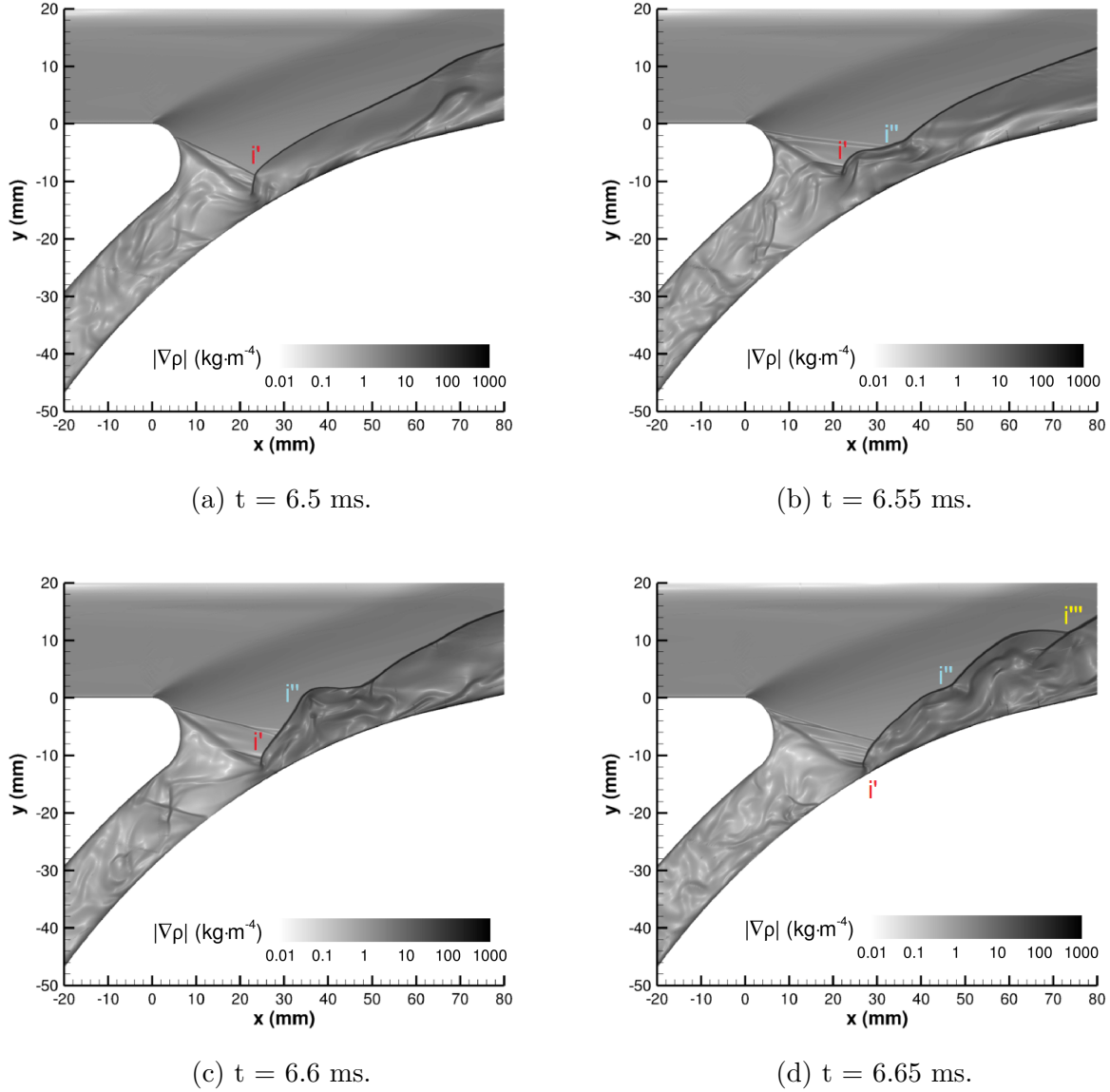
Figure 3.5. Instantaneous density gradient magnitude contours at the wing-elevon juncture centerline, $z = 0$ m. The marker i′ corresponds to shock impingement. The markers i″ and i‴ correspond to shock distortions.

Coherent vortex structures in turbulent flows can form due to flow instabilities, such as the Kelvin-Helmholtz instability in separated shear-layers [75], [76], [80], [142] or the Görtler centrifugal instability [87], [90], [143], [144]. Görtler vortices comprise periodic counter-rotating vortices produced by the centrifugal instabilities in the boundary-layer. Importantly, Görtler vortices in hypersonic flows are associated with exceedingly high surface heat flux
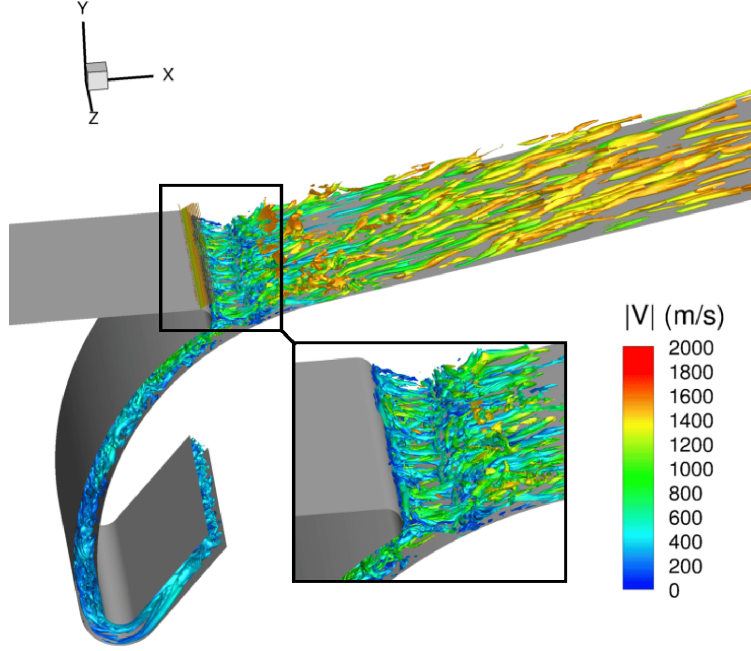
Figure 3.6. Instantaneous Q-Criterion iso-surfaces contour-colored by velocity magnitude, $|V|$. An enlarged frame of the local cove juncture is included.

rates and the development of non-homogenous surface streak formations. These structures are produced in this flow as a result of the large concave streamline curvature present. The streamline curvature in the shock-wave/boundary-layer interaction is caused by the deflected elevon surface. There is also large streamline curvature produced as the flow is entrained into the cove. The average Görtler number associated with the streamline curvature at reattachment is $\mathcal{G}_{\mathrm{ret}} = 6.4$. The average Görtler number associated with the flow entrainment streamline curvature is $\mathcal{G}_{\mathrm{ent}} = 8.2$. The average spacing between adjacent vortices, λ, is approximately equal to δ_{cove}. The average growth rate, which can be approximated with the ratio between heat flux at boundary-layer reattachment and separation, is $\sigma = 2.2$.

Görtler vortices were observed to originate in shock-wave/boundary-layer interaction region and propagate downstream of reattachment. These structures exist within the redeveloping boundary-layer and are visualized with a planar extract in Figure 3.7. This figure displays an instantaneous vorticity magnitude contour, $|\omega|$. The two-dimensional extraction plane is highlighted for reference in the top-left corner. This plane cuts through the elevon center of rotation, located at $(x, y) = (0.228, -0.387)$ m, and is normal to the elevon surface.

The surface-normal distance, y_n, and spanwise distance, z, are non-dimensionalized by the boundary-layer thickness at the reference location, δ_{cove}. One coherent Görtler vortex is visualized in an enlarged frame, which includes sectional streamlines to display the counter-rotating structure. The dividing region between the high and low vorticity represents the local boundary-layer thickness. The regions of maximum vorticity indicate the formation of the counter-rotating vortices, which are clearly displayed in Figure 3.7. This figure depicts the local structure of the Görtler vortices in the redeveloping boundary-layer. However, there is unsteadiness in the size, number, and spacings of Görtler vortices present at any computational time. For example, during the distortions of the reattachment shock-wave, shown in Figure 3.5, the local boundary-layer thickness varies, which proportionally affects the size of the structures. As the flow moves from reattachment to downstream, these structures become larger and eventually dissipate. This behavior is aligned with the elongation of the vortical structures seen in Figure 3.6. The appearance of these structures displays the three-dimensionality of the flow downstream of reattachment. The resultant heat flux streaks discussed in the following section are also attributed to these structures.
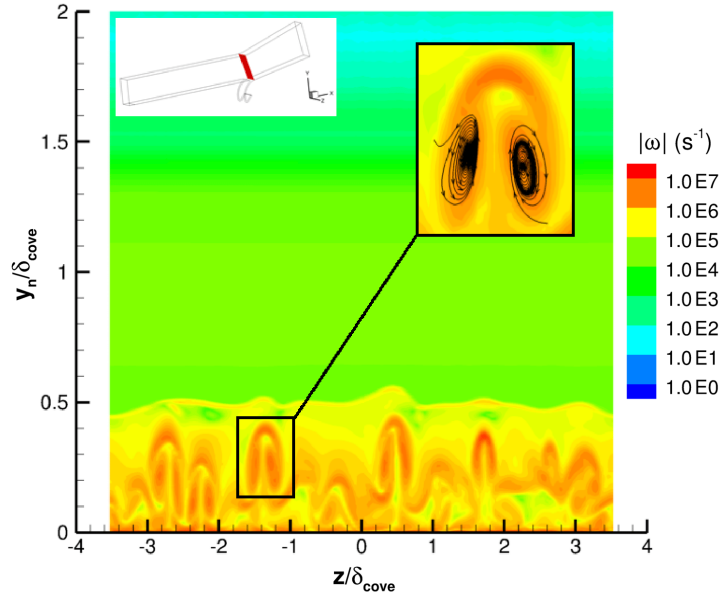
Figure 3.7. Instantaneous contour of vorticity magnitude, $|\omega|$, with the planar extraction location highlighted. An enlarged frame of one Görtler vortex, with sectional streamlines, is included.

3.2 Aerothermodynamic Loading

The resultant time-averaged aerothermodynamic loading is visualized and discussed in this section. The published experimental results include centerline pressure and heat flux data on the edge of the main wing element surface, the elevon surface, and the interior cove surfaces. To match the experimental notation, surface pressure and heat flux results were non-dimensionalized by reference values. These values were obtained on the wing surface, located 25.4 mm upstream of the configuration's coordinate system origin. Both the computational and experimental configuration's coordinate system have the origin located at $(x, y, z) = (0, 0, 0)$ m. This origin is located at the junction of the flat portion of the wing and the curved edge of the main wing element, which is immediately prior the wing-elevon juncture. Reference surface pressure on the upstream wing is $P_{\text{ref}} = 10.16$ kPa and reference surface heat flux is $\dot{q}_{\text{ref}} = 205$ kW/m². The experimental reference values were 10.3 kPa and 193 kW/m², respectively.

The three-dimensional time-averaged surface heat flux, $\bar{\dot{q}}$, is provided in Figure 3.8. Surface streaks, which are associated with Görtler-type vortices, exist on the elevon surface downstream of reattachment. Numerous hypersonic compression ramp studies have observed these streaks [49], [73], [74], [90], [143], [145]. These streaks are comprised of alternating regions of high and low heat flux. The coherent line of reattachment can be seen with a region of high aerothermal loading on the elevon surface. The heat flux reaches a local maximum at reattachment and decreases significantly afterward. The heat flux gradually rises downstream along the elevon and eventually asymptotes. Far enough downstream, the spanwise streaks coalesce and surface variables become constant in the spanwise direction.

The three-dimensional time-averaged surface skin friction, $\overline{C_{fx}}$, is provided in Figure 3.9. In this figure, the values of skin friction below zero are blanked out in order to show reverse flow directions and the line of reattachment. The skin friction at the edge of the main wing element, where the boundary-layer separates, is large. At reattachment, there is a coherent line of $C_f = 0$, which is symmetric in the span. Despite this, the downstream surface loading display non-homogenous spanwise distributions. After reattachment, there is a gradual rise in skin friction from reattachment to downstream. The hypersonic streaks
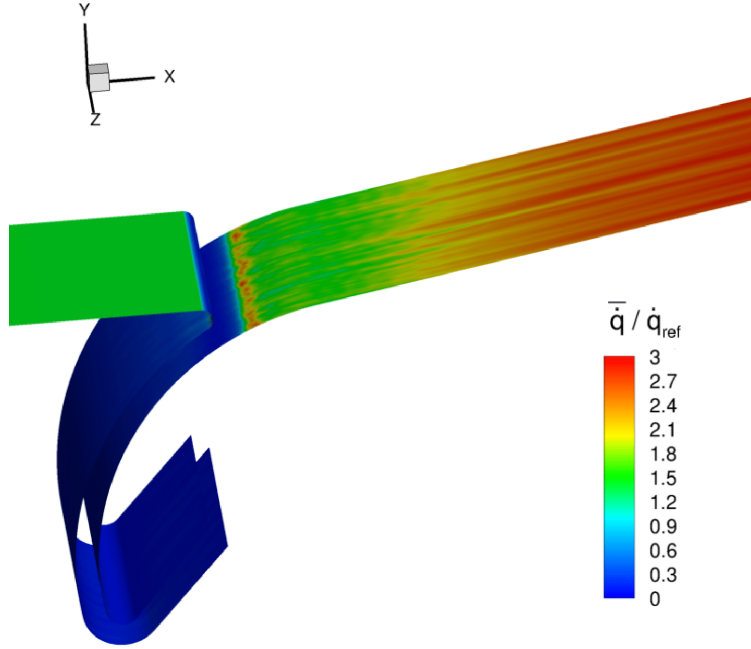
Figure 3.8. Three-dimensional time-averaged visualization of the surface heat flux, $\bar{\dot{q}}$, non-dimensionalized by the reference value, $\dot{q}_{\mathrm{ref}}$.

seen in the previous figure are also visible here. The reversed flow inside of the cove, caused by the secondary separation vortex, can be seen with positive skin friction upstream of reattachment. Similarly, as the flow turns to exit through the cove pressure outlet, the skin friction becomes positive.

The time-averaged centerline interior wing surface pressure and heat flux are plotted and compared with experimental data in Figure 3.10a. Tabulated experimental data were provided by the experimental study with a distance variable, s, which represents a natural coordinate, i.e., running length along the interior wing surface and the interior and exterior elevon surface. To match this notation, the same natural coordinate was used. For the interior wing surface, this coordinate was measured from the reference point moving into the cove region. The aerothermodynamic loading in the cove region is relatively constant, with non-dimensional surface pressure and heat flux of $\overline{P}/P_{\mathrm{ref}} = 0.1$ and $\bar{\dot{q}}/\dot{q}_{\mathrm{ref}} = 0.2$, respectively. Inside of the cove, the predicted surface pressure agreed well with the experiment and was within 5-10% of experimental data. The surface heat flux also agreed well and was within 5-30% of experimental data. The data points with the highest discrepancy in heat flux occur
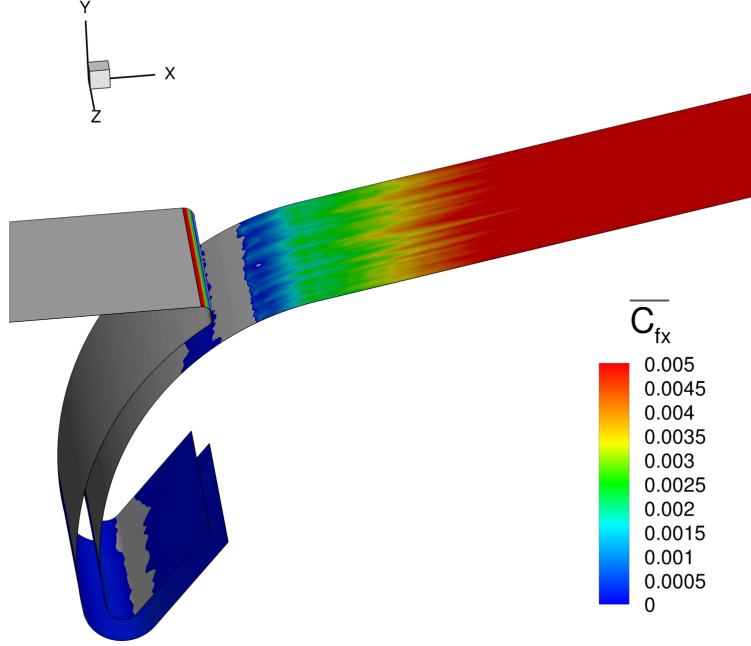
Figure 3.9. Three-dimensional time-averaged visualization of the surface skin friction, $\overline{C_{fx}}$. Values below zero are blanked out.

where the heat flux values change rapidly, which may have affected the reported experimental values due to the spatial averaging of probes.

The time-averaged centerline surface pressure and heat flux on the interior/exterior elevon surface are compared in Figure 3.10b. However, the focus of this plot is on the exterior elevon surface data. For the elevon surface, the natural coordinate is measured moving outward of the cove. The starting reference point is located at the closest surface point parallel to the center of rotation, which is located at $(x, y) = (0.228, -0.387)$ m. On the interior elevon surface, the computational data showed reasonable agreement with experimental data. The initial sharp rise in surface variable data at $s = 0.2$ m is attributed to the mean reattachment location. The mean reattachment location was overpredicted by roughly 15 mm. The aerothermodynamic loading at reattachment is a local maximum, with non-dimensional surface pressure and heat flux values of $\overline{P}/P_{\text{ref}} = 3$ and $\bar{\dot{q}}/\dot{q}_{\text{ref}} = 2.2$, respectively. These values were predicted within 5%-10% of the experimental data, showing excellent agreement. Both surface pressure and heat flux eventually reach asymptotic values far downstream of the interaction. The downstream values of non-dimensional surface pressure and heat flux val-

ues of $\overline{P}/P_{\mathrm{ref}} = 3.5$ and $\overline{\dot{q}}/\dot{q}_{\mathrm{ref}} = 2.8$, respectively. On average, the pressure and heat flux computational data were computed within 5-20% of the experimental data.

(a) Interior wing surface.　　　　　　(b) Interior and exterior elevon surface.
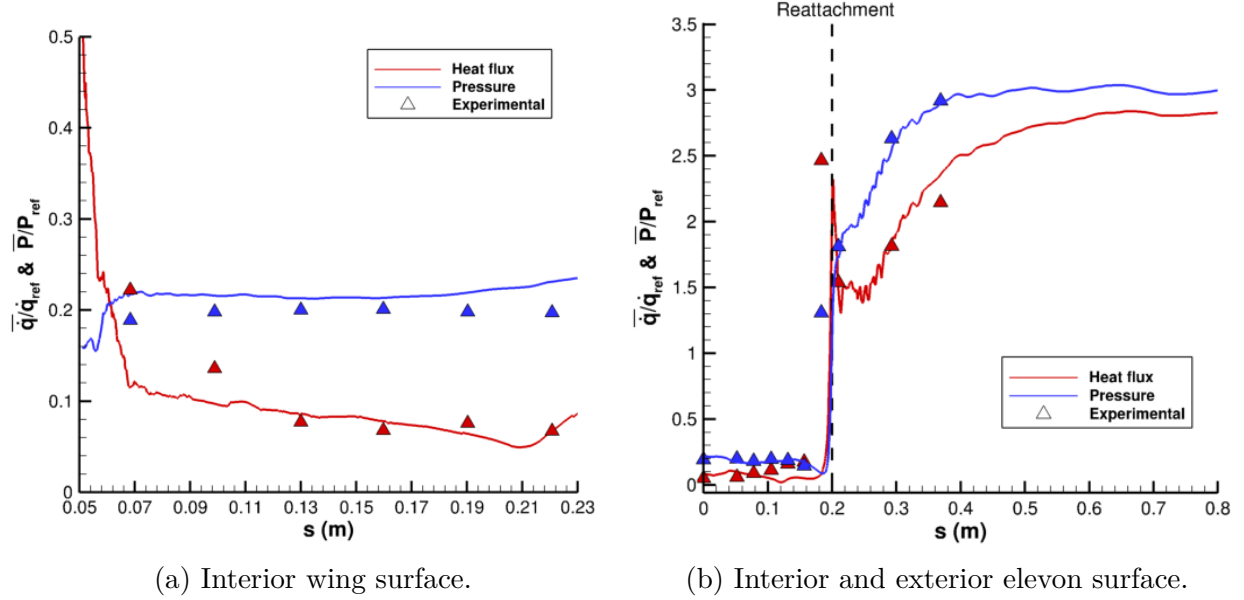
Figure 3.10. Centerline, $z = 0$ m, time-averaged heat flux, $\overline{\dot{q}}$, and pressure, $\overline{P}$, non-dimensionalized by reference values, $\dot{q}_{\mathrm{ref}}$ and P_{ref}, obtained 25.4 mm upstream of the origin. Experimental data [42] included for comparison.

3.3　Statistical Analysis

The primary research goal of this project was to analyze and characterize the unsteady hypersonic flowfield. Therefore, a large portion of the work revolved around statistical analysis of the unsteady fluctuations in the flow. This section provides these analyses and a discussion of the statistics. The statistical analyses that were done include calculations of space-time correlations, power spectral densities, and coherence. The calculations of these statistical quantities were previously defined in (2.28)-(2.32). This section is presented in two separate parts. The first portion provides the unsteady shock-wave/boundary-layer interaction flow statistics and analyses, and the second portion provides similar analyses for the intermittent wall pressure fluctuations.

71

The time-series data in this section were obtained with a constant sampling frequency of $f_s = 10$ MHz. This value corresponds to a sample at every computational time step. Time-averaging and data statistics were done after an initial period of 3 ms to avoid including transient phenomena in the data collection. Therefore, each time-series contains computational data up to 12 ms. Zero-mean, weakly-stationary signals are required for statistical analysis. Consequently, mean values are removed from all time-series data. In addition, time-series data are zero-padded to a power of two to facilitate fast Fourier transforms. Power spectral density calculations were done using Welch's method and employed a Hamming window with a segment length of 8192 points and 50% overlap. The transient cut-off time was taken by examining the time-series data at various locations. A moving-average mean was calculated for the heat flux near reattachment, $\dot{q}_{\mathrm{ret}}$, and for the reattachment position time-series, L'_r. The moving average of an example variable, ϕ, is calculated as

$$\phi_{\mathrm{avg}}(N\Delta t) = \frac{1}{N} \sum_{n=0}^{n=N-1} \phi(n\Delta t), \tag{3.1}$$

where N is an integer, $N = 1, 2, 3...$, and Δt is the inverse sampling frequency. Figure 3.11 provides the moving average over the computational time for the heat flux at reattachment and for the reattachment position time-series. The initial transient phenomena, where the flow is evolving from a starting point of freestream conditions, are evident in this figure. After about 3 ms of time, the value for heat flux appears to asymptote to its mean value, showing convergence to a statistically steady state.

The reattachment position time-series, L$'_r$, was created using the location of zero skin friction on the centerline elevon surface. The mean reattachment position is $\overline{L_r} = 0.02$ m. This time-series is used in the shock-wave/boundary-layer interaction analyses and is provided in Figure 3.12. The displacement from the mean reattachment position, Δs, is obtained using the natural coordinate, s, outlined in the previous section. This figure provides an example of the zero-padded, zero-mean, time-series data, excluding initial transient data, used in the following analyses.
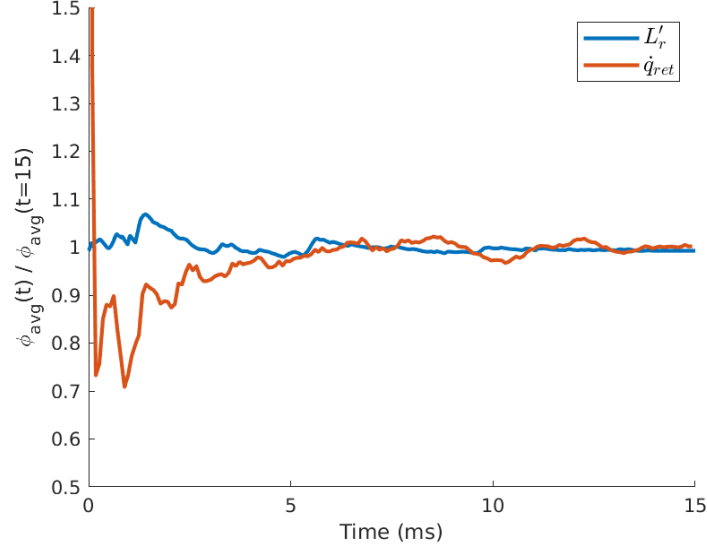
Figure 3.11. Moving average of the heat flux at reattachment, $\dot{q}_{\mathrm{ret}}$, and the unsteady reattachment position, L_r'.
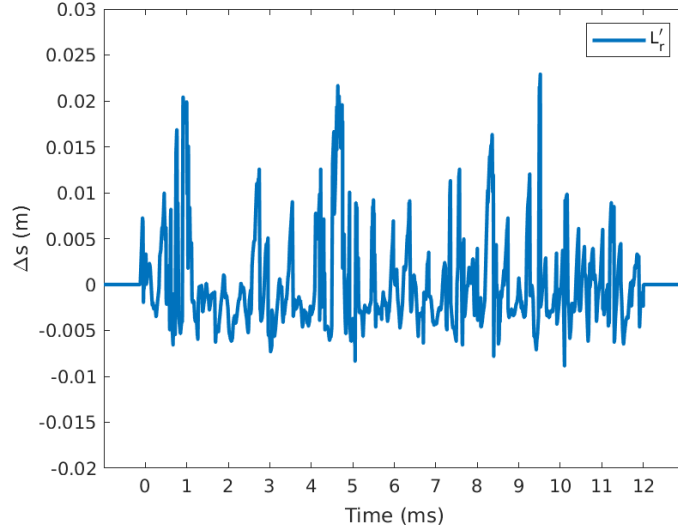
Figure 3.12. Zero-padded, zero-mean, unsteady time-series of reattachment position, L_r', excluding initial transient data.

3.3.1 Unsteady Shock-Wave/Boundary-Layer Interaction

The mechanism in which unsteady motion affects the mean flow can be characterized by the single-point covariance of velocity fluctuations, or resolved Reynolds stress [79]. The

resolved Reynolds stress components, $\overline{u'_i u'_j}$, non-dimensionalized by the freestream velocity squared, u_∞^2, are provided in Figure 3.13 for the shock-wave/boundary-layer interaction. These contours are two-dimensional centerline, $z = 0$ m, planar slices. The general structure of the shock-wave/boundary-layer interaction is depicted in these figures. Many of the phenomena observed in the previous sections are visible, such as the shear-layer, the shock-wave, and the shear-layer/shock-wave impingement.

The shear-layer/shock-wave impingement location strongly contributes to the resolved Reynolds normal stress, R_{11}, shown in Figure 3.13a. Similarly, the reattachment shock-wave produces maximum resolved Reynolds normal stress, R_{22}, shown in Figure 3.13b. The development of the reattaching shear-layer affects both resolved Reynolds Stresses. The resolved Reynolds normal stress, R_{33}, shown in Figure 3.13c, displays maximum values near the wing surface where flow accelerates as it is entrained into the cove. The resolved Reynolds shear stress, R_{12}, shown in Figure 3.13d, displays negative streamwise and vertical velocity fluctuation correlation, which is characteristic of the turbulent transport by eddies in a shear flow [146]–[148]. Inside of the cove region, a small region of velocity fluctuations is shown to be positively correlated. This is caused by the aligned orientation of the shear flow moving into the cove along the elevon surface. All resolved Reynolds stresses display non-zero values immediately inside of the cove and downstream of reattachment. However, outside of the shock-wave/boundary-layer interaction region, the resolved Reynolds stresses approach zero. This could be a factor of the grid stretching, which may have damped out the unsteadiness in the boundary-layer. The main goal of this project was to evaluate the unsteadiness in the cove, and thus a trade in resolution was made downstream of reattachment.

The coherent movements in the shock-wave/boundary-layer interaction region correspond to shear-layer flapping, u'_2, shock-wave oscillation, u'_1, and separation vortex breathing, p'. The unsteadiness of the shock-wave/boundary-layer interaction can be characterized by these coupled mechanisms. These shock system components were analyzed with two-point zero time-delay cross-correlations. Contours of these correlations are provided in Figure 3.14. All time-series data for the reference and surrounding signals are taken at the centerline, $z = 0$ m, aside from L'_r. The unsteady vertical velocity fluctuations, u'_2, were used to depict the coherent movement of the shear-layer. The shear-layer correlation reference time-series is

(a) $R_{11} = \overline{u'_1 u'_1}$.

(b) $R_{22} = \overline{u'_2 u'_2}$.

(c) $R_{33} = \overline{u'_3 u'_3}$.

(d) $R_{11} = \overline{u'_1 u'_2}$.
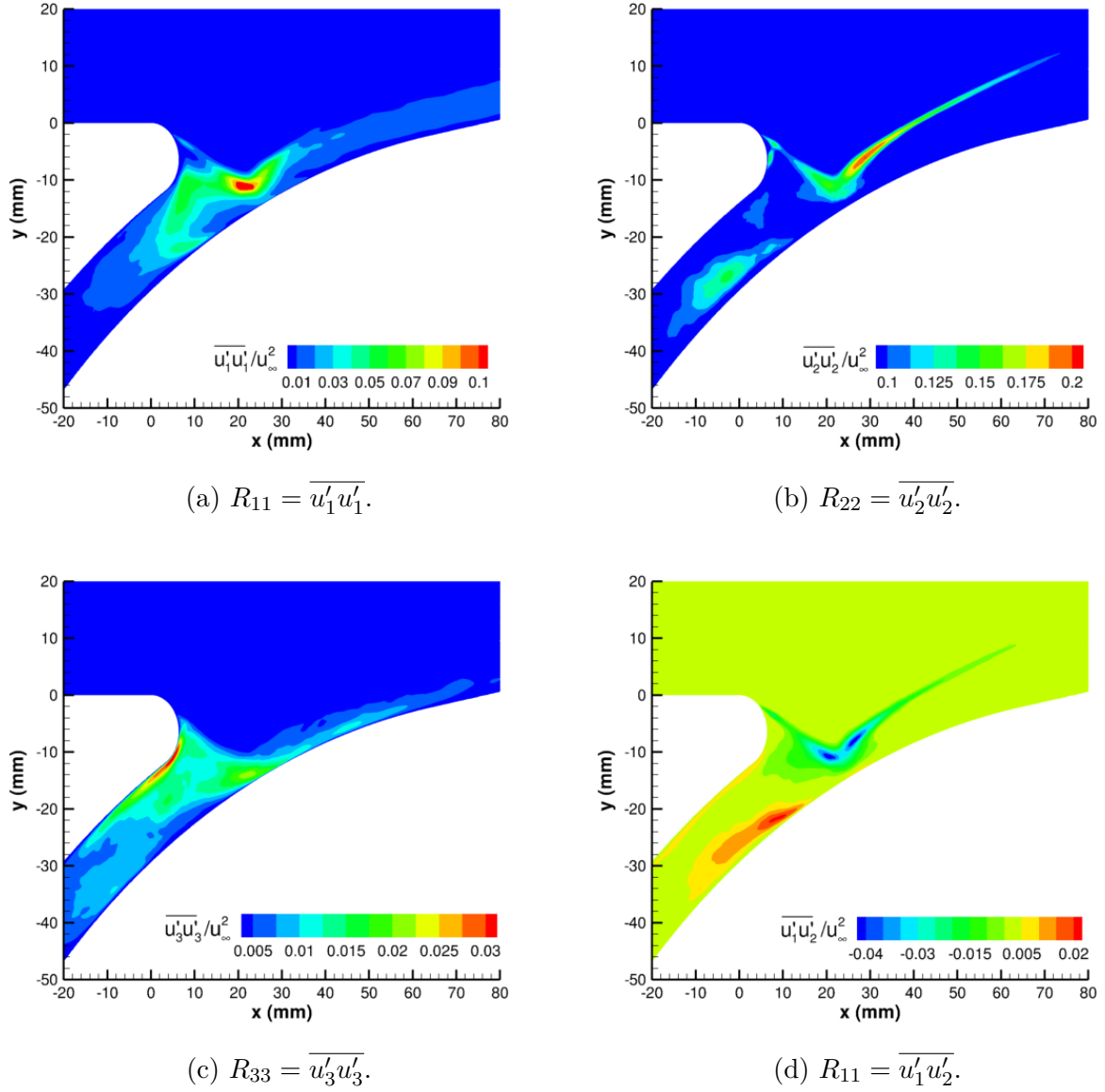
Figure 3.13. Centerline, $z = 0$ m, contours of resolved Reynolds stress, $\overline{u'_i u'_j}$, non-dimensionalized by the freestream velocity squared, u_∞^2.

located at $(x, y) = (14, -5.1)$ mm. The unsteady streamwise velocity fluctuations, u'_1, were used to depict the shock-wave oscillation. The shock-wave correlation reference time-series is located at $(x, y) = (30.1, -4.8)$ mm. Similarly, the unsteady pressure fluctuations, p', were used to analyze separation expansion and contraction. The separation reference time-series

is located at $(x, y) = (9.8, -8.0)$ mm. Lastly, the reattachment position time-series, L'_r, is correlated with surrounding vertical velocity fluctuations, u'_2.

The shear-layer correlation contour provided by Figure 3.14a displays a 20 mm region of high positive correlation ranging $0.7 \leq R \leq 0.9$. This high correlation indicates that the majority of the shear-layer moves coherently together. In addition, a region of negative correlation, ranging $-0.1 \leq R \leq -0.3$, can be seen both near the shock-wave and near reattachment. The shock-wave correlation contour is provided in Figure 3.14b. Similar to the shear-layer, this contour depicts the oscillation of the shock-wave through a 10 mm region of high positive correlation ranging $0.7 \leq R \leq 0.9$. As expected, the shear-layer displays negative correlation, indicating the two movements oppose each other. Reattachment can be identified with a region of negative correlation, $R \geq -0.3$. The downstream shock distortion is seen with a 40 mm region of negative correlation ranging $-0.3 \leq R \leq -0.1$. The separation vortex correlation contour in Figure 3.14c displays a 10 mm by 10 mm region of high positive correlation ranging $0.7 \leq R \leq 0.9$. In addition, a positive correlation of $R = 0.3$ depicts the shock-wave structure. Similar to the other correlations, a region of negative correlation is seen near reattachment. Lastly, the reattachment time-series correlation contour is provided in Figure 3.14d. The components of the unsteady shock system are depicted and display small regions of correlation to the reattachment position time-series. In this figure, the reattachment shock-wave and separation vortex are visible, with a positive correlation of $R = 0.1$. The shear-layer/shock-wave impingement location is also visible with a region of negative correlation of $R = -0.1$. Collectively, these contours depict the large correlation within individual shock system components and the coupled nature of the shock system.

Space-time cross-correlations in the shear-layer, the shock-wave, and the primary separation vortex were calculated and are provided in Figure 3.15. Data were obtained at the centerline, $z = 0$ m. Time-series data in the shear-layer correspond to vertical velocity fluctuations, u'_2, and were obtained at $(x, y) = (14, -5.1) \pm (0, 1)$ mm. The time-series data in the shock-wave correspond to horizontal velocity fluctuations, u'_1, and were obtained at $(x, y) = (30.1, -4.8) \pm (1, 0)$ mm. Time-series data in the separation vortex correspond to pressure fluctuations, p', located at $(x, y) = (9.8, -8.0) \pm (1, 0)$ mm. The time-delays of the cross-correlations are non-dimensionalized by the freestream velocity, u_∞, and the spac-

(a) Shear-layer, u_2'. Ref. $(14, -5.1)$ mm.

(b) Shock-wave, u_1'. Ref. $(30.1, -4.8)$ mm.

(c) Separation, p'. Ref. $(9.8, -8.0)$ mm.

(d) Reattachment position, L_r'.
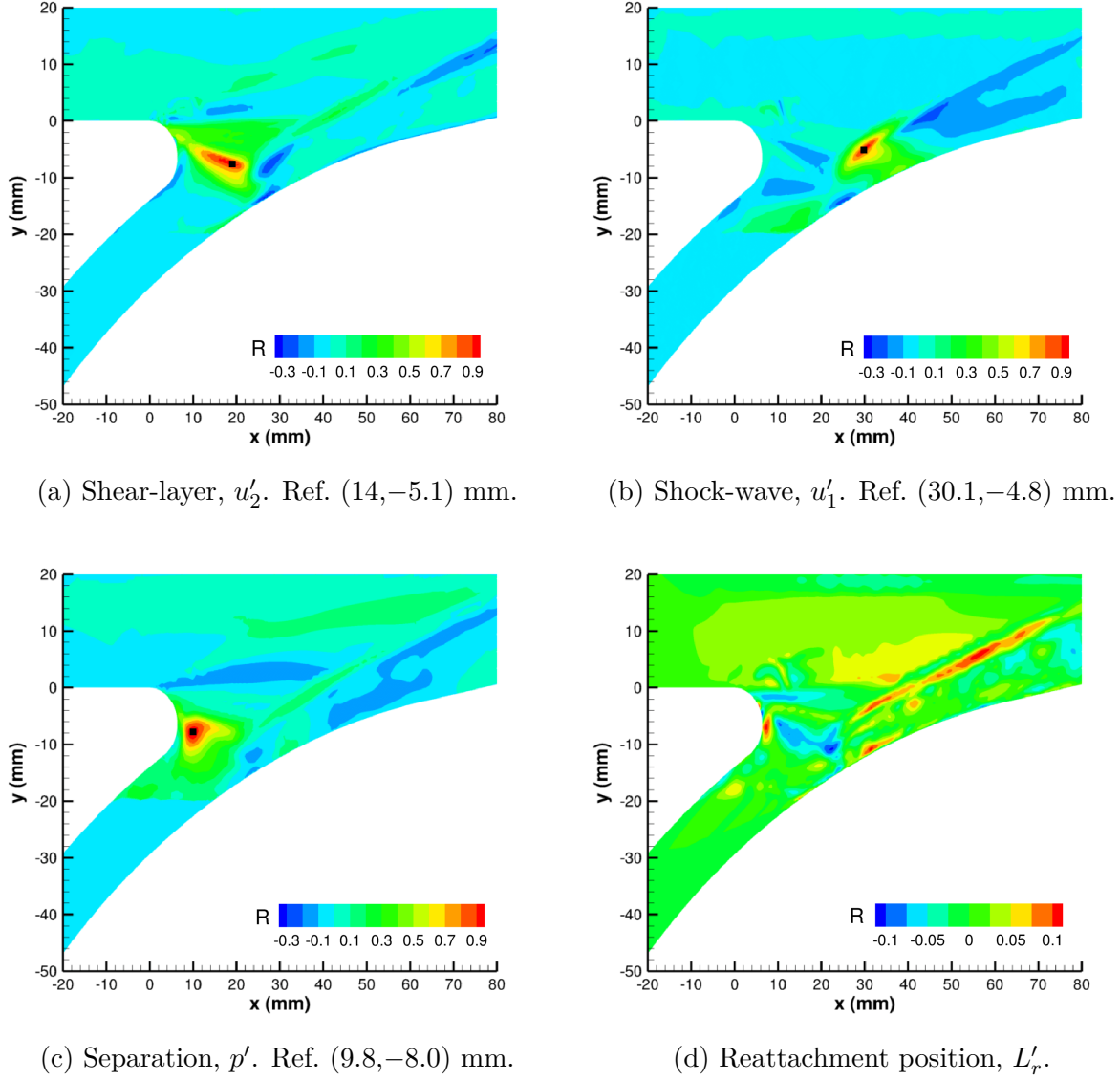
Figure 3.14. Zero time-delay cross-correlations in the shock-wave/boundary-layer interaction. Reference locations are marked with black squares.

ing between data locations, $\Delta x = \sqrt{(x_\beta - x_\alpha)^2 + (y_\beta - y_\alpha)^2}$. The optimal time-delay, at peak correlation, allows for a convection velocity, U_c, to be approximated. This calculation determines the speed at which flow information is propagated in separate locations throughout the shock-wave/boundary-layer interaction region. The convection velocity across the shear-layer is approximately equal to $U_c = 1028$ m/s, with a peak correlation of 0.72. The convection velocity throughout the shock-wave is approximately equal to $U_c = 372$ m/s, with

a peak correlation of 0.64. The convection velocity across the primary separation vortex is approximately equal to $U_c = 588$ m/s, with a peak correlation of 0.38. All three space-time cross-correlations oscillate about $R = 0$ as the dimensionless time-delay, $\Delta t u_\infty / \Delta x$, increases above ± 50. Collectively, the non-dimensional convection velocities in the shock-wave/boundary-layer interaction were $U_c/u_\infty = 0.50$, 0.20, and 0.30 for the shear-layer, the shock-wave, and the separation vortex, respectively. These convection velocities are notably lower than those calculated for the elevon surface pressure fluctuations.
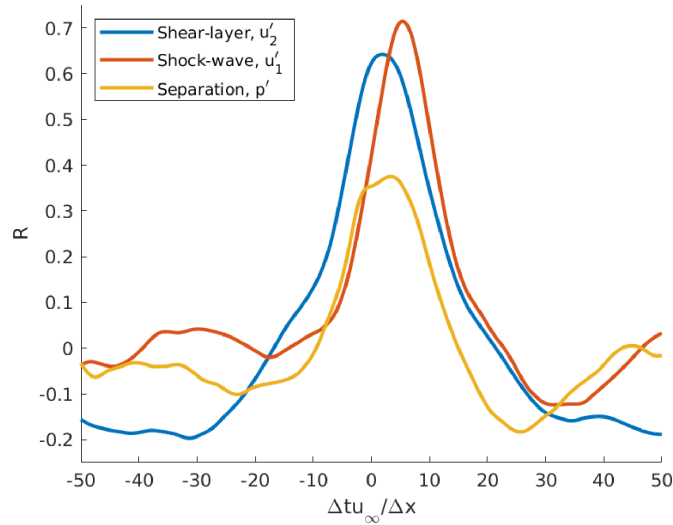
Figure 3.15. Space-time cross-correlations for unsteady fluctuations in the shear-layer, the shock-wave, and the separation vortex.

Spectral analysis of the unsteady fluctuations in the shock-wave/boundary-layer interaction was conducted with power spectral density and coherence calculations. The time-series data in this region correspond to shear-layer flapping, u_2', shock-wave oscillation, u_1', separation vortex breathing, p', and reattachment position movement, L_r'. Aside from L_r', these time-series data were obtained on the centerline, $z = 0$ m, and at $(x, y) = (14, -15.1)$ mm, $(30.1, -4.8)$ mm, and $(9.8, -8.0)$ mm, respectively.

The power spectral densities, $G(f)$, non-dimensionalized by f/σ^2, are provided in a semi-log plot in Figure 3.16. The frequency, f, is non-dimensionalized by the reciprocal of the characteristic frequency, $f_c = u_\infty / \overline{L_r} = 100$ kHz. The non-dimensional frequency is defined as the Strouhal number, S_t, and the non-dimensional power spectra are premultiplied power

78

spectral densities, $fG(f)/\sigma^2$. This figure provides the power spectra for several important shock-wave/boundary-layer interaction phenomena. There are distinct low-frequency peaks for all spectra in the Strouhal number range of $0.02 \leq S_t \leq 0.04$. The shock-wave and reattachment spectra show larger premultiplied power spectra magnitudes in this range. The separation vortex contains slightly higher frequency content, in the Strouhal number range of $0.5 \leq S_t \leq 1$, compared to the other time-series spectra. The peak spectra magnitudes for all signals are in the narrow Strouhal number range of $0.08 \leq S_t \leq 0.09$. The shock-wave and separation vortex show a second peak of similar magnitude, at a Strouhal number of $S_t = 0.12$. These frequency ranges are also similar in magnitude to the shock-wave distortions depicted in Figure 3.5. The spectra depict similar roll-offs from low-to-high frequencies. After $S_t = 1$, there are only low amounts of high-frequency spectral content displayed.

The spectra here are contained within the range of $0.01 \leq S_t \leq 1$, but most of the spectral energy exists within the low-frequency range of $0.01 \leq S_t \leq 0.1$. These frequency ranges are within many reported shock-motion ranges in the literature. For example, Dolling and Or analyzed unsteadiness of the shock-wave structure in compression ramp flows [149]. Experiments were done using Mach 3 flow at a high Reynolds number. Deflections ranging from 8 deg to 20 deg produced premultiplied power spectra which were contained in the Strouhal number range of $0.02 \leq S_t \leq 1$. Similarly, Priebe and Pino Martín simulated a 24 deg compression ramp at Mach 2.9 in order to analyze the low-frequency unsteadiness of the shock-wave/boundary-layer interaction [150]. They obtained premultiplied power spectra, at separation and reattachment, in the Strouhal number range of $0.01 \leq S_t \leq 0.1$. Agostini, et al., analyzed shock reflections on a turbulent boundary-layer and also found shock-motion in the Strouhal number ranges of $0.1 \leq S_t \leq 1$ and $0.03 \leq S_t \leq 0.5$ [151].

Coherence, γ, of time-series data is a useful tool in statistical analysis that provides insight into the frequency behavior of two signals. Coherence has been calculated using the unsteady fluctuations in the shock-wave/boundary-layer interaction region. The signals used in this region once again correspond to shear-layer flapping, u_2', shock-wave oscillation, u_1', separation vortex breathing, p', and reattachment position movement, L_r'. Coherence can be used to investigate the influence of other major components of the shock-wave/boundary-layer interaction on the shock-motion. Therefore, the coherence of the shock-wave signal
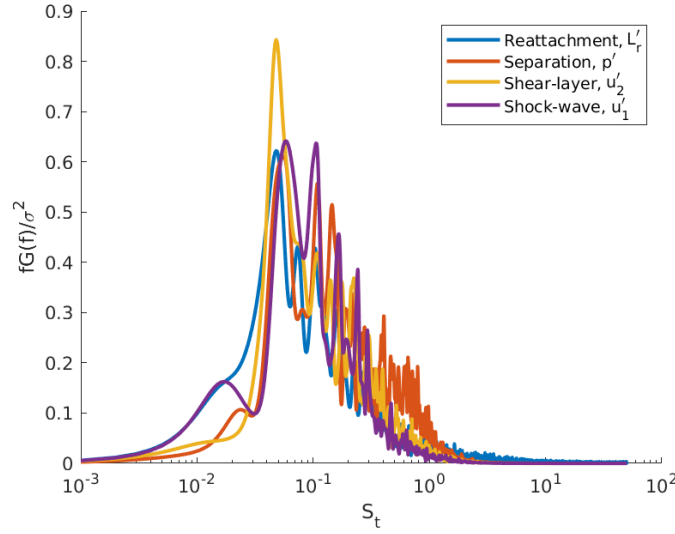
Figure 3.16. Premultiplied power spectral density for the unsteady fluctuations in the shock-wave/boundary-layer interaction. Spectra for reattachment, L'_r, separation, p', the shear-layer, u'_2, and the shock-wave, u'_1.

with all other flow signals has been calculated, along with the coherence between separation and reattachment. These coherence calculations are provided in Figure 3.17. There is strong coherence of the shock-wave time-series with the shear-layer and separation signals, in the Strouhal number range of $0.06 \leq S_t \leq 0.08$. There is weaker, but still noticeable, coherence in the same frequency range between the shock-wave and the separation vortex. There appear to be similar peaks in the same frequency range of $0.1 \leq S_t \leq 0.4$ as well. Signal coherence at higher frequencies than $S_t = 1$ are ignored and assumed to be caused by lack of statistical convergence. The strong coherence shown for Strouhal numbers between $0.06 \leq S_t \leq 0.08$ once again highlights this low-frequency range for this interaction.

3.3.2 Intermittent Surface Loading

Spanwise two-point cross-correlations at zero time-delay were calculated, which determine the correlation between spanwise time-series data with the centerline, $z = 0$ m. Shown in Figure 3.18, the correlations of spanwise surface pressure fluctuations, p', are plotted at various stations. All correlations, by definition, start at $R = 1$ at the reference location and drop to lower values at the sides of the domain. Inside of the cove, $s_1 = 0.18$ m, the correlation
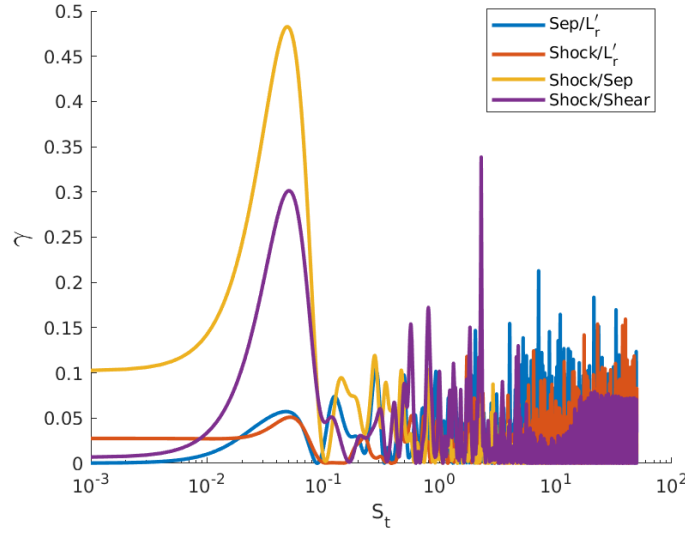
Figure 3.17. Coherence, γ, between the unsteady fluctuations in the shock-wave/boundary-layer interaction.

coefficient drops to roughly 0.4 by $z = \pm 3.5\delta_{cove}$. These large levels of correlation indicate that, inside of the cove, the periodic sides are correlated with the centerline. This occurs because of the coherent low-frequency oscillation of the separated shear-layer across the entire span. Consequently, this indicates that the computational span may not be sufficiently large. The width required to decorrelate the sides with the centerline for this region, however, is likely to be computationally unaffordable and also is unlikely to affect the flowfield behavior outside of the cove. At reattachment, $s_2 = 0.2$ m, the correlation at the edge of the domain drops to low levels of $R = 0.2$. The spanwise distribution is identical at the next downstream station, $s_3 = 0.28$ m. However, much farther downstream, $s_4 = 0.43$ m, the correlation at the sides quickly drops to zero, indicating no correlation with the centerline.

Space-time cross-correlations were calculated for each of the four locations, s_1, s_2, s_3, and s_4. These quantities were calculated by using two time-series datasets, $\alpha(t)$ and $\beta(t)$, which correspond to pressure fluctuations at separate locations. Each location uses surface data obtained ± 1 mm away from the reference location. The time-delays of the cross-correlations are non-dimensionalized by the freestream velocity, u_∞, and the spacing between time-series locations, $\Delta x = \sqrt{(x_\beta - x_\alpha)^2 + (y_\beta - y_\alpha)^2}$. Figure 3.19 provides the plots of the space-time zero time-delay cross-correlations. The general trend in behavior is similar

81
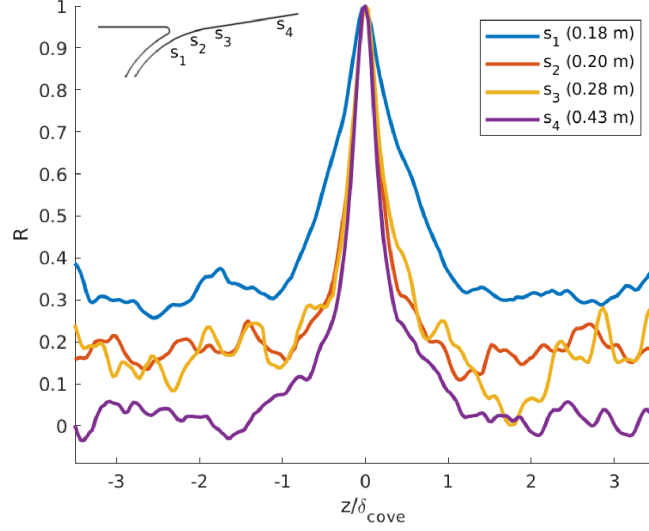
Figure 3.18. Spanwise two-point zero time-delay cross-correlations for s_1, s_2, s_3, and s_4. Spanwise stations are correlated with the centerline, $z/\delta_{cove} = 0$.

to the space-time cross-correlations shown in Figure 3.15. Similarly, all cross-correlations oscillate about $R = 0$ as the dimensionless time-delay, $\Delta t u_\infty / \Delta x$, increases above ± 50. The optimal non-dimensional time-delays for s_1, s_2, s_3, and s_4 are $\Delta t u_\infty / \Delta x = 2.85$, 1.56, 1.33, 1.22, respectively. Using these optimal time-delays, the convection velocities for s_1, s_2, s_3, and s_4 are $U_c/u_\infty = 0.35$, 0.64, 0.75, and 0.82, respectively. This increase in convection velocity downstream is consistent with the behavior of similar interactions [152]–[154]. The convection velocities in the shock-wave/boundary-layer interaction were $U_c/u_\infty = 0.50$, 0.20, and 0.30 for the shear-layer, the shock-wave, and the separation vortex, respectively.

The full spectra for elevon surface pressure fluctuations, p', are provided in Figure 3.20, on the left. The axes are represented by the base-10 log of the Strouhal number, S_t, and the position along the elevon surface, s. The contour is colored by the premultiplied power spectral density. Four different s-locations are extracted and plotted alongside the contour in semi-log scale, on the right. These positions correspond to the secondary separation vortex inside the cove, s_1, mean reattachment, s_2, peak premultiplied power spectral density, s_3, and a downstream station, s_4. The energy levels inside of the cove, up until reattachment, depict similar low-frequency dominated spectra as the shock-wave/boundary-layer interaction. The secondary separation vortex, s_1, shows the lowest peak power spectral density frequency of
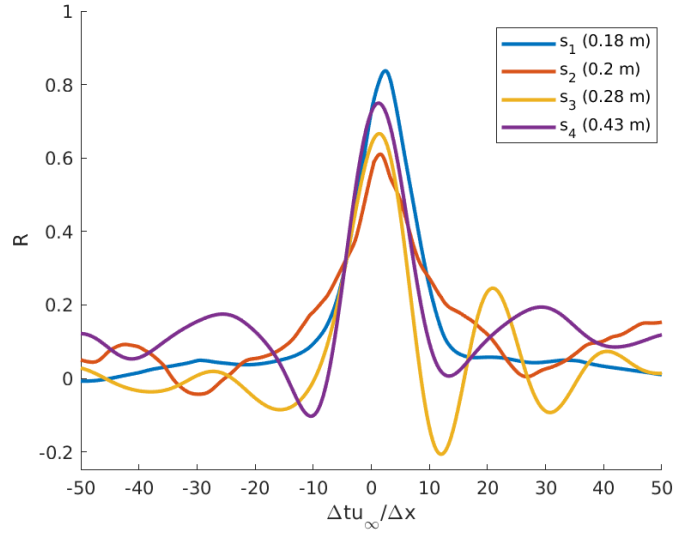
Figure 3.19. Space-time cross-correlations for unsteady surface pressure fluctuations at various downstream elevon surface locations, s_1, s_2, s_3, and s_4.

$S_t = 0.07$ and has a sharp roll-off, which levels off to non-zero energy at intermediate frequencies of $0.3 \leq S_t \leq 1$. The spectrum at reattachment, s_2, shows modal peak power spectral density magnitudes at frequencies of $S_t = 0.08$ and $S_t = 0.16$. The spectral content for this time-series contains equal low, $0.01 \leq S_t \leq 0.1$, and intermediate, $0.1 \leq S_t \leq 1$, frequencies. About 80 mm downstream of mean reattachment, s_3, the spectrum shifts to much higher frequencies. The majority of the energy is constrained to $0.2 \leq S_t \leq 2$, with a peak frequency of $S_t = 1$. As the boundary-layer redevelops away from the interaction, the energy content of the spectrum returns to lower frequencies. For instance, the downstream station, s_4, shifts back to lower frequencies, with peak spectral energy at a frequency of $S_t = 0.3$. This high-to-low shift in frequencies, however, is contrary to what is seen in the computation presented in Chapter 5. As a result, this may have been produced by the grid-stretching and damping of turbulence far downstream.

Lastly, the coherence, γ, of the wall pressure fluctuations for s_1, s_2, s_3, and s_4 are provided in Figure 3.21. This figure shows the coherence between wall pressure fluctuations near reattachment, s_2, with wall pressure fluctuations in the cove, s_1, and downstream, s_3 and s_4. There is relatively high coherence found at very low frequencies of $S_t \leq 0.01$. There are large peaks in coherence in the range of Strouhal numbers between $0.06 \leq S_t \leq 0.08$,
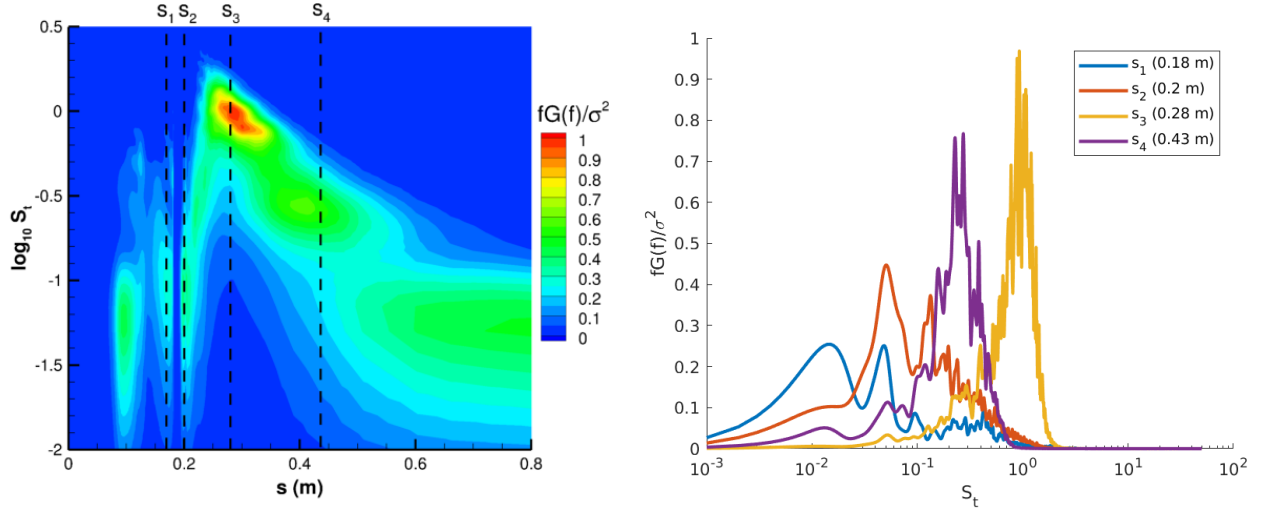
Figure 3.20. Premultiplied power spectral density of surface pressure fluctuations on the elevon. Contour of the complete power spectra is provided (left), with individual power spectra for s_1, s_2, s_3, and s_4 plotted (right).

further highlighting this frequency range. Additionally, there are noticeable lower frequency coherence peaks at $S_t = 0.02$. As with the previous coherence plot, the numerical noise at frequencies larger than $S_t = 1$ are ignored.
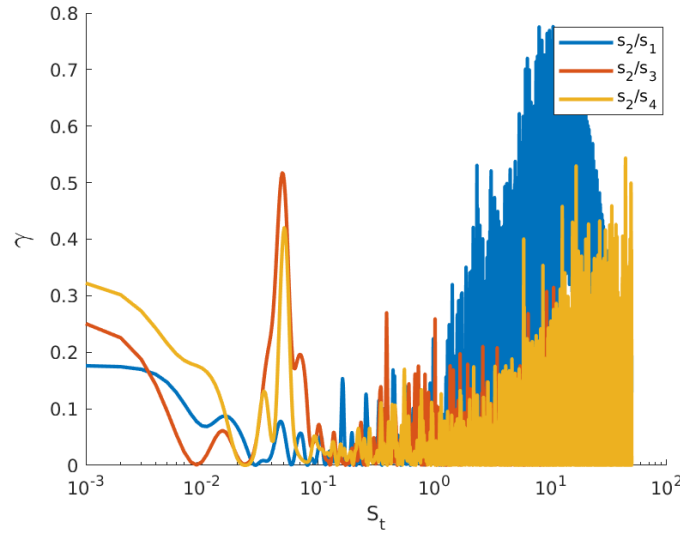
Figure 3.21. Coherence, γ, between the wall pressure time-series data near reattachment, s_2, with those inside the cove, s_1, and downstream, s_2 and s_3.

3.4 Chapter Discussion

This project focused on the 1978 NASA experimental study conducted by Deveikis and Bartlett [42]. For this experiment, hypersonic flow was experimentally generated over a wing-elevon-cove model to simulate the windward surface of a shuttle-type reentry vehicle. A total of 41 tests were done by Deveikis and Bartlett, focusing on the aerothermodynamic loading on the interior and exterior wing and elevon surfaces. These experiments only reported time-averaged aerothermodynamic results and did not publish flow visualizations or conduct statistical analysis. Thus, an important goal of this work was to explore these two areas. One of the NASA experimental tests was computed, corresponding to a Mach 6.9 flow at $Re = 4.29 \times 10^6$ m. The model was set to a -12 deg angle of attack and the elevon was deflected by 15 deg. The order of the data presentation for this chapter followed flow visualization, aerothermodynamic loading, and unsteady statistical analysis.

The hypersonic wing-elevon-cove flow was visualized at the centerline, $z = 0$ m, in the span, and in three-dimensions. Centerline contours of time-averaged temperature and velocity, provided in Figure 3.2 and Figure 3.3, depicted the mean local cove flow structure. In this region, there is an expansion-fan, a separated shear-layer, a separation vortex, shock-waves, and cove flow entrainment. There is also a secondary vortex attached to the elevon surface, which is present in all wing-elevon-cove computations. The unsteadiness of the shock-wave/boundary-layer interaction was visualized with instantaneous density gradient magnitude snapshots in Figure 3.5. The large distortions in the shock-wave, shear-layer, and redeveloping boundary-layer were displayed. The three-dimensional flowfield was visualized with Q-Criterion iso-surfaces in Figure 3.6. The Görtler vortices, which exist in the redeveloping boundary-layer, were visualized in the spanwise y-z plane in Figure 3.7. There are five to eight coherent Görtler vortex structures apparent in the boundary-layer. Comparison with the experiment was done for the centerline time-averaged heat flux and pressure, provided in Figure 3.10. These results show that the mean surface aerothermodynamic loading were predicted reasonably well compared to the experiment. Figure 3.8 provided a visualization of the resultant time-averaged aerothermodynamic loading. This figure shows the non-homogenous spanwise heat flux distributions produced as a result of

85

the Görtler vortices. There is locally high aerothermal heating found at reattachment, as well as characteristic heat flux streaks on the downstream elevon surface. These features are also highlighted in the time-averaged surface skin friction provided in Figure 3.9.

The last section contained most of the data analysis and focus of the project. These results were separated into two portions, one focusing on the unsteady fluctuations in the shock-wave/boundary-layer interaction and the other focusing on the unsteady wall pressure fluctuations. Single-point covariances of velocity fluctuations, or resolved Reynolds Stresses, were calculated, and were presented in Figure 3.13. Contours of these values highlight important flow features such as regions of strong unsteadiness. The primary regions high-lighted in these figures are the shock-wave, the shear-layer, and the shear-layer/shock-wave impingement. The coupled nature of the shock system was investigated with zero time-delay cross-correlations for the shock system signals. These correlations were shown in Figure 3.14 and displayed strong correlation regions for each of the signals. These correlation regions also depicted the distinct structure of the shock system with positive and negative correlations. In addition, space-time correlations were calculated to determine approximate convection veloc-ities, U_c. These space-time cross-correlations were provided in Figure 3.15 and Figure 3.19. The convection velocities in the shock-wave/boundary-layer interaction were $U_c/u_\infty = 0.50$, 0.20, and 0.30 for the shear-layer, the separation vortex, and the shock-wave, respectively. The convection velocities along the elevon ranged $0.35 \leq U_c/u_\infty \leq 0.82$.

The power spectra for signals in the shock-wave/boundary-layer interaction region was investigated to detect low-frequency behavior that is often found in these interactions [151], [155]–[157]. The signals in the shock region were windowed in order to pick up the primary frequency ranges. The premultiplied power spectral densities for the unsteady reattachment position, the separation contraction and expansion, the shear-layer flapping, and the shock-wave oscillation were provided in Figure 3.16. The characteristic frequency for this flow was $f_c = 100$ kHz. Most of the energy in the shock-wave/boundary-layer interaction spectra was contained within the Strouhal number range of $0.02 \leq S_t \leq 1$, which correspond to dimensional frequencies equal to $2 \leq f \leq 100$ kHz. These frequency ranges have been reported for similar shock-wave/boundary-layer interactions [149]–[151], [158], [159]. These frequency ranges are also similar to the instantaneous shock-wave distortions depicted in

Figure 3.5. There exists strong coherence between the signals in the shock system with the shock-motion, shown in Figure 3.17. These coherences peak in the Strouhal number range of $0.01 \leq S_t \leq 0.1$.

The power spectra for the intermittent wall pressure signals along the elevon provide the complete wall frequency behavior for this flow. These spectra were provided in Figure 3.20. This figure plots the spectra for Strouhal numbers ranging $0.01 \leq S_t \leq 3$. There exists low-frequency behavior inside of the cove region due to the entrainment of flow through the unsteady mechanisms of the shock system. There is a distinct shift from low-to-high frequencies at reattachment. This shift is also produced by the low-frequency shock-wave/boundary-layer interaction, corresponding to frequencies in the range of $0.2 \leq S_t \leq 1$. After reattachment, there is a shift from high-to-low frequencies. It is unknown if this behavior is affected by the damping of turbulence on the less-resolved stretched grid in this region. In the computation presented in Chapter 5, where high resolution was withheld for the entire model, there is a shift to higher frequencies down the elevon surface; this is commonly seen downstream of these interactions [54], [58], [90], [143], [144], [158]. There is strong coherence for the elevon between downstream stations and the upstream flow, shown with the coherence plots in Figure 3.21. There is peak coherence at the Strouhal number of $S_t = 0.08$.

The results of this project suggest that improved delayed detached-eddy simulation can be a valuable tool for analysis of hypersonic wing-elevon-cove flows. This project attempted to expand the research done by Deveikis and Bartlett and focused on the low-frequency unsteady shock-wave/boundary-layer interaction. It is important to thoroughly characterize the unsteadiness of these interactions. For instance, the low-frequency oscillations of the shock-wave produce prolonged fluctuations of intense aerothermodynamic loading, which can lead to structural failure [46], [52], [155], [156], [160], [161]. Therefore, the associated research on these interactions has many practical applications to hypersonic vehicle design and development efforts. Overall, the research for this project adds to the community knowledge on hypersonic wing-elevon-cove flows and unsteady shock-wave/boundary-layer interactions. This work has also motivated continued research efforts by Purdue and UTSI. The following two chapters provide the computations associated with these experimental studies.

4. PURDUE BAM6QT WING-ELEVON-COVE

This chapter provides the computational results for the second wing-elevon-cove project. The purpose of this work was to conduct further research and analysis on hypersonic wing-elevon-cove flows. This project was done in collaboration with the Purdue ASL experimental team. The model that was used was the Purdue swept wing-elevon-cove model. The model introduces increased complexity compared to the previous project and includes significant three-dimensionality, such as side gap regions and the wind tunnel surface. This model is being employed in ongoing Purdue BAM6QT wind tunnel experiments. Experimental tests were first conducted with a blockage model, which is a base swept-wing model with no elevon or cove. These tests were done to determine the maximum allowable experimental model size possible without choking the flow. Full wing-elevon-cove model tests are being run currently, but there are no published results yet. The available data for these experiments only include several flow visualizations for the blockage model and preliminary unsteady flow statistics for the wing-elevon-cove model. The initial research goal was to compare the computational results to the experimental wind tunnel data. This was not accomplished due to the overall timing of the experimental and computational projects. However, this research provides practical flow visualization and aerothermodynamic loading analysis associated with hypersonic wing-elevon-cove flows. This work has also been published in conference proceedings [162], and the computational data have aided in the experimental research efforts.

The improved delayed detached-eddy simulation was unable to resolve significant unsteadiness in the shock-wave/boundary-layer interaction at the cove juncture. While the computation did not produce unsteadiness, the preliminary experimental pressure measurements did show low-frequency spectral content for the inside of the cove; however, the overall unsteadiness in the shock-wave/boundary-layer interaction was low. To facilitate an unsteady computation, a parametric sweep was done by modifying various geometric parameters, such as cove length, L_{cove}, and flow conditions, such as stagnation pressure, P_o. These computations employed a partial three-dimensional mesh with a small spanwise extension, at the same resolution, to reduce computational cost. The discussion and visualization of these computations are included in this chapter for reference and context to the primary computa-

tion. The results of this parametric sweep depicted a Reynolds number dependence for the resolved unsteadiness in the cove region. Flows with stronger shock-wave/boundary-layer interactions, or significantly higher cove Reynolds numbers, Re_{cove}, successfully produced unsteady shock-wave/boundary-layer interactions. This proportionality of flow unsteadiness to stronger shock-wave/boundary-layer interactions is consistent with literature [163], [164]. Despite having a large freestream Reynolds number of $Re = 1.1 \times 10^7 \text{ m}^{-1}$, the wing-elevon-cove configuration has the lowest Görtler number, $\mathcal{G} = 1.5$, and cove Reynolds number, $Re_{\text{cove}} = 6 \times 10^6$, of all three computations. The Görtler number is associated with the centrifugal instability in the cove region and is proportional to the local Reynolds number [88], which is consistent with these findings. While several of these computational modifications produced significant flow unsteadiness, the required configurations were unobtainable in the Purdue BAM6QT wind tunnel. The goal of this research involved collaborative efforts with the Purdue ASL experimental team. Therefore, the flow conditions and swept wing-elevon-cove model used in the Purdue BAM6QT experiments were used in the computation.

The primary computation involved simulation of the entire swept wing-elevon-cove surface model and the surrounding wind tunnel surface. A three-dimensional perspective of these computational surfaces is provided in Figure 4.1. This frame of reference rotates the experimental physical frame of reference by 180 deg, i.e., the surrounding wind tunnel surface represents the BAM6QT ceiling. The model consists of a swept wing, at constant sweep of 25 deg, and a trailing-edge elevon deflected by 12 deg. The 0.66 m long flat plate surface upstream of the model allows the boundary-layer to develop and match the corresponding BAM6QT wind tunnel displacement thickness at the beginning of the model, $\delta^* = 5.8$ mm. This configuration includes the BAM6QT wind tunnel surface, the side gap regions, and an embedded elevon. As a result of this significant three-dimensionality, however, it was not possible to create a computational mesh consisting of completely structured blocks. The mesh for the primary computation was therefore created with T-Rex hybrid unstructured meshing, which allows for structured meshing near and around surfaces. A visualization of the computational mesh was provided previously in Figure 2.7. For this mesh, all surfaces have high near-wall resolution, with $\Delta y_w^+ \leq 1$. Focus regions, in the cove, near the wing-root, in the gap regions, and in the wake, have high resolution where possible.
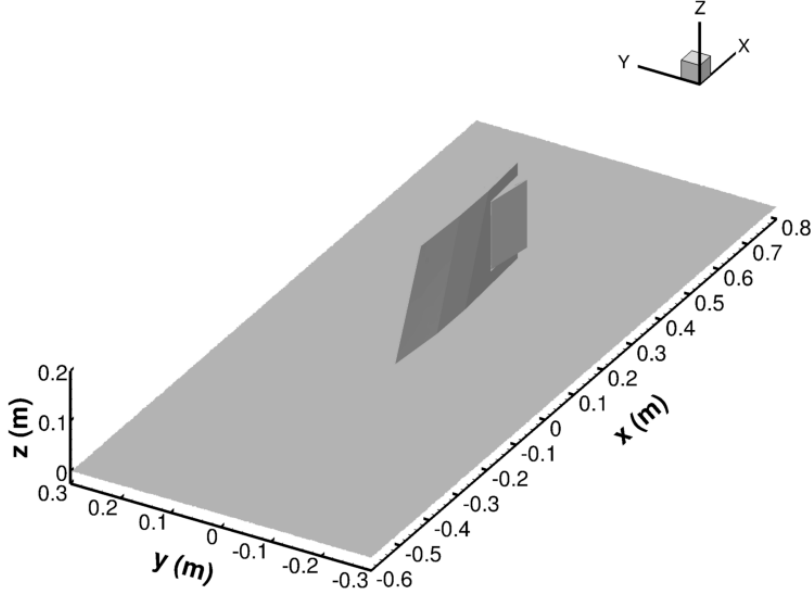
Figure 4.1. Three-dimensional perspective of the swept wing-elevon-cove surface model and the surrounding wind tunnel surface.

Planar perspectives of the swept wing-elevon-cove model are provided in Figure 4.2. These perspectives consist of multiple model schematics with included dimensions. The three frames of reference in this figure correspond to the x-y (a), x-z (b), and y-z (c) planes. These planes are also referred throughout the chapter as the bottom-up, side, and frontal perspectives, respectively. The airfoil cross-section of the wing consists of two straight ramped sections connected by a flat section, seen in the bottom-up (a) perspective. The root cord length of the swept wing-elevon-cove model is 0.423 m, the centerline chord length is 0.379 m, and the wing tip chord length is 0.334 m. The chord length of the elevon is 0.1 m and is constant along its span. The span of the wing is 0.19 m and the span of the elevon is 0.135 m. The cove region and the side gaps between the wing and elevon are 2.52 mm long. The radii of the wing leading-edge and the elevon trailing-edge are equal to 425 μm. The elevon centerline refers to the center-most, $z = 95$ mm, airfoil cross-section of the swept wing-elevon-cove model. The center model perspective refers to the $y = 0$ mm side (b) plane.

The primary computation utilized the BAM6QT flow conditions that were used in the Purdue experiments. While these conditions normally produce laminar or transitional flow,
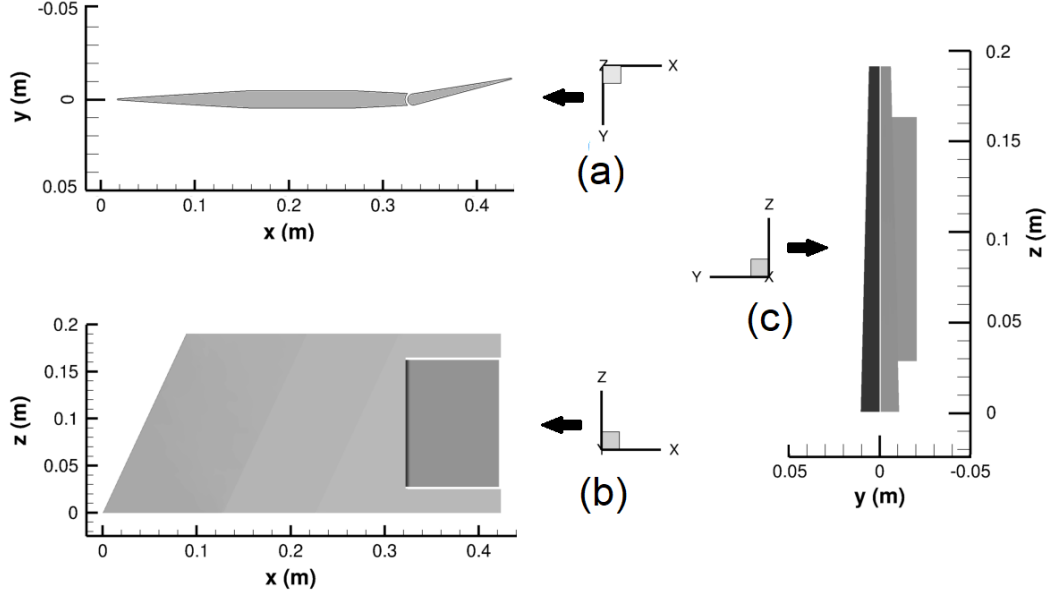
Figure 4.2. Bottom-up (a), side (b), and frontal (c) perspectives of the swept wing-elevon-cove surface model.

transition was outside the scope of this work. Therefore, the computational flow was simulated as fully turbulent. The freestream conditions correspond to high Reynolds number, $Re = 1.1 \times 10^7$ m^{-1}, hypersonic flow at Mach 6. The angle of attack, $\alpha = 0$ deg, was set to match the experiments. For reference, the relevant flow parameters can be found in Table 2.2. The computational model used was improved delayed detached-eddy simulation. The total number of iterations was 200,000, resulting in a simulated time of 20 ms. All data were averaged over the computational time, and time-averaged notations are dropped in this chapter. No periodic boundary conditions were used, and all freestream boundaries used modified Riemann invariant conditions. Surfaces used isothermal wall boundary conditions, set to $T_w = 293.15$ K. This wall temperature matches the approximate experimental value for non-sequential runs. Computational data were collected for the entire flowfield and all surfaces. These data were utilized to investigate the hypersonic flowfield, visualize the three-dimensional flow structure, and depict the resultant aerothermodynamic loading.

4.1 Flow Visualization

This section provides flow visualizations and discussion of the hypersonic flowfield. This flow involves significant amounts of three-dimensionality. There are large-scale vortex structures apparent in the flow and a three-dimensional lambda shock-wave/boundary-layer interaction. The flowfield is visualized in all reference planes, i.e., the x-y plane (bottom-up perspective), the x-z plane (side perspective), and the y-z plane (frontal perspective). In addition, the large-scale vortex structures are visualized in the computational domain through volume streamlines. Collectively, these flow visualizations depict the complexity of the three-dimensional swept wing-elevon-cove flowfield, where the increased geometric three-dimensionality introduces a plethora of additional flow phenomena.

Figure 4.3 provides contours of Mach number for the x-y (bottom-up) plane at the elevon centerline, $z = 95$ mm. This extract location is far enough from the gap regions and the wind tunnel ceiling to not display flow three-dimensionality. These figures provide the general flow structure near the center of the elevon. The entire flowfield shown in Figure 4.3a depicts a generic cross-sectional flow for a supersonic airfoil with a deflected elevon. There is a detached bow-shock at the leading-edge of the wing. The boundary-layer develops along the wing and experiences two small favorable pressure gradient expansion-fan regions. With a symmetric cross-sectional geometry at zero angle of attack, the flow is symmetric about the center chord line up until the elevon. The elevon deflection of 12 deg creates a shock-wave/boundary-layer interaction as the reattaching boundary-layer is abruptly deflected upwards. For this deflection, the flow on the leeward side of the elevon separates, creating a large region of separation. This is seen in the localized contour provided in Figure 4.3b. The separation region spans about 60% of the elevon surface. The boundary-layer sheds from the elevon surface through an expansion-fan region at the trailing-edge and propagates downstream in the wake region. The flow structures along parallel airfoil cross-sections, within the elevon span and away from the side gaps, are all nearly identical to the flow depicted in Figure 4.3. There are minor scaling differences between these cross-sections caused by the sweep angle affecting the wing-elevon-cove chord lengths.

(a) Entire flowfield.

(b) Local elevon region.
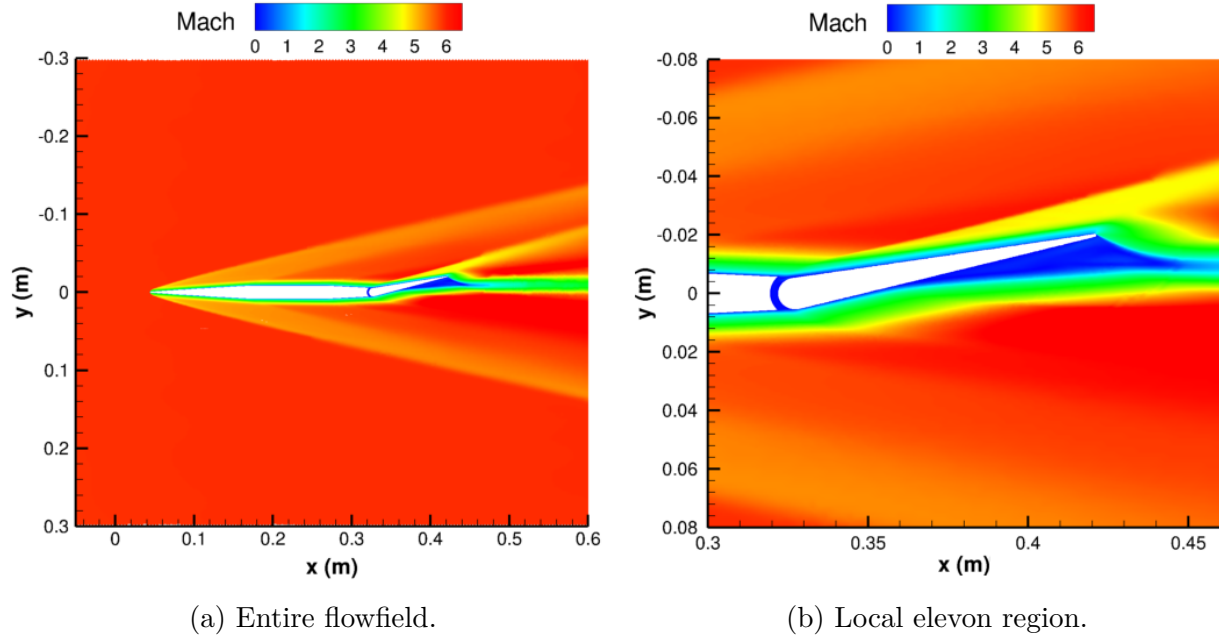
Figure 4.3. Contours of Mach number in the bottom-up plane at the elevon centerline, $z = 95$ mm, for the entire flowfield (left) and the local elevon (right).

The cylindrical cove region for the model is created by two concentric circles with a center of rotation located at the elevon's hinge point $(x, y) = (0.3275, 0)$ m. The radius of curvature of the concave wing-cove surface is 8.15 mm. The radius of curvature of the convex elevon-cove surface is 5.63 mm. The local cove juncture flow structure is visualized with a non-dimensional velocity, u/u_∞, contour in Figure 4.4. This figure is a x-y (bottom-up) planar extract at the elevon centerline, $z = 95$ mm. Sectional streamlines are included to facilitate the depiction of the relevant flow structure components. There are several important phenomena seen here, such as the separation vortex inside of the cove, the flow entrainment, and boundary-layer separation/reattachment. The secondary vortex depicted inside of the cove is observed in all three wing-elevon-cove computations. However, this figure provides a different flow structure compared to the previous project, which was shown in Figure 3.3. The local cove flow structure is strongly affected by the magnitude of the pressure gradient between the external boundary-layer and the internal cove, which proportionally affects flow entrainment. Wing-elevon-cove computations with angles of attack have produced increased flow entrainment, reduced separation size, and increased streamline curvature caused by

the downward deflection of the shear-layer. Without an angle of attack, and at relatively low local Reynolds numbers, there is only weak entrainment of the boundary-layer, and the separation vortex extent is large.
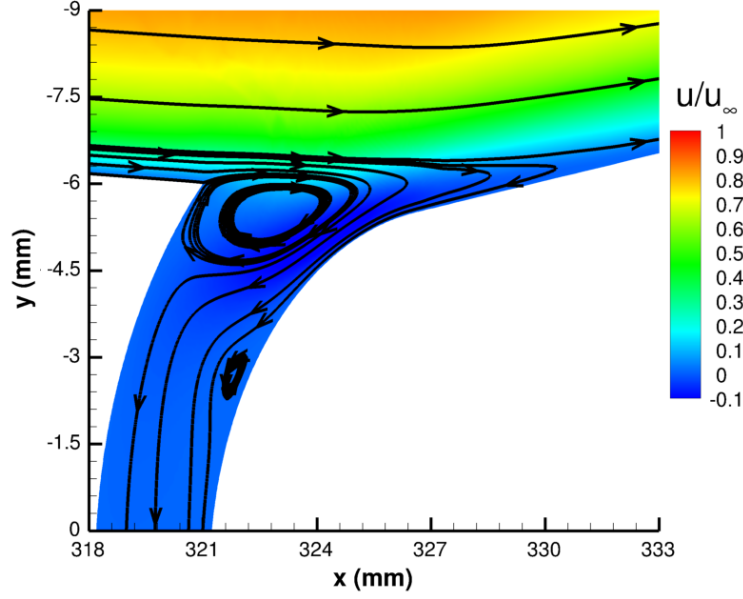
Figure 4.4. Contour of non-dimensional mean velocity, u/u_∞, with sectional streamlines, in the bottom-up plane at the elevon centerline, $z = 95$ mm.

The flow structure in the y-z (side) plane at the swept wing-elevon-cove model center, $y = 0$ m, is visualized in Figure 4.5. This plane slices through the deflected elevon, which is protruding out-of-the-page in this figure. The incoming turbulent boundary-layer separates near the wing-root and flows downstream of the wing's leading-edge. The leading-edge produces a detached bow-shock in the inviscid freestream flow. The average shock standoff distance is roughly 300 μm. This shock-wave produces high rates of aerothermal heating similar to a blunt-body flow [165], [166]. A low-momentum region develops along the wing-tip, where flow from the boundary-layers developing on the surrounding model surfaces are entrained into two counter-rotating wing-tip vortices. There is a weak Mach wave propagating from the start of the wing-tip. The wake of the model involves regions of subsonic flow near the edges of the wing-tip and the wing-root, as well as regions of supersonic flow expanding in the wake of the leeward side of the elevon.
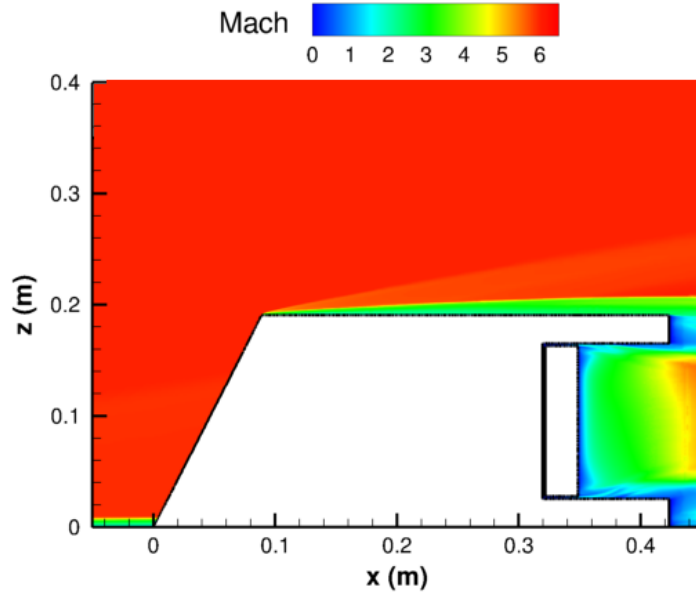
Figure 4.5. Contour of mean Mach number in the side plane at the swept wing-elevon-cove model center, $y = 0$ m, for the entire flowfield.

The swept wing-elevon-cove model and surrounding wind tunnel surface produce a three-dimensional lambda shock-wave/boundary-layer interaction. This three-dimensional shock formation is seen in several hypersonic flowfields, such as sharp fins [167]–[169] or cylindrical protuberances [170]–[172]. The interaction simulates the effect of a fuselage on the resultant wing-elevon-cove hypersonic flowfield. In Figure 4.6, the lambda shock-wave/boundary-layer interaction is depicted in the y-z (frontal) plane, located upstream of the elevon, $x = 0.3$ m. In this figure, a contour of normalized pressure, P/P_∞, is provided with an included frame of surface pressure plotted along the wind tunnel surface. The model surface is on the right end of the figure, near $y = 0$ m. The lambda shock structure is apparent in this figure through the initial jump in normalized pressure. There is a region of large local maximum pressure immediately after the shock. The near-surface horseshoe vortex distorts the pressure field near the wing-root. After developing along the wing-elevon surface, the boundary-layer perpendicular to the surface is depicted with a region of lower normalized pressure. The influence of the wing-tip vortex can be seen in the top-right corner of the model. The surface pressure profile for this region is also included here, showing the gradual increase

of pressure through the lambda shock formation and eventual drop in pressure through the horseshoe vortex and surface boundary-layer.
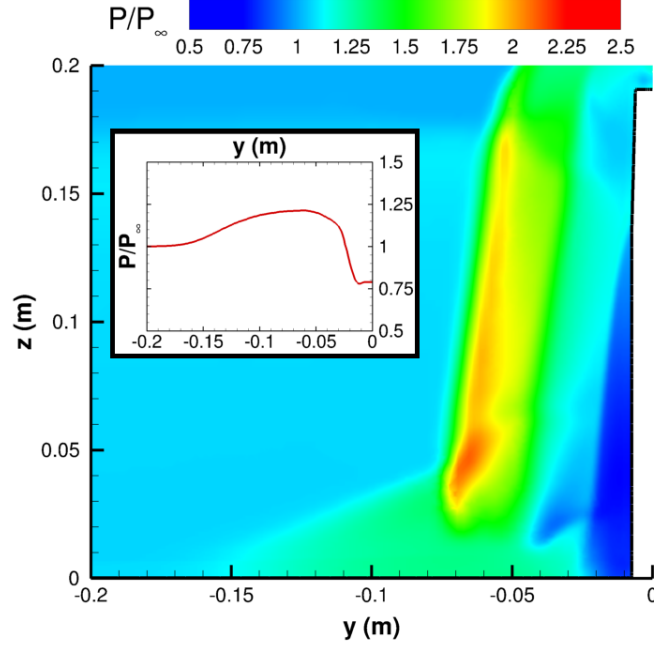
Figure 4.6. Contour of non-dimensional mean pressure, P/P_∞, in the frontal plane upstream of the elevon, $x = 0.3$ m. An included frame plots the non-dimensional surface pressure for $z = 0$ m.

4.1.1 Large-Scale Vortex Structures

There are large-scale vortex structures present in the hypersonic flowfield. One of these structures is a horseshoe vortex that develops along the wind tunnel wall at the root of the wing-elevon-cove model. Leading up to the leading-edge of the model, a turbulent boundary-layer develops along the wind tunnel wall. The boundary-layer thickness at the leading-edge of the wing-root is $\delta = 9.2$ mm. The boundary-layer separates 1.9 mm ahead of the leading-edge at the model center, $y = 0$ m. The height of the separation vortex at this location is 1.4 mm. This separation produces a horseshoe vortex that extends along the surrounding surface. A secondary horseshoe vortex is also observed forming close to the model surface. This flow behavior and associated length-scales are typical for a hypersonic blunt-fin interaction [173], [174]. The structures of the two horseshoe vortices are depicted

96

in Figure 4.7 with use of volume streamlines contour-colored by non-dimensional velocity, u/u_∞. In this figure, the upstream boundary-layer separation can be seen near the leading-edge wing-root. The boundary-layer redirects at the leading-edge and flows around the model. The larger primary horseshoe vortex is seen propagating downstream of the leading-edge. The flow that extends along the wing-root eventually curls and produces the secondary horseshoe vortex along the side of the model.
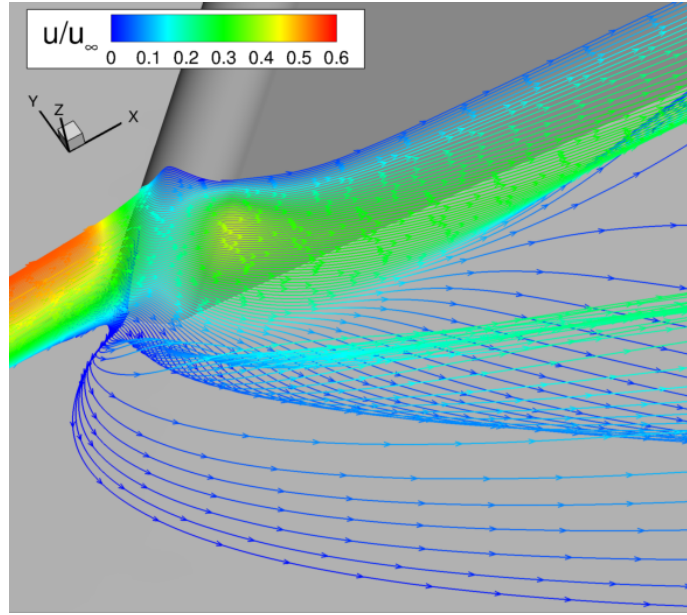
Figure 4.7. Three-dimensional interaction of the boundary-layer and the model surface at the leading-edge wing-root. Mean volume streamlines contour-colored by non-dimensional velocity, u/u_∞.

Volume streamlines, contour-colored by non-dimensional velocity, u/u_∞, are employed again in Figure 4.8. This figure depicts the large-scale vortex structures located near the leeward elevon trailing-edge in the back plane perspective (opposite of frontal). Near the wing-root, the horseshoe vortex visualized in Figure 4.7 is depicted rolling-up and entraining flow from the windward surface through the side gaps. At the wing-tip, the flow curls around the top portion of the wing, bends down into the wake region of the flowfield, and is eventually entrained into the vortex formed in the top side gap. This vortex is produced from the entrainment and subsequent mixing of the windward boundary-layer into the leeward boundary-layer. The velocity contour-coloring depicts the gradual increase in streamwise

velocity as the wake flow expands into the freestream. Overall, this figure visualizes the large-scale vortices in the flowfield, which exist away from the elevon centerline. As a result, the flow at the centerline is shown to be relatively unaffected by the three-dimensionality of the surrounding flowfield.
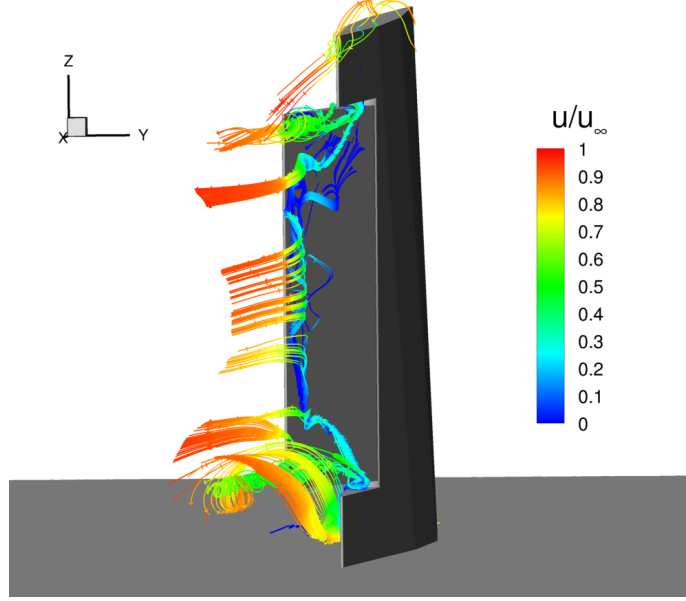
Figure 4.8. Three-dimensional large-scale vortex structures at the trailing-edge of the swept wing-elevon-cove model (back perspective). Mean volume streamlines contour-colored by non-dimensional velocity, u/u_∞.

To further visualize the large-scale vortex structures in the flow, contours of vorticity magnitude, $|\omega|$, in z-y (frontal) planes located at various streamwise locations, are provided in Figure 4.9. The four planes were extracted at $x = 0.33$ m, 0.36 m, 0.40 m, and 0.42 m. Individual focus regions, corresponding to the wing-tip, the top side gap, and the bottom side gap and wing-root, are highlighted and enlarged in each figure. These contours depict the evolution of the main vortex structures present in the flow, i.e., the wing-tip vortices, the top and bottom elevon side gap vortices, and the horseshoe vortex. In addition, the three-dimensional shock structure is depicted through regions of large vorticity magnitude. The counter-rotating wing-tip vortices grow along the wing-tip of the swept wing-elevon-cove model and entrain flow from the developing boundary-layers on the surrounding surfaces. This is similar to general wing-tip vortices [175], [176]. Moving in the streamwise direction

along the elevon, from $x = 0.32$ m to $x = 0.42$ m, the wing-tip vortex in the top-left focus frame develops asymmetry as the topside leeward boundary-layer is entrained into the leeward elevon separation region. This causes the wing-tip vortices near both the windward and leeward surfaces to produce associated streaks of locally high aerothermal heating. The entrainment of flow through the side gaps is seen in each of the figures, where the elevon deflection gradually causes larger amounts of flow entrainment through streamwise stations. This type of flow entrainment is similar to what is found in mutli-element airfoil configurations [177]–[179]. The large-scale top and bottom elevon gap vortex structures are clearly depicted in these contours. Like the wing-tip vortex, these vortices produce associated streaks of locally high aerothermal heating on the leeward elevon surface. The horseshoe vortex that wraps around the model is depicted on both ends of the wing-root in the bottom-left focus regions. Eventually, the regions of high and low pressure mix and become larger vortex structures, depicted in the bottom-left and right focus regions. The extracted plane in the last figure is located immediately after the swept wing-elevon-cove model and depicts the vortex structures in the wake. These structures expand into the freestream and propagate to the end of the computational domain. Once again, these figures collectively visualize the large-scale vortex structures in the flow, the inherent flow three-dimensionality of this configuration, and the relatively unaffected centerline flowfield.

4.2 Aerothermodynamic Loading

This section provides visualizations and discussion of the resultant aerothermodynamic surface loading on the swept wing-elevon-cove model and the surrounding wind tunnel surface. The focus of this section is specifically on the aerothermal heating, or heat flux. The heat flux for all computational surfaces is displayed with three-dimensional perspectives, two-dimensional planar extracts, and several line plots. The aerothermal heating on the windward surface, resulting from the shock-wave/boundary-layer interaction, was a primary focus. The vortex-induced aerothermal heating on the leeward elevon surface was also another focus for this research. The three major heat flux streaks on the leeward elevon surface correspond to the wing-tip streak, the top elevon streak, and the bottom elevon streak. These
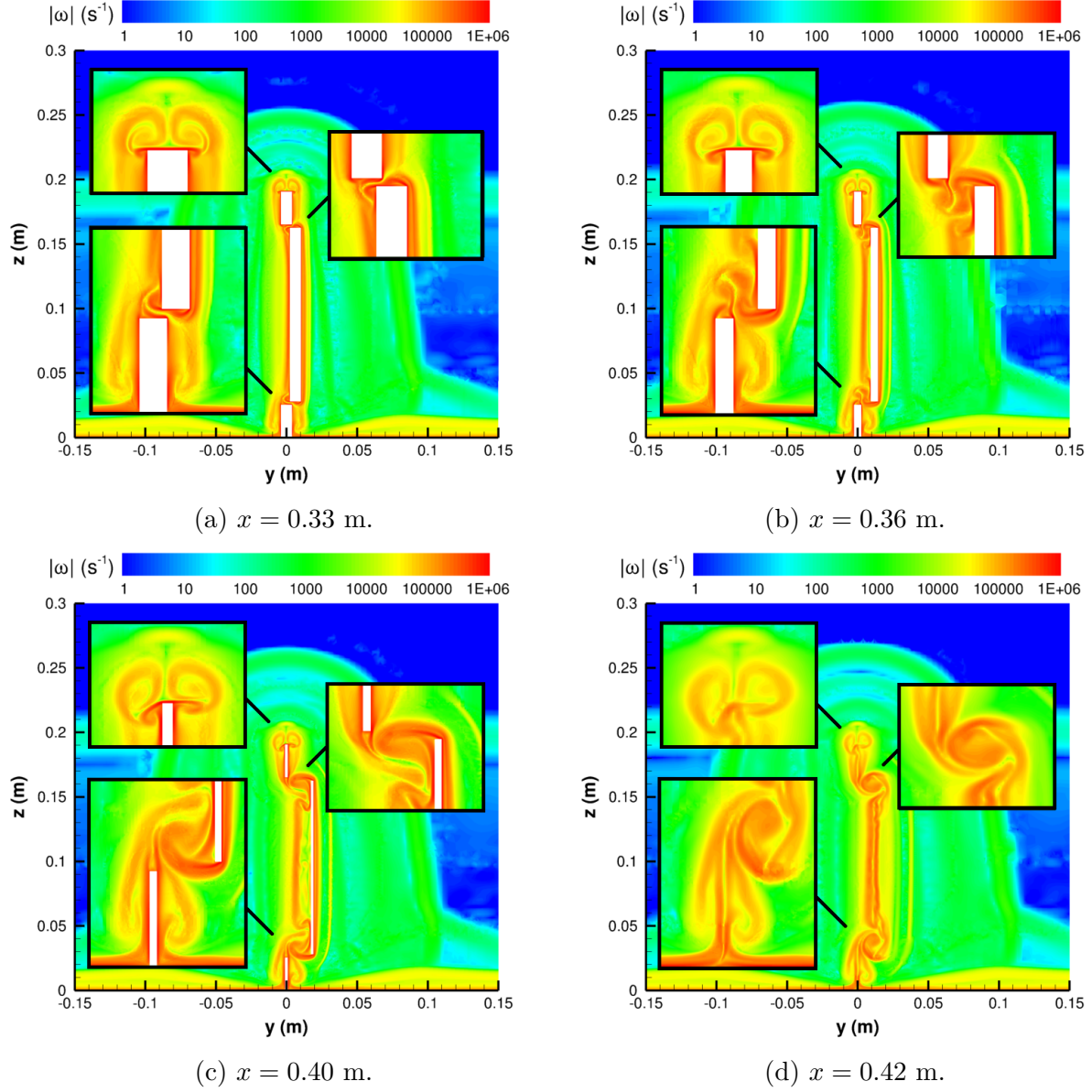
Figure 4.9. Contours of mean vorticity magnitude, $|\omega|$, in the frontal plane at $x = 0.33$ m, 0.36 m, 0.40 m, and 0.42 m, with several enlarged focus regions.

streaks are visualized and discussed throughout this section and are a primary focus of research investigation and analysis. An experimental blockage test photograph, provided with permission by Carson Lay, of Purdue University, is also included to display experimental proof of the vortex-induced aerothermal heating.

A three-dimensional perspective of the aerothermal heating on the swept wing-elevon-cove model is provided in Figure 4.10. The blunt-fin interaction at the leading-edge of the wing produces the highest magnitudes of heat flux. As the boundary-layer develops along the wing surface, in the streamwise direction, the heat flux decreases as expected. On the windward elevon surface, which is outward facing in this figure, large aerothermal heating is produced by the shock-wave/boundary-layer interaction. On the surrounding wind tunnel surface, the aerothermal heating produced by the three-dimensional shock structure and the wing-root horseshoe vortex is depicted. The wake region leaves an aerothermal heating distribution on the windward side of the wind tunnel surface that is also induced by the three-dimensional shock-wave/boundary-layer interaction.
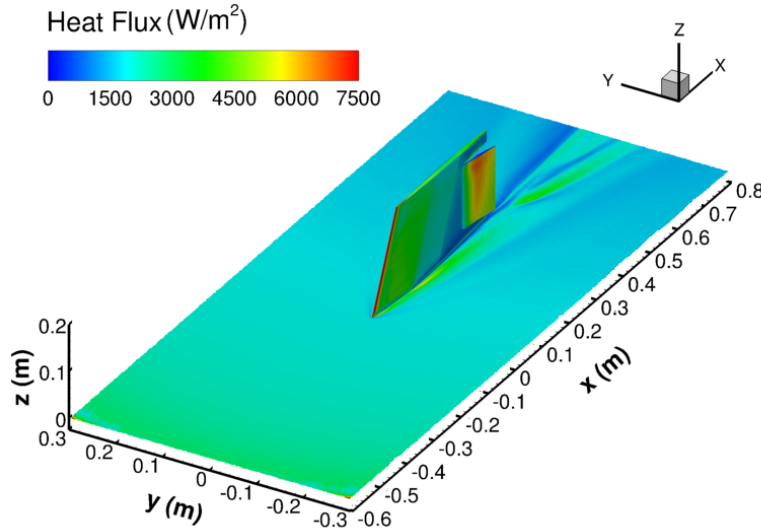
Figure 4.10. Three-dimensional perspective of the mean aerothermal loading on the swept wing-elevon-cove model and the surrounding wind tunnel surface.

The heat flux at the wind tunnel wall is depicted with skin friction trajectories in Figure 4.11. This figure provides a top-down perspective view, in the x-y plane, at the wind tunnel surface, $z = 0$ m. In this figure, these trajectories are contour-colored by heat flux. The three-dimensional shock structure visualized in the previous section produces the parabolic-like shear trajectories. There are high heat flux magnitudes produced at the leading-edge and near the first expansion region, where the horseshoe vortex moves up along the model

101

surface. These patterns are associated with the three-dimensional shock structure and are consistent with research on hypersonic blunt-fin interactions [180]–[182].
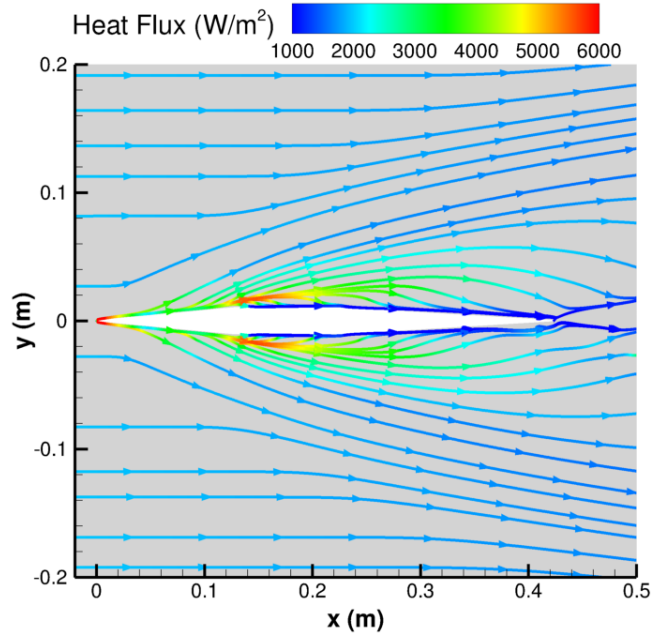
Figure 4.11. Top-down perspective of the wind tunnel surface, $z = 0$ m, with mean skin friction trajectories contour-colored by heat flux.

The x-z (side) plane perspectives of aerothermal heating on the windward and leeward swept wing-elevon-cove model surfaces are displayed in Figure 4.12. As the turbulent boundary-layer develops along the model surface, there is a reduction of surface heating. At the first cross-section expansion region, $x = 0.12$ m, a streak associated with the horse-shoe vortex develops along the root of the wing. At the cove juncture, the boundary-layer on the wing separates due to the cove gap region. The boundary-layer reattaches onto the windward elevon surface and thins, increasing the aerothermal heating. The shock-wave/boundary-layer interaction, produced by the 12 deg elevon deflection, induces local heat flux maxima downstream on the elevon surface. On the leeward surface, the opposite occurs. The boundary-layer develops through a large expansion region, and the aerothermal heating is consequently negligible. On the upper and lower portions of the side gaps, there are regions of larger heat flux caused by the local flow entrainment. The heat flux streaks on the top of both sides of the wing are produced by the counter-rotating wing-tip vortices

visualized in Figure 4.9. On the leeward side of the elevon, two large vortex-induced streaks are also seen. These streaks are associated with the large-scale vortex structures produced by the side gap flow entrainment, visualized in Figure 4.8.
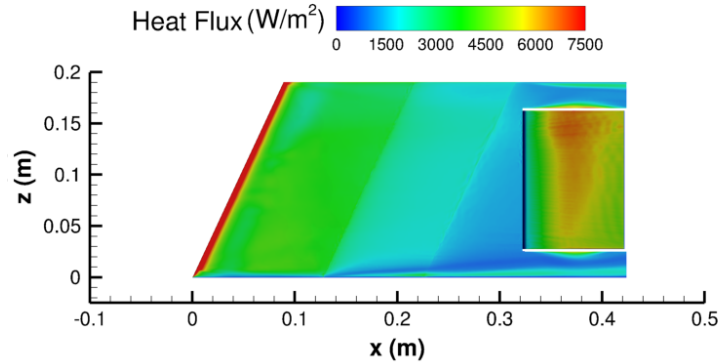
(a) Windward side.
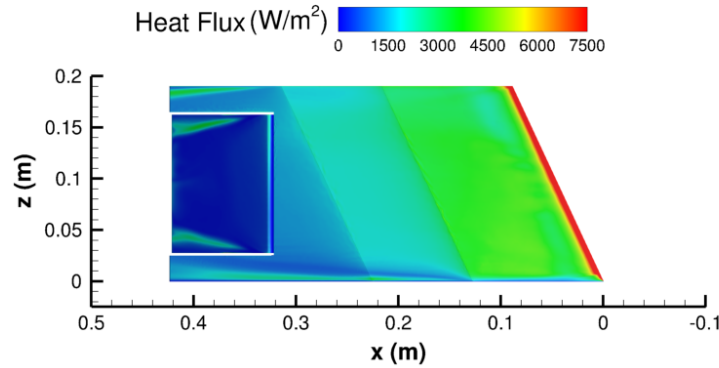
(b) Leeward side.

Figure 4.12. Windward and leeward side plane perspectives of the mean aerothermal loading on the three-dimensional model surface.

Maximum aerothermal heating on the windward elevon surface is produced by the shock-wave/boundary-layer interaction. The spanwise heat flux distributions here are asymmetric because of variations in the redeveloping boundary-layer profiles. These variations are caused by the linear decline of the cross-sectional chord lengths, root-to-tip, resulting from the model sweep. Seven boundary-layer profiles of non-dimensional velocity, u/u_∞, were obtained at $x = 0.37$ m and are plotted along the perpendicular surface displacement, Δy, in Figure 4.13. The first group, z_{1-3}, refers to three upper stations on the windward elevon surface located

at $z = 0.14$ m, 0.12 m, and 0.10 m, respectively. The second group, z_{4-6}, refers to three lower stations on the windward elevon surface located at $z = 0.08$ m, 0.06 m, and 0.04 m, respectively. The last boundary-layer included provides the reference upstream profile, located at $x = 0.28$ m, for the center-most station, $z = 0.1$ m. A schematic of these locations on the swept wing-elevon-cove surface model is included in the figure. The large distortion in the elevon boundary-layer profiles is caused by the reattachment shock, and the last small distortion is caused by the leading-edge oblique shock. This figure depicts the boundary-layer thinning between the upper and lower stations along the windward elevon surface. This thinning, in turn, produces the asymmetric aerothermal surface heating distribution shown in Figure 4.12a. This figure also depicts the differences between boundary-layer thickness upstream, $\delta_{\text{cove}} = 15.6$ mm, and in this region, $\delta_{1-6} \geq 40$ mm.
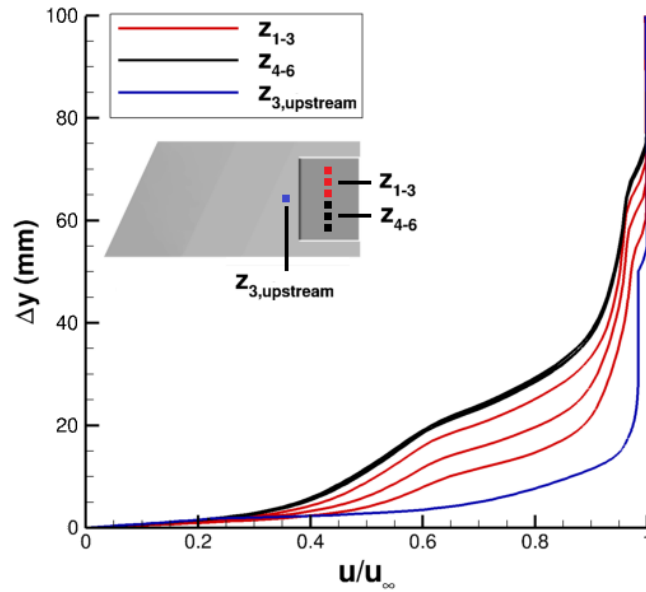
Figure 4.13. Mean boundary-layer profiles in the region of maximum aerothermal loading on the elevon.

The heat flux distributions along various chord lines of the windward elevon surface are plotted in Figure 4.14a. As seen in the various visualizations provided in this chapter, the leading-edge of the model produces the highest heat flux magnitudes. Since no transition model was employed, the boundary-layer immediately transitions to turbulence. At each of

the segmental turns along the wing, the heat flux peaks momentarily and then continue to drop as the boundary-layer develops. The cove is located near $x = 0.32$ m, which is where the large drop in heat flux occurs. The flow reattaches on the windward elevon surface quickly and causes the heat flux to exponentially rise until reaching peak values near $x = 0.37$ m. The aerothermal loading distributions for chord lines along the elevon span show generally the same trend and magnitudes. Differences in the distributions are primarily caused by the sweep, as described previously.

The heat flux distributions in the local cove region for both the windward and leeward surfaces are provided in Figure 4.14b. In this figure, the windward surface distributions are represented by solid lines and the leeward surface distributions are represented with dashed lines. As can be seen in this figure, the aerothermal load is negligible near the center of the cove. The heat flux on the leeward elevon surface is relatively low, however, there are distinct peaks in heat flux shown in this figure associated with the boundary-layer reattachment on the leeward elevon surface. Outside of this frame, the heat flux distributions on the leeward surface remain lower than the windward surface by an order of magnitude.

(a) Windward model surface.　　　　　(b) Windward/leeward local cove surfaces.
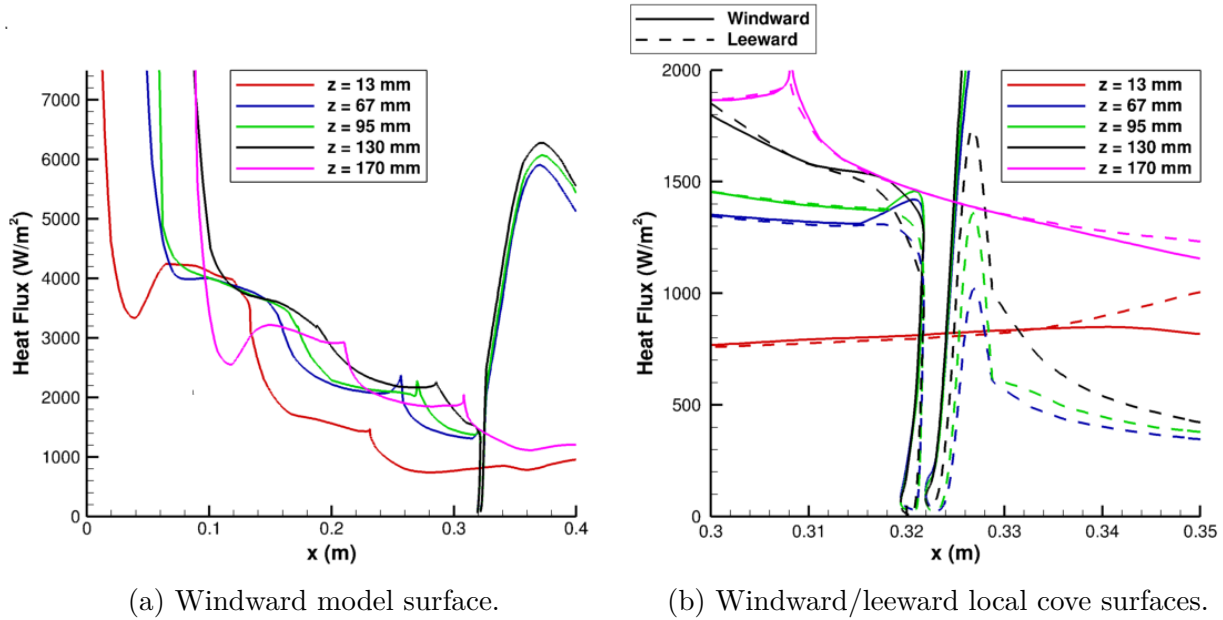
Figure 4.14. Plots of mean aerothermal heating for chord lines along the model surface (left) and local cove surfaces (right).

Figure 4.15 displays spanwise surface heat flux distributions on the wing-cove surface, inside of the cove region, and along the elevon surface. In this figure, the solid lines represent the windward surface, and the dashed lines represent the leeward surface. On the left, Figure 4.15a displays the heat flux distribution along the wing-cove surface at five different stations, located at $y = 0$ mm, ± 3 mm, and ± 6 mm. The exact center of the cove is $y = 0$ mm. Near the center of the cove, the heat flux is negligible, which was previously shown in Figure 4.14. This can be seen for the $y = 0$ mm and ± 3 mm heat flux distributions. The heat flux distributions in this region are mostly constant along the span. At the outer edges of the cove, $y = \pm 6$ mm, the heat flux magnitudes are significantly higher. The influence of the flow three-dimensionality near the side gaps can be seen in these distributions. These heat flux magnitudes are relatively low compared to the external loading.

The heat flux distributions along the span of the elevon, at various streamwise locations, are provided in Figure 4.15b. Once again, the solid lines represent the windward surface, and the dashed lines represent the leeward surface. The heat flux distributions are provided for six different streamwise stations, located at $x = 0.33$ m, 0.35 m, 0.37 m, 0.39 m, 0.41 m, and 0.42 m. As shown in this figure, the heat flux distributions on the windward elevon surface far exceed those on the leeward side. The first station, $x = 0.33$ m, which is located upstream of reattachment, displays the lowest heat flux magnitudes on the windward surface. At the next station, $x = 0.35$ m, the heat flux magnitude significantly increases due to boundary-layer reattachment. The heat flux maxima are found at the following station, $x = 0.37$ m, which are produced by the shock-wave/boundary-layer interaction. Afterwards, at stations $x = 0.39$ m, 0.41 m, and 0.42 m, the heat flux magnitudes along the elevon span decrease to reattachment levels. The heat flux along the span of the elevon is relatively constant, however, the distribution is asymmetric and increases from the wing-root to the wing-tip. This trend is not observed on the leeward elevon surface, shown with the dashed lines. The two large local peaks in heat flux at the bottom and top of the elevon are attributed to the large-scale vortex-induced heat flux streaks. The streaks comprise regions of heat flux magnitudes that are two-five times larger than the surrounding surface, which can be seen in this figure. The next section provides further discussion of these streaks.

(a) Wing-cove surface. (b) Elevon surface.
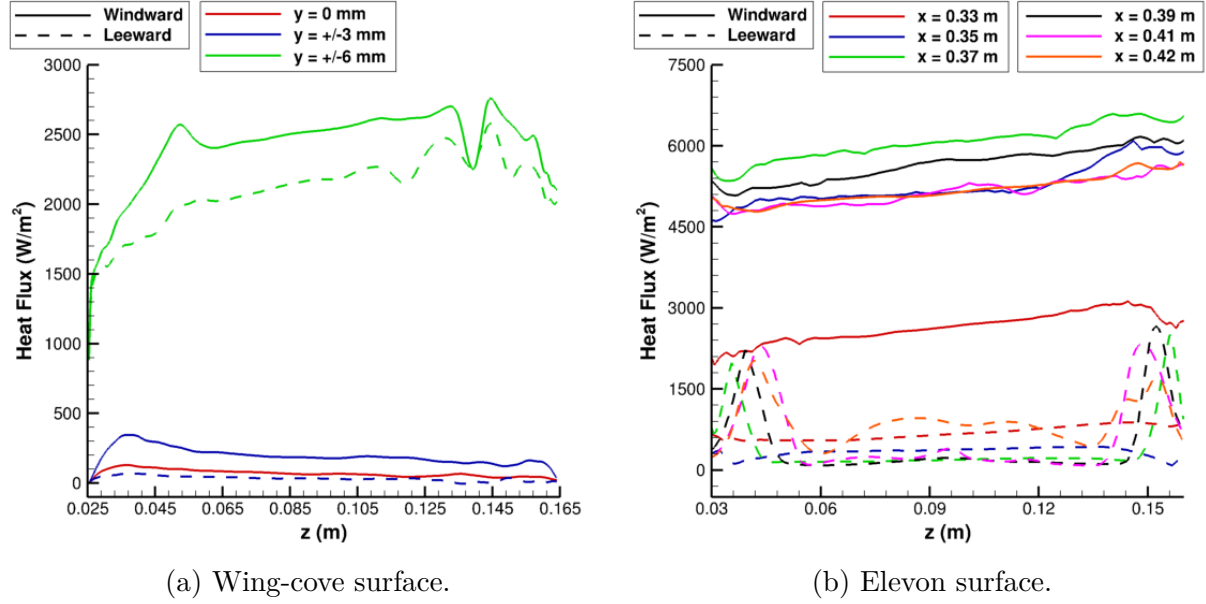
Figure 4.15. Plots of mean aerothermal heating distributions along the span of the wing-cove surface (left) and the elevon surface (right).

4.2.1 Vortex-Induced Aerothermal Heating

This section provides an overview of the heat flux-induced streak formations on the swept wing-elevon-cove model. The three major streaks correspond to the wing-tip streak, the top elevon streak, and the bottom elevon streak. These three streaks are caused by the large-scale vortex structures in the flowfield. The horseshoe vortex is also discussed here, however, its effect on the surface loading near the wing-root is not thoroughly analyzed. The primary streak formations are found on the leeward elevon surface. While the wing-tip associated heat flux streaks exist on both the windward and leeward elevon surface, the leeward surface streak is more prominent due to mechanisms visualized in Figure 4.9. Therefore, the majority of the following content focuses on the leeward elevon surface.

The vortex-induced wing-tip heat flux streak was also observed in the Purdue experimental BAM6QT blockage tests. While these tests employed a wing model, without an elevon, cove, or side gaps, the model structure is otherwise identical to the full swept wing-elevon-cove configuration. During these experiments, temperature sensitive paint (TSP) was employed to display the aerothermal heating on the model surface. An experimental

photograph, included with permission by Carson Lay, of Purdue University, is displayed in Figure 4.16a. The figure shows a portion of the top-side of the experimental blockage model. The development of the wing-tip vortex-induced heat flux streak is seen with the local region of high surface temperature. The wind tunnel surface is outside of the viewable experimental test-section and not coated with TSP, so the horseshoe vortex is not depicted here. Additionally, without the three-dimensional trailing-edge geometry of the full configuration, the large-scale vortex-induced heat flux streaks on the leeward elevon are also not visible here.

The computational heat flux streak is depicted with surface skin friction trajectories, contour-colored by heat flux, in Figure 4.16b. The computational skin friction trajectories show the trend lines of the shear loading on the swept wing-elevon-cove model top leeward surface. The wing-tip vortex reattaches to the surface, creating the diverging line of shear trajectories. The contour-coloring of these lines depict the high levels of aerothermal loading produced by the wing-tip vortex. Both the windward and leeward sides have these streaks. Comparing side-by-side to the experimental image on the left, the two heat flux streaks show significant qualitative similarities. As a result, the experimental image provides experimental validation of the heat flux streak seen in the computation.

(a) Experimental TSP photograph.   (b) Computational mean skin friction trajectories.
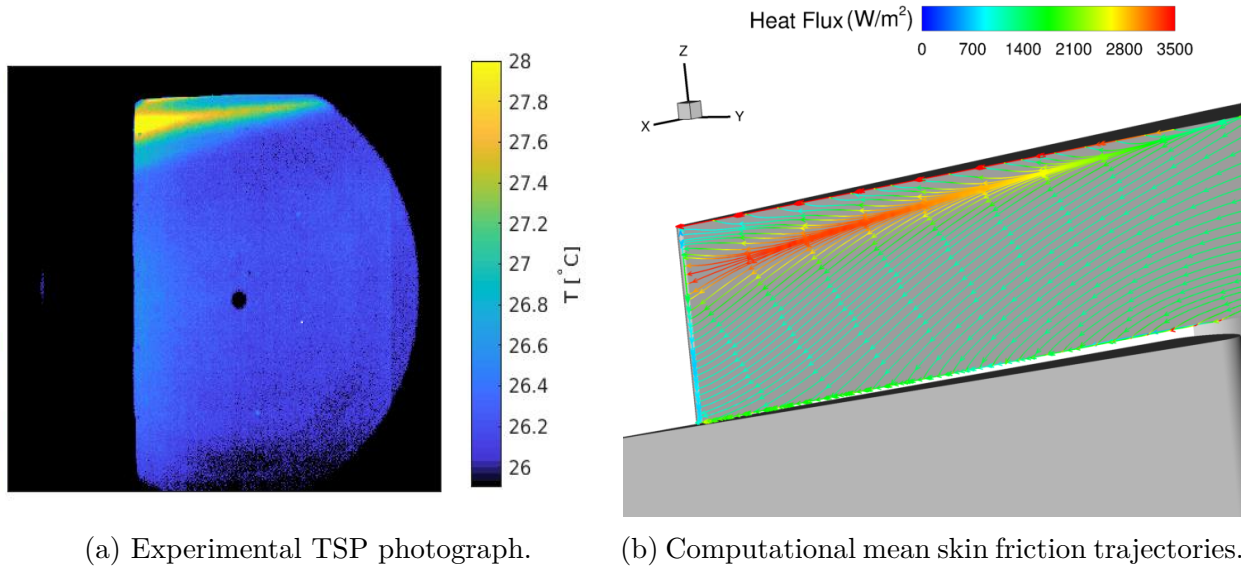
Figure 4.16. A TSP photograph from blockage model experiments (left) is compared to computational data in the same region (right). The experimental image was included with permission by Carson Lay, of Purdue University.

The elevon is a lifting surface, therefore, the pressure is higher on the windward elevon side compared to the leeward elevon side. As a result, pressure gradients exist in the flow which induce flow entrainment through the side gaps. This entrainment produces the large-scale vortex structures near the top and bottom of the leeward elevon surface. These vortices attach to the elevon surface and produce streaks of locally high aerothermal loading, similar to the wing-tip vortex-induced heat flux streak depicted in Figure 4.16. The leeward elevon surface aerothermal loading is provided in the x-y (side) plane in Figure 4.17a. The three major streaks investigated, the wing-tip streak, the top elevon streak, and the bottom elevon streak, are depicted and labeled in this figure. The resulting heat flux distributions along each of these streak is provided on the right, in Figure 4.17b. The differences in these three distributions are caused by the local flow three-dimensionality. These distributions plot the heat flux along the running-length distance, s, for the total streak length, L_{streak}. The wing-tip vortex-induced heat flux distribution gradually increases from the start to the end of the streak. The top elevon vortex-induced heat flux distribution gradually increases from the start to halfway along the streak, reaches a maximum value, and subsequently decreases as the vortex sheds from the trailing-edge. The bottom elevon vortex-induced heat flux streak shows similar behavior but at a lower magnitude and with a more constant distribution.

To further visualize the vortex-induced heat flux, the shear loading trends on the leeward elevon surface are depicted with skin friction trajectories, contour-colored by heat flux, in Figure 4.18. As with the skin friction trajectories displayed for the wing-tip in Figure 4.16b, the top and bottom elevon vortex-induced heat flux streaks are depicted on the elevon surface with divergent trend lines. The larger aerothermal loading is seen for the top-elevon vortex-induced heat flux streak. The detaching of the vortex from the surface, and consequential reduction of aerothermal loading, is seen at the trailing-edge of the elevon. This figure also depicts the general three-dimensional leeward surface loading. The main region of separation is also easily seen with the bifurcating skin friction trajectories in the middle of the elevon surface, which produce a separation region over 60% of the elevon surface. Along the main diverging bifurcation line, near the two ends of the elevon surface, two nodes are created as an artifact of the oncoming reattaching top and bottom vortices. This figure displays the intricate leeward surface loading produced by the flow three-dimensionality.

(a) Vortex-induced heat flux streaks.

(b) Heat flux along streak length, L_{streak}.
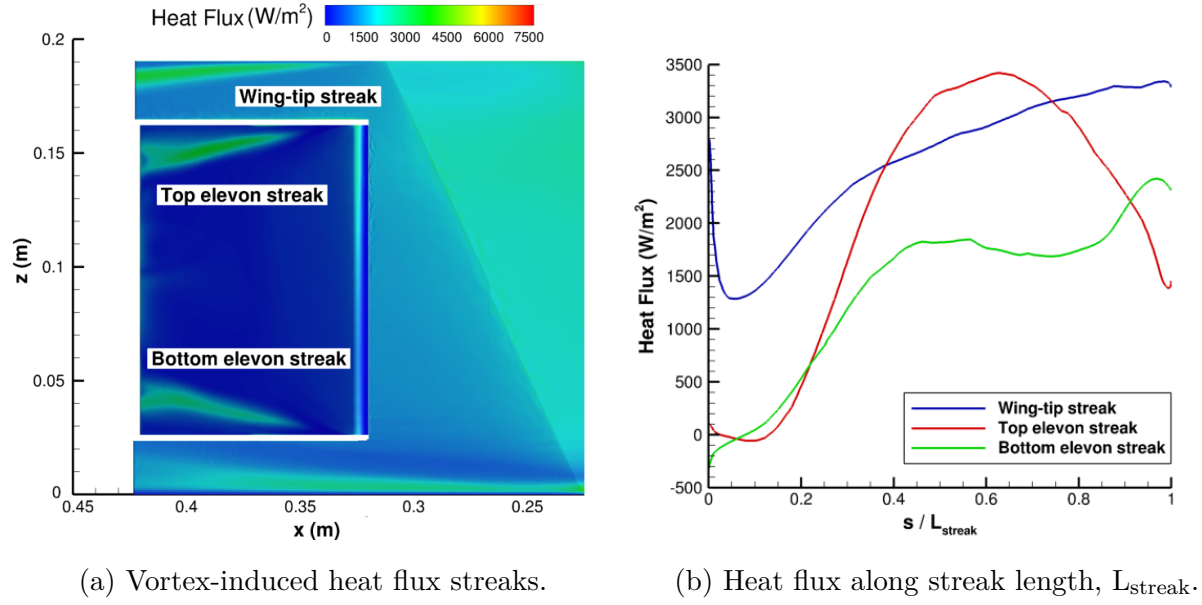
Figure 4.17. Leeward side plane perspective of mean vortex-induced heat flux streaks (left) and mean heat flux distributions along streaks (right).
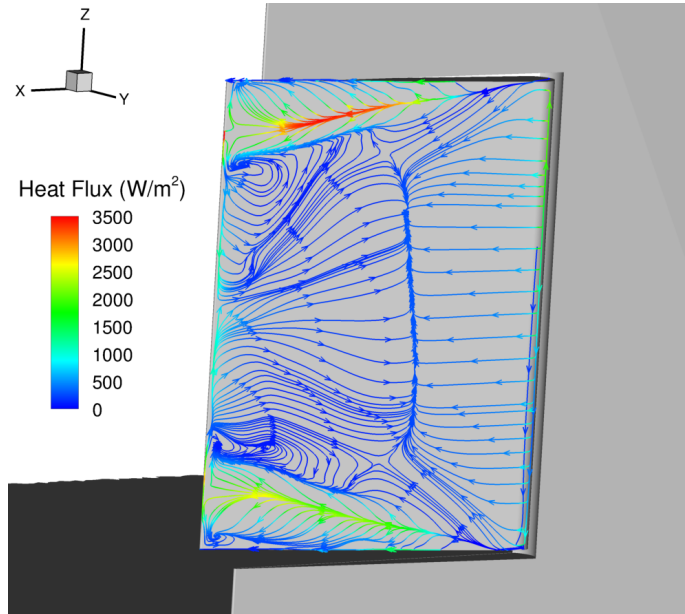
Figure 4.18. Three-dimensional perspective of mean skin friction trajectories, contour-colored by heat flux, on the leeward elevon surface.

4.3 Influence of Geometric and Flowfield Modifications

The primary purpose of the parametric sweep computations was to investigate the on-set of unsteadiness in the improved delayed detached-eddy simulation for the Purdue swept wing-elevon-cove model. However, these data can also be utilized to provide context for modifications to the flow conditions or the geometry. The auxiliary computations provided one modification each to the primary computation. The computations employed a simplified mesh that focused on the elevon centerline flow. This mesh is similar to the one employed in the UTSI TALON computation, shown in Figure 2.10. In addition, several computations used various model sizes which were 10-20% the size of the full model used in the primary computation. These sizes correspond to the small and medium blockage models and were employed because the allowable experimental model size was unknown at the time of the computations. In order to depict general behaviors and trends, three auxiliary computations, labeled $\mathcal{A}_1$, $\mathcal{A}_2$, and $\mathcal{A}_3$, are utilized in this section. These computations are a small set of the larger set of modifications done for the parametric sweep. The first computation, $\mathcal{A}_1$, modified the geometry of the cove by increasing the length by a factor of two. The second computation, $\mathcal{A}_2$, doubled the stagnation pressure used in the freestream, effectively doubling the freestream Reynolds number. The third computation, $\mathcal{A}_3$, introduced a -6 deg angle of attack to the flow. This section discusses the qualitative and quantitative effects of these geometric and flow condition modifications. The local cove flow structure and resultant aerothermal surface loading are depicted for each computation. As with the primary computation, all data from the auxiliary computations are time-averaged.

Figure 4.19 provides contours of non-dimensional streamwise velocity, u/u_∞, for the primary computation and each of the auxiliary computations. These planes are taken at the elevon cove centerline, $z = 95$ m, for the primary computation and at the domain centerline, $z = 0$ m, for the three auxiliary computations. In these figures, the origin of the axes, $(x, y) = (0, 0)$ m, is set to the edge of the main wing element, and the axes are non-dimensionalized by the cove length of the primary computation, $L_{\text{cove}} = 2.52$ mm. The first figure, Figure 4.19a, provides the flow visualization of the primary computation presented in this chapter. This flow structure was previously discussed and visualized in Figure 4.4. The

flow visualizations for the three auxiliary computations, $\mathcal{A}_1$, $\mathcal{A}_2$, and $\mathcal{A}_3$, are provided in Figures 4.19c-4.19d. Due to the slightly different models used in these computations, and the scaling of the following figure, the cove geometries are not all identical. However, this does not strongly affect the qualitative flow structure in this region. In general, the surrounding flowfield for each computation are relatively similar. There is an external boundary-layer, a separation vortex, a shock-wave/boundary-layer interaction, and facilitated/hindered flow entrainment. There is also a secondary vortex seen in all computations, which further supports its characteristic appearance for wing-elevon-cove flows.

The effect of a larger cove length is displayed in Figure 4.19b. The size of the separation vortex shown here encompasses the entire cove, depicting the effects of local geometric modifications on the flow structure. The flow entrainment through the cove is entirely hindered. Due to this lack of flow entrainment, the flow structure in the cove region is symmetric about the center. The reattachment position on the elevon surface is comparatively much farther upstream as well. The effects of different flow conditions are presented in the remaining two figures. The third figure, Figure 4.19c, provides the wing-elevon-cove flowfield with a Reynolds number twice as large as the primary computation. Flow entrainment is once again hindered, and the length of separation consists of the entire cove. The last figure, Figure 4.19d, provides a computation with an angle of attack of -6 degrees. Angle of attack, however, was not obtainable in the BAM6QT wind tunnel experiments. This angle of attack produces a strong leading-edge bow-shock and as a result, large pressure gradients between the windward and elevon surfaces are created. As outlined previously, this facilitated the flow entrainment through the cove, which is depicted in this figure. The local flow conditions cause a downward deflection in the shear-layer, similarly to what was shown in shown in Figure 3.3 for the NASA wing-elevon-cove computation. The structure and size of the separation vortex are also completely different in this auxiliary computation, and the separation vortex penetrates deep into the cove. These last two figures show the general qualitative differences induced by modifications of the freestream conditions.

The centerline aerothermal loading distributions for the primary and auxiliary, $\mathcal{A}_1$, $\mathcal{A}_2$, and $\mathcal{A}_3$, computations are provided in Figure 4.20. This figure provides the quantitative effects of each respective configurational modification on the resultant surface loading. The

(a) Primary computation.

(b) $\mathcal{A}_1$ ($2 \times L_{cove}$).

(c) $\mathcal{A}_2$ ($2 \times P_o$).

(d) $\mathcal{A}_3$ ($\alpha = -6$ deg).
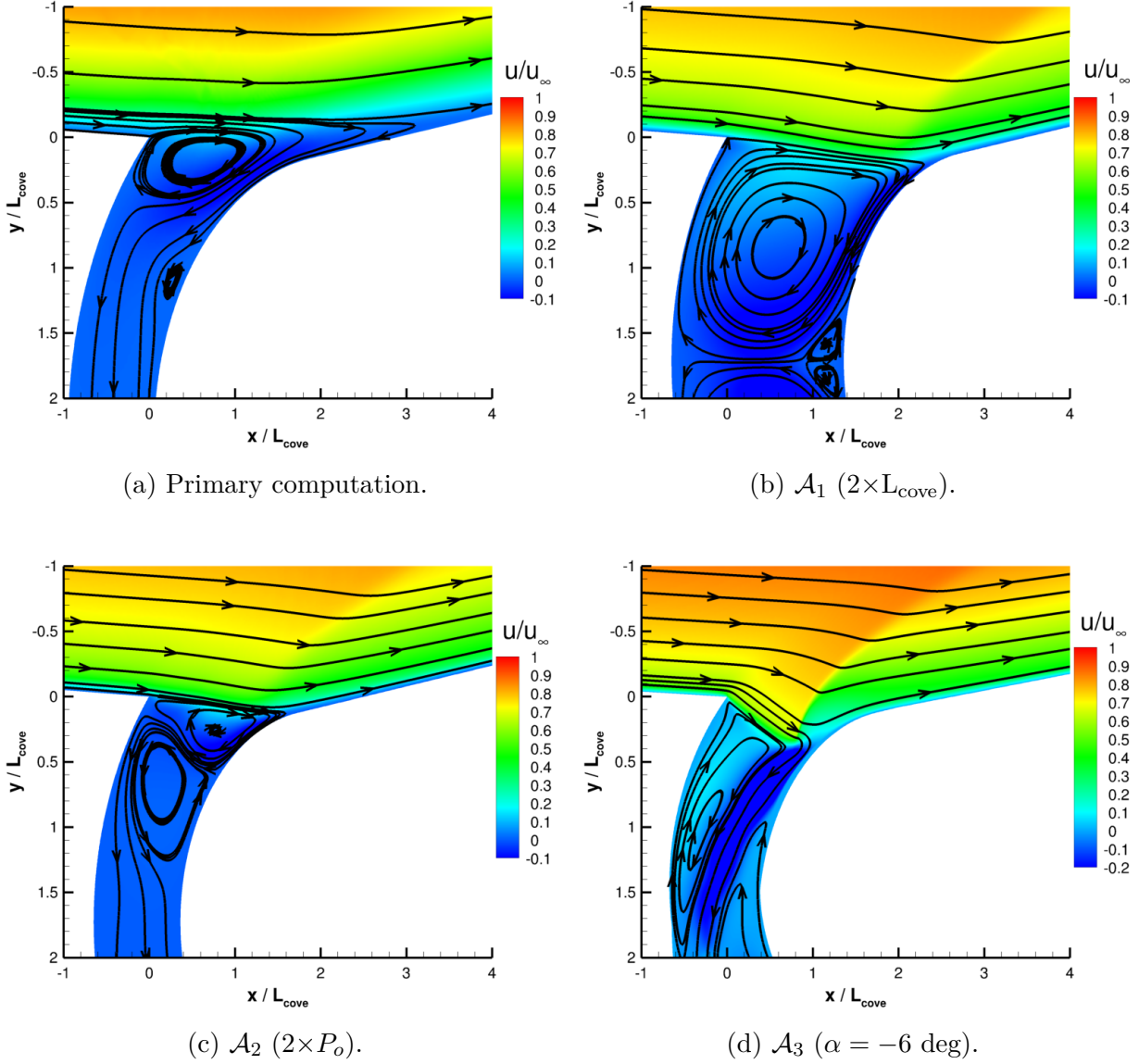
Figure 4.19. Centerline contours of non-dimensional mean velocity, u/u_∞, with sectional streamlines, for primary and auxiliary computations.

coordinate system axes, x and y, are non-dimensionalized by the length of the cove, L_{cove}. The left plot, Figure 4.20a, displays the heat flux distributions for the entire swept wing-elevon-cove windward surface. The boundary-layers immediately transition to turbulence at the start of the leading-edge and develop through the two sequential expansion-fan regions along the model cross-section. There are significant differences in the aerothermal loading

magnitudes and distributions for these computations. The heat flux distributions for $\mathcal{A}_1$ and the primary computation are nearly identical. The major differences come from the geometric differences and flow three-dimensionality of the primary computation. Increasing the stagnation pressure by a factor of two, in $\mathcal{A}_2$, proportionality increased the aerothermal loading on the elevon surface. The general trend of the distribution is the same as for $\mathcal{A}_1$ and $\mathcal{A}_2$. The angle of attack produces the highest levels of heat flux, which is due to the increased aerothermodynamic loading induced by the leading-edge bow-shock. This heat flux is the same magnitude as the double stagnation pressure computation, $\mathcal{A}_2$. The right plot, Figure 4.20b, provides the local heat flux distributions near the cove for both the windward and the leeward surfaces. Upstream of the cove, all heat flux distributions follow the same distributions as the windward surface except for $\mathcal{A}_3$, which had negligible heat flux on the leeward surface. As the leeward boundary-layer reattaches, there are local peaks in all computations heat flux distributions, which is followed by negligible heat flux in the leeward surface expansion region. These heat flux distributions generally depict the same trends, behaviors, and orders of magnitude as primary computation.
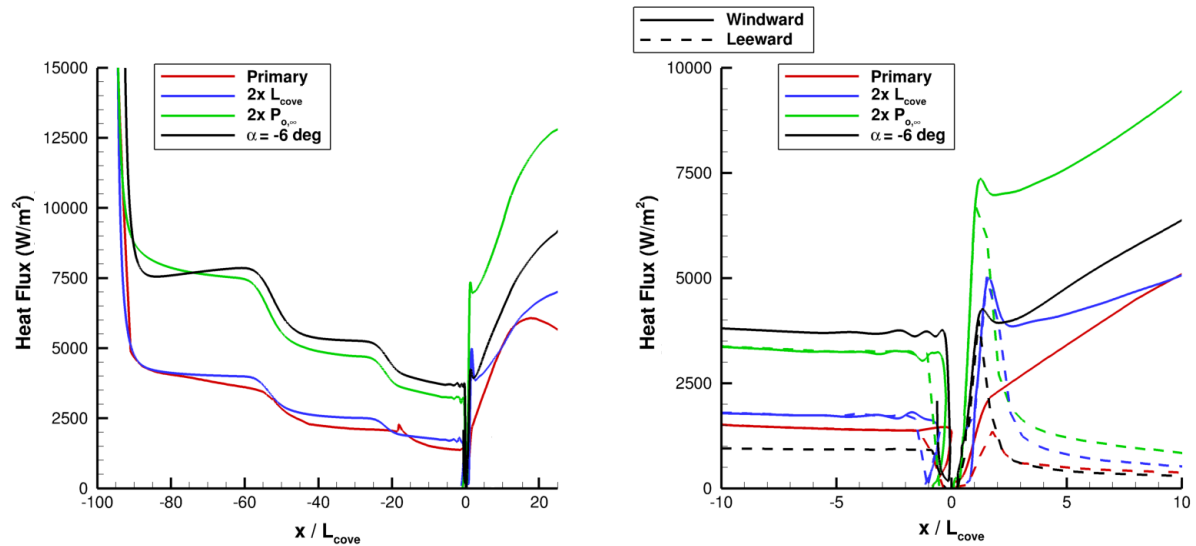
(a) Windward wing-elevon-cove surface.   (b) Windward/leeward local cove surfaces.

Figure 4.20. Plots of centerline mean aerothermal heating for primary and auxiliary computations along the model surface (left) and the cove (right).

4.4 Chapter Discussion

This chapter provided the results for the second wing-elevon-cove project. This project was done in collaboration with the Purdue ASL experimental team. The purpose of this work was to conduct further research and analysis on hypersonic wing-elevon-cove configurations. The experimental and computational models correspond to the Purdue swept wing-elevon-cove model. The primary computation involved the full swept wing-elevon-cove model configuration. The full model includes the BAM6QT wind tunnel ceiling, side gap regions, and an embedded elevon. The computation utilized the experimental BAM6QT wind tunnel flow conditions. While the initial research goal involved comparison of the computational and experimental data, no quantitative comparison was made. This was due to the different timeline of the experimental and computational projects.

The order of the data presentation for this chapter followed flow visualization, resultant aerothermodynamic loading, and then discussion of computational modifications. The flow visualizations collectively visualize the large-scale vortex structures in the flow, the inherent flow three-dimensionality of this configuration, and the relatively unaffected center-line flowfield. There is a three-dimensional lambda shock-wave/boundary-layer interaction around the swept wing-elevon-cove model and the surrounding wind tunnel surface, which is seen in several hypersonic flowfields, e.g., sharp fins [167]–[169] and cylindrical protuberances [170]–[172]. The counter-rotating wing-tip vortices grow along the top of the swept wing-elevon-cove model and entrain flow from the developing boundary-layers on the surrounding surfaces. The large-scale vortex structures on the leeward elevon are produced by flow entrainment through the side gaps. The aerothermal heating on the swept wing-elevon-cove model was displayed with three-dimensional perspectives, two-dimensional planar extracts, and several line plots. The windward surface heat flux, resulting from the shock-wave/boundary-layer interaction, was a focus region. The vortex-induced aerothermal heating on the leeward elevon was another focus for this research. The three major heat flux streaks on the leeward elevon surface correspond to the wing-tip streak, the top elevon streak, and the bottom elevon streak. The vortex-induced wing-tip heat flux streak

was also observed in the Purdue experimental BAM6QT blockage model tests, where the development of the heat flux streak was depicted with local regions of high surface TSP.

The improved delayed detached-eddy simulation was unable to resolve significant unsteadiness in the shock-wave/boundary-layer interaction. While the computation did not produce unsteadiness, the preliminary experimental data did show low-frequency content in the pressure spectra inside of the cove; however, the overall unsteadiness in the shock-wave/boundary-layer interaction was low. To facilitate an unsteady computation, a parametric sweep was done by modifying various geometric parameters and flow conditions. The primary purpose of the parametric sweep computations was to investigate the onset of unsteadiness in the computation. However, these data were also utilized to provide context to the effects of the modifications. The configurational modifications each produced qualitative and quantitative differences in the local cove flow structure and resultant aerothermal heating. An extensive analysis of these auxiliary computations, however, was outside the scope of this work. This parametric sweep also depicted a Reynolds number dependence for the resolved unsteadiness in the cove region. Flows with stronger shock-wave/boundary-layer interactions, or significantly higher cove Reynolds numbers, Re_{cove}, produced unsteady shock-wave/boundary-layer interactions consistently with the literature [88], [163], [164].

Collectively, the work done for this project provides research and analysis on hypersonic wing-elevon-cove characteristics with increased three-dimensionality. The computational data were primarily used to provide practical flow visualization and aerothermodynamic loading analysis of the Purdue swept wing-elevon-cove model in the BAM6QT wind tunnel flow conditions. The results presented in this chapter have been published in conference proceedings [162], and the computational data have aided in the experimental research efforts; the flow visualizations were useful to Purdue experimentalists by identifying focus regions to investigate, such as the regions of vortex-induced heating. This work also provides baseline information for future computations and experiments done for the same model. Another useful outcome of this work was observing that the elevon centerline flowfield was not strongly affected by the flow three-dimensionality. The subsequent computational investigation that succeeded this one, done on the Purdue wing-elevon-cove model in the UTSI TALon conditions, used this information to produce a focused computational domain.

5. UTSI TALON WING-ELEVON-COVE

This third project involves a computational investigation associated with the scaled Purdue wing-elevon-cove model. The experimental conditions correspond to the UTSI TALon Mach 4 Ludwieg tube. The scaled wing-elevon-cove model is twice the size of the model used in the Purdue BAM6QT computation. The TALon experimental team is conducting ongoing wind tunnel experiments for this wing-elevon-cove model. One goal of this computational study was to aid and collaborate with these experimental efforts. The other goal was to conduct statistical analyses for the unsteady shock-wave/boundary-layer interaction that was not possible for the Purdue BAM6QT computation, which predicted steady flow.

To moderate the computational cost of the simulation, the wing-elevon-cove model was idealized in the span, omitting the side gap regions and the surrounding wind tunnel surface. The centerline cross-section of the scaled Purdue wing-elevon-cove model was symmetrically extruded in the span to allow for flow three-dimensionality; however, the leading-edge sweep of the model was not included. This reduction of the computational domain allows for more precise meshing and data collection, compared to the unstructured T-Rex hybrid meshing used in the Purdue BAM6QT computation. In addition, it was shown that the centerline flowfield of the full Purdue swept wing-elevon-cove model was not strongly affected by the increased three-dimensionality of the full model. The scaled wing-elevon-cove model is provided in Figure 5.1, with the dimensions of the model included. The wing is 0.658 m long, the cove is 6 mm in length, the elevon is 0.188 m long, the airfoil thickness is 0.04 m, and the span of the domain is 0.05 m. For reference, the span of the full scaled model elevon is 0.27 m, and the computation modeled roughly 20% of this span.
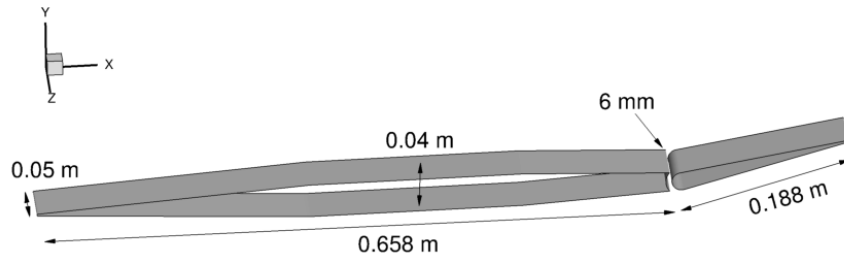
Figure 5.1. Three-dimensional perspective of the scaled wing-elevon-cove model, with included dimensions, used in the UTSI TALon computation.

This project focused on the unsteadiness of the shock-wave/boundary-layer interaction and the generation, propagation, and growth of coherent turbulent structures. After the NASA wing-elevon-cove project was completed, it became clear that the grid stretching downstream of the cove environment resulted in a damping of turbulence along the elevon. This confined the statistical analysis to only regions near the wing-elevon-cove juncture, such as in the shock-wave/boundary-layer interaction or slightly downstream. The issue was fixed in these computations by incorporating refined meshing along the entire surface of the wing and elevon, facilitating the resolution of turbulence. Additionally, the trailing-edge flow characteristics were simulated in this computation by allowing the boundary-layer to separate from the elevon trailing-edge. The boundary conditions on either side of the domain were periodic, and surface boundary conditions were no-slip isothermal surfaces, set to $T_w = 293.15$ K. Unsteady data were collected for the complete flowfield, in two-dimensional planes, for all surfaces, and in various individual locations in the domain.

The results obtained from the computational investigation are presented in this chapter. Visualizations of the time-averaged and instantaneous flowfields are first provided, which depict the generic wing-elevon-cove flow structure, at the cove region, and unsteady shock motion, similar to what was found in the NASA wing-elevon-cove computation. The resultant time-averaged and instantaneous aerothermodynamic loadings, for the complete span of the elevon, are also provided and discussed. The aerothermal spanwise distributions are largely different than those for the Purdue BAM6QT wing-elevon-cove computation. However, surface loading patterns associated with Görtler vortices are depicted, which are similar to those observed in the NASA wing-elevon-cove computation. The statistical analyses on unsteady flow fluctuations, e.g., space-time cross-correlations, power spectral densities, and coherences, are then provided to characterize the unsteady hypersonic flowfield. An overview and discussion of these results is included at the end of this section.

5.1 Flow Visualization

A contour of time-averaged velocity magnitude, $|\overline{V}|$, is provided in Figure 5.2, which depicts the overall hypersonic flowfield for this computation. Velocity magnitude is calculated

as $|\overline{V}| = \sqrt{\bar{u_1}^2 + \bar{u_2}^2 + \bar{u_3}^2}$. The contour is a two-dimensional slice of the three-dimensional domain at the centerline, $z = 0$ m. This figure contains two zoomed-in focus regions. These are the blunt nose interaction at the wing's leading-edge, on the left, and the flowfield at the elevon trailing-edge, on the right. Due to the similar cross-sectional geometries of the models, this flow structure is qualitatively identical to that of the Purdue BAM6QT computation, which was shown in Figure 4.3. The incoming freestream flowfield interacts with the leading-edge of the wing, producing a detached bow-shock. This view is seen in the left-most frame in Figure 5.2. This shock-wave extends through the domain but does not interact with the downstream flow. In this configuration, with no wind tunnel surface and zero angle of attack, the mean flow is symmetric over the length of the wing. The boundary-layer develops along the surface of the wing, through two expansion-fan regions, and separates at the cove juncture. After the boundary-layer separates from the surface, there is a region of separation, a separated shear-layer, separation and reattachment shock-waves, and flow entrainment into the cove.

The elevon deflection produces a shock-wave/boundary-layer interaction at the cove. The oblique shock-wave, originating at the intersection of the separation and reattachment shock-waves, can be seen in the downstream flowfield in Figure 5.2. There is significant flow entrainment into the cove and into the separation vortex. The flow exits the cove, on the leeward side, and mixes with the leeward reattaching boundary-layer. At windward reattachment, there is a divergence point where the flow either continues downstream, along the elevon, or is entrained into the cove environment. The boundary-layer reattaches and redevelops along the windward elevon surface. The boundary-layer separates at the trailing-edge of the elevon where there is a large expansion-fan. The boundary-layer sheds from the trailing-edge and exits the computational domain in the wake region. On the leeward side, the boundary-layer separates prior to the trailing-edge, similar the Purdue BAM6QT computation, which creates a large-scale separation region. There is a shock-wave that originates at this location caused by the downward deflection of the shear-layer. The trailing-edge of the model is enlarged in the right frame in Figure 5.2, which displays the windward boundary-layer shedding and the leeward elevon boundary-layer separation.
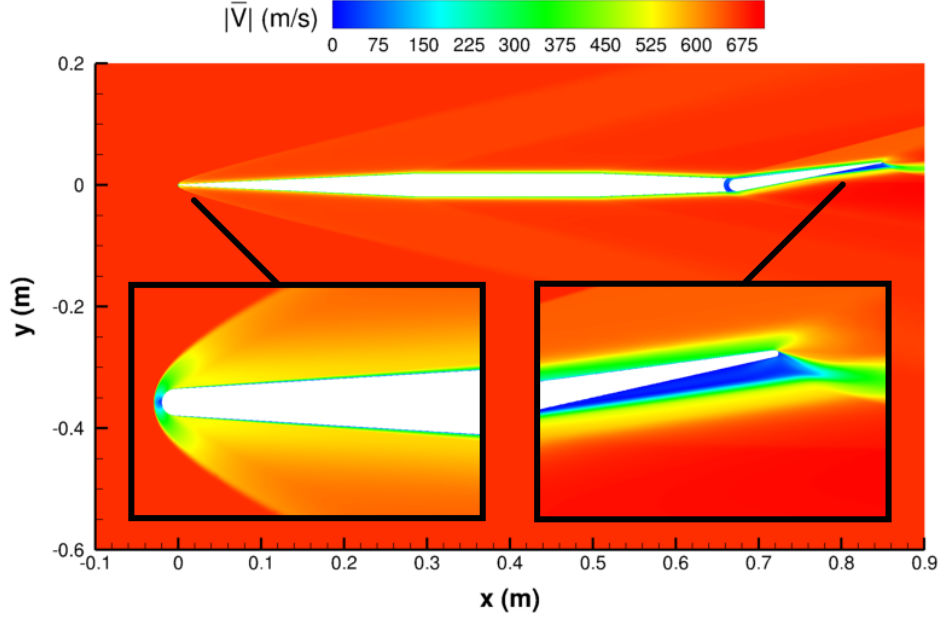
Figure 5.2. Centerline, $z = 0$ m, contour of time-averaged velocity magnitude, $|\overline{V}|$, with focus on the leading-edge (left) and trailing-edge (right).

A contour of time-averaged velocity magnitude, $|\overline{V}|$, with included sectional streamlines, is provided in Figure 5.3. This contour is a two-dimensional slice of the three-dimensional domain, taken at the centerline $z = 0$ m, and is focused on the local cove region. As with the previous figure, the flow structure here is identical to that of the Purdue BAM6QT computation shown in Figure 4.4. The streamlines in this figure depict the mean structure of the shear-layer, the separation vortex, the flow entrainment, and the interior cove flow. The shear-layer has relatively little curvature, until reattachment, and the Görtler number for this streamline curvature is $\mathcal{G} = 3.4$. The separation vortex is long and narrow, with an approximate size of 30 mm by 3 mm. The region of flow entrainment, located upstream of reattachment, experiences significant unsteadiness and is associated with the generation of turbulent structures. This region creates larger higher streamline curvature, and the Görtler number associated with this curvature is $\mathcal{G} = 7.2$.

Additional features depicted in this figure include the external redeveloping boundary-layer, the reattachment shock-wave, and a secondary vortex in the cove environment. This secondary vortex has been observed in all three wing-elevon-cove computations. The time-

averaged reattachment location for the computation is $x_r = 0.6914$ m, which is relatively far downstream from the cove. The reattachment position, measured from the boundary-layer separation location on the wing surface, is $\overline{L_r} = 30$ mm. This extension of separation far onto the elevon surface was also observed in the Purdue BAM6QT computation. However, for the NASA wing-elevon-cove computation, the angle of attack moved the reattachment location upstream on the elevon surface. The time-averaging done here eliminates the unsteady characteristics of the flow. For example, the time-dependent boundary-layer reattachment and the shear-layer streamline curvature fluctuate significantly. This flow behavior is depicted in the following section with instantaneous flow snapshots.
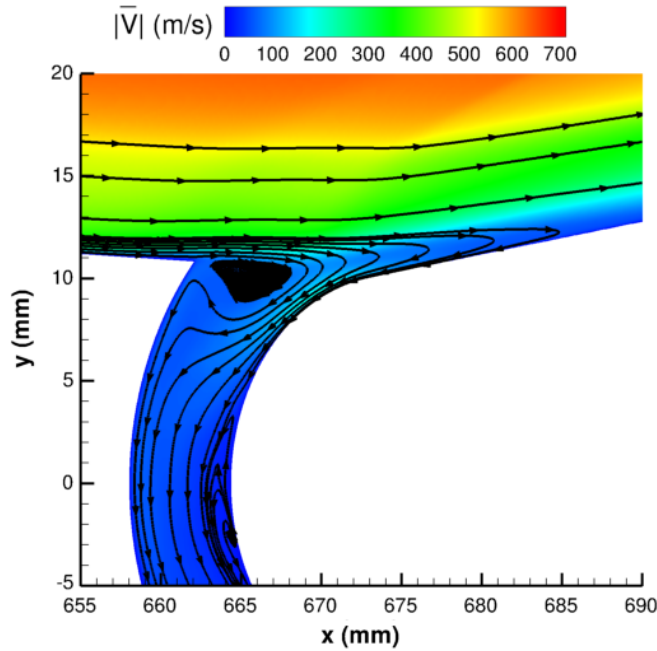
Figure 5.3. Centerline, $z = 0$ m, contour of time-averaged velocity magnitude, $|\overline{V}|$, including sectional streamlines, at the local cove region.

Regions of high density gradients, e.g., boundary-layers, shock-waves, expansion-fans, and vortices, are important to the flow structure. Contours of density gradients, therefore, can be useful in depiction of these important flow phenomena. A visualization of the time-averaged density gradient magnitude, $|\overline{\nabla \rho}|$, for the downstream flowfield, is provided in Figure 5.4. The contour is a two-dimensional slice of the three-dimensional domain, taken at the centerline, $z = 0$ m. The upstream bow-shock, originating at the wing's leading-edge,

is displayed with regions of high density gradients, above and below the model surface. The upstream and redeveloping boundary-layers, near the windward and leeward surfaces of the wing and the elevon, are also visible. The shock system near the cove environment is depicted, including components such as the separation vortex, the separated shear-layer, and the separation and reattachment shock-waves. At the trailing-edge, the windward and leeward elevon flowfields contain different flow phenomena, as shown previously in Figure 5.2. The windward trailing-edge boundary-layer separates from the trailing-edge and is deflected downward through a high density gradients in the expansion-fan. In this region, there is a separated windward shear-layer, which fluctuates rapidly due to the Kelvin-Helmholtz instability, and trailing-edge vortex shedding. The leeward elevon boundary-layer separates upstream of the trailing-edge, which creates a large region of recirculation and a separation shock. Downstream of the trailing-edge, there is another shock-wave produced as the separated boundary-layer turns and mixes with the wake. This figure provides a reference time-averaged flowfield for the following instantaneous snapshots.
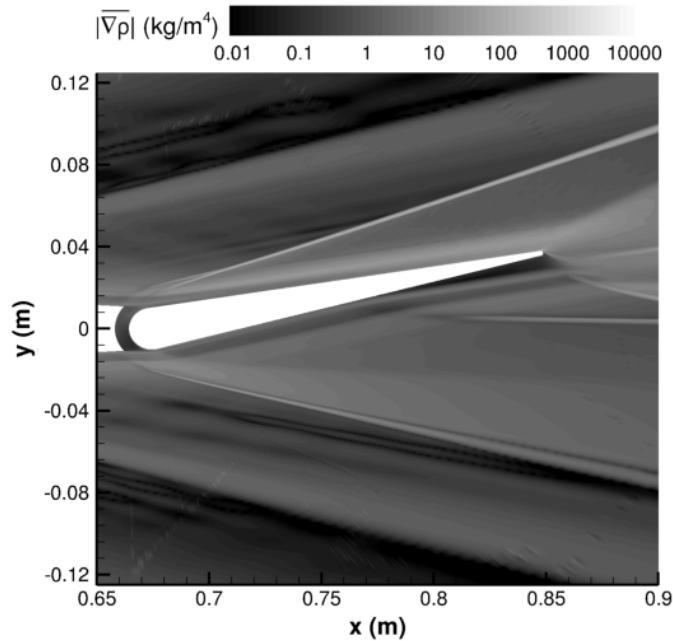
Figure 5.4. Centerline, $z = 0$ m, contour of time-averaged density gradient magnitude, $|\overline{\nabla \rho}|$, for the downstream flowfield.

5.1.1   Instantaneous Flow

This flowfield exhibits significant large-scale unsteadiness, which is associated with the unsteady shock-wave/boundary-layer interaction at the cove juncture. Large coherent turbulent structures, i.e., Görtler vortices, are generated in this region. These structures propagate downstream along the elevon, in the redeveloping boundary-layer, and eventually shed off the trailing-edge through a vortex shedding mechanism. Coherent turbulent structures strongly affect the flow characteristics, such as the unsteady shock-motion, the overall flow structure, and the resultant aerothermodynamic loading. This was previously depicted with the unsteady statistical analyses done for the NASA wing-elevon-cove computation in Chapter 3. Overall, this section attempts to visualize the flow unsteadiness in the shock-wave/boundary-layer interaction, as well as the generation, propagation, and growth of turbulent structures. This is done by providing several instantaneous flowfield snapshots, as well as three-dimensional flow perspectives.

The flow unsteadiness and propagation of large coherent structures can be seen with contours of instantaneous density gradient magnitude, $|\nabla\rho|$, which are provided in Figure 5.5. This figure includes two instantaneous flow snapshots, which start at the computational time $t = 10.7$ ms and are separated by the time difference $\Delta t = 0.1$ ms. These contours are two-dimensional slices of the three-dimensional domain, taken at the centerline, $z = 0$ m, and are focused on the local cove region. The unsteady flow entrainment is depicted here, as well as the forming and collapsing of turbulent eddies in the cove. These eddies are shown to damp out towards the leeward elevon cove exit. The generation of turbulent vortex structures and the unsteady shock system can also be seen between Figure 5.5a and Figure 5.5b. There is visible coherent movement of the shear-layer, in a flapping motion, and growth and contraction of the separation vortex in these figures, as well. As the shear-layer flaps, and the separation vortex grows and contracts, there is induced oscillation of the reattachment and separation shock-waves. The shock system moves in a coherent fashion, and as a result, the cove flow entrainment is either facilitated, or hindered, and the coherent turbulent structures are either formed, or are shed.

(a) $t = 10.7$ ms.   (b) $t = 10.8$ ms.
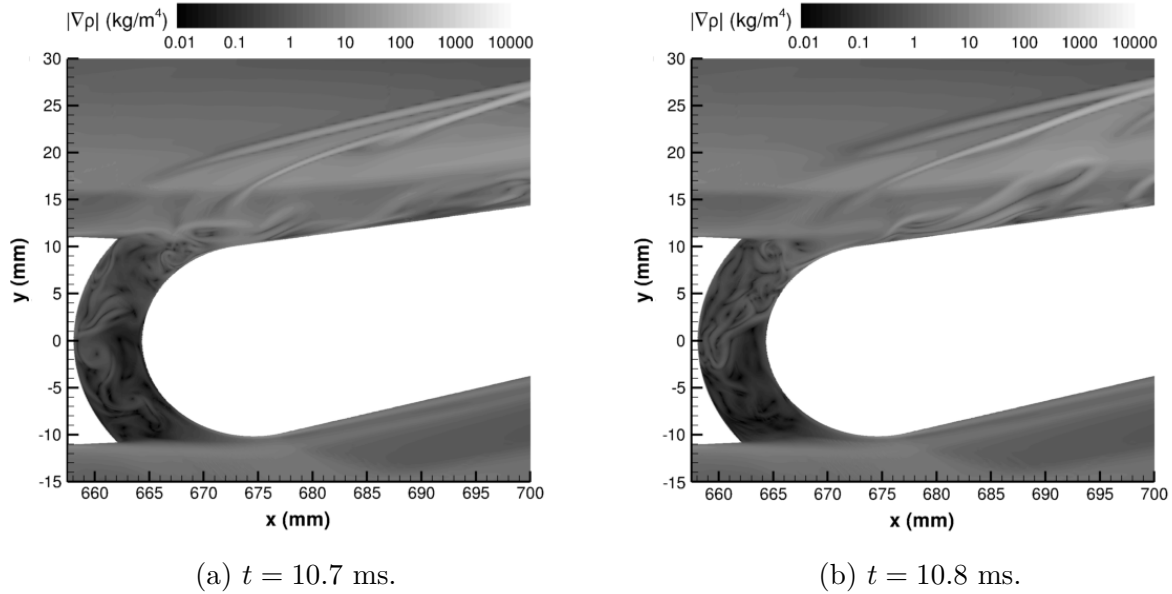
Figure 5.5. Centerline, $z = 0$ m, contours of instantaneous density gradient magnitude, $|\nabla\rho|$, in the shock-wave/boundary-layer interaction.

The generation, propagation, and growth of coherent turbulent structures in the re-developing boundary-layer are depicted in the density gradient magnitude, $|\nabla\rho|$, contours provided in Figure 5.6. This figure provides four different instantaneous snapshots. As with the previous figures, these contours are two-dimensional slices of the three-dimensional do-main, taken at the centerline $z = 0$ m. The computational time difference between each of the four snapchats is $\Delta t = 0.1$ ms. Many features of the instantaneous flow, which are averaged away in the time-averaging done for Figure 5.4, can be seen in these figures. For instance, the existence of the coherent structures in the redeveloping boundary-layer and the acoustic waves, which reflect off these structures, are depicted in these instantaneous snapshots. Four color-coded coherent vortex structures are highlighted in Figure 5.6. These vortices are color-coded, starting from upstream to downstream, as green, orange, blue, and red. Beginning at a computational time of $t = 10.5$ ms, in Figure 5.6a, the four structures are about half way along the elevon surface. After $\Delta t = 0.1$ ms, in Figure 5.6b, the four structures have propagated farther along the elevon. The red and blue vortices have moved farther distances than the orange and green vortices as a result of the increase in convec-tion velocities associated with vortex development [152]–[154]. Another $\Delta t = 0.1$ ms later,

124

in Figure 5.6c, the red vortex has shed from the trailing-edge and the three other vortices have continued to propagate, grow, and mix as they continue downstream. After another $\Delta t = 0.1$ ms, in Figure 5.6d, the blue vortex also sheds, leaving only the green and orange vortex, which are mostly amorphous by this time. Collectively, these figures depict the propagation of coherent vortex structures, which have significant effect on the overall flow structure and the resultant aerothermodynamic loading.

(a) $t = 10.5$ ms.

(b) $t = 10.6$ ms.

(c) $t = 10.7$ ms.

(d) $t = 10.8$ ms.
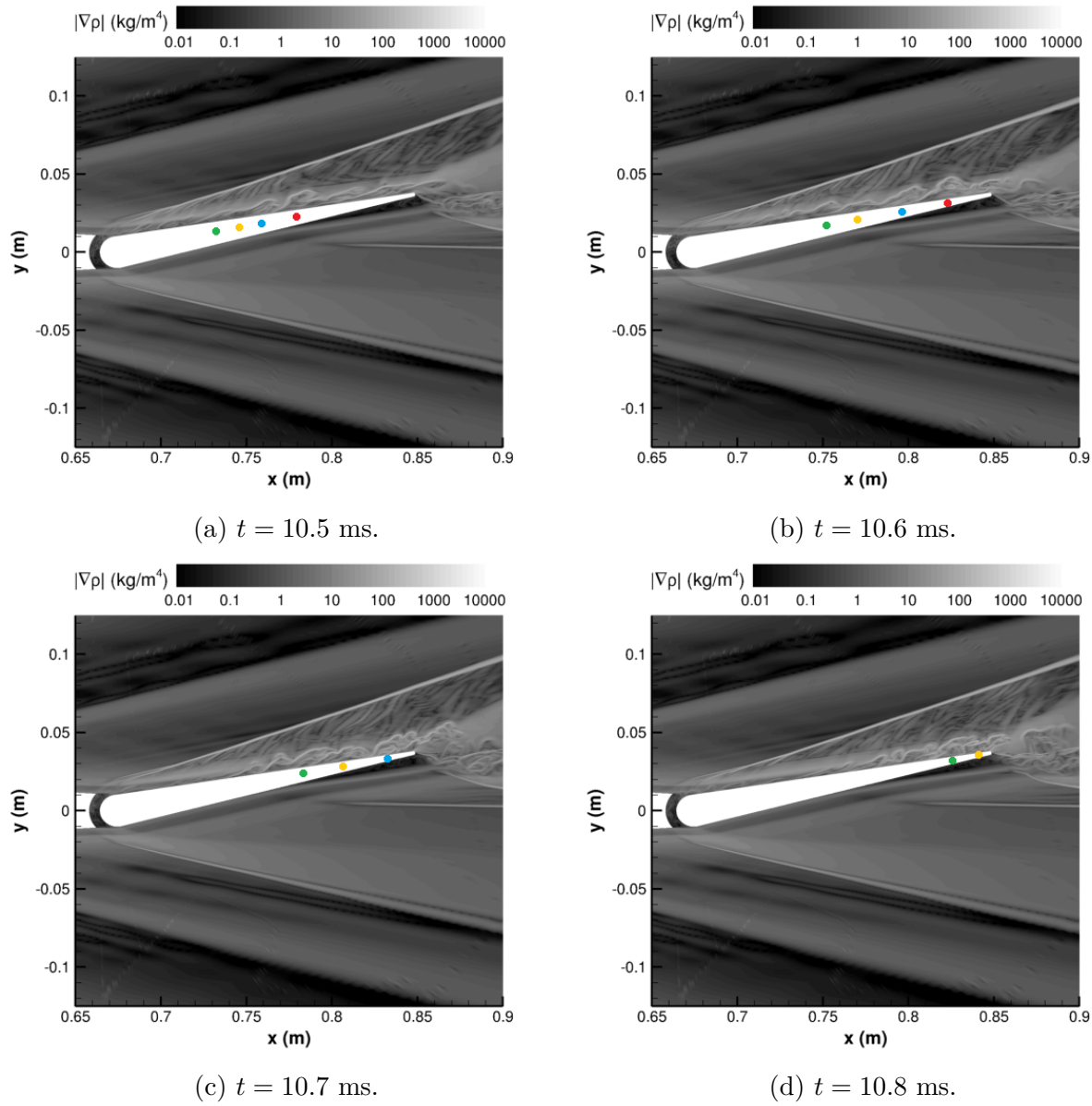
Figure 5.6. Centerline, $z = 0$ m, contours of instantaneous density gradient magnitude, $|\nabla \rho|$, for the downstream flowfield.

125

Q-criterion is a useful tool for detecting and visualizing vortex structures in a three-dimensional flowfield. Q-criterion is defined as the second invariant of the velocity gradient tensor, where values larger than zero depict a relative dominance of vorticity over the strain rate [141]. Specific Q-criterion levels can be employed as iso-surfaces in order to visualize turbulent structures in three-dimensions. Therefore, to visualize the instantaneous three-dimensional turbulent flowfield, iso-surfaces of Q-Criterion were utilized, as shown in Figure 5.7. These iso-surfaces are contour-colored by velocity magnitude, $|V|$, providing the local velocities of the structures in the redeveloping boundary-layer. Additionally, the shock-wave, which originates at the cove, is highlighted with an iso-surface of $u \cdot |\nabla \rho|$. This quantity provides large values for high density gradients in the flowfield which are aligned with the streamwise flow direction, i.e., the oblique shock-wave. The large-scale vortex structures are also displayed in this visualization, which are shown to propagate, grow, and combine along the elevon surface. The decay of turbulent structures in the cove region, and the lack thereof on the leeward elevon surface, are also depicted here. On the windward elevon surface, coherent structures originate near the cove region. These structures elongate, combine, and become more chaotic downstream as the turbulent boundary-layer develops. At the trailing-edge of the wing-elevon-cove, the vortex shedding of these structures and the separated trailing-edge shear-layer can be seen.
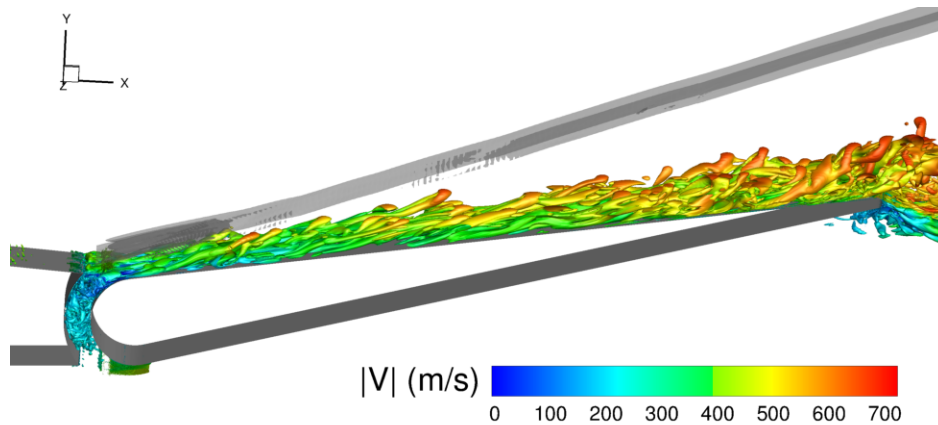
Figure 5.7. Instantaneous Q-Criterion iso-surfaces, contour-colored by velocity magnitude, $|V|$, and a gray $u \cdot |\nabla \rho|$ iso-surface.

126

As has been shown to be characteristic of hypersonic wing-elevon-cove flows, Görtler vortices are present for this configuration. The Görtler numbers associated with this flow, corresponding to the streamline curvature at reattachment and flow entrainment, are $G_{\mathrm{ret}} = 3.4$ and $G_{\mathrm{ent}} = 7.2$, respectively. These vortices originate in the cove region due to the centrifugal instability. The non-homogeneous spanwise heat flux distribution shown in Figure 5.10 is related to this phenomenon. The elongation of the coherent structures results in lower aerothermal heating, and the turbulent mixing of structures near the trailing-edge produces higher aerothermal loading. The evolution of the spanwise Görtler vortices is visualized in Figure 5.8. In this figure, four y-z planes were extracted from the three-dimensional domain. The streamwise locations in which these extracts are obtained are $x = 0.75$ m, 0.775 m, 0.8 m, and 0.825 m. These instantaneous planar extracts were taken at the computational time $t = 10.6$ ms. The extract locations roughly align with the green, orange, blue, and red coherent structures labeled in Figure 5.6. Each frame in Figure 5.10 encompasses the entire computational span, 50 mm, is contour-colored with instantaneous vorticity magnitude, $|\omega|$, and utilizes an exponential scale. These snapshots visualize the spanwise variation of the three-dimensional flowfield and the existence of the Görtler vortices.

The first plane, at $x = 0.75$ m and shown in Figure 5.8a, displays what appears to be approximately eight Görtler vortices. The length-scale between adjacent vortices is $\lambda \approx 5$ mm, and the height of the vortices is approximately 3.8 mm. The spanwise plane also slices through the oblique shock-wave, which is visible in this frame. The height of the boundary-layer here is approximately 8 mm. The second plane, at $x = 0.775$ m and shown in Figure 5.8b, depicts the development of the Görtler vortices. There are five to six distinguishable vortices in this frame with distance between adjacent structures averaging $\lambda \approx 6$ mm and structure heights averaging approximately 5 mm. The oblique shock-wave is also visible in this frame. The height of the boundary-layer is approximately 7 mm off the surface, depicting the slight thinning of the boundary-layer. By the third plane, taken at $x = 0.8$ m and shown in Figure 5.8c, the Görtler vortices have now started to mix and comprise the entire boundary-layer. In this frame, there are five to six distinct vortex structures, and the distance between adjacent structures is $\lambda \approx 10$ mm. The height of the coherent structures, and the boundary-layer, is approximately 8 mm. In the last plane, taken at $x = 0.825$ m and

shown in Figure 5.8c, there are no coherent structures identifiable, and the Görtler vortices are amorphous; however, there are several small eddies that are visible. The height of the turbulent boundary-layer is approximately 9 mm in this location. Collectively, these four contours depict the significant spanwise variation in the flowfield and the spatial development of the three-dimensional Görtler vortices in the redeveloping boundary-layer.

(a) $x = 0.7$ m.

(b) $x = 0.775$ m.

(c) $x = 0.8$ m.

(d) $x = 0.825$ m.
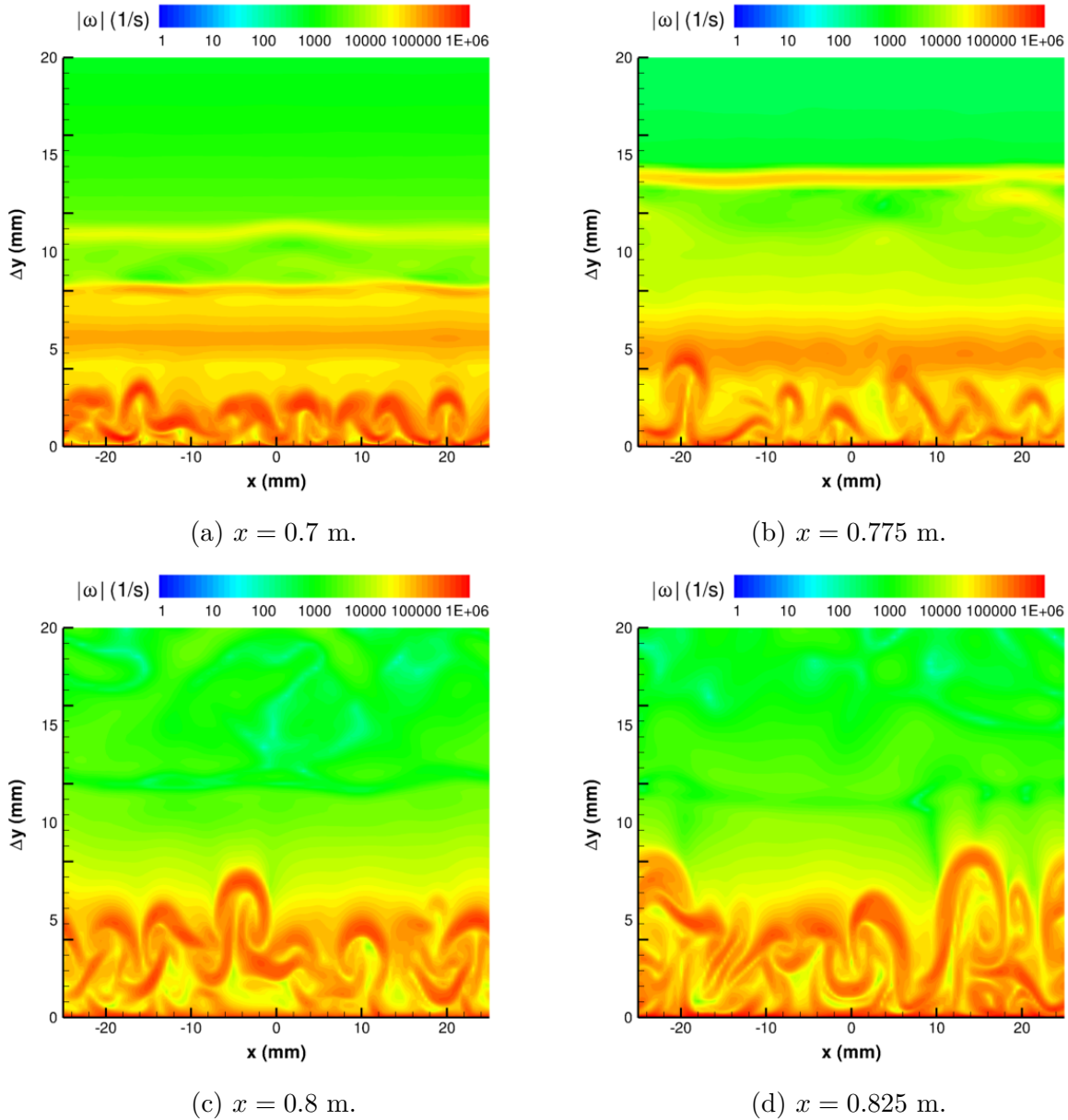
Figure 5.8. Spatial evolution and growth of Görtler vortices, at $t = 10.6$ ms. Instantaneous spanwise planar extracts located at $x = 0.75$ m, 0.775 m, 0.8 m, and 0.825 m.

5.2   Aerothermodynamic Loading

The pressure loading for this configuration follows the basic trends found in a compression ramp shock-wave/boundary-layer interaction. The time-averaged surface pressure on the entire windward elevon is provided in Figure 5.9. This figure depicts little spanwise variation in the time-averaged pressure loading. The surface pressure is constant, and relatively low, prior to reattachment. There is a notable isobar found at the time-averaged reattachment location, $x_r = 0.6914$ m. After reattachment, there is a rapid increase of pressure, caused by the shock-wave/boundary-layer interaction. This surface pressure is held constant along the remainder of the elevon surface, until a drop in surface pressure occurs at the trailing-edge. This drop in surface pressure is caused by boundary-layer separation and flow expansion.
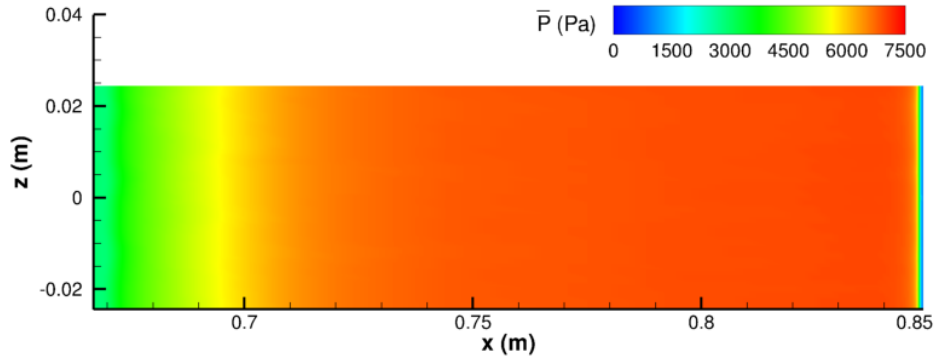
Figure 5.9. Time-averaged surface pressure, $\overline{P}$, on the windward elevon surface.

The time-averaged heat flux distributions for the entire windward and leeward elevon surfaces are provided in Figure 5.10a. This figure depicts the non-homogenous spanwise surface loading on the windward elevon surface. The spanwise streaks of localized heat flux are associated with Görtler vortices. Near the cove region, $x = 0.67$ m, there is a spanwise nodal pattern, which corresponds to the rapid flow entrainment. In the region immediately after, between 0.68 m $\leq x \leq 0.7$ m, there are distinct nodal patterns of low heat flux caused by large-scale flow separation. Downstream of this, there are three patterns aligned with the previous nodal patterns. These patterns consist of higher aerothermal loading, which is associated with the thinning of the boundary-layer. The surface heat flux drops slightly, as the boundary-layer momentarily develops, and then rises as the turbulent structures begin

129

to mix along the elevon. The surface heat flux then begins to exponentially rise, prior to the shedding of the boundary-layer at the trailing-edge. The time-averaged heat flux on the leeward elevon is provided in Figure 5.10b, for further context. There is little spanwise variation in the leeward elevon surface loading due to the lack of resolved unsteadiness in this region. The aerothermal heating inside of the cove is low, but there is a local spike in heat flux produced as the leeward boundary-layer reattaches. The heat flux then steadily drops as the boundary-layer develops along the leeward elevon surface. Eventually, near $x = 0.76$ m, the boundary-layer separates, leading to negligible aerothermal loading for the remainder of the leeward elevon surface. This behavior is expected in large regions of separation [160], [183], [184]. The heat flux rises again at the trailing-edge elevon face, which is attributed to the vortex shedding in the region.
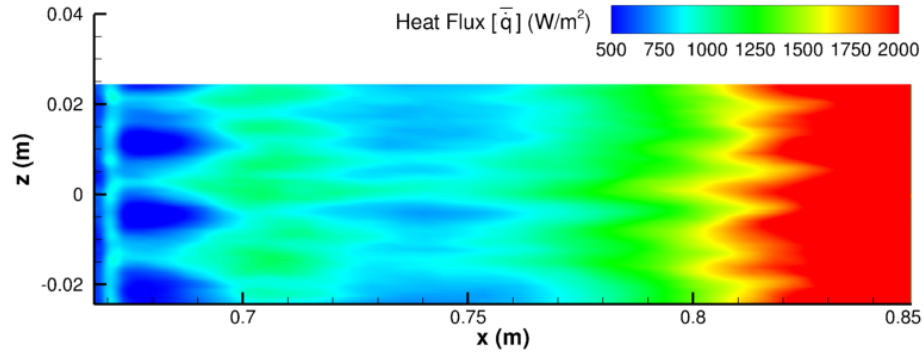
(a) Windward elevon surface.
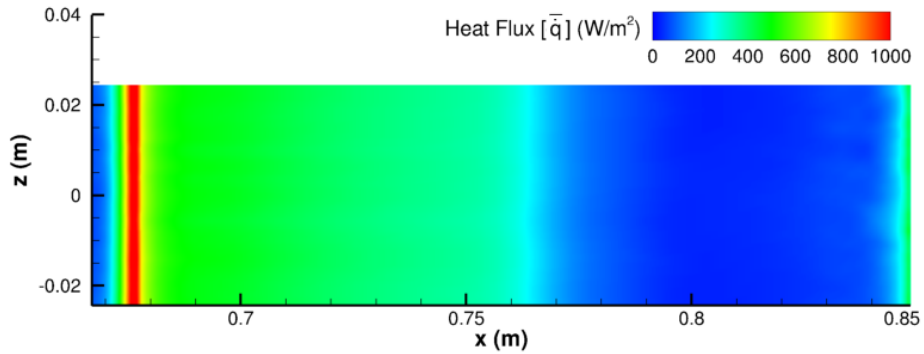
(b) Leeward elevon surface.

Figure 5.10. Time-averaged heat flux, $\bar{q}$, on the windward and leeward elevon surfaces.

To quantify these aerothermodynamic loading trends, centerline, $z = 0$ m, surface loading data were collected for the windward and leeward elevon surfaces. These data, corresponding to the time-averaged heat flux and pressure, are plotted in Figure 5.11. The elevon surface is split into the windward and leeward surfaces by the center chord line. As a result, half of the interior cove and trailing-edge faces are included for the windward and leeward plot lines. The trends and behaviors of the resultant loadings follow those depicted in the previous chapters. Shown in Figure 5.11a, the pressure on the windward surface behaves logistically, reaching high levels downstream of the shock-wave/boundary-layer interaction. On the leeward surface, the pressures inside of the cove are larger than those for the leeward boundary-layer. There is a large drop in pressure as the two meet, which is followed by a steady drop in pressure as the leeward boundary-layer develops. On this side of the elevon, there is a large expansion region causing this reduction in pressure. At the region of leeward separation, the pressure initially increases, and then remains constant. These centerline surface pressure trends are identical for different spanwise locations, due to the non-homogenous spanwise loading distribution depicted in Figure 5.9.

The centerline heat flux distribution, provided in Figure 5.11b, depicts the same general trends. However, as shown in Figure 5.10, these loadings are non-similar in the span. In Figure 5.11b, the y-axis scale is exponential in order to depict heat flux values which are orders of magnitude different. As in the Purdue BAM6QT computations, reattachment does not produce the highest levels of heat flux for this configuration. There is high aerothermal loading produced on the windward elevon in the flow entrainment region. This region is strongly associated with the vortex production, which was discussed in the previous section. Downstream, the heat flux drops slightly but then increases to a local peak at the time-averaged reattachment position, $x_r = 0.6914$ m. After reattachment, the heat flux remains relatively constant before rapidly increasing as the boundary-layer develops along the elevon. The global heat flux maximum is located at the trailing-edge face where the boundary-layer sheds from the windward surface. On the leeward elevon surface, there is a large spike in heat flux at boundary-layer reattachment. The heat flux then steadily drops until reaching the leeward separation region. In this region, the surface heat flux drops to exceedingly low,

negligible levels. On the trailing-edge face, the heat flux increases exponentially due to the separated shear-layer flapping and turbulent vortex shedding.

(a) Surface pressure.
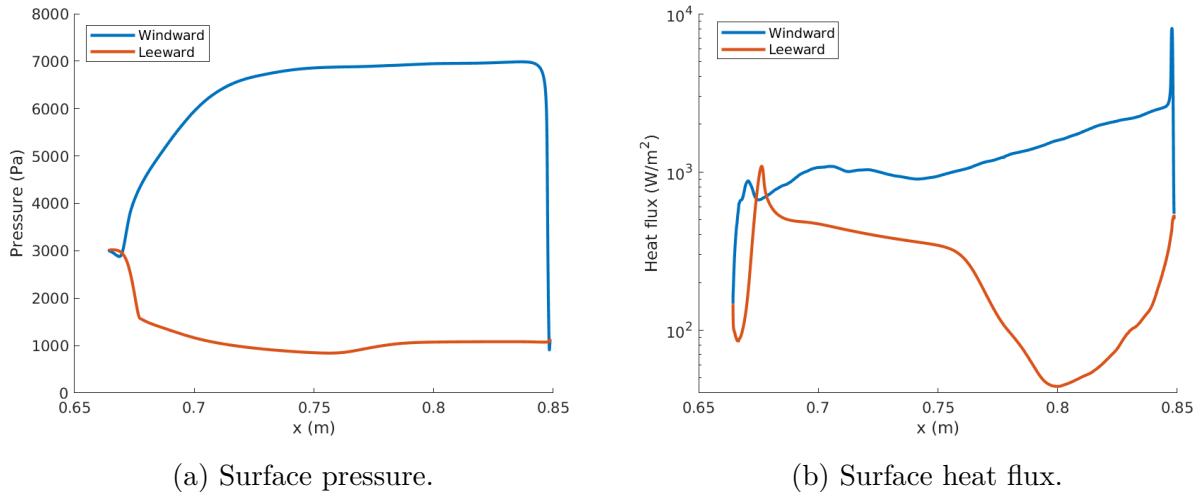
(b) Surface heat flux.

Figure 5.11. Time-averaged centerline surface pressure and heat flux distributions on the windward and leeward elevon surfaces.

The time-averaged aerothermodynamic surface loading distributions provided in the previous figures depict the general resultant surface loading. However, the time-dependent flow produces unsteady surface loads associated with the propagation of turbulent structures. The instantaneous surface loading distributions do not display any coherent structure, like what was shown in Figure 5.10 for the time-averaged surface heat flux. To display this, the instantaneous windward elevon surface heat flux is provided in Figure 5.12. These two contours are separated by $\Delta t = 0.1$ ms and start at $t = 10.5$ ms. In these figures, there are no clear structure in the heat flux distributions. There are, however, numerous unsteady regions of locally high heat flux, which are induced by the turbulent structures. There are also adjacent regions of locally low heat flux. The two snapshots in Figure 5.12a and Figure 5.12b also display the propagation of the local regions of high and low heat flux, which is aligned with the propagation of turbulent structures downstream. Together, these figures also display the chaotic nature of the unsteady aerothermodynamic loadings, and consequently, depict the necessity for unsteady flow analysis.
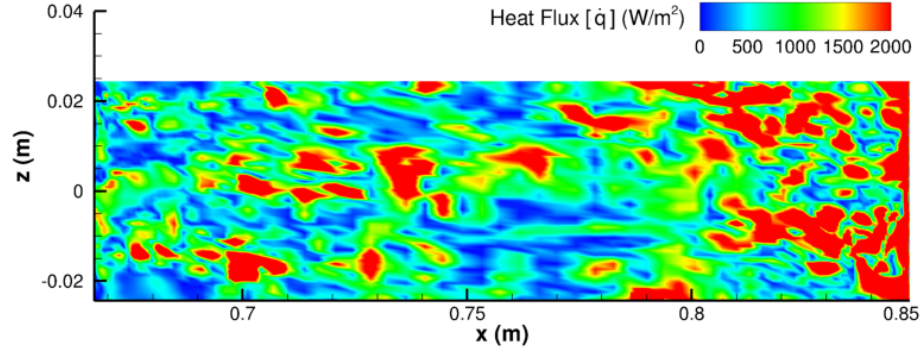
(a) $t = 10.5$ ms.
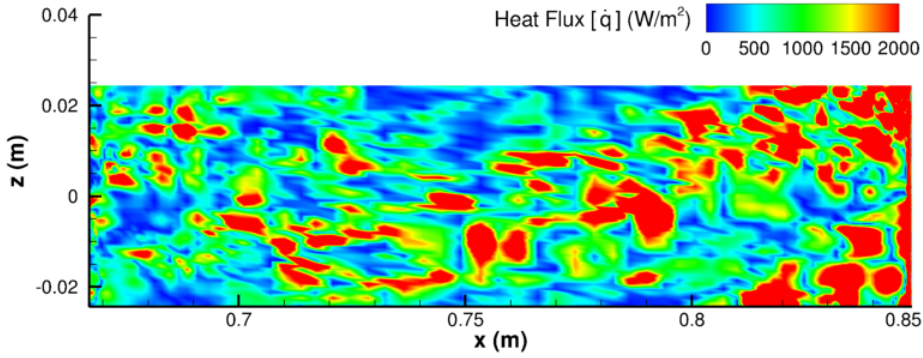
(b) $t = 10.6$ ms.

Figure 5.12. Instantaneous snapshots of heat flux, $\dot{q}$, on the windward elevon surface.

In order to determine the time-averaged reattachment location, surface skin friction data were collected and averaged over time. These data are provided in Figure 5.13a, which is a contour of time-averaged directional skin friction, $\overline{C_{f,x}}$, on the windward elevon surface. Since skin friction is proportional to the wall shear stress, this figure visualizes the shear loading on the windward elevon surface. In this figure, any value of skin friction below zero is blanked out, which depicts the coherent line of reattachment. The general trend of the wall shear consists of a steady increase along the elevon surface from reattachment to the trailing-edge, where a global maximum occurs as the boundary-layer sheds. There is significant spanwise nonuniformity of the line of reattachment. The spanwise distribution of reattachment is aligned with the spanwise heat flux nodal patterns depicted in Figure 5.10a. This figure also provides a visualization of the resultant hypersonic streak formations, which are known to be produced by the unsteady Görtler vortices [90], [92]–[94]. There are approximately seven

133

to eight distinct streaks, which originate near reattachment and continue downstream. This is the same number of Görtler vortices depicted at reattachment in Figure 5.8a.

To visualize the unsteady wall shear loading and reattachment location, an instantaneous skin friction, $C_{f,x}$, contour is provided in Figure 5.13b for the computational time of $t = 10.6$ ms. In this figure, it is clear that it is impossible to define a continuous line of reattachment. There are locations of zero skin friction that reach as far upstream as $x = 0.67$ m and as far downstream as $x = 0.7$ m. This provides a fluctuation in the reattachment location of ± 0.03 m. In addition, this figure shows the hypersonic streak formations as well as the locations of localized hot spots visualized in Figure 5.12b. These are both associated with the propagation of the Görtler vortices in the redeveloping boundary-layer.
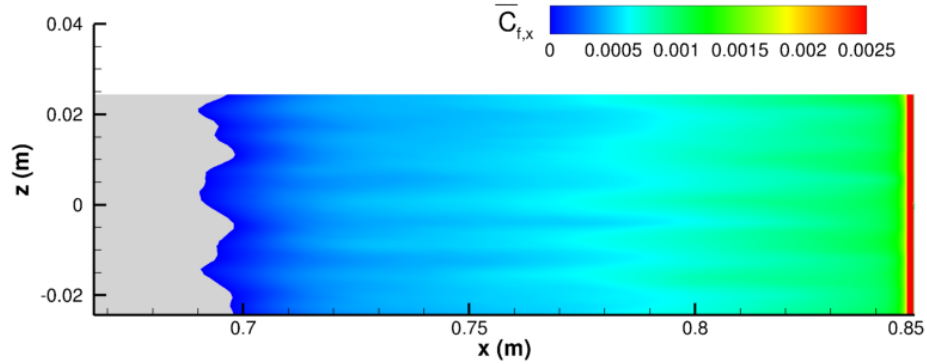
(a) Time-averaged.
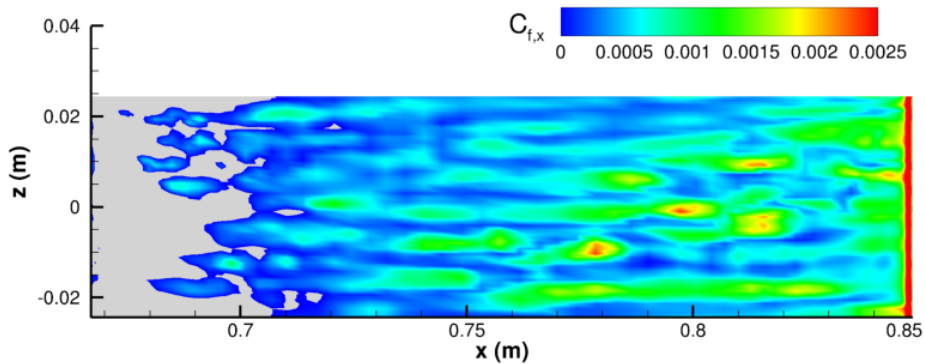
(b) Instantaneous ($t = 10.6$ ms).

Figure 5.13. Time-averaged and instantaneous contours of directional skin friction, $C_{f,x}$, on the windward elevon surface.

5.3 Statistical Analysis

This section provides the analyses on unsteady fluctuations in the shock-wave/boundary-layer interaction, in the redeveloping boundary-layer, and at the trailing-edge. The focus of this study was on the unsteady shock system and the generation, propagation, and shedding of turbulent structures. Unsteady flow signals were taken from the shock system, in the redeveloping boundary-layer, in the vortex shedding region at the trailing-edge, and along the windward elevon surface. These signals correspond to velocity fluctuations, u'_1 and u'_2, and pressure fluctuations, p'. A reattachment signal is also created, L'_r, utilizing a time-dependent reattachment position. This time-series is created through the location of the zero centerline skin friction on the windward elevon surface. All signals in this section were obtained with a sampling frequency of $f_s = 10$ MHz, corresponding to a sample at every computational time step. Signals are zero-padded to a power of two for fast Fourier transforms. Power spectral density calculations were done employing Welch's method and a Hamming window, with a segment length of 8192 points and 50% overlap. This windowing length and method are used to discern multiple features in signal's power spectrum.

Spanwise spatial correlations were calculated to determine if the periodic boundary sides were correlated with the centerline. This was a concern for this computation; for periodic sidewall boundary conditions, the span should be large enough that it does not influence the statistical results. To cover the entire elevon, spanwise wall pressure distributions were collected for five streamwise stations, located at $x = 0.67$ m, 0.69 m (x_r), 0.74 m, 0.78 m, and 0.82 m. These distributions were correlated with the centerline. The two-point zero time-delay cross-correlations for these locations are provided in Figure 5.14. Several correlations are non-symmetric despite the spanwise surface symmetry. The first station corresponds to the flow entrainment region, where high aerothermal loading and spanwise variation were observed. This station depicts fluctuating positive and negative spanwise correlation with the centerline, but at low levels. There are moderate correlations at $z = \pm 0.01$ m for the flow entrainment region, $x = 0.67$ m, and the two downstream stations, $x = 0.78$ m and $x = 0.82$ m. However, all spanwise correlations gradually drop to zero at the computational boundaries, $z = \pm 0.025$ m.
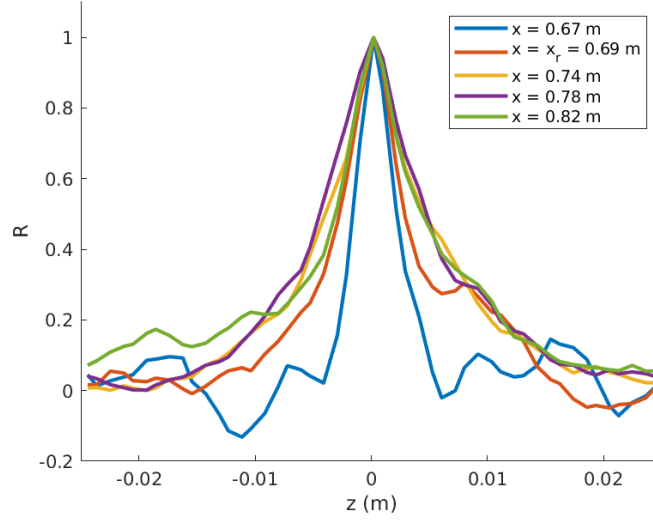
Figure 5.14. Spanwise centerline zero time-delay cross-correlations for stations located at $x = 0.67$ m, 0.69 m (x_r), 0.74 m, 0.78 m, and 0.82 m.

5.3.1 Resolved Reynolds Stress

The resolved Reynolds stress can identify regions of strong unsteadiness or turbulence production [185]–[187]. The Reynolds stress tensor is obtained through the single-point covariance of velocity fluctuations. Therefore, regions of high resolved Reynolds stress depict large fluctuations in the velocity field. Centerline, $z = 0$ m, contours of the resolved Reynolds normal stress components, R_{11}, R_{22}, and R_{33}, and shear stress, R_{12}, are provided in Figure 5.15. In this figure, the resolved Reynolds stress components, $\overline{u_i' u_j'}$, non-dimensionalized by the freestream velocity squared, u_∞^2, are provided for the entire flowfield, with an enlarged frame focused on the cove. There are high levels of resolved Reynolds stress found in the cove environment, in the shock system, in the redeveloping boundary-layer, and at the trailing-edge. The features of the shock system, such as the shear-layer, the separation vortex, the shock-wave, and flow entrainment, are depicted with high resolved Reynolds stress. The fluctuations in the trailing-edge shear-layer produce significant resolved Reynolds stress, as well. The separation shock-wave is also visible in many of the resolved Reynolds stress components. The redeveloping boundary-layer depicts the propagation and sustainment of turbulence for this computation. The Reynolds normal stress components, R_{11}, R_{22}, and R_{33},

display the general unsteadiness in the flowfield. The Reynolds shear stress, R_{12}, displays regions of both negative and positive velocity correlations. There are positive correlations near reattachment and in the redeveloping boundary-layer. Additionally, there are negative values at the trailing-edge and in the separation vortex, which indicts the turbulent transport of eddies [146]–[148].

(a) $R_{11} = \overline{u_1' u_1'}$.

(b) $R_{22} = \overline{u_2' u_2'}$.

(c) $R_{33} = \overline{u_3' u_3'}$.

(d) $R_{12} = \overline{u_1' u_2'}$.
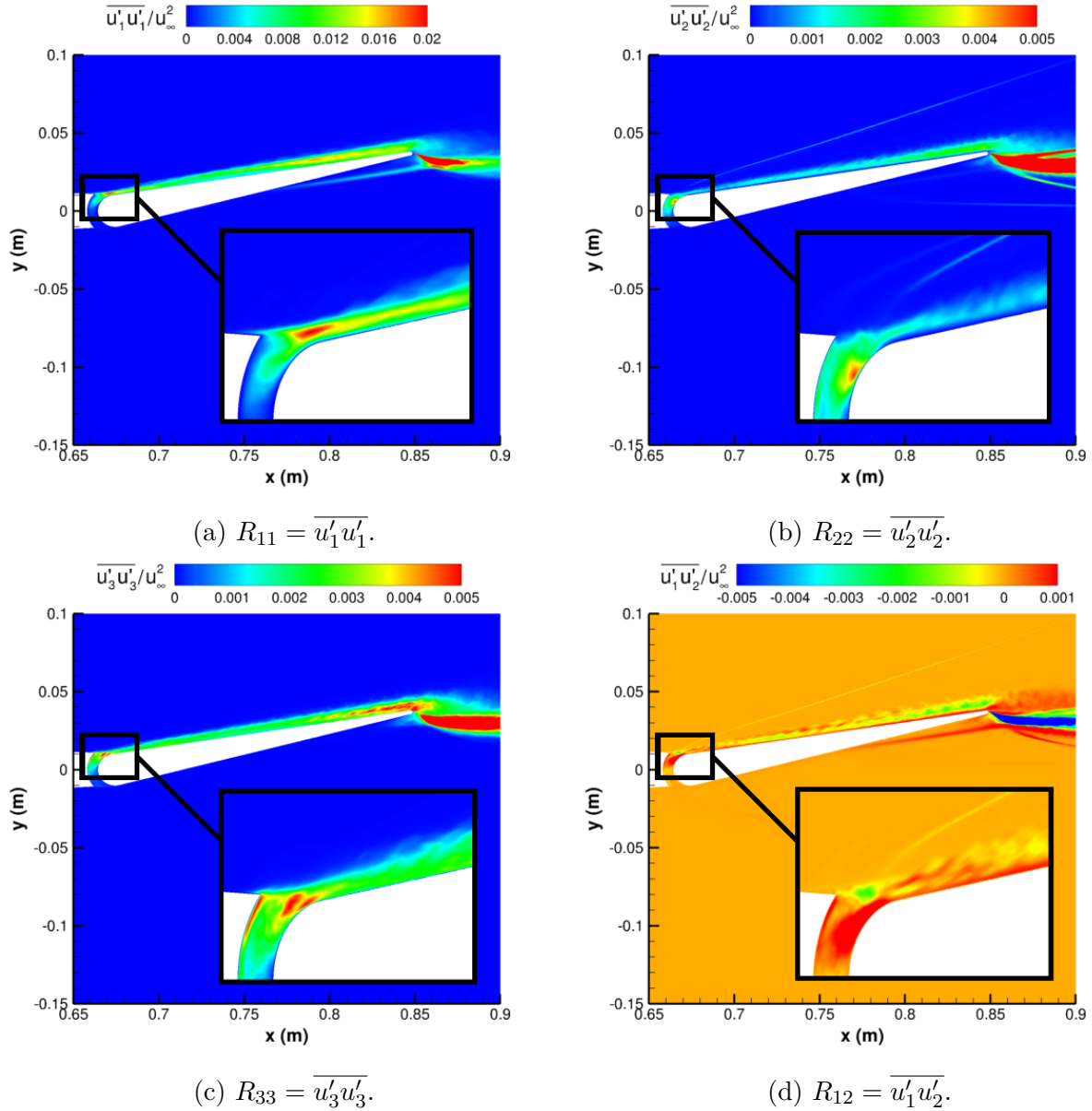
Figure 5.15. Centerline, $z = 0$ m, contours of resolved Reynolds stress, $\overline{u_i' u_j'}$, non-dimensionalized by the freestream velocity squared, u_∞^2.

5.3.2 Space-Time Correlation and Convection Velocity

The coherent nature of the shock-wave/boundary-layer interaction and the trailing-edge flow was analyzed with two-point zero time-delay cross-correlations. Contours of the correlation coefficient, R, are provided in Figure 5.16, for four correlation signals. These signals, which are correlated with the surrounding flow, correspond to reattachment position movement, L'_r, shear-layer flapping, u'_2, shock-wave oscillation, u'_1, and trailing-edge shear-layer vortex shedding, u'_2. The signals, aside from L'_r, were collected at $(x, y) = (0.665, 0.0115)$ m, $(x, y) = (0.68, 0.175)$ m, and $(x, y) = (0.852, 0.365)$ m, respectively. These reference locations are marked with black squares in Figure 5.16.

The first figure, Figure 5.16a, provides the local flowfield cross-correlation for the reattachment position signal. Several significant flow phenomena are highlighted with positive correlation to this signal. There is a large region of correlation near the general region of boundary-layer reattachment, and a region of negative correlation region immediately downstream. The center of the separation vortex is visible with a high level of correlation, depicting the significant correlation between the reattachment position fluctuation and the separation expansion and contraction. This signal also depicts small correlations with the separation and reattachment shock-waves, as well as a pocket at the centerline cove. The second figure, Figure 5.16b, provides the local flowfield cross-correlation for the separated shear-layer signal. The separated shear-layer shows a large region of high correlation above the cove, which is associated with its coherent movement. The reattachment shock-wave shows high levels of negative correlation, depicting inverse unsteady oscillations. There is a region of flow entrainment which produces negative correlation to the shear-layer flapping. Overall, this figure depicts the coherent flapping of the shear-layer, which inverses the reattachment shock-wave motion and breathing of the separation vortex.

The local flowfield cross-correlation for the reattachment shock-wave signal is provided in the third figure, Figure 5.16c. The structure of the shock-wave is depicted with the surrounding region of high positive correlation to the reference signal. There are small-valued correlations elsewhere in this region, such as near the shear-layer and separation vortex; however, no other discernable features can be seen. The last figure, Figure 5.16d,

provides the local flowfield cross-correlation for the trailing-edge shear-layer. Here, there is a large region of positive correlation for the trailing-edge shear-layer, depicting its coherent structure and the growth of the shear-layer. There also exists negative correlation of the region above the trailing-edge shear-layer, where turbulent structures in the boundary-layer shed. All the other three signals displayed small, but non-zero, correlations in this region.

(a) Ret. position, L_r'.

(b) Shear-layer, ref. $(0.66, 0.01)$ mm.

(c) Ret. shock-wave, ref. $(0.68, 0.17)$ mm.

(d) Trail.-edge shear-layer, ref. $(0.85, 0.36)$ mm.
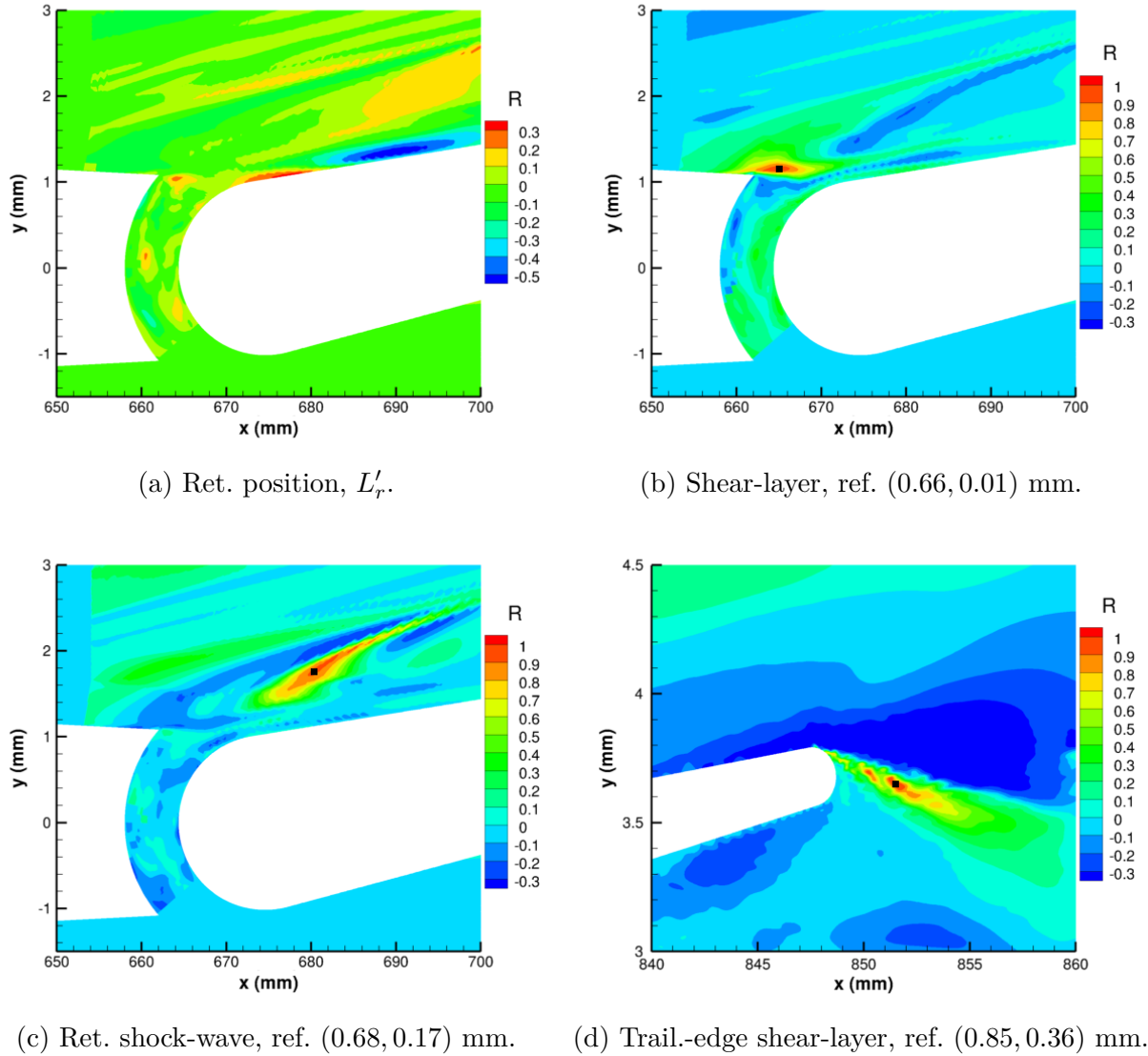
Figure 5.16. Zero time-delay cross-correlations in the shock-wave/boundary-layer interaction. Reference locations are marked with black squares.

At the cove juncture, there is a centrifugal instability which is associated with the production of Görtler vortices. These turbulent structures propagate downstream, where they expand and mix. The boundary-layer becomes fully turbulent by the trailing-edge of the elevon. To visualize the evolution of structural correlation in the redeveloping boundary-layer, zero time-delay two-point cross-correlations were calculated for four reference signals, s_1, s_2, s_3, and s_4, with the surrounding flowfield. These reference signals are roughly located at $x = 0.7$ m, 0.75 m, 0.8 m, and 0.85 m, respectively, and correspond to velocity fluctuations, u'_1, in the boundary-layer. Contours of the spatial cross-correlations are provided in Figure 5.17 for these four reference signals, which include enlarged frames focused on the reference signals. At the first station, s_1, shown in Figure 5.17a, the spatial correlation spans a small region, the size of 10 mm by 200 mm. In the next figure, Figure 5.17b, the elongation of turbulent structures is depicted with the proportional elongation of the correlation region around the s_2 reference signal, which spans 10 mm by 500 mm. In the next figure, Figure 5.17c, the correlation for the s_3 reference signal is similar to the previous station. The last figure, Figure 5.17d, depicts a smaller region of correlation near the trailing-edge. In this figure, there is correlation with the shedding boundary-layer; however, there is noticeably no correlation in the separated shear-layer. This shows that upstream boundary-layer turbulence is not correlated with the unsteady separated shear-layer flapping at the trailing-edge of the elevon.

Utilizing the reference signals, s_1, s_2, s_3, and s_4, space-time cross-correlations, at non-zero time-delays, were also calculated. In order to determine the correlation between upstream and downstream regions of the redeveloping boundary-layer, the upstream reference signal, s_1, was correlated with the downstream signals, s_2, s_3, and s_4. These correlations are provided in Figure 5.18, where the x-axis is the non-dimensional time-delay, $\Delta t u_\infty / \Delta x$. The inverse of the non-dimensional time-delay can be approximated as the convection velocity, U_c, for the redeveloping boundary-layer. This figure displays the local peak correlation region for each of the space-time cross-correlations. These peaks depict the high levels of correlation between the signals in the boundary-layer, and are equal to $R = 0.62$, 0.55, and 0.48, for s_1/s_2, s_1/s_3, and s_1/s_4, respectively. In addition, the optimal time delays associated with these peaks provide the convection velocities of $U_c/u_\infty = 0.6$, 0.65, and 0.7, respectively.

(a) s_1 ($x = 0.7$ m).

(b) s_2 ($x = 0.75$ m).

(c) s_3 ($x = 0.8$ m).

(d) s_4 ($x = 0.85$ m).
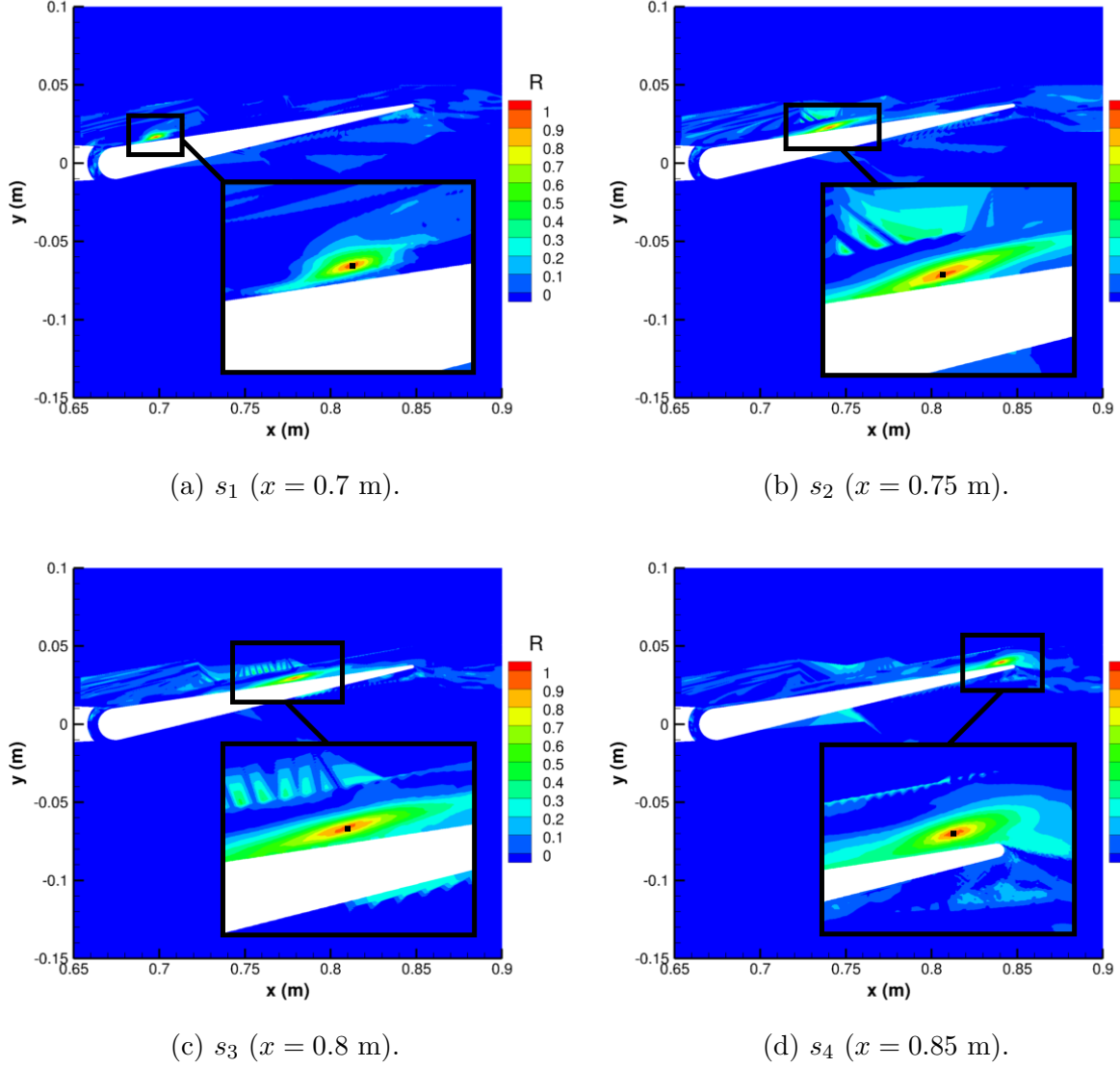
Figure 5.17. Two-point zero time-delay cross-correlations in the redeveloping boundary-layer. Reference locations are marked with black squares.

These values are similar to the convection velocities calculated with nearby wall pressure signals, which are plotted in Figure 5.20. In addition, the increasing of convection velocities, as the boundary-layer develops, is observed with these correlations, which is consistent with the literature [188]. Outside of the temporal range provided, $0 \leq \Delta t u_\infty / \Delta x \leq 5$, the correlations between these regions oscillate around zero.
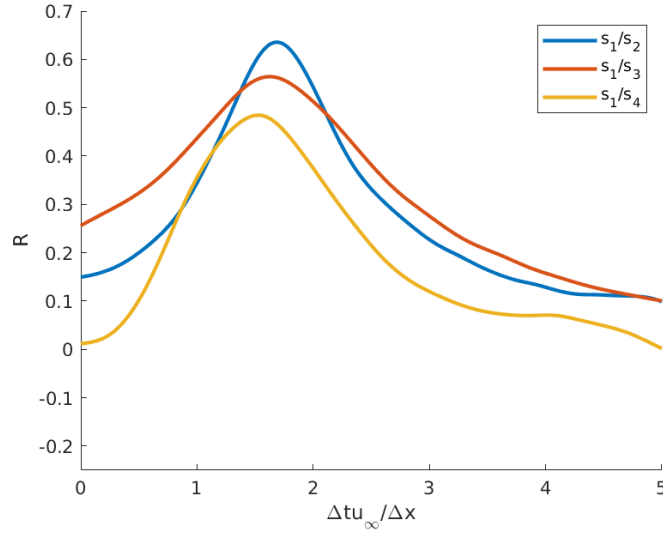
Figure 5.18. Space-time cross-correlations for the upstream signal, s_1, with downstream signals, s_2, s_3, and s_4, in the redeveloping boundary-layer.

In order to continue the investigation on the redeveloping boundary-layer, space-time cross-correlations of wall pressure signals along the windward elevon surface were calculated. The cross-correlation contours for four different reference signals, with the surrounding surfaces, are provided in Figure 5.19. These locations correspond to the cove region, $x = 0.67$ m, reattachment, $x = x_r = 0.69$ m, and two downstream stations, $x = 0.74$ m and $x = 0.78$ m. These figures are contour-colored with the correlation coefficient, R. The x-axis is the spatial separation, Δx, and the y-axis is the signal time-delay, Δt. The spatial separation is calculated as $\Delta x_s = \sqrt{(x_i - x_s)^2 + (y_i - y_s)^2}$, where x_s and y_s are the reference signal coordinate locations. The time-delay represents the temporal difference in computational time. Therefore, any spot away from the origin corresponds to the cross-correlation between the reference signal and a spatially and temporally separated signal. The angle of these correlations, in the space-time domain, is associated with the development of the turbulent boundary-layer. Space-time correlations of this nature will produce an inclined distribution in the space-time domain for fully developed hairpin vortices in a turbulent boundary-layer [189]–[192]. Additionally, these calculations can subsequently be used to calculate the convection velocities, U_c, by using the optimal time delay, Δt_{opt}, for each spatial separation, Δx.

142

The space-time cross-correlation is at a relatively steep angle for the first station, at $x = 0.67$ m and shown in Figure 5.19a. In this figure, the primary correlation spatial region spans 0.02 m, and the primary time-delay range is 0.01 ms. The following station, at $x = x_r = 0.69$ m and shown in Figure 5.19b, displays a similar space-time cross-correlation structure, with a slightly larger spatial correlation and time-delay correlation range. Moving downstream, to stations $x = 0.74$ m and $x = 0.78$ m shown in Figure 5.19c and Figure 5.19d, the incline of the cross-correlation depicts the fully-developed boundary-layer. These regions have a much larger spatial correlation region, ranging over 0.1 m, and time-delay range, ranging 0.1 ms. The space-time cross-correlation for a region inside of the cove, at $y = 0$ m, is provided in Figure 5.19e. The correlation contour in this figure is very different than those shown along the downstream elevon, consisting of a circular correlation distribution. Overall, this reference location displays low-spatial correlation, but a relatively high temporal correlation, depicting the low-frequency influence in the region.

Using the same data employed in Figure 5.19, the convection velocities were calculated for the surrounding area, $\Delta x \leq 20$ mm, of each reference signal, s_1, s_2, s_3, and s_4. The non-dimensional convection velocities, U_c/u_∞, are plotted in Figure 5.20. In general, these plots depict the relatively constant convection velocity values obtained for each reference station. This behavior is due to the linearly inclined space-time correlation distributions, which were displayed in Figure 5.19. Each signal shows relatively constant convection velocities, with the largest variations found near the region of flow entrainment. The average convection velocity range, for all stations, is $0.65 \leq U_c/u_\infty \leq 0.75$. These values are also in line with the convection velocities calculated for velocity fluctuations in the redeveloping boundary-layer. There is a clear increase in convection velocities moving downstream, which is consistent with the literature [188]. The convection velocities at $x = 0.67$ m do not precisely follow this trend, which may be due to the unsteady shock-wave/boundary-layer interaction. The center cove convection velocities are not shown in this figure, and were much lower, with an approximate value of $U_c/u_\infty = 0.3$. This value is constant for the majority of the cove, up until $x = 0.67$ m.
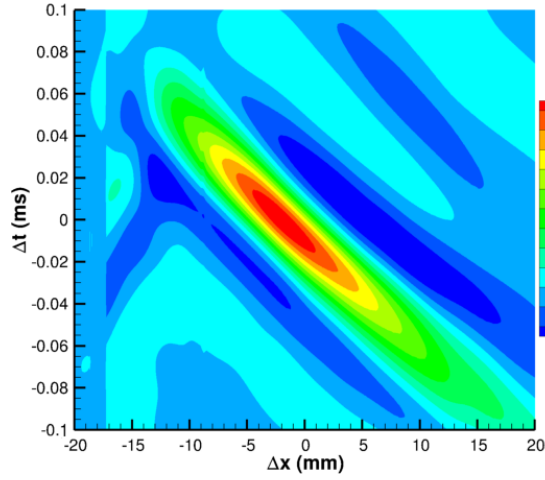
(a) $x = 0.67$ m.
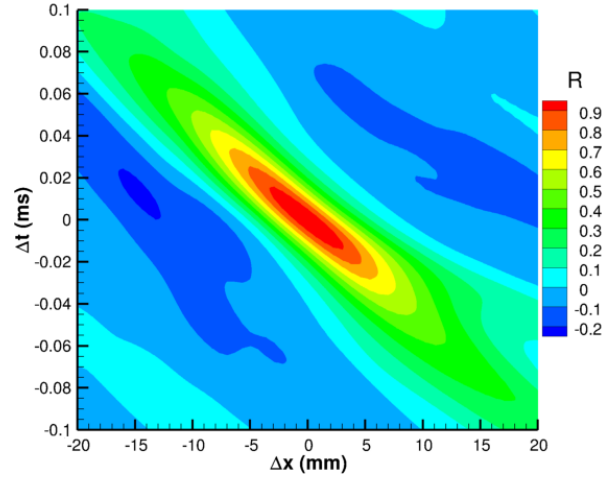
(b) $x = x_r = 0.69$ m.
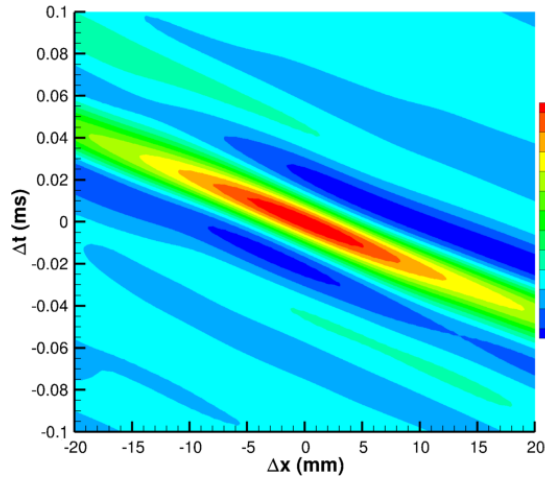
(c) $x = 0.74$ m.
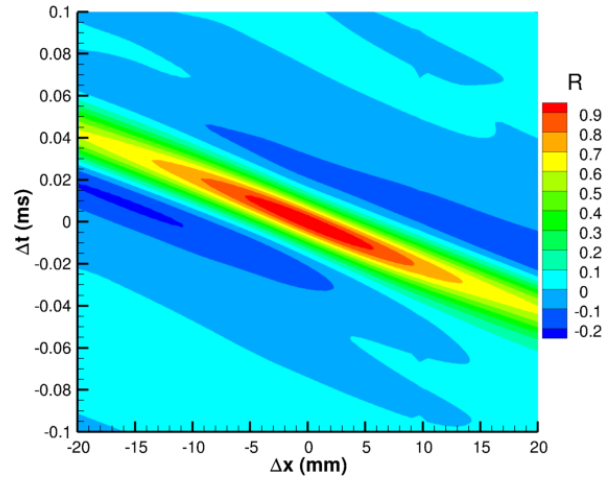
(d) $x = 0.78$ m.
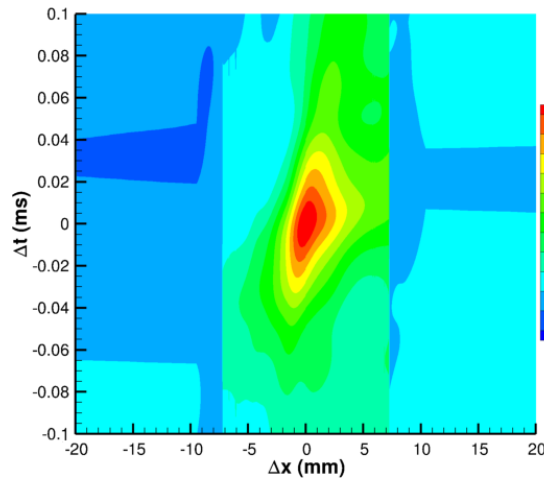
(e) Cove center ($y = 0$ m).

Figure 5.19. Space-time cross-correlation contours of wall pressure signals, $x = 0.67$ m, 0.69 m, 0.74, 0.78 m, and $y = 0$ m, and the surrounding surfaces.
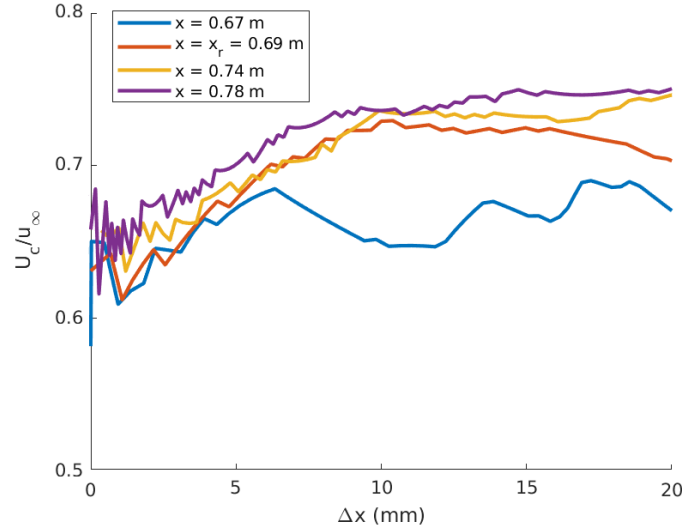
Figure 5.20. Convection velocities corresponding to the reference signals, $x = 0.67$ m, 0.69 m, 0.74, and 0.78 m, and the surrounding areas, $\Delta x \leq 20$ mm.

5.3.3 Power Spectral Density and Coherence

Statistical signal analyses were done for various regions of the unsteady flowfield. In this section, the frequencies are non-dimensionalized as the Strouhal number S_t. The length-scale and velocity-scale used for non-dimensionalization are the time-averaged reattachment length, $\overline{L_r}$, and the freestream velocity, u_∞. The characteristic frequency is $f_c = 20$ kHz. Data for each signal are collected at every time step, with a sampling frequency of $f_s = 10$ MHz. This section provides analyses of unsteady fluctuations in the shock-wave/boundary-layer interaction, in the redeveloping boundary-layer, along the elevon surface, and at the trailing-edge. Signals used here correspond to vertical velocity fluctuations, u_2', in the shear-layer, collected at $(x, y) = (0.666, 0.011)$ m, and in the trailing-edge shear-layer, collected at $(x, y) = (0.851, 0.036)$ m. Streamwise velocity fluctuations, u_1', were collected in the separation and reattachment shock-waves, at $(x, y) = (0.67, 0.019)$ m and $(x, y) = (0.6725, 0.015)$ m, respectively. Separation fluctuations, p', were collected in the separation vortex, at $(x, y) = (0.664, 0.009)$ m. The reattachment position movement, L_r', is also included in several of these analyses.

The premultiplied power spectral densities, $fG(f)/\sigma^2$, for six important flow phenomena are provided in Figure 5.21. These signals correspond to components of the shock-wave/boundary-layer interaction. The trailing-edge shear-layer and reattachment position are included as well. It is evident that the shock system contains low-frequency spectral content. The majority of the spectral energy for the signals in this region are within the Strouhal number range of $0.01 \leq S_t \leq 2$. Specifically, the reattachment position spectrum is contained within the Strouhal number range of $0.01 \leq S_t \leq 5$. The primary shear-layer signal spectrum is contained within the Strouhal number range of $0.1 \leq S_t \leq 4$. The separation vortex signal spectrum spans the largest frequency range and is contained within the Strouhal number range of $0.02 \leq S_t \leq 3$. The separation shock-wave signal spectrum is contained within the Strouhal number range of $0.01 \leq S_t \leq 1$, and the reattachment shock-wave spectrum is within the Strouhal number range of $0.1 \leq S_t \leq 2$. For comparison, there is a clear shift to higher frequencies in the trailing-edge shear-layer signal spectrum, which is contained within the Strouhal number range of $0.1 \leq S_t \leq 10$.

Separation provides the lowest initial spectral frequency peak, at a Strouhal number of $S_t = 0.02$. The reattachment position spectrum has the second lowest frequency peak, at a Strouhal number of $S_t = 0.08$. The separation and reattachment shocks have slightly higher frequency spectral peaks, at Strouhal numbers of $S_t = 0.15$ and $S_t = 0.25$, respectively. Surprisingly, both the primary shear-layer, at the cove, and the trailing-edge shear-layer signals do not have dominant low frequency peaks. These spectra also generally have higher frequency spectral energy content. The six signals have modal peaks, in the Strouhal number range of $0.1 \leq S_t \leq 0.3$, that may correspond to Rossiter Modes [193]–[196]. For the reattachment position spectrum, these peaks occur at Strouhal numbers of $S_t = 0.09$, 0.18, and 0.45. For the cove shear-layer spectrum, there are distinct modal peaks that occur at Strouhal numbers of $S_t = 0.125$, 0.2, 0.35, and so forth. For the separation vortex spectrum, peaks occur at Strouhal numbers of $S_t = 0.11$, 0.18, 0.25 and 0.3. For the reattachment shock-wave spectrum, there are modal peaks at Strouhal numbers of $S_t = 0.3$ and $S_t = 0.5$. For the separation shock-wave spectrum, there are modal peaks at Strouhal numbers of $S_t = 0.32$ and $S_t = 0.48$, and for the trailing-edge shear-layer spectrum, there are modal peaks at Strouhal numbers of $S_t = 0.2$, 0.35, and 0.5.
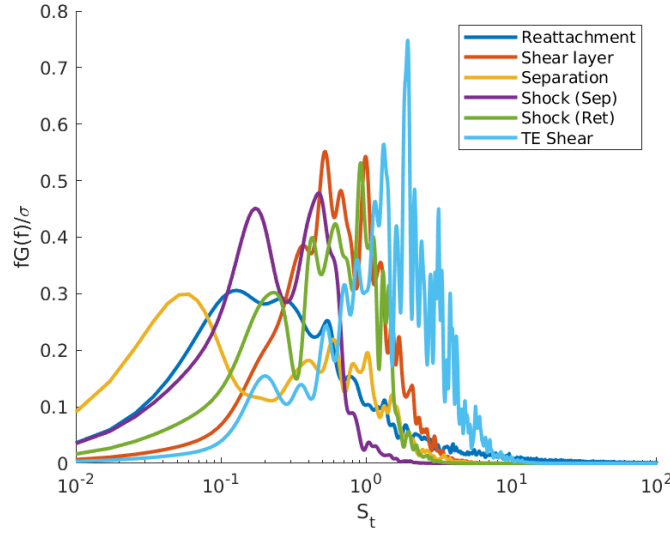
Figure 5.21. Premultiplied power spectral densities, $fG(f)/\sigma^2$, for flowfield signals in the shock-wave/boundary-layer interaction and at the trailing-edge.

These signals were also used to analyze the spectral correlation of reattachment shock-motion and separation vortex contraction and expansion. Coherences with the reattachment shock-wave signal are provided in Figure 5.22a, and coherences with the separation vortex signal in Figure 5.22b. At low-frequencies, in the Strouhal number range of $0.01 \leq S_t \leq 0.1$, the reattachment shock-wave and the reattachment position signal have the strongest coherence, followed by the reattachment shock-wave and the primary shear-layer signal. In these ranges, the separation shock-wave and the trailing-edge shear-layer signals have zero coherence with the reattachment shock-wave. There are distinct peaks in the Strouhal number range of $0.1 \leq S_t \leq 1$ for all coherences with the reattachment shock-wave signal. There is also significant coherence with the trailing-edge shear-layer signal at the Strouhal number of $S_t = 0.8$, as well. The rest of the frequency range contains too much statistical uncertainty to form a clear interpretation.

The coherence with the separation vortex contraction and expansion is provided in Figure 5.22b. At low-frequencies, in the Strouhal number range of $0.01 \leq S_t \leq 0.1$, there is strong coherence between the separation vortex signal and the reattachment shock-wave, the shear-layer, and the trailing-edge shear-layer signals. At moderate frequencies, in the Strouhal number range of $0.1 \leq S_t \leq 1$, there are also distinct modal peaks for each of the

signal's coherence with the separation vortex signal. The coherence between the separation vortex and the reattachment shock-wave is the strongest in this region, displaying a peak coherence at the Strouhal number of $S_t = 0.8$. In addition, there is peak coherence between the separation vortex signal and the trailing-edge shear-layer signal found at a lower frequency Strouhal number of $S_t = 0.7$. The separation vortex signal and the reattachment position signal also show significant coherence at local peak of $S_t = 0.6$. Collectively, these coherence plots further highlight the spectral frequencies that were depicted in Figure 5.21.

(a) Shock-wave coherence.　　　　　(b) Separation coherence.
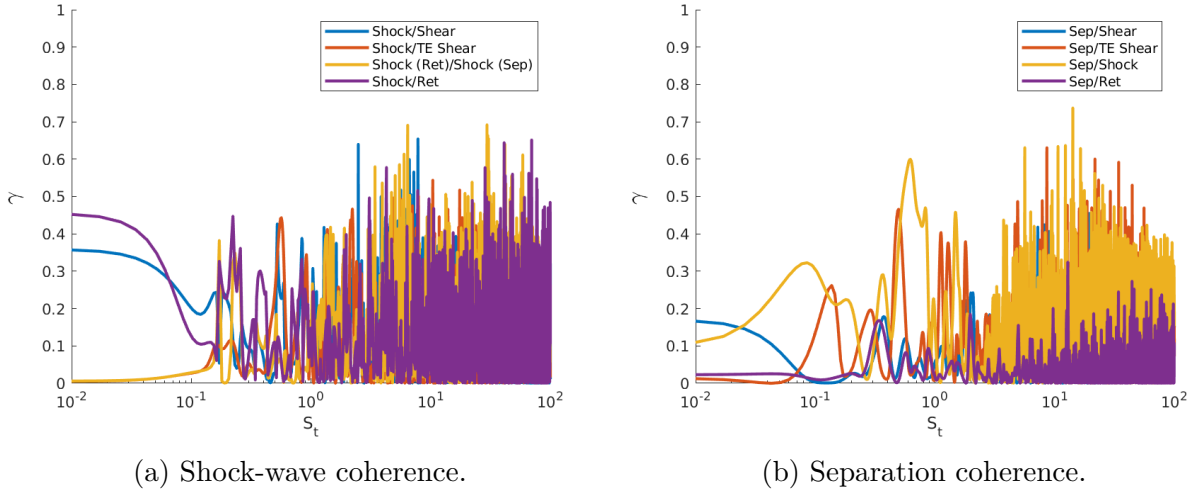
Figure 5.22. Coherence between the shock-wave and separation signals with other shock-wave/boundary-layer interaction signals.

The power spectra and coherence in the redeveloping boundary-layer were analyzed using the four signals, s_1, s_2, s_3, and s_4, which were discussed previously. The premultiplied power spectral density of these signals is provided in Figure 5.23a. The coherences between the upstream, s_1, and the other downstream signals, s_2, s_3, s_4, are provided in Figure 5.23b. Since these signals are all within the redeveloping boundary-layer, the spectra are all relatively similar. The primary Strouhal number range here, where most of the energy is contained, is $0.01 \leq S_t \leq 1$. There exists a slight shift in spectral energy to higher frequencies between s_1 to s_4. This shift is consistent with evidence that is presented later in this section. There is significant coherence between these signals at low-to-moderate frequencies, in the Strouhal number range of $0.01 \leq S_t \leq 0.8$, which is shown in Figure 5.23b. The strongest coherence

is between the two closest signals, s_1 and s_2, with a peak at the frequency of $S_t = 1$. The coherence between the two downstream signals and the upstream signal drop near $S_t = 0.15$, but there are modal peak values at higer frequencies, in the Strouhal number range of $0.1 \leq S_t \leq 1$. Once again, there is statistical uncertainty at $S_t \geq 1$.

(a) Premultiplied power spectral density.

(b) Coherence.
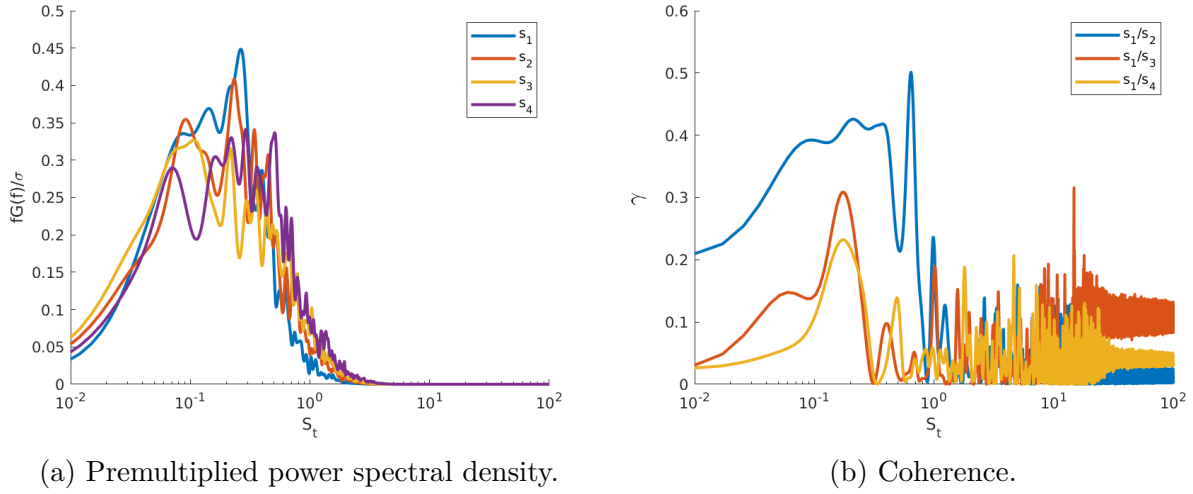
Figure 5.23. Spectral statistics for wall pressure signals in the redeveloping boundary-layer, s_1, s_2, s_3, and s_4.

There were additional focus areas of the flow investigated, such as regions of aerothermal maxima near the cove and at the elevon's trailing-edge. These locations, which can be seen in the plot of elevon surface heat flux in Figure 5.11b, roughly translate to the location of rapid flow entrainment, in the cove, and the vortex shedding of the windward boundary-layer. Unsteady surface heat flux signals were collected at these peak locations on the windward elevon surface. The premultiplied power spectral densities and coherences of these signals are provided in Figure 5.24, with the reattachment position signal, L'_r, included for reference. Each of the peak heat flux spectra are concentrated at higher frequencies, comparatively to other locations in the flow, in the Strouhal number range $0.5 \leq S_t \leq 10$. This shift is made clear with the inclusion of the reattachment position signal, which is strongly concentrated at low frequencies, in the Strouhal number range $0.01 \leq S_t \leq 2$. There is also a distinct shift to higher frequencies in the trailing-edge vortex shedding spectrum, compared to the flow entrainment. The coherence plots between the two heat flux maxima signals and the

149

reattachment position signal are provided in Figure 5.24b. Here, there is significant coherence at moderate frequencies, $S_t \leq 1$, and distinct modal peaks at $S_t = 0.5$, 0.7, and 0.8. The rest of the coherence, at frequencies larger than $S_t = 1$, are associated with statistical uncertainty.

(a) Premultiplied power spectral density.

(b) Coherence.
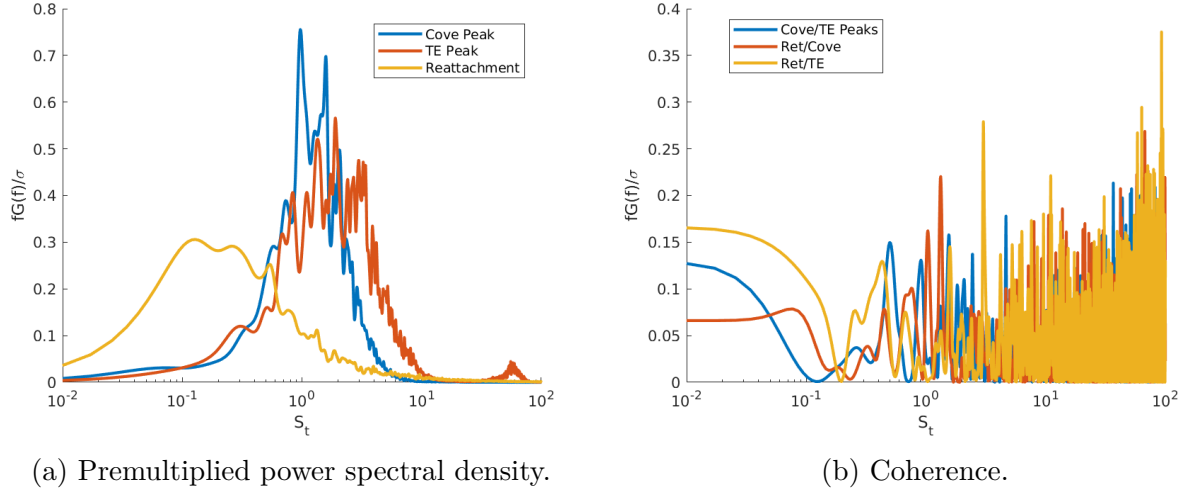
Figure 5.24. Spectral statistics for windward elevon surface heat flux maxima signals, and the reattachment signal, L'_r, for reference.

Analysis of the intermittent wall pressure signals along the windward elevon surface was done to provide further context to the unsteady flow characteristics. The premultiplied power spectral densities were calculated with these signals. The complete power spectra for the windward elevon are provided in Figure 5.25. This figure is contour-colored by premultiplied power spectral density, $fG(f)/\sigma^2$. The x-axis is the distance, x, in the spatial reference frame, and the y-axis is the frequency domain, scaled as the base-10 log of the Strouhal number, S_t. This scaling facilities the depiction of power spectra at frequencies of different orders of magnitude. This power spectra contour highlights several important characteristics of the fluctuating wall pressure. The most important of which is that a large frequency shift from low-to-high frequencies, starting in the cove region, moving to reattachment, and then to downstream, which is consistent with spectra for other relevant flows [54], [58], [90], [143], [144], [158]. However, this trend is opposite to what was found for the NASA wing-elevon-cove computation, where a shift from high-to-low frequencies was found downstream of reattachment, as displayed in the similar plot provided in Figure 3.20.

The primary Strouhal number range in Figure 5.25 is considered within green/blue contour levels, and the peak Strouhal number range is within the red/orange contour levels. In the cove environment, $x = 0.665$ m to $x = 0.67$, the primary Strouhal number range is $0.17 \leq S_t \leq 2$, and the peak Strouhal number range is $0.6 \leq S_t \leq 1.1$. Slightly upstream, at the time-averaged reattachment location, $x = 0.69$ m to $x = 0.7$, the frequency ranges are similar in magnitude. The primary Strouhal number range is $0.2 \leq S_t \leq 2.4$, and the peak Strouhal number range is $0.8 \leq S_t \leq 1.5$. Moving half a meter down the elevon results in the large shift to higher frequencies. At the midpoint of the elevon, near $x = 0.75$ m, the primary Strouhal number range is $0.36 \leq S_t \leq 3.5$, and the peak Strouhal number range is $1.13 \leq S_t \leq 2.4$. These frequency ranges are nearly twice as high as those closer to the upstream cove region. The primary and peak Strouhal number ranges are mostly unchanged until the trailing-edge. In this region, the spectra contain low, moderate, and high frequencies for this flow, with a primary Strouhal number range is $0.143 \leq S_t \leq 3.6$ and peak range of $1.46 \leq S_t \leq 2.32$.
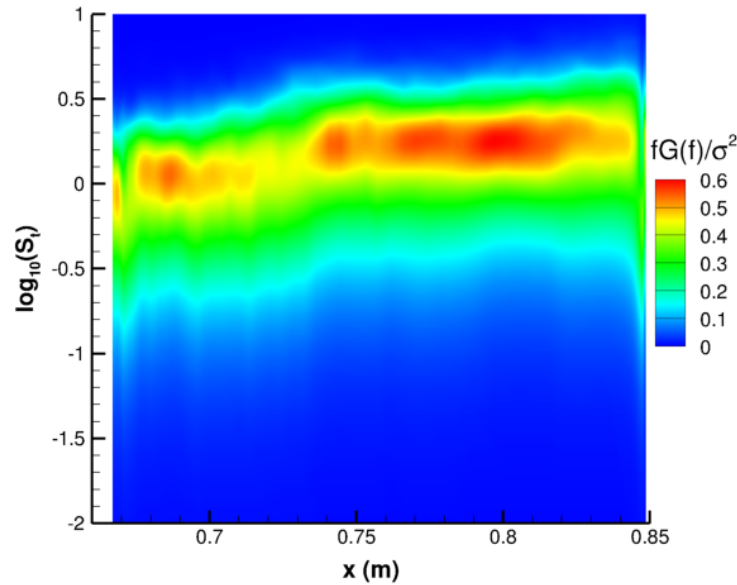
Figure 5.25. Premultiplied power spectral density contour for the complete windward elevon surface pressure response, in the spatial-frequency domain.

To further analyze the wall pressure signals, the power spectra at specific streamwise locations were extracted from the complete wall pressure spectra and are plotted in Figure 5.26. The spectra of four signals, ranging from the cove region to the trailing-edge of the elevon, located at $x = 0.68$ m, 0.69 m, 0.75 m, and 0.80 m, are plotted in Figure 5.26a. The power spectra for another four signals, inside of the cove environment and located at $y = \pm 2$ mm and $y = \pm 6$ mm, are provided in Figure 5.26b. The spectra for four signals, which are located at the trailing-edge of the elevon, $x = 0.8$ m, 0.82 m, 0.84 m, and 0.85 m, are provided in Figure 5.26c. Lastly, the power spectra for two signals near the cove, at $x = 0.665$ m and 0.70 m, and two signals from the trailing-edge, 0.82 m, and 0.85 m, are compared in Figure 5.26d.

The power spectra along the elevon are similar, displayed in Figure 5.26a, and are contained within the Strouhal number range of $0.1 \leq S_t \leq 5$. There are distinct peaks at $S_t = 0.2$ and $S_t = 0.4$ for the upstream locations, $x = 0.68$ m and $x = 0.7$ m. The time-averaged reattachment location, $x = x_r = 0.69$ m, contains lower frequency spectral content, between $0.08 \leq S_t \leq 0.4$, than the other three locations. The shift from low-to-high frequencies is also seen at the right-end of the spectra, depicted with the shift in trailing-edge spectra, between $x = 0.68$ m and $x = 0.8$ m, at frequencies of $S_t \geq 1$. This can also be seen in peak spectra locations for the $x = 0.75$ m and $x = 0.8$ m signals, which display spectra at frequencies twice as high as the upstream $x = 0.68$ m signal spectrum. The power spectra for signals inside of the cove, provided in Figure 5.26b, depict characteristically low-frequency dominated spectra. The spectra inside of the cove are confined to the Strouhal number range of $0.01 \leq S_t \leq 1$. Near the center of the cove, there are distinct peaks at very low-frequency peaks of $S_t = 0.04$. There are also modal peaks between $0.1 \leq S_t \leq 0.3$. There is little spectral content for these signals in the high frequency range of $S_t \geq 10$.

The wall pressure spectra at the trailing-edge of the elevon are plotted in Figure 5.26c. The power spectra in this region depict higher frequency spectral content, as well as distinct low-frequency peaks in similar ranges as those found upstream. These modal peaks correspond to Strouhal numbers of $S_t = 0.02$ and $S_t = 0.04$. At the trailing-edge, there is large unsteadiness attributed to the shedding of the turbulent boundary-layer and the flapping of the separated shear-layer. These spectra are compared to those upstream in Figure 5.26d.

The large difference in spectral content is depicted in this figure. There is a large concentration of spectral energy in the low-frequency range of $0.08 \leq S_t \leq 0.5$ for these signals. The shift from low-to-high frequencies, from upstream to the trailing-edge, is also depicted in this plot. The cove signal contains the largest majority of low-frequency spectra, followed by the reattachment position signal, the trailing-edge signal, and the far downstream elevon signal. Collectively, these plots display what was shown in Figure 5.25, with higher clarity. The shift from low-to-high frequencies depicts the propagation of turbulence along the re-developing boundary-layer. The similar peaks at low-frequencies found throughout the flow also highlight the influence of the low-frequency shock-motion.
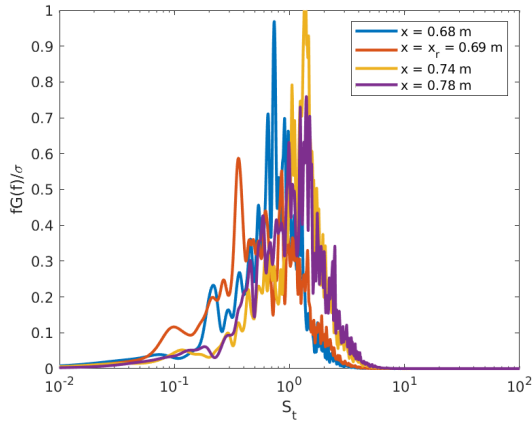
(a) $x = 0.68$ m, 0.69 m, 0.74 m, and 0.78 m.
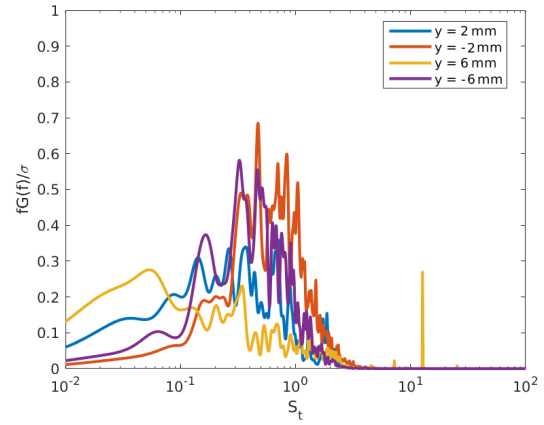
(b) $y = \pm 2$ mm and $y = \pm 6$ mm.
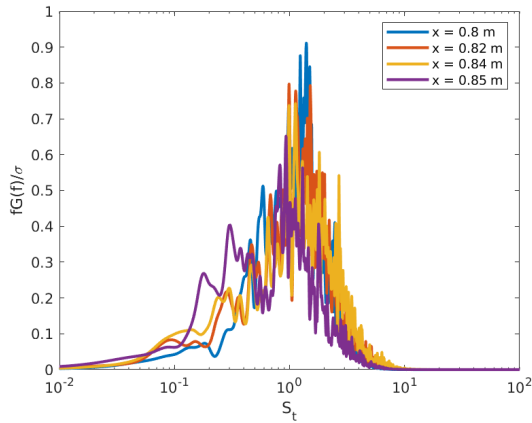
(c) $x = 0.8$ m, 0.82 m, 0.84 m, and 0.85 m.
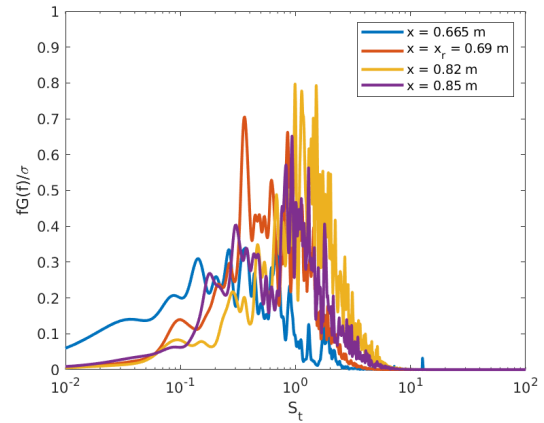
(d) $x = 0.665$ m, 0.69 m, 0.82 m, and 0.85 m

Figure 5.26. Premultiplied power spectral densities, $fG(f)/\sigma^2$, of wall pressure signals at various locations on the windward elevon surface.

Snapshots of specific frequencies in the wall pressure power spectra can highlight the frequency-dependent unsteady flow characteristics. In addition, by specifying a frequency, two-dimensional surface spectra can be displayed. Three power spectra snapshots are provided in Figure 5.27. This figure includes contours of premultiplied power spectral density, $fG(f)/\sigma^2$, for wall pressure spectra at low, moderate, and high frequencies. In order to highlight the low-frequency behavior, the Strouhal number $S_t = 0.07$ was used, corresponding to the frequency $f = 1.4$ kHz. The moderate frequency behavior is depicted with the Strouhal number of $S_t = 0.2$, corresponding to the frequency $f = 4$ kHz. The high frequency behavior is depicted with a Strouhal number of $S_t = 1.7$, corresponding to the frequency $f = 34$ kHz. For reference, the time-frame between the instantaneous snapshots provided in Figure 5.5 and Figure 5.6, is equivalent to a frequency of $f = 10$ kHz.

Collectively, these snapshots depict the resultant aerothermodynamic surface loading distributions that were apparent in the time-averaged heat flux plot shown in Figure 5.10a. The low-frequency power spectra, plotted in Figure 5.27a, displays the distinct nodal pattern at the flow entrainment region. This region is also associated with the low-frequency shockwave/boundary-layer interaction and the generation of coherent turbulent structures. This figure highlights the three nodal formations in the cove environment, which were observed in the time-averaged heat flux plot, Figure 5.10a, but not in the time-averaged pressure loading, Figure 5.9. Interestingly, these patterns are not symmetric in the span. There are also distinct streaks downstream of this location, which are associated with the Görtler vortices. The trailing-edge shows high levels of premultiplied power spectral density at this frequency, associated with the vortex shedding mechanism. The last two premultiplied power spectral density snapshots, shown in Figure 5.27b and Figure 5.27c, display the moderate and high frequency surface power spectra. These figures depict the spanwise loading patterns found at reattachment and the downstream streak formations. The upstream region is shown to contain larger power spectra magnitudes in moderate frequencies, compared to high frequencies, whereas the downstream region follows the opposite trend. This, once again, depicts the low-to-high frequency shift, upstream to downstream, which has been observed in spectra for relevant flows [54], [58], [90], [143], [144], [158].
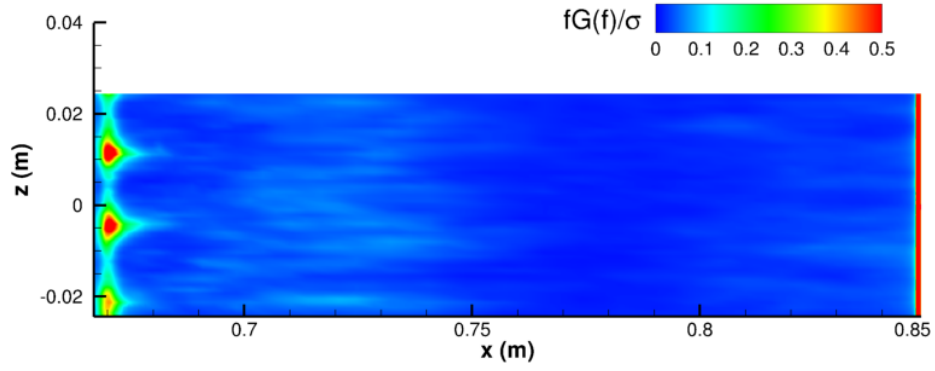
(a) $S_t = 0.07$.
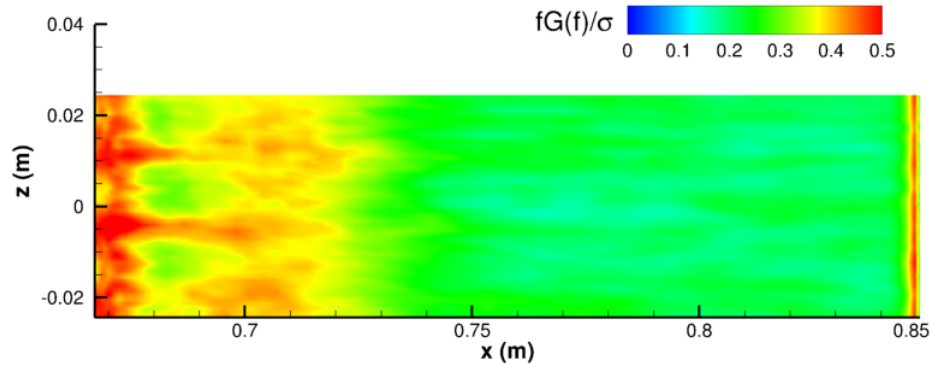
(b) $S_t = 0.2$.
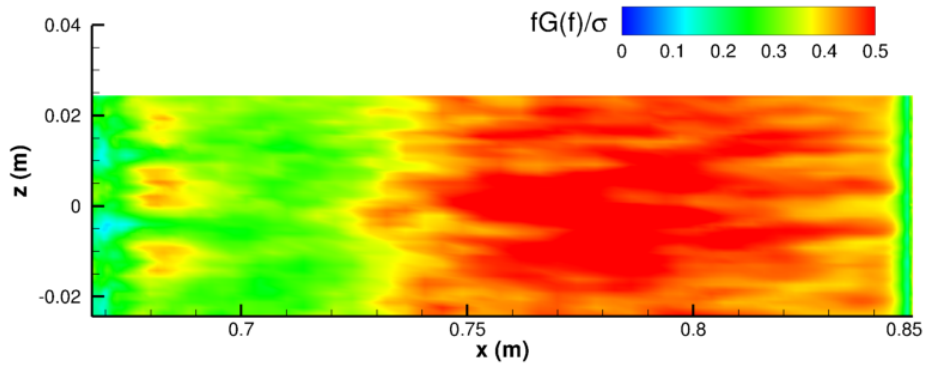
(c) $S_t = 1.7$.

Figure 5.27. Low, moderate, and high frequency snapshots of premultiplied power spectral density, $fG(f)/\sigma^2$, of wall pressure for the complete windward elevon surface.

5.4 Chapter Discussion

This project focused on the center portion of the scaled Purdue wing-elevon-cove model, in the UTSI TALon wind tunnel conditions. A three-dimensional model, provided in Figure 5.1, was created by extruding the surfaces of the centerline wing-elevon-cove cross-section. As a result, the wind tunnel surface, side-gaps, and wing-tip are ignored. However, doing so allows for a structured meshing approach, where focus region resolutions can be refined and carefully tuned. The mesh for this model was provided in Figure 2.10, and the freestream flow conditions were provided in Table 2.3. The UTSI TALon wind tunnel produces higher freestream, and cove, Reynolds numbers compared to the Purdue BAM6QT wind tunnel. This facilitated the onset of unsteadiness in the shock-wave/boundary-layer interaction, which allowed for the characterization of the unsteady flowfield.

The order of data presentation in this chapter followed time-averaged and instantaneous flow visualization, aerothermodynamic loading, and then unsteady signal analysis. The time-averaged centerline flow structure for this configuration is identical to the Purdue BAM6QT wing-elevon-cove computation. The unsteady instantaneous flowfield depicted the production, propagation, and growth of Görtler vortices downstream of the shock-wave/boundary-layer interaction. The Görtler vortices, which originate in the cove region, propagate and grow through the redeveloping boundary-layer, which eventually sheds from the trailing-edge of the model. The behavior of these vortices and their resultant effects on the flowfield, such as inducing non-homogonous spanwise surface loading distributions, were found to be consistent with similar findings on relevant flows [73], [85], [90], [91], [143].

The statistical analyses provided a comprehensive investigation of the unsteady fluctuations in the flowfield. The mechanisms that were investigated include the unsteady coherent motion of the shock-wave/boundary-layer interaction, and the generation, propagation, and growth of coherent turbulent structures. Cross-correlations in the flowfield depicted the coherent movement of the shock-system and of the trailing-edge shear-layer. In addition, there are large-scale correlations and coherences found in the redeveloping boundary-layer. The convection velocities associated with the redeveloping boundary-layer were in the range

$0.65 \leq U_c/u_\infty \leq 0.75$. These values are aligned with those found in the NASA wing-elevon-cove computation, as well as literature [188].

The premultiplied power spectral densities and coherences between unsteady fluctuations in the shock system displayed a primary Strouhal number range of $0.01 \leq S_t \leq 0.1$. This range is similar to the frequencies of the NASA wing-elevon-cove spectra, as well as other published shock-wave/boundary-layer interactions [149]–[151], [158], [159]. The premultiplied power spectral densities and coherences for fluctuations in the redeveloping boundary layer and regions of maximum heat flux were analyzed, as well, and depicted similar frequency ranges. The entire wall pressure power spectra was calculated and displayed a general shift from low-to-high frequencies along the elevon, which is consistent with literature [54], [58], [90], [143], [144], [158]. Several individual power spectra distributions on the windward elevon surface were also analyzed. The power spectra, at specified frequencies, depicts several unsteady flow characteristics. Three different frequencies were chosen, $S_t = 0.07$, 0.2, and 1.7, which represent the low, moderate, and high frequency spectra. These snapshots provided further evidence of the frequency behavior of the flow discussed throughout this chapter. Collectively, the flowfield and surface loading visualizations presented in this chapter, as well as the unsteady statistical analyses, provide the characteristics for this hypersonic wing-elevon-cove flow.

This project improved on the configuration faults of the NASA wing-elevon-cove computation, such as downstream grid-stretching, and provided additional statistical analyses. Such improvements include better mesh quality and new, or improved, data analysis techniques. The refined mesh, compared to the NASA wing-elevon-cove mesh, allowed for the propagation of turbulence in the redeveloping boundary-layer to be studied. Improved data analysis also provided enhanced insight into the unsteady flow characteristics. At the time of writing, there are currently no experimental data available for this wing-elevon-cove configuration. However, the UTSI experimental team is currently running ongoing wind tunnel experiments on this model. As a result, the data produced from this project can be used to aid experimentalists and may possibly be published in future works. Overall, this work provides fundamental research on hypersonic wing-elevon-cove flows and unsteady shock-wave/boundary-layer interactions, similar to the previous two projects.

6. CONCLUSION

The accurate characterization of hypersonic flows is required for the development of hypersonic flight vehicles. For example, the reliable prediction of aerothermodynamic loads in the hypersonic regime is critical for thermal protection and material design [2], [3], [40], [41], [43], [197], [198]. Hypersonic flowfields are often complex, three-dimensional, and introduce a plethora of phenomena, such as shock-wave/boundary-layer interactions. These interactions influence vehicle performance by introducing large-scale flow separation, unsteadiness, and increased aerothermodynamic loading [7], [8], [69], [160], [187]. The low-frequency unsteady motion of the shock system and boundary-layer reattachment produce intense fluctuations in local surface loading, which can lead to structural failure. Consequently, this low-frequency shock-motion is a research topic many in the aerospace community have focused on [46], [50], [52]–[54], [71], [144], [156], [157], [159]. By studying and characterizing the nature of shock-wave/boundary-layer interactions, such as the mechanisms that control unsteadiness and the production of turbulent structures, a better understanding of the design requirements for hypersonic flight vehicles can be obtained.

The computational capability to simulate these interactions has significantly advanced over the last century [108]–[110], [199]. However, unsteady hypersonic shock-wave/boundary-layer interactions require high fidelity computational tools, such as large-eddy simulation or detached-eddy simulation, to accurately model. Steady-state computations of these interactions do not fully characterize the relevant flow behavior, i.e., the unsteady shock-motion and its resultant effect on the flowfield and aerothermodynamic loading. The large computational costs associated with higher fidelity methods, however, routinely leads to the idealization of models and configurations in research studies. This idealization may ignore local geometric imperfections, such as gaps or cavities, which can strongly affect both the mean and instantaneous flowfields. Experimental studies often idealize the geometry of models as well, due to physical experimental limitations [9]–[13]. Therefore, there is an increasing need for computational and experimental studies focused on hypersonic flight vehicle geometric imperfections. As a result, the overall goal of this dissertation was to provide comprehensive research and analysis on this topic.

This research involved a computational investigation into hypersonic wing-elevon-cove flows. This investigation included three projects associated with various wing-elevon-cove models and flow conditions, in order to cover a range of configurations. Each computation employed improved delayed-detached eddy simulation to achieve high fidelity results in focus regions, i.e., the cove juncture. The overall goal of the research was to analyze the flow behavior and characteristics of these configurations. The characterization of these flows was provided by flowfield visualizations, depiction of aerothermodynamic loadings, and statistical analysis of unsteady flow fluctuations. The primary focus region was the cove at the edge of the juncture of the main wing element and the elevon. This region could be considered a geometric imperfection, from the perspective of aerodynamics, and contains the shock-wave/boundary-layer interaction produced by the control surface deflection and the centrifugal Görtler instability. The last two wing-elevon-cove computations were done in collaboration with the Purdue and UTSI experimental teams. While experimental data were not included, for the most part, the work here has facilitated experimental research efforts and may be employed in future published works.

The discussion of the collective works presented in this dissertation is provided in this chapter. As such, the three wing-elevon-cove projects are overviewed and compared. By discussing the various similarities and differences, the characteristic behaviors of these flows can be inferred. These discussions allow for larger context to be drawn from the associated research projects, as well. At the end of the chapter, the discussion of how this research could be expanded or improved is provided, followed by several closing concluding remarks.

6.1 Research Overview

The following section provides an overview and discussion of the three hypersonic wing-elevon-cove flows presented in this dissertation. The first project involved the computation of the NASA experimental study, detailed in Chapter 3. The second project involved the computation of, and the associated experiment on, the Purdue swept wing-elevon-model in the Purdue BAM6QT wind tunnel conditions, detailed in Chapter 4. Lastly, the third

project involved the computation of, and the associated experiment on, the scaled Purdue model in the UTSI TALon wind tunnel conditions, detailed in Chapter 5.

6.1.1 NASA Wing-Elevon-Cove

This first project focused on the 1978 experimental study conducted by NASA engineers W.D. Deveikis and W. Bartlett [42]. In these experiments, a wing-elevon-cove model was employed in hypersonic flow to simulate the windward surface of a shuttle-type reentry vehicle. A total of 41 tests were done by Deveikis and Bartlett, which focused on the aerothermodynamic loading on the interior and exterior wing and elevon surfaces. The improved delayed detached-eddy simulation produced excellent agreement with the experimental data. Grounded with the agreement with mean surface data, this project expanded on the topics explored in the NASA experimental study, to include topics such as flow visualization and statistical analysis.

As the upstream boundary-layer separates at the cove, a region shock-wave/boundary-layer interaction is created, consisting of an expansion-fan, a shear-layer, a separation vortex, and a shock-wave. The pressure gradient imparted by the cove environment produces significant flow entrainment. The shock-wave/boundary-layer interaction exhibits unsteady behavior, such as large-scale distortions in the shock-wave. The three-dimensional Görtler vortices in the redeveloping boundary-layer originate in this region and propagate downstream. The downstream elevon spanwise surface loading is non-homogenous, as a result of the Görtler vortices, and the flow contains characteristic heat flux streaks. Görtler vortices, and these associated streaks, are often found in hypersonic shock-wave/boundary-layer interactions that are induced by surface deflection [73], [85], [90], [91], [143].

The energy in the shock-wave/boundary-layer interaction spectra for this wing-elevon-cove flow was primarily contained within the low-frequency Strouhal number range of $0.02 \leq S_t \leq 1$. This range corresponds to the dimensional frequency range of $2 \leq f \leq 100$ kHz. These non-dimensional frequency ranges have been reported for compression ramp flows and various shock-wave/boundary-layer interactions [149]–[151], [158], [159]. Low-frequency spectra were also found inside of the cove region. There is then a shift from low-to-high fre-

quencies at reattachment, followed by a gradual decrease in spectral frequencies downstream. It is unknown if this behavior is affected by the grid stretching and consequent damping of turbulence. In the UTSI TALon computation, there is a shift to higher frequencies downstream of reattachment, which has been observed in spectra for relevant flows [54], [58], [90], [143], [144], [158].

6.1.2 Purdue BAM6QT Wing-Elevon-Cove

The second project was done in collaboration with the Purdue experimental team. The computation for this project simulated the Purdue swept wing-elevon-cove model in the Purdue BAM6QT wind tunnel conditions. Compared to the two other wing-elevon-cove configurations, the full Purdue model introduced increased three-dimensionality, such as the side gap regions and the surrounding wind tunnel surface. The initial research goal was to compare the computational results to the experimental wind tunnel data. This was not accomplished due to the overall timing of the projects. However, this research provided practical flow visualization and aerothermodynamic loading analysis for this hypersonic wing-elevon-cove configuration.

There is significant flow three-dimensionality present in this flowfield. A three-dimensional lambda shock-wave/boundary-layer interaction forms around the swept wing-elevon-cove model and the surrounding wind tunnel surface. This depicts the similarity of this configuration to hypersonic blunt-fin interactions [167]–[174], [180]–[182]. Large-scale vortex structures are produced in several regions near the model surface. The vortices at the leeward elevon surface are produced by the flow entrainment through gap regions. At the top of the model, the wing-tip vortices are created through the flow entrainment of the surrounding surface boundary-layers. These vortices induce distinct streaks of locally high aerothermal heating on the wing-elevon-cove surface, which have also been experimentally validated.

The improved delayed detached-eddy simulation was unable to resolve significant unsteadiness in the shock-wave/boundary-layer interaction at the cove juncture. While the computation did not produce unsteadiness, experimental data did show low-frequency spectra inside of the cove; however, the overall unsteadiness in the shock-wave/boundary-layer

161

interaction was low. A parametric sweep was done by modifying various geometric parameters and flow conditions. These modifications significantly affected the flow structure, resultant aerothermodynamic loading, and flow unsteadiness. In general, the parametric sweep computations with stronger shock-wave/boundary-layer interactions, or significantly higher cove Reynolds numbers, Re_{cove}, successfully produced unsteady shock-wave/boundary-layer interactions. This outcome is consistent with literature findings [88], [163], [164].

6.1.3 UTSI TALon Wing-Elevon-Cove

The final project involved a computational investigation of the scaled Purdue wing-elevon-cove model. The UTSI TALon Mach 4 Ludwieg tube experimental flow conditions were utilized in the computation. One goal of this work was to aid and collaborate with ongoing UTSI experimental efforts. The other goal was to conduct comprehensive statistical analysis on the unsteady flowfield for the Purdue model, which was not possible with the Purdue BAM6QT wind tunnel conditions. The computational surface model consisted of only the center portion of the full swept wing-elevon-cove model, omitting the side gap regions and the surrounding wind tunnel surface. This reduction of the computational domain allows for more precise meshing and data collection, comparatively to unstructured T-Rex hybrid meshing [200]. It was also shown, in the second project, that the centerline flow for the full swept wing-elevon-cove model was not strongly affected by the side gap entrainment regions.

The UTSI TALon flow conditions produce higher freestream and cove Reynolds numbers compared to the Purdue BAM6QT wind tunnel, which facilitated the onset of unsteadiness in the shock-wave/boundary-layer interaction. The time-averaged flow structure is similar in nature to the previous wing-elevon-cove computations. The unsteady instantaneous flowfield depicted the production, propagation, and growth of Görtler vortices in the redeveloping boundary-layer. These structures were also observed to have significant effect on the resultant aerothermodynamic loading, producing non-homogonous spanwise surface loading distributions, which is consistent with similar flows [73], [85], [90], [91], [143].

The statistical analyses done for this project focused on the unsteady fluctuations in the shock-wave/boundary-layer interaction, along surfaces, and in the redeveloping boundary-

layer. The shock-wave/boundary-layer interaction spectra was contained within the Strouhal number range of $0.01 \leq S_t \leq 0.1$, corresponding to the dimensional frequency range of $0.2 \leq f \leq 2$ kHz. These non-dimensional frequency ranges are consistent with the spectra for the NASA wing-elevon-cove and other published shock-wave/boundary-layer interactions [149]–[151], [158], [159]. There is a shift from low-to-high frequencies in the wall pressure spectra downstream of reattachment, from moderate frequencies of $0.6 \leq S_t \leq 1$ to higher frequencies of $1.13 \leq S_t \leq 2.4$, which is also consistent with published data.

6.2 Comparison of Wing-Elevon-Cove Flows

The three research projects presented in this dissertation provided a computational investigation into hypersonic wing-elevon-cove flows. This was done, as a collective effort, to produce research and analysis on geometric imperfections, from the perspective of aerodynamics, in hypersonic flight vehicles. The computational tool employed for all three projects was improved delayed detached-eddy simulation, which employs large-eddy simulation in focus regions, i.e., the cove juncture. These flows, in general, were shown to produce similar flow characteristics, behavior, and aerothermodynamic loading distributions. For example, the shock-wave/boundary-layer interactions produced increased aerothermodynamic loading downstream of the cove in all projects, as expected. The components of the shock systems for all wing-elevon-cove computations include the shock-wave, separated shear-layer, separation vortex, secondary separation vortex, boundary-layer separation/reattachment, and cove flow entrainment. The NASA and UTSI TALon wing-elevon-cove computations also depict large similarities in the unsteady flow behavior and the low-frequency spectra of the shock-wave/boundary-layer interaction.

There were also qualitative and quantitative differences for these wing-elevon-cove computations. This is primarily attributed to the large range of freestream conditions and wing-elevon-cove geometries and scales. For instance, the non-zero angle of attack for the NASA wing-elevon-cove produced significant effects on the local cove juncture flow, which were not seen in the other two computations. Additionally, as a consequence of the lack of unsteadiness in the computation, the unsteady flowfield could not be characterized for the

Purdue BAM6QT wing-elevon-cove computation. Therefore, structures such as Görtler vortices, which are produced by the streamline curvature in the separated shear-layer, were only present in the NASA and the UTSI TALon wing-elevon-cove computations. The Purdue BAM6QT swept wing-elevon-cove model did, however, introduce increased three-dimensionality compared to the other two projects. This complexity led to additional flow phenomena, such as a three-dimensional lambda shock-wave/boundary-layer interaction and large-scale vortex formations, which were not present in the NASA and UTSI TALon wing-elevon-cove computations.

While all surface models used in these projects consist of wing-elevon-cove configurations, each project model contains different geometric features. The NASA experimental wing-elevon-cove model consisted of a flat plate wing, downstream elevon, and a comparatively complex cove environment. This model was also angled, relative to the freestream, to produce the angle of attack. The model represented the windward wing-elevon-cove surface of a shuttle-type reentry vehicle. As a result, the leeward side of the model was not simulated in the computation. The Purdue swept wing-elevon-cove model was utilized for the Purdue BAM6QT and UTSI TALon computations. However, the full model was employed in the Purdue BAM6QT computation, whereas the centerline portion of the scaled model was used in the UTSI TALon computations. The scaled model used in the UTSI experiments and computations was approximately twice the size of the Purdue model. The NASA wing-elevon-cove model was the largest of three, with a wing-elevon span of 1.85 m. The Purdue BAM6QT and UTSI TALon wing-elevon spans were 0.4 m and 0.8 m, respectively.

A structured meshing approach was applied to the NASA and UTSI TALon computational meshes, whereas a hybrid T-Rex unstructured meshing approach was used for the full swept wing-elevon-cove. T-Rex hybrid unstructured meshing incorporates structured meshing near surfaces and allows for higher fidelity results, compared to pure unstructured meshes; however, this technique reduces the overall computational fidelity compared to a completely structured mesh. The NASA and UTSI TALon computations employed periodic side boundary conditions at each side of the computational domain, whereas the Purdue BAM6QT computation simulated the entire three-dimensional flowfield. Each mesh, however, used approximately 230-250 million cell volumes, which was associated with the limit

on mesh size for Kestrel KCFD at the time. All surfaces for every computation had high near-wall resolution, with $\Delta y^+ \leq 1$. The mesh for the NASA wing-elevon-cove had cove region grid spacings, in inner coordinates, of $\Delta x^+ \approx 70$, $\Delta y^+ \approx 60$, and $\Delta z^+ \approx 80$. These spacings are held nearly constant in the focus region, however, the grid is stretched downstream of reattachment with a ratio of 1.2. This has shown to damp out the propagation of turbulence in the flow, which was resolved in the meshing for the UTSI TALon wing-elevon-cove computation. The full three-dimensional swept wing-elevon-cove model used in the Purdue BAM6QT computations employed T-Rex hybrid unstructured meshing. Because of the complicated structure of this model near the deflected elevon, grid spacing is not held constant, which may have affected the improved delayed detached-eddy simulation numerical fidelity. Unfortunately, due to mesh volume size limitations in KCFD, further refinement was not possible. The grid spacings, in inner coordinates, for the focus regions, ranged from $\Delta x^+ \approx 50 - 200$, $\Delta y^+ \approx 80 - 160$, and $\Delta z^+ \approx 70 - 300$. The mesh for the UTSI TALon computations consisted of only the center portion of the Purdue swept wing-elevon-cove model, which facilitated structured meshing and data collection. In the focus regions, the grid spacings, in inner coordinates, were $\Delta x^+ \approx 50$, $\Delta y^+ \approx 50$, and $\Delta z^+ \approx 60$. These values are similar to those for the NASA wing-elevon-cove, however, this spacing was held constant along the entire downstream elevon. The NASA and UTSI TALon wing-elevon-cove mesh spacings are aligned with the required resolution of large-eddy simulation [118], [128], [129]. These mesh properties are collectively tabulated, for reference, in Table 6.1.

Table 6.1. Mesh properties for the NASA, Purdue BAM6QT, and UTSI TALon wing-elevon-cove computations.

Parameter	NASA	BAM6QT	TALon
Volume Cells (million)	230	250	250
Δy_w^+	≤ 1	≤ 1	≤ 1
Δ_{max} (m)	5×10^{-4}	1×10^{-3}	2×10^{-5}
Δx^+	80	$50 - 200$	50
Δy^+	60	$80 - 160$	50
Δz^+	80	$70 - 300$	60

Each of the wing-elevon-cove computations utilized hypersonic wind tunnel flow conditions. The NASA Langley wind tunnel conditions used in the computation correspond to Mach 6.9 flow at a unit Reynolds number of $Re = 4.29 \times 10^6$ m^{-1}. The Purdue BAM6QT wind tunnel conditions correspond to Mach 6 flow at a unit Reynolds number of $Re = 1.10 \times 10^7$ m^{-1}, and the UTSI TALon wind tunnel conditions correspond to Mach 4 flow at a unit Reynolds number of $Re = 1.80 \times 10^7$ m^{-1}. The NASA wing-elevon-cove is the only configuration with an angle of attack relative to the freestream. During the computational parametric sweep associated with the Purdue BAM6QT project, it was found that non-zero angles of attack facilitated the onset of unsteadiness at the cove by introducing larger pressure gradients between the windward and leeward surfaces. The NASA model also employed the largest elevon deflection angle, 15 deg, compared to the 12 deg deflection used for the Purdue BAM6QT and UTSI TALon wing-elevon-cove computations. The remainder of the relevant freestream and configuration properties for the three computations are tabulated in Table 6.2.

Table 6.2. Freestream and configuration properties for the NASA, Purdue BAM6QT, and UTSI TALon wing-elevon-cove computations.

Parameter	NASA	BAM6QT	TALon
M_∞	6.86	6	4
$T_{o,\infty}$ (K)	2300	433	295
$P_{o,\infty}$ (kPa)	7030	1034	483
u_∞ (m/s)	2040	874	672
Re_∞ (m^{-1})	4.29×10^6	1.10×10^7	1.90×10^7
$Re_{x,\text{cove}}$	6.15×10^6	3.50×10^6	1.14×10^7
α (deg)	-12	0	0
δ_f (deg)	15	12	12

The flow structures for the three hypersonic wing-elevon-coves are predominately similar. The three different configurations depicted the same flow phenomena and shock-wave/boundary-layer interaction components. These include the shock-wave, separated shear-layer, primary/secondary separation vortices, and boundary-layer separation/reattachment. The time-averaged reattachment positions for the three computations, measured from the centerline separation point on the wing surface, were $\overline{L_r} = 20$ mm, 12 mm, and 30 mm,

respectively. The NASA configuration boundary-layer thickness at the cove, $\delta_{\text{cove}} = 21.6$ mm, was within the same magnitude as the cove length and has a ratio of boundary-layer thickness to cove length of $\delta/L_{\text{cove}} = 1.6$. Comparatively, the Purdue swept wing-elevon-cove model computations have larger ratios of $\delta/L_{\text{cove}} = 6.0$ and $\delta/L_{\text{cove}} = 5$, corresponding to the Purdue BAM6QT and UTSI TALon computations, respectively. The boundary-layer heights for these computations were $\delta_{\text{cove}} = 15.6$ mm and $\delta_{\text{cove}} = 30$ mm, respectively. The angle of attack in the NASA configuration moves the relative reattachment position upstream. For the other two wing-elevon-cove computations, the separation region extends farther onto the downstream elevon surface. The structure of these separation vortices varies between the three configurations, due to the local cove geometry and overall flow conditions. The separation vortex for the NASA wing-elevon-cove computation is the largest and most rounded, comparatively, and spans 20 mm by 20 mm. The separation vortices for the Purdue swept wing-elevon-cove computations are more narrow, due to local geometry at the cove. For the Purdue BAM6QT computation, the separation vortex spanned 12 mm by 1.5 mm, and for the UTSI TALon computation, the vortex spanned 30 mm by 3 mm. These flow structure properties are tabulated in Table 6.3.

Table 6.3. Cove region mean flow parameters for the NASA, Purdue BAM6QT, and UTSI TALon wing-elevon-cove computations.

Parameter	NASA	BAM6QT	TALon
δ_{cove} (mm)	21.6	15.6	30
$\delta_{\text{cove}}/L_{\text{cove}}$	1.6	6	5
$\overline{L_r}$ (mm)	20	12	30
Separation (mm x mm)	20×20	12×1.5	30×3

The resultant aerothermodynamic loadings were analyzed for each of the three wing-elevon-cove computations. To facilitate comparison, the reported surface loading parameters in this section are non-dimensionalized by reference aerothermodynamic loadings located at the upstream trailing-edge of the wing, $\dot{q}_{\text{ref}}$ and P_{ref}. The reference values for the NASA wing-elevon-cove computation correspond to $\dot{q}_{\text{ref}} = 205$ kW/m^2 and $P_{\text{ref}} = 10.16$ kPa. The reference values for the Purdue BAM6QT computation are $\dot{q}_{\text{ref}} = 1400$ W/m^2 and $P_{\text{ref}} = 500$ Pa, and the reference values for the UTSI TALon computation are $\dot{q}_{\text{ref}} = 950$ W/m^2 and

$P_{ref} = 3000$ Pa. All of these relevant aerothermodynamic loading parameters are tabulated in Table 6.4.

The surface pressure loading for all three wing-elevon-cove computations follow expected trends for hypersonic compression ramp interactions [149]–[151], [158], [159]. For each computation, there was little spanwise variation found in the time-averaged surface pressure distributions, compared to other surface loading variables. The general trend in the surface pressure distributions follows a consistent exponential increase through the shock-wave/boundary-layer interaction, until global maxima are reached at the trailing-edge. The non-dimensional surface pressure maxima were nearly identical for each computation. The pressure maxima for the NASA, Purdue BAM6QT, and UTSI TALon wing-elevon-cove computations were $P_{max}/P_{ref} = 3$, $P_{max}/P_{ref} = 4$, and $P_{max}/P_{ref} = 3.5$, respectively.

The aerothermal loading for the three wing-elevon-cove computations showed significant variations. In the NASA wing-elevon-cove computation, the non-dimensional heat flux at reattachment was $\dot{q}_{ret}/\dot{q}_{ref} = 2.25$. The aerothermal heating continued to increase along the elevon, downstream of reattachment, until the global maximum, $\dot{q}_{max}/\dot{q}_{ref} = 2.8$, was reached. The three-dimensional flowfield in the Purdue swept wing-elevon-cove computation produced locally high aerothermal regions, such as the vortex-induced heat flux streak, which were not present in the other computations. These regions reached non-dimensional heat flux values as high as $\dot{q}_{max}/\dot{q}_{ref} = 8$. For this computation, the aerothermal heating in the cove region was low, but there was an exponential rise in heat flux through the flow entrainment region until reattachment. The non-dimensional heat flux at reattachment reached $\dot{q}_{ret}/\dot{q}_{ref} = 1.6$. The heat flux continued to increase along the elevon and eventually reached a local maximum value of $\dot{q}/\dot{q}_{ref} = 4$ at the trailing-edge. For the same centerline portion of the model, the UTSI TALon conditions produced different aerothermal loading distributions, as a result of the unsteady shock-wave/boundary-layer interaction and the turbulent flowfield. There was a local maxima non-dimensional heat flux, $\dot{q}/\dot{q}_{ref} = 0.9$, near the region of rapid flow entrainment. At reattachment, the non-dimensional heat flux reached $\dot{q}_{ret}/\dot{q}_{ref} = 1.2$. The heat flux continued to increase along the elevon, where non-homogeneous spanwise streak develops due to the unsteady Görtler vortices. Halfway along the elevon, the non-dimensional heat flux reached local maxima of $\dot{q}/\dot{q}_{ref} = 4$. Afterward, the heat flux on the elevon began

to rapidly increase, as opposed to the NASA and Purdue BAM6QT computations, which is caused by the unsteady shedding of the boundary-layer. The global heat flux maximum, located at the trailing-edge, was equal to $\dot{q}_{max}/\dot{q}_{ref} = 10$.

Table 6.4. Aerothermodynamic loading parameters for the NASA, Purdue BAM6QT, and UTSI TALon wing-elevon-cove computations.

Parameter	NASA	BAM6QT	TALon
P_{ref} (kPa)	10.16	0.5	3
$\dot{q}_{ref}$ (kW/m^2)	205	1.4	0.95
P_{max}/P_{ref}	3	4	3.5
$\dot{q}_{ret}/\dot{q}_{ref}$	2.25	1.6	1.2
$\dot{q}_{max}/\dot{q}_{ref}$	2.8	8	10

In the three hypersonic wing-elevon-cove flows, the separated shear-layer at the cove region produces streamline curvature. This streamline curvature is associated with a centrifugal instability and the production of Görtler vortices. Coincidentally, the computation with the lowest Görtler, $\mathcal{G}$, corresponded to the Purdue BAM6QT wing-elevon-cove, which did not produce unsteadiness. The average Görtler numbers at reattachment for the NASA, Purdue BAM6QT, and UTSI TALon wing-elevon-cove computation were $\mathcal{G}_{ret} = 6.4$, 1.5, and 3.4, respectively. However, using the curvature of the interior cove flow entrainment streamlines provides higher Görtler numbers of $\mathcal{G}_{ent} = 8.2$, 3.5, and 7.2, respectively.

For the unsteady NASA and UTSI TALon computations, the mechanisms of turbulence structure generation are associated with the centrifugal instability, caused by streamline curvature, as well as the Kelvin-Helmholtz instability in the separated shear-layer. For the NASA wing-elevon-cove computation, the separated shear-layer is deflected downward, which produces large streamline curvature. This is likely associated with the production of Görtler vortices for this flow. Alternatively, the flow entrainment region was shown to be associated with the production of Görtler vortices in the UTSI TALon wing-elevon-cove computation. The approximate initial distance between adjacent spanwise Görtler vortices, λ, in the NASA and UTSI TALon wing-elevon-cove redeveloping boundary-layers were $\lambda = 10$ mm and $\lambda = 5$ mm, respectively. The space between adjacent Görtler vortices increases downstream as the vortices merge into fully-developed turbulent boundary-layers. The Görtler growth

rates, σ, which can be approximated with the increased aerothermal heating produced by the Görtler vortices, were $\sigma = 2.2$ and $\sigma = 1.2$ for the NASA and UTSI TALon wing-elevon-cove computations, respectively. The relevant Görtler centrifugal instability parameters for the NASA and UTSI TALon wing-elevon-cove computations are provided below in Table 6.5.

Table 6.5. Görtler centrifugal instability parameters for the NASA and UTSI TALon wing-elevon-cove computations.

Parameter	NASA	TALon
$\mathcal{G}$, reattachment	6.4	3.4
$\mathcal{G}$, entrainment	8.2	7.2
λ (mm)	10	5
σ	2.2	1.2

The unsteady characteristics of the flow can be further compared for the NASA and UTSI TALon wing-elevon-cove computations. All of the relevant information for these statistics discussed here are provided in Table 6.6. The characteristic frequencies, associated with the unit Strouhal number, are $f_c = 100$ kHz, for the NASA wing-elevon-cove computation, and $f_c = 20$ kHz, for the UTSI TALon wing-elevon-cove computation. Both of the wing-elevon-cove computations produced low-frequency unsteady shock-wave/boundary-layer interactions. Space-time cross-correlations in these flows depicted similar coherent movement of components of the shock system, which include shear-layer flapping, separation vortex expansion and contraction, and shock-wave oscillation. The convection velocities, calculated with wall pressure space-time correlations, in each flow were similar in magnitude. These values range $0.6 \leq U_c/u_\infty \leq 0.75$ in redeveloping boundary-layer and $0.3 \leq U_c/u_\infty \leq 0.5$ in the shock-wave/boundary-layer interaction, and are within the same convection velocity range for similar flows [152]–[154].

While both wing-elevon-cove computations employ largely different configurations and flow conditions, the spectra display significant similarities. The power spectra for the unsteady shock-wave/boundary-layer interaction in the NASA wing-elevon-cove computation were contained in the Strouhal numbers in the range of $0.01 \leq S_t \leq 1$. Similarly, the frequencies in the shock-wave/boundary-layer interaction for the UTSI TALon wing-elevon-cove computation were contained in the Strouhal number range of $0.05 \leq S_t \leq 2$. Co-

herences of signals in these regions also produced peaks in these frequency ranges. These ranges are consistent with the spectra report for similar hypersonic compression ramp shock-wave/boundary-layer interactions [149]–[151], [158], [159]. Instantaneous flowfield visualizations of the cove region depicted unsteady coherent movement of the shock system and the generation of turbulent structures in the same frequencies, as well.

The wall pressure spectra for each computation, however, produced diametrically different results. For the NASA wing-elevon-cove computation, the wall pressure spectra exhibited similar low-frequency behavior in the cove as the shock-wave/boundary-layer interaction, in the Strouhal number range $0.01 \leq S_t \leq 1$. The spectra shift to higher frequencies at reattachment, in the Strouhal number range of $0.1 \leq S_t \leq 2$, and then back to lower frequencies of $0.05 \leq S_t \leq 1$ downstream. In the UTSI TALon wing-elevon-cove computation, the wall pressure spectra in the cove depict low-frequencies of $0.01 \leq S_t \leq 0.1$. At reattachment, the spectra are contained within the Strouhal number range of $0.1 \leq S_t \leq 2$. The spectra shift to higher frequencies of $0.5 \leq S_t \leq 5$ downstream, rather than back to lower frequencies. Additional evidence in the UTSI TALon wing-elevon-cove statistical analyses, as well as in literature [54], [58], [90], [143], [144], [158], support this the shift from low-to-high frequencies downstream. Due to the NASA wing-elevon-cove grid stretching, and the contradictory literature data, it can be concluded that the characteristic nature of the unsteady flow is more accurately depicted in the UTSI TALon wing-elevon-cove computation.

Table 6.6. Unsteady flowfield characteristics for the NASA and UTSI TALon wing-elevon-cove computations.

Parameter	NASA	TALon
f_c (kHz)	100	20
U_c/u_∞, shock system	0.3 - 0.4	0.3 - 0.5
U_c/u_∞, downstream elevon	0.6 - 0.7	0.65 - 0.75
S_t, shock system	0.01 - 1	0.05 - 2
S_t, cove	0.01 - 0.1	0.01 - 1
S_t, reattachment	0.1 - 2	0.1 - 2
S_t, downstream elevon	0.05 - 1	0.5 - 5

6.3 Future Investigation

This dissertation attempted to provide a characterization of hypersonic wing-elevon-cove flows through a computational investigation of three projects. The work for these projects could be expanded in several meaningful ways. One of which is future collaboration with experimental studies. While the final projects related to the Purdue swept wing-elevon-cove were meant to be compared with experimental data, the overall timing of the projects were not aligned. However, while the experiments at Purdue and UTSI are still ongoing, the data provided by this work can be used for comparison in future published works.

Improved meshing and computational models could provide increased accuracy and fidelity of these computations. For instance, while it was not possible to create a completely structured mesh for the Purdue BAM6QT computations, unstructured meshing has shown to have computational accuracy issues [133], [200], [201]. In addition, wall-resolved large-eddy simulation, or direction numerical simulation, could also be employed for a further increase in numerical fidelity. However, these methods would be extremely costly for the computations in this dissertation and would not be worth the extra computational hours needed for the small increase in fidelity achieved.

This research could be expanded by implantation of new techniques. For example, upstream turbulence in the boundary-layer has shown to be correlated with shock-wave/boundary-layer interaction unsteadiness [46], [62], [71], [72]. Simulations have shown that using synthetic turbulence in detached-eddy simulation can produce quality turbulence statistics [202], [203]. Haryl Ngoh, of Purdue University, is working on injecting synthetic turbulence into improved delayed detached-eddy simulations of shock-wave/boundary-layer interactions [63], [204]. His work has shown that while synthetic turbulence injection has little effect on mean and root-mean-square fluctuations of primitive flow variables, there were differences in the shock-wave/boundary-layer interaction statistical analysis. The characteristic behavior of these flows could be further analyzed with this technique, where the data presented in this thesis could provide baseline results.

Additional examples of future investigations come from suggestions made by reviewers of the published works associated with these results [78], [138]–[140], [162]. It has been

noted that wall temperature may prove to be a disparity in computations. All three projects employed wall temperatures at a room temperature value of $T_w = 293.15$ K. It is possible that there might be discrepancy in wall temperatures when comparing to experimental data. Research has shown that aerodynamic surface quantities do in fact show a small sensitivity to wall temperature, which would impact the flow statistics [205]. Even more so, the wall temperatures would reach adiabatic temperatures in representative flight conditions, which are much higher. A fluid-structure interaction approach could also be applied, in order to determine the effect of surface heat conduction on the unsteady flowfield [49], [206], [207].

The work in this dissertation could also be expanded to cover a larger range of flowfields. The primary focus of this research was on configurations with strong elevon deflection, i.e., 15 deg and 12 deg. There was not a thorough analysis done for lower elevon deflections, which occur more frequently on realistic flight vehicles [208], [209]. The last two projects were done at zero angle of attack to facilitate wind tunnel collaboration. Large angles of attack have shown to produce stronger shock-wave/boundary-layer interactions and unsteadiness, as depicted with the NASA wing-elevon-cove computation. The three projects revolved around wing-elevon-cove computations which were directly associated with wind tunnel configurations. As a result, a thorough analysis centered on flight conditions, as opposed to wind tunnel conditions, was not done. An investigation of flight Reynolds numbers would provide further context for hypersonic wing-elevon-cove flows. For instance, a parametric sweep of different flight conditions, elevon deflections, and angles of attack could provide flow characterization for a representative flight trajectory. Collectively, these are just some examples of the many research avenues which could be explored to expand on this work.

6.4 Concluding Remarks

This dissertation provided a computational investigation of three separate wing-elevon-cove flowfields. The computational tool employed was improved delayed detached-eddy simulation, which produced high fidelity results for reasonable computational cost. These flows were extensively visualized, analyzed, and discussed throughout this dissertation. A large focus was on the resultant aerothermodynamic loading and the unsteady shock-

wave/boundary-layer interaction at the cove. A large amount of this work has been previously published [138]–[140], [162], and the rest is in the process of publication review. The general research goal for this dissertation was to characterize hypersonic wing-elevon-cove flows, specifically the unsteadiness of shock-wave/boundary-layer interactions at the cove. Three hypersonic wing-elevon-cove configurations were computed and subsequently analyzed. The first project started off the investigation, where the unsteady analysis depicted low-frequency motion in shock-wave/boundary-layer interaction and a correlated shock system. This investigation led to experimental interest in the Purdue and UTSI experimental teams. These projects revolved around a three-dimensional swept wing-elevon-cove model that was designed by Carson Lay, of Purdue University. This model is currently being employed in Purdue BAM6QT and UTSI TALon experiments. A computational investigation was done on both wind tunnel configurations and models. While there are no current published experimental results, the computational research and analysis done for this dissertation aided experimentalists in several meaningful ways.

The focus of this work, as a whole, was on the unsteady characteristics and flow behavior of these flows. As a result, there was significant effort to produce unsteady results for this flow in both wind tunnel configurations. Unfortunately, the improved delayed detached-eddy simulation did produce unsteadiness for the Purdue BAM6QT wing-elevon-cove configuration. Therefore, while there was collaborative effort for the second project with the Purdue team, the data presentation focuses on visualization of the complex three-dimensional flowfield. This provides an argument for fidelity to vehicle geometry, as another step away from idealization led to very complex flow configurations elsewhere in the flowfield. Future collaboration with the UTSI experimental team may be done with the unsteady statistics done for the UTSI TALon wing-elevon-cove computation. The Purdue experimental team was able measure low-frequency unsteadiness in the cove, however, the lack of unsteadiness of the shock system was also observed. There is strong evidence of a dependence on Reynolds number to produce unsteadiness in the flow and in the computations. Since the Reynolds number for the wind tunnels are well below realistic flight Reynolds numbers, this may cause a discrepancy between computational, experimental, and flight data for hypersonic wing-elevon-cove flows.

This work has led to an expansion in the communitive research knowledge on geometric imperfections in hypersonic regime. The three hypersonic wing-elevon-cove flows provide general context for the unsteadiness and aerothermodynamic loading for these flows. This material can be applied to hypersonic flight vehicle design, as well as continued fundamental research efforts on hypersonic wing-elevon-cove characteristics. The experimental teams at UTSI and Purdue may use the computational data presented in this dissertation to further compare experimental and computational capabilities. The continued collaboration between experimental and computational methods provides facilitation of research and is needed to further expand the knowledge in this field. As Leonardo da Vinci once said, "Art is never finished, only abandoned."

REFERENCES

[1]   S. Gudmundsson, *General Aviation Aircraft Design Applied Methods and Procedures*, 2nd. Butterworth-Heinemann, 2022, ISBN: 978-0128184653.

[2]   H. Grallert and K. Keller, "Metallic thermal protection concept for hypersonic vehicles," *Journal of Aircraft*, vol. 28, no. 6, pp. 410–416, 1991.

[3]   E. H. Hirschel and C. Weiland, "Design of hypersonic flight vehicles: Some lessons from the past and future challenges," *CEAS Space Journal*, vol. 1, no. 1, pp. 3–22, 2011.

[4]   P. Kutler, "Computational fluid dynamics past, present and future," National Aeronautics and Space Administration, Moffett Field, CA, Tech. Rep. NASA ARC-11738, 1988.

[5]   D. Wilcox, *Turbulence Modeling for CFD*, 3rd. La Cañada Flintridge, California: DCW Industries, Inc., 2006, ISBN: 978-1928729082.

[6]   J. D. Anderson, *Modern Compressible Flow with Historical Perspective*, 4th. New York, NY: McGraw-Hill New York, 2020, ISBN: 978-1260570823.

[7]   J. Délery, J. G. Marvin, and E. Reshotko, "Shock-wave boundary layer interactions," Advisory Group for Aerospace Research and Development, Neuilly-Sur-Seine, France, Tech. Rep. 280, 1986.

[8]   D. V. Gaitonde, "Progress in shock-wave/boundary-layer interactions," *Progress in Aerospace Sciences*, vol. 72, pp. 80–99, 2015.

[9]   W. Saric and E. Reshotko, "Review of flow quality issues in wind tunnel testing," *20th Advanced Measurement and Ground Testing Technology Conference*, AIAA 2613, 1998.

[10]   A. Cenko, "F/A-18C/JDAM CFD challenge wind tunnel and flight test results," *37th Aerospace Sciences Meeting and Exhibit*, AIAA 120, 1999.

[11]   M. Kammeyer, "Wind tunnel facility calibrations and experimental uncertainty," *20th Advanced Measurement and Ground Testing Technology Conference*, AIAA 2715, 1998.

[12] S. Nagai and H. Iijima, "Uncertainty identification of supersonic wind-tunnel testing," *Journal of Aircraft*, vol. 48, no. 2, pp. 567–577, 2011.

[13] D. Belter, "Comparison of wind-tunnel data repeatability with uncertainty analysis estimates," *20th Advanced Measurement and Ground Testing Technology Conference*, AIAA 2714, 1998.

[14] U. Piomelli, "Wall-layer models for large-eddy simulations," *Progress in Aerospace Sciences*, vol. 44, no. 6, pp. 437–446, 2008.

[15] P. R. Spalart, "Strategies for turbulence modelling and simulations," *International Journal of Heat and Fluid Flow*, vol. 21, no. 3, pp. 252–263, 2000.

[16] W. C. Reynolds, "The potential and limitations of direct and large eddy simulations," in *Whither Turbulence? Turbulence at the Crossroads*, Springer, 1990, pp. 313–343.

[17] D. R. Chapman, "Computational aerodynamics development and outlook," *AIAA Journal*, vol. 17, no. 12, pp. 1293–1313, 1979.

[18] The X-43A (Hyper-X) Hypersonic Vehicle, National Aeronautics and Space Administration, [Accessed Online 06-02-22]. https://www.nasa.gov/missions/research/x43-main.html.

[19] L. Keirsbulck, L. Labraga, A. Mazouz, and C. Tournier, "Surface roughness effects on turbulent boundary layer structures," *Journal of Fluids Engineering*, vol. 124, no. 1, pp. 127–135, 2002.

[20] K. D. Fong, X. Wang, and X. Zhong, "Numerical simulation of roughness effect on the stability of a hypersonic boundary layer," *Computers & Fluids*, vol. 96, pp. 350–367, 2014.

[21] P.-Å. Krogstadt and R. A. Antonia, "Surface roughness effects in turbulent boundary layers," *Experiments in Fluids*, vol. 27, no. 5, pp. 450–460, 1999.

[22] C. D. Aubertine, J. K. Eaton, and S. Song, "Parameters controlling roughness effects in a separating boundary layer," *International Journal of Heat and Fluid Flow*, vol. 25, no. 3, pp. 444–450, 2004.

[23]   J. E. Gronvall, N. J. Bisek, and J. Poggie, "High fidelity computational study of the HIFiRE-1 boundary layer trip," *52nd Aerospace Sciences Meeting and Exhibit*, AIAA 433, 2014.

[24]   Q. Tang, Y. Zhu, X. Chen, and C. Lee, "Development of second-mode instability in a Mach 6 flat plate boundary layer with two-dimensional roughness," *Physics of Fluids*, vol. 27, no. 6, 064105, 2015.

[25]   R. L. Kimmel, J. Poggie, and S. N. Schwoerke, "Laminar-turbulent transition in a Mach 8 elliptic cone flow," *AIAA Journal*, vol. 37, no. 9, pp. 1080–1087, 1999.

[26]   J.-M. Charbonnier and H. Boerrigter, "Contribution to the study of gap induced boundary layer transition in hypersonic flow," *5th International Aerospace Planes and Hypersonics Technologies Conference*, AIAA 5111, 1993.

[27]   R. C. Palharini, T. J. Scanlon, and J. M. Reese, "Aerothermodynamic comparison of two- and three-dimensional rarefied hypersonic cavity flows," *Journal of Spacecraft and Rockets*, vol. 51, no. 5, pp. 1619–1630, 2014.

[28]   G. Candler, D. Mavriplis, and L. Trevino, "Current status and future prospects for the numerical simulation of hypersonic flows," *47th Aerospace Sciences Meeting and Exhibit*, AIAA 153, 2009.

[29]   M. Hinderks, A. Gülhan, and R. Radespiel, "Simulation of hypersonic gap flow with consideration of fluid structure interaction," *34th Fluid Dynamics Conference and Exhibit*, AIAA 2238, 2004.

[30]   I. Stern and W. H. Rowe, "Effect of gap size on pressure and heating over the flap of a blunt delta wing in hypersonic flow," *Journal of Spacecraft and Rockets*, vol. 4, no. 1, pp. 109–114, 1967.

[31]   X. Jing, H. Haiming, H. Guo, and M. Song, "Numerical simulation of supersonic gap flow," *PLOS ONE*, vol. 10, no. 1, S. Roy, Ed., 2015.

[32]   L. Cooper and K. E. Putz, "Generalized flow in gaps and slots including the effects of ablation," *Journal of Spacecraft and Rockets*, vol. 11, no. 5, pp. 287–294, 1974.

[33]   A. G. Mikhail, "Assessment of two fast aerodynamic codes for guided projectiles," *Journal of Spacecraft and Rockets*, vol. 24, no. 4, pp. 303–310, 1987.

[34] R. D. Neumann and J. R. Hayes, "Aerodynamic heating in the fin interaction region of generalized missile shapes at Mach 6," Air Force Flight Dynamics Laboratory Wright-Patterson, Dayton, OH, Tech. Rep. NASA TM-79-3066, 1979.

[35] L. R. Hunt, "Aerothermal environment in chordwise gaps between split elevons at Mach 6.8," NASA Langley Research Center Hampton, Tech. Rep. NASA-TP-1783, 1980.

[36] H. Wong and F. Kremer, "Numerical assessment on the heating of the rudder/fin gap in the X-38 space vehicle," in *Proceedings of the Third European Symposium on Aerothermodynamics for Space Vehicles*, ser. ESA Special Publication, vol. 426, 1999, pp. 77–85.

[37] E. R. van Driest, "The problem of aerodynamic heating," *Aeronautical Engineering Review*, vol. 15, pp. 26–41, 1956.

[38] K. H. Gruenewald, "Temperature recovery factors in the transitional and turbulent boundary layer on a 40-degree cone cylinder at Mach number of 2.9," Naval Ordnance Lab, White Oak, MD, Tech. Rep. Navord Report 2742, 1953.

[39] J. Bertin and W. Goodrich, "Aerodynamic heating for gaps in laminar and transitional boundary layers," *18th Aerospace Sciences Meeting and Exhibit*, AIAA 287, 1980.

[40] D. E. Nestler, A. R. Sayhad, and W. L. Auxer, "Heat transfer to steps and cavities in hypersonic turbulent flow," *AIAA Journal*, vol. 7, no. 7, pp. 1368–1370, 1969.

[41] D. E. Nestler, "The effects of surface discontinuities on convective hear transfer in hypersonic flow," *20th Thermophysics Conference*, AIAA 971, 1985.

[42] W. D. Deveikis and W. Bartlett, "Pressure and heat-transfer distributions in a simulated wing-elevon cove with variable leakage at a free-stream Mach number of 6.9," National Aeronautics and Space Administration, Tech Report NASA TM-74095, 1978.

[43] A. Wieting, J. Walsh, and K. Bey, "Aerothermal environment in control surface gaps in hypersonic flow - an overview," National Aeronautics and Space Administration, Moffett Field, CA, Tech. Rep. NASA TM-89224, 1983.

[44] E. Keshock, "Analysis of heat transfer in a simulated wing-elevon cove in hypersonic flow," *16th Aerospace Sciences Meeting and Exhibit*, AIAA 40, 1978.

[45]   R. L. Hunt, "Aerothermal analysis of a wing-elevon cove with variable leakage," National Aeronautics and Space Administration, Technical Paper NASA-TP-1703, 1980.

[46]   N. T. Clemens and V. Narayanaswamy, "Low-frequency unsteadiness of shock wave / turbulent boundary layer interactions," *Annual Review of Fluid Mechanics*, vol. 46, pp. 469–492, 2014.

[47]   J. Poggie and A. J. Smits, "Shock unsteadiness in a reattaching shear layer," *Journal of Fluid Mechanics*, vol. 429, pp. 155–185, 2001.

[48]   S. B. Verma, C. Manisankar, and P. Akshara, "Control of shock-wave boundary layer interaction using steady micro-jets," *Shock Waves*, vol. 25, no. 5, pp. 535–543, 2015.

[49]   T. J. Whalen, A. G. Schöneich, S. J. Laurence, *et al.*, "Hypersonic fluid–structure interactions in compression corner shock-wave/boundary-layer interaction," *AIAA Journal*, vol. 58, no. 9, pp. 4090–4105, 2020.

[50]   A. S. Deshpande and J. Poggie, "Large-scale unsteadiness in a compression ramp flow confined by sidewalls," *Physical Review Fluids*, vol. 6, 024610, 2 2021.

[51]   Y. Wu, S. Yi, L. He, Z. Chen, and Y. Zhu, "Flow visualization of Mach 3 compression ramp with different upstream boundary layers," *Journal of Visualization*, vol. 18, pp. 631–644, 2015.

[52]   J. K. Eaton and J. P. Johnston, "Low-frequency unsteadyness of a reattaching turbulent shear layer," in *Turbulent Shear Flows*, 3rd, Springer, 1982, pp. 162–170.

[53]   T. Leger, N. Bisek, and J. Poggie, "Detached-eddy simulation of a supersonic reattaching shear layer," *AIAA Journal*, vol. 55, no. 11, pp. 3722–3733, 2017.

[54]   A. S. Deshpande and J. Poggie, "Unsteady characteristics of compressible reattaching shear layers," *Physics of Fluids*, vol. 32, no. 6, 066103, 2020.

[55]   S. Terhaar, A. Velazquez, J. Arias, and M. Sanchez-Sanz, "Experimental study on the unsteady laminar heat transfer downstream of a backwards facing step," *International Communications in Heat and Mass Transfer*, vol. 37, no. 5, pp. 457–462, 2010.

[56]   D. M. Driver, H. L. Seegmiller, and J. G. Marvin, "Time-dependent behavior of a reattaching shear layer," *AIAA Journal*, vol. 25, no. 7, pp. 914–919, 1987.

[57] O. U. Khan and K. A. Hoffmann, "Flow control over a backward-facing step with application of a magnetic field," *Journal of Spacecraft and Rockets*, vol. 45, no. 2, pp. 255–263, 2008.

[58] N. J. Mullenix and D. V. Gaitonde, "Analysis of unsteady behavior in shock / turbulent boundary layer interactions with large-eddy simulations," *51st Aerospace Sciences Meeting*, AIAA 404, 2013.

[59] L. P. Riley, R. Ranjan, and D. V. Gaitonde, "Unsteadiness in a supersonic backward-facing step flow," *Aviation Forum*, AIAA 3343, 2019.

[60] J.-P. Dussauge, P. Dupont, and J.-F. Debiève, "Unsteadiness in shock wave boundary layer interactions with separation," *Aerospace Science and Technology*, vol. 10, no. 2, pp. 85–91, 2006.

[61] M. Wu and P. Martin, "Analysis of shock motion in shockwave and turbulent boundary layer interaction using direct numerical simulation data," *Journal of Fluid Mechanics*, vol. 594, pp. 71–83, 2008.

[62] L. Brusniak and D. S. Dolling, "Physics of unsteady blunt-fin-induced shock wave / turbulent boundary layer interactions," *Journal of Fluid Mechanics*, vol. 273, pp. 375–409, 1994.

[63] H. Ngoh and J. Poggie, "Detached eddy simulation of blunt-fin-induced shock-wave / boundary-layer interaction," *AIAA Journal*, vol. 60, no. 4, pp. 2097–2114, 2022.

[64] J.-P. Dussauge and S. Piponniau, "Shock/boundary-layer interactions: Possible sources of unsteadiness," *Journal of Fluids and Structures*, vol. 24, no. 8, pp. 1166–1175, 2008.

[65] T. Leger, N. Bisek, and J. Poggie, "Detached-eddy simulation of a supersonic reattaching shear layer," *AIAA Journal*, vol. 55, no. 11, pp. 3722–3733, 2017.

[66] D. M. Driver, H. L. Seegmiller, and J. G. Marvin, "Time-dependent behavior of a reattaching shear layer," *AIAA Journal*, vol. 25, no. 7, pp. 914–919, 1987.

[67] A. S. W. Thomas, "The unsteady characteristics of laminar juncture flow," *The Physics of Fluids*, vol. 30, no. 2, pp. 283–285, 1987.

[68] J. Poggie and A. Smits, "Experimental evidence for Plotkin model of shock unsteadiness in separated flow," *Physics of Fluids*, vol. 17, no. 1, 018107, 2005.

[69] M. Kussoy, J. Brown, and J. Brown, "Fluctuations and massive separation in three-dimensional shock-wave/boundary-layer interactions," National Aeronautics and Space Administration, Moffett Field, CA, Tech. Rep. NASA TM-89224, 1988.

[70] R. Gramann and D. S. Dolling, "Detection of turbulent boundary-layer separation using fluctuating wall pressure signals," *AIAA Journal*, vol. 28, no. 6, pp. 1052–1056, 1990.

[71] M. E. Erengil and D. S. Dolling, "Correlation of separation shock motion with pressure fluctuations in the incoming boundary layer," *AIAA Journal*, vol. 29, no. 11, pp. 1868–1877, 1991.

[72] S. J. Beresh, N. T. Clemens, and D. S. Dolling, "Relationship between upstream turbulent boundary-layer velocity fluctuations and separation shock unsteadiness," *AIAA Journal*, vol. 40, no. 12, pp. 2412–2422, 2002.

[73] S. Cao, I. Klioutchnikov, and H. Olivier, "Görtler vortices in hypersonic flow on compression ramps," *AIAA Journal*, vol. 57, no. 9, pp. 3874–3884, 2019.

[74] Y. Zhuang, H.-J. Tan, Y.-Z. Liu, Y.-C. Zhang, and Y. Ling, "High resolution visualization of Görtler-like vortices in supersonic compression ramp flow," *Journal of Visualization*, vol. 20, no. 3, pp. 505–508, 2017.

[75] S. R. Choudhury and R. Lovelace, "On the Kelvin-Helmholtz instabilities of supersonic shear layers," *The Astrophysical Journal*, vol. 283, pp. 331–342, 1984.

[76] S. Martens, K. W. Kinzie, and D. K. McLaughlin, "Measurements of Kelvin-Helmholtz instabilities in a supersonic shear layer," *AIAA Journal*, vol. 32, no. 8, pp. 1633–1639, 1994.

[77] S. Thangam and N. Hur, "A highly-resolved numerical study of turbulent separated flow past a backward-facing step," *International Journal of Engineering Science*, vol. 29, no. 5, pp. 607–615, 1991.

[78] R. Alviani, J. Poggie, and G. A. Blaisdell, "Computation of backwards-facing step-ramp induced shock-wave boundary-layer interaction," *SciTech Forum*, AIAA 817, 2020.

[79] S. Pope, *Turbulent Flows*. Cambridge, UK: Cambridge University Press, 2000, ISBN: 978-0521598866.

[80]   W. C. Wan, G. Malamud, A. Shimony, *et al.*, "Observation of single-mode, Kelvin-Helmholtz instability in a supersonic flow," *Physical Review Letters*, vol. 115, no. 14, 145001, 2015.

[81]   P. Hall, "The linear development of Görtler vortices in growing boundary layers," *Journal of Fluid Mechanics*, vol. 130, pp. 41–58, 1983.

[82]   J. Ren and S. Fu, "Secondary instabilities of Görtler vortices in high-speed boundary layer flows," *Journal of Fluid Mechanics*, vol. 781, pp. 388–421, 2015.

[83]   F. Li and M. R. Malik, "Fundamental and subharmonic secondary instabilities of Görtler vortices," *Journal of Fluid Mechanics*, vol. 297, pp. 77–100, 1995.

[84]   A. M. O. Smith, "On the growth of Taylor-Görtler vortices along highly concave walls," *Quarterly of Applied Mathematics*, vol. 13, no. 3, pp. 233–262, 1955.

[85]   M. Sun, N. D. Sandham, and Z. Hu, "Turbulence structures and statistics of a supersonic turbulent boundary layer subjected to concave surface curvature," *Journal of Fluid Mechanics*, vol. 865, pp. 60–99, 2019.

[86]   M. Grilli, S. Hickel, and N. A. Adams, "Large-eddy simulation of a supersonic turbulent boundary layer over a compression–expansion ramp," *International Journal of Heat and Fluid Flow*, vol. 42, pp. 79–93, 2013.

[87]   H. Görtler, "On the three-dimensional instability of laminar boundary layers on concave walls," The National Advisory Committee for Aeronautics, Tech. Rep. NACA TM-1375, 1954.

[88]   W. S. Saric, "Görtler vortices," *Annual Review of Fluid Mechanics*, vol. 26, no. 1, pp. 379–409, 1994.

[89]   J. M. Floryan and W. S. Saric, "Stability of Görtler vortices in boundary layers," *AIAA Journal*, vol. 20, no. 3, pp. 316–324, 1982.

[90]   S. Navarro-Martinez and O. R. Tutty, "Numerical simulation of Görtler vortices in hypersonic compression ramps," *Computers and Fluids*, vol. 34, pp. 225–247, 2005.

[91]   F. Schrijer, "Investigation of Görtler vortices in a hypersonic double compression ramp flow by means of infrared thermography," *Quantitative Infrared Thermography Journal*, vol. 7, no. 2, pp. 201–215, 2010.

[92]   P. D. McCormack, H. Welker, and M. Kelleher, "Taylor-Görtler vortices and their effect on heat transfer," *Journal of Heat Transfer*, vol. 92, no. 1, pp. 101–112, 1970.

[93]   R. Toe, A. Ajakh, and H. Peerhossaini, "Heat transfer enhancement by Görtler instability," *International Journal of Heat and Fluid Flow*, vol. 23, no. 2, pp. 194–204, 2002.

[94]   M. Méndez, M. S. Shadloo, and A. Hadjadj, "Heat-transfer analysis of a transitional boundary layer over a concave surface with Görtler vortices by means of direct numerical simulations," *Physics of Fluids*, vol. 32, no. 7, 074111, 2020.

[95]   F. M. White, *Viscous Fluid Flow*, 4th. New York, NY: McGraw-Hill New York, 2021, ISBN: 978-0073529318.

[96]   Y. Cengel and A. Ghajar, *Heat and Mass Transfer Fundamentals and Applications*, 5th. McGraw Hill, 2014, ISBN: 978-9339223199.

[97]   D. Wilcox, "Turbulence modeling-an overview," *39th Aerospace Sciences Meeting and Exhibit*, AIAA 724, 2001.

[98]   J. Jovanović, *The Statistical Dynamics of Turbulence*, 1st. Heidelberg, Berlin: Springer Science & Business Media, 2004, ISBN: 978-3540203360.

[99]   W. D. McComb, "Theory of turbulence," *Reports on Progress in Physics*, vol. 58, no. 10, pp. 1117–1205, 1995.

[100] P. R. Spalart and S. Allmaras, "A one-equation turbulence model for aerodynamic flows," *30th Aerospace Sciences Meeting and Exhibit*, AIAA 439, 1992.

[101] R. Paciorri, W. Dieudonne, G. Degrez, J.-M. Charbonnier, and H. Deconinck, "Validation of the Spalart-Allmaras turbulence model for application in hypersonic flows," *28th Fluid Dynamics Conference*, AIAA 2023, 1997.

[102] Č. Kostić, "Review of the Spalart-Allmaras turbulence model and its modifications to three-dimensional supersonic configurations," *Scientific Technical Review*, vol. 65, no. 1, pp. 43–49, 2015.

[103] M. Breuer, N. Jovičić, and K. Mazaev, "Comparison of DES, RANS and LES for the separated flow around a flat plate at high incidence," *International Journal for Numerical Methods in Fluids*, vol. 41, no. 4, pp. 357–388, 2003.

[104] D. Corson, R. Jaiman, and F. Shakib, "Industrial application of RANS modelling: Capabilities and needs," *International Journal of Computational Fluid Dynamics*, vol. 23, no. 4, pp. 337–347, 2009.

[105] R. Schwarze and F. Obermeier, "Performance and limitations of the unsteady RANS approach," in *Proceedings in Applied Mathematics and Mechanics*, vol. 6, Wiley Online Library, 2006, pp. 543–544.

[106] R. Alviani, "Assessment of Wilcox κ-ω turbulence model in regions of shock-wave turbulent boundary-layer interaction," M.S. thesis, Rutgers University, School of Graduate Studies, 2018.

[107] D. S. Dolling, "Fifty years of shock-wave / boundary-layer interaction research: What next?" *AIAA Journal*, vol. 39, pp. 1517–1531, 2001.

[108] D. Knight and G. Degrez, "Shock wave boundary layer interactions in high Mach number flows a critical survey of current numerical prediction capabilities," AGARD, AGARD Advisory Report AR-319, Vol. 2, 1998.

[109] D. Knight, H. Yan, A. Panaras, and A. Zheltovodov, "Advances in CFD prediction of shock wave turbulent boundary layer interactions," *Progress in Aerospace Sciences*, vol. 39, pp. 121–184, 2003.

[110] A. Oliver, R. Lillard, A. Schwing, G. Blaisdell, and A. Lyrintzis, "Assessment of turbulent shock boundary layer interaction computations using the OVERFLOW code," *45th Aerospace Sciences Meeting and Exhibit*, AIAA 104, 2007.

[111] L. Wang, R. Hu, and X. Zheng, "A comparative study on the large-scale-resolving capability of wall-modeled large-eddy simulation," *Physics of Fluids*, vol. 32, no. 3, 035102, 2020.

[112] F. F. Grinstein, L. G. Margolin, and W. J. Rider, *Implicit Large Eddy Simulation.* Cambridge University Press Cambridge, 2007, vol. 10, ISBN: 978-0521869829.

[113] J. Fröhlich and D. Von Terzi, "Hybrid LES/RANS methods for the simulation of turbulent flows," *Progress in Aerospace Sciences*, vol. 44, no. 5, pp. 349–377, 2008.

[114] P. R. Spalart, W. Jou, M. Stretlets, and S. Allmaras, "Comments on the feasibility of LES for wings, and on a hybrid RANS/LES approach," in *Proceedings of the First AFOSR International Conference on DNS/LES*, 1997.

[115]   P. R. Spalart, "Detached-eddy simulation," *Annual Review of Fluid Mechanics*, vol. 41, no. 1, pp. 181–202, 2009.

[116]   A. Travin, M. Shur, and M. Strelets, "Improvement of delayed detached-eddy simulation for LES with wall modelling," *European Conference on Computational Fluid Dynamics*, 2006.

[117]   M. Shur, P. R. Spalart, M. Strelets, and A. Travin, "A hybrid RANS-LES approach with delayed-DES and wall-modelled LES capabilities," *International Journal of Heat and Fluid Flow*, vol. 29, no. 6, pp. 1638–1649, 2008.

[118]   N. J. Georgiadis, D. P. Rizzetta, and C. Fureby, "Large-eddy simulation: Current capabilities, recommended practices, and future research," *AIAA Journal*, vol. 48, no. 8, pp. 1772–1784, 2010.

[119]   J. Smagorinsky, "General circulation experiments with the primitive equations: I. The basic experiment," *Monthly Weather Review*, vol. 91, no. 3, pp. 99–164, 1963.

[120]   P. R. Spalart, S. Deck, and M. Shur, "A new version of detached-eddy simulation, resistant to ambiguous grid densities," *Theoretical Computational Fluid Dynamics*, vol. 20, no. 3, pp. 181–195, 2006.

[121]   R. M. Gray and L. D. Davisson, *An Introduction to Statistical Signal Processing*, 1st. New York, NY: Cambridge University Press, 2004, ISBN: 978-0521838603.

[122]   J. Proakis and C. M. Rader, *Algorithms for Statistical Signal Processing*, 1st. London, UK: Prentice Hall, 2002, ISBN: 978-0130622198.

[123]   U. Spagnolini, *Statistical Signal Processing in Engineering*, 1st. Hoboken, NJ: John Wiley & Sons, 2018, ISBN: 978-1119293972.

[124]   D. McDaniel, T. Tuckey, and S. Morton, "The HPCMP CREATE-AV Kestrel computational environment and its relation to NASA's CFD vision 2030," *55th Aerospace Sciences Meeting and Exhibit*, AIAA 813, 2017.

[125]   B. Einfeldt, "On Godunov-type methods for gas dynamics," *SIAM Journal on Numerical Analysis*, vol. 25, no. 2, pp. 294–318, 1988.

[126] R. F. Tomaro, W. Z. Strang, and L. N. Sankar, "An implicit algorithm for solving time dependent flows on unstructured grids," *35th Aerospace Sciences Meeting and Exhibit*, AIAA 333, 1997.

[127] W. D. Deveikis, J. R. Bruce, and J. Karns, "Techniques for aerothermal tests of large, flight weight thermal protection panels in a Mach 7 wind tunnel," *8th Aerodynamic Testing Conference*, AIAA 617, 1974.

[128] P. R. Spalart, "Young-person's guide to detached-eddy simulation grids," National Aeronautics and Space Administration, NASA CR 2001-211032, 2001.

[129] J. Poggie, N. J. Bisek, and R. Gosse, "Resolution effects in compressible, turbulent boundary layer simulations," *Computers and Fluids*, vol. 120, pp. 57–69, 2015.

[130] S. Schneider, S. Rufer, C. Skoch, E. Swanson, and S. Matsumura, "Hypersonic transition research in the Boeing/AFOSR Mach-6 quiet tunnel," *33rd Fluid Dynamics Conference and Exhibit*, AIAA 3450, 2003.

[131] B. C. Chynoweth, J. Edelman, K. Gray, G. McKiernan, and S. P. Schneider, "Measurements in the Boeing/AFOSR Mach-6 quiet tunnel on hypersonic boundary-layer transition," *47th Fluid Dynamics Conference*, AIAA 3632, 2017.

[132] H. Xin, Z. Laiping, Z. Zhong, and C. Xinghua, "The research and development of structured-unstructured hybrid CFD software," *Transactions of Nanjing University of Aeronautics & Astronautics*, vol. 30, pp. 116–126, 2013.

[133] S. Crippa, "Application of novel hybrid mesh generation methodologies for improved unstructured CFD simulations," *28th Applied Aerodynamics Conference*, AIAA 4672, 2010.

[134] J. P. Steinbrenner, "Construction of prism and hex layers from anisotropic tetrahedra," *22nd Computational Fluid Dynamics Conference*, AIAA 2296, 2015.

[135] C. E. Prakash and S. Manohar, "Volume rendering of unstructured grids—a voxelization approach," *Computers & Graphics*, vol. 19, no. 5, pp. 711–726, 1995.

[136] K. Brodlie and J. Wood, "Recent advances in volume visualization," *Computer Graphics Forum*, vol. 20, no. 2, pp. 125–148, 2001.

[137] P. A. Kreth, M. Gragston, K. Davenport, and J. D. Schmisseur, "Design and initial characterization of the UTSI Mach 4 Ludwieg tube," *SciTech Forum*, AIAA 384, 2021.

[138] R. Alviani, J. Poggie, and G. Blaisdell, "Detached eddy simulation of supersonic wing-elevon cove boundary-layer ingestion," *Aviation Forum*, AIAA 3008, 2020.

[139] R. Alviani, J. Poggie, and G. Blaisdell, "Unsteady aspects of shock-wave/boundary-layer interaction resulting from control surface deflection," *Aviation Forum*, AIAA 2823, 2021.

[140] R. Alviani, J. Poggie, and G. Blaisdell, "Unsteady aspects of shock-wave/boundary-layer interaction resulting from control surface deflection," *AIAA Journal*, vol. 60, no. 8, pp. 4649–4659, 2022.

[141] Y. Dubief and F. Delcayre, "On coherent-vortex identification in turbulence," *Journal of Turbulence*, vol. 1, no. 1, N11, 2000.

[142] H. E. Fiedler, "Coherent structures in turbulent flows," *Progress in Aerospace Sciences*, vol. 25, no. 3, pp. 231–269, 1988.

[143] S. Cao, I. Klioutchnikov, and H. Oliver, "Görtler vortices in hypersonic flow on compression ramps," *AIAA Journal*, vol. 57, no. 9, pp. 3874–3884, 2019.

[144] S. Priebe, J. H. Tu, C. W. Rowley, and M. P. Martín, "Low-frequency dynamics in a shock-induced separated flow," *Journal of Fluid Mechanics*, vol. 807, pp. 441–477, 2016.

[145] A. Dwivedi, G. S. Sidharth, J. Nichols, G. V. Candler, and M. R. Jovanović, "Reattachment streaks in hypersonic compression ramp flow: An input–output analysis," *Journal of Fluid Mechanics*, vol. 880, pp. 113–135, 2019.

[146] O. M. Phillips, "The maintenance of Reynolds stress in turbulent shear flow," *Journal of Fluid Mechanics*, vol. 27, no. 1, pp. 131–144, 1967.

[147] O. M. Phillips, "Shear-flow turbulence," *Annual Review of Fluid Mechanics*, vol. 1, no. 1, pp. 245–264, 1969.

[148] S. B. Korsholm, P. K. Michelsen, V. Naulin, *et al.*, "Reynolds stress and shear flow generation," *Plasma Physics and Controlled Fusion*, vol. 43, no. 10, pp. 1377–1395, 2001.

[149] D. S. Dolling and C. T. Or, "Unsteadiness of the shock wave structure in attached and separated compression ramp flows," *Experiments in Fluids*, vol. 3, no. 1, pp. 24–32, 1985.

[150] S. Priebe and M. P. Martín, "Low-frequency unsteadiness in shock wave-turbulent boundary layer interaction," *Journal of Fluid Mechanics*, vol. 699, pp. 1–49, 2012.

[151] L. Agostini, L. Larchevêque, P. Dupont, J.-F. Debiève, and J.-P. Dussauge, "Zones of influence and shock motion in a shock/boundary-layer interaction," *AIAA Journal*, vol. 50, no. 6, pp. 1377–1387, 2012.

[152] P. Dimotakis, "On the convection velocity of turbulent structures in supersonic shear layers," *22nd Fluid Dynamics, Plasma Dynamics and Lasers Conference*, AIAA 1724, 1991.

[153] P.-Å. Krogstad, J. H. Kaspersen, and S. Rimestad, "Convection velocities in a turbulent boundary layer," *Physics of Fluids*, vol. 10, no. 4, pp. 949–957, 1998.

[154] C. Atkinson, N. A. Buchmann, and J. Soria, "An experimental investigation of turbulent convection velocities in a turbulent boundary layer," *Flow, Turbulence and Combustion*, vol. 94, no. 1, pp. 79–95, 2015.

[155] M. Wu and M. P. Martin, "Analysis of shock motion in shockwave and turbulent boundary layer interaction using direct numerical simulation data," *Journal of Fluid Mechanics*, vol. 594, pp. 71–83, 2008.

[156] S. Piponniau, J.-P. Dussauge, J.-F. Debieve, and P. Dupont, "A simple model for low-frequency unsteadiness in shock-induced separation," *Journal of Fluid Mechanics*, vol. 629, pp. 87–108, 2009.

[157] P. Ligrani, M. Cox, and K. Goethals, "Spatial coherence of low-frequency unsteadiness associated with a normal shock wave," *Aerospace Science and Technology*, vol. 112, 106637, 2021.

[158] P. Dupont, C. Haddad, and J. F. Debieve, "Space and time organization in a shock-induced separated boundary layer," *Journal of Fluid Mechanics*, vol. 559, pp. 255–277, 2006.

[159] E. Touber and N. D. Sandham, "Large-eddy simulation of low-frequency unsteadiness in a turbulent shock-induced separation bubble," *Theoretical and Computational Fluid Dynamics*, vol. 23, no. 2, pp. 79–107, 2009.

[160] B. John, V. N. Kulkarni, and G. Natarajan, "Shock wave boundary layer interactions in hypersonic flows," *International Journal of Heat and Mass Transfer*, vol. 70, pp. 81–90, 2014.

[161] J. J. Bertin and R. M. Cummings, "Critical hypersonic aerothermodynamic phenomena," *Annual Review of Fluid Mechanics*, vol. 38, pp. 129–157, 2006.

[162] R. Alviani, G. A. Blaisdell, and J. Poggie, "Computational analysis of planned high-speed swept wing-elevon experiments," *SciTech Forum*, AIAA 2198, 2022.

[163] L. J. Souverein, P. Dupont, J.-F. Debieve, J.-P. Dussauge, B. W. Van Oudheusden, and F. Scarano, "Effect of interaction strength on unsteadiness in shock-wave-induced separations," *AIAA Journal*, vol. 48, no. 7, pp. 1480–1493, 2010.

[164] J. A. Threadgill and P. J. Bruce, "Unsteadiness in shock wave boundary layer interactions across multiple interaction configurations," *53rd Aerospace Sciences Meeting and Exhibit*, AIAA 1977, 2015.

[165] T. Li and R. Geiger, "Stagnation point of a blunt body in hypersonic flow," *Journal of the Aeronautical Sciences*, vol. 24, no. 1, pp. 25–32, 1957.

[166] E. Reshotko and C. Cohen, "Heat transfer at the forward stagnation point of blunt bodies," Lewis Flight Propulsion Laboratory, Technical Report NACA TN-3513, 1955.

[167] D. Knight, C. C. Horstman, B. Shapey, and S. Bogdonoff, "Structure of supersonic turbulent flow past a sharp fin," *AIAA Journal*, vol. 25, no. 10, pp. 1331–1337, 1987.

[168] F. K. Lu and G. S. Settles, "Upstream-influence scaling of sharp fin interactions," *AIAA Journal*, vol. 29, no. 7, pp. 1180–1181, 1991.

[169] B. Gibson and D. S. Dolling, "Wall pressure fluctuations near separation in a Mach 5, sharp fin-induced turbulent interaction," *29th Aerospace Sciences Meeting and Exhibit*, AIAA 646, 1991.

[170] R. Sedney and C. W. Kitchens Jr, "Separation ahead of protuberances in supersonic turbulent boundary layers," *AIAA Journal*, vol. 15, no. 4, pp. 546–552, 1977.

[171] P. V. Hahn and A. Frendi, "Interaction of three-dimensional protuberances with a supersonic turbulent boundary layer," *AIAA Journal*, vol. 51, no. 7, pp. 1657–1666, 2013.

[172] S. A. Lindörfer, C. S. Combs, P. A. Kreth, and J. D. Schmisseur, "Numerical simulations of a cylinder-induced shock wave/boundary layer interaction," *55th Aerospace Sciences Meeting and Exhibit*, AIAA 534, 2017.

[173] D. S. Dolling and S. M. Bogdonoff, "Blunt fin-induced shock wave/turbulent boundary-layer interaction," *AIAA Journal*, vol. 20, no. 12, pp. 1674–1680, 1982.

[174] A. Houwing, D. Smith, J. Fox, P. Danehy, and N. Mudford, "Laminar boundary layer separation at a fin-body junction in a hypersonic flow," *Shock Waves*, vol. 11, pp. 31–42, 2001.

[175] W. Devenport, M. Rife, S. Liapis, I. Stergios, and G. Follin, "The structure and development of a wing-tip vortex," *Journal of Fluid Mechanics*, vol. 312, pp. 67–106, 1996.

[176] A. Uzun and M. Hussaini, "Simulations of vortex formation around a blunt wing tip," *AIAA Journal*, vol. 48, no. 6, pp. 1221–1234, 2010.

[177] R. Satti, Y. Li, R. Shock, and S. Noelting, "Unsteady flow analysis of a multi-element airfoil using lattice boltzmann method," *AIAA Journal*, vol. 50, no. 9, pp. 1805–1816, 2012.

[178] C. L. Rumsey and S. X. Ying, "Prediction of high lift: Review of present CFD capability," *Progress in Aerospace Sciences*, vol. 38, no. 2, pp. 145–180, 2002.

[179] C. L. Rumsey, E. M. Lee-Rausch, and R. D. Watson, "Three-dimensional effects in multi-element high lift computations," *Computers & Fluids*, vol. 32, no. 5, pp. 631–657, 2003.

[180] D. McMaster and J. Shang, "A numerical study of three-dimensional separated flows around a sweptback blunt fin," *26th Aerospace Sciences Meeting and Exhibit*, AIAA 125, 1988.

[181] P. Schuricht and G. Roberts, "Hypersonic interference heating induced by a blunt fin," *8th International Space Planes and Hypersonic Systems and Technologies Conference*, AIAA 1579, 1998.

[182] E. V. Kolesnik and A. A. Smirnovsky, "Numerical study of the vortex structure influence on heat transfer in the supersonic flow past a plate and a blunt fin junction," *Journal of Physics*, vol. 1400, no. 7, 077030, 2019.

[183] U. Pathak, S. Roy, and K. Sinha, "A phenomenological model for turbulent heat flux in high-speed flows with shock-induced flow separation," *Journal of Fluids Engineering*, vol. 140, no. 5, 051203, 2018.

[184] M. Bernardini, I. Asproulias, J. Larsson, S. Pirozzoli, and F. Grasso, "Heat transfer and wall temperature effects in shock wave turbulent boundary layer interactions," *Physical Review Fluids*, vol. 1, no. 8, 084403, 2016.

[185] P. S. Bernard, J. M. Thomas, and R. A. Handler, "Vortex dynamics and the production of Reynolds stress," *Journal of Fluid Mechanics*, vol. 253, pp. 385–419, 1993.

[186] J. Fang, A. A. Zheltovodov, Y. Yao, C. Moulinec, and D. R. Emerson, "On the turbulence amplification in shock-wave/turbulent boundary layer interaction," *Journal of Fluid Mechanics*, vol. 897, A32, 2020.

[187] J. Délery and J.-P. Dussauge, "Some physical aspects of shock wave/boundary layer interactions," *Shock Waves*, vol. 19, no. 6, pp. 453–468, 2009.

[188] M. Bernardini and S. Pirozzoli, "Wall pressure fluctuations beneath supersonic turbulent boundary layers," *Physics of Fluids*, vol. 23, no. 8, 085102, 2011.

[189] D. M. Chase, "Modeling the wavevector-frequency spectrum of turbulent boundary layer wall pressure," *Journal of Sound and Vibration*, vol. 70, no. 1, pp. 29–67, 1980.

[190] T. M. Farabee and M. J. Casarella, "Spectral features of wall pressure fluctuations beneath turbulent boundary layers," *Physics of Fluids*, vol. 3, no. 10, pp. 2410–2420, 1991.

[191] R. L. Kimmel, A. Demetriades, and J. C. Donaldson, "Space-time correlation measurements in a hypersonic transitional boundary layer," *AIAA Journal*, vol. 34, no. 12, pp. 2484–2489, 1996.

[192] S. Robinson, "Space-time correlation measurements in a compressible turbulent boundary layer," *4th Joint Fluid Mechanics, Plasma Dynamics and Lasers Conference*, AIAA 1130, 1986.

[193] T. Colonius, A. Basu, and C. Rowley, "Numerical investigation of the flow past a cavity," *5th Aeroacoustics Conference and Exhibit*, AIAA 1912, 1999.

[194] D. Williams, D. Fabris, and J. Morrow, "Experiments on controlling multiple acoustic modes in cavities," *6th Aeroacoustics Conference and Exhibit*, AIAA 1903, 2000.

[195] L. Larchevêque, P. Sagaut, T.-H. Lê, and P. Comte, "Large-eddy simulation of a compressible flow in a three-dimensional open cavity at high Reynolds number," *Journal of Fluid Mechanics*, vol. 516, pp. 265–301, 2004.

[196] M. A. Kegerise, E. F. Spina, S. Garg, and L. N. Cattafesta III, "Mode-switching and nonlinear effects in compressible flow over a cavity," *Physics of Fluids*, vol. 16, no. 3, pp. 678–687, 2004.

[197] D. Sziroczak and H. Smith, "A review of design issues specific to hypersonic flight vehicles," *Progress in Aerospace Sciences*, vol. 84, pp. 1–28, 2016.

[198] E. H. Hirschel and C. Weiland, *Selected Aerothermodynamic Design Problems of Hypersonic Flight Vehicles*. Springer Science & Business Media, 2009, vol. 229.

[199] D. Knight, J. Longo, D. Drikakis, *et al.*, "Assessment of CFD capability for prediction of hypersonic shock interactions," *Progress in Aerospace Sciences*, vol. 48, pp. 8–26, 2012.

[200] A. Katz and V. Sankaran, "Mesh quality effects on the accuracy of CFD solutions on unstructured meshes," *Journal of Computational Physics*, vol. 230, no. 20, pp. 7670–7686, 2011.

[201] K. Nakahashi, Y. Ito, and F. Togashi, "Some challenges of realistic flow simulations by unstructured grid CFD," *International Journal for Numerical Methods in Fluids*, vol. 43, no. 6-7, pp. 769–783, 2003.

[202] A. Issakhov, "Modeling of synthetic turbulence generation in boundary layer by using zonal RANS/LES method," *International Journal of Nonlinear Sciences and Numerical Simulation*, vol. 15, no. 2, pp. 115–120, 2014.

[203] N. Jarrin, R. Prosser, J.-C. Uribe, S. Benhamadouche, and D. Laurence, "Reconstruction of turbulent fluctuations for hybrid RANS/LES simulations using a synthetic-eddy method," *International Journal of Heat and Fluid Flow*, vol. 30, no. 3, pp. 435–442, 2009.

[204] H. Ngoh and J. Poggie, "Forced separation unsteadiness in a supersonic blunt fin flow," *Physical Review Fluids*, vol. 7, no. 9, 093903, 2022.

[205]   E. H. Hirschel, "Thermal surface effects in aerothermodynamics," *Aerothermodynamics for Space Vehicles*, vol. 426, p. 17, 1999.

[206]   E. H. Dowell and K. C. Hall, "Modeling of fluid-structure interaction," *Annual Review of Fluid Mechanics*, vol. 33, p. 445, 2001.

[207]   T. Belytschko, "Fluid-structure interaction," *Computers & Structures*, vol. 12, no. 4, pp. 459–469, 1980.

[208]   D. M. Bushnell, "Scaling: Wind tunnel to flight," *Annual Review of Fluid Mechanics*, vol. 38, pp. 111–128, 2006.

[209]   E. J. Saltzman and T. G. Ayers, "Review of flight-to-wind-tunnel drag correlation," *Journal of Aircraft*, vol. 19, no. 10, pp. 801–811, 1982.